

**Università degli Studi Roma TRE**

**e**

**Consorzio Nazionale Interuniversitario per le Scienze  
Fisiche della Materia**

**Dottorato di Ricerca in Scienze Fisiche della Materia  
XXV ciclo**

**Electron-vibron interaction effects on the electronic  
transport through molecular systems**

**Tesi di dottorato del dott. Alberto Nocera**

Relatori:  
Prof. Vittorio Cataudella  
Dott. Carmine Antonio Perroni  
Prof. Vincenzo Marigliano Ramaglia

Coordinatore Dottorato  
Prof. Settimio Mobilio

a. a. 2012/2013

# Contents

|  |           |
|--|-----------|
| <b>List of Figures</b>   | <b>2</b>  |
| <b>Abstract</b>  | <b>10</b> |
| <b>1 Introduction</b>  | <b>12</b> |
| 1.1 Towards molecular electronics . . . . .  | 12        |
| 1.1.1 Conductance of single molecules . . . . .  | 15        |
| 1.1.2 NDR and Hysteresis in molecular junctions . . . . .  | 17        |
| 1.1.3 Incoherent vs coherent transport . . . . .   | 19        |
| 1.2 Nanoelectromechanical Systems . . . . .  | 21        |
| 1.2.1 Applications of NEMS . . . . .   | 21        |
| 1.2.2 Carbon nanotubes: Nonlinear high-Q nanomechanical resonators . . .   | 23        |
| 1.2.3 Nonlinear effects in Carbon Nanotube resonators . . . . .  | 25        |
| 1.3 Electronic correlation in transport through Nanostructures . . . . .   | 26        |
| 1.3.1 The Kondo Effect in Nanostructures . . . . .   | 26        |
| 1.3.2 Key experiments on correlated nanotransport . . . . .  | 28        |
| 1.4 Theoretical methods . . . . .  | 30        |
| 1.5 Outline of the thesis . . . . .  | 31        |
| <b>2 Electronic transport through an interacting molecular junction:<br/>coupling to a low frequency vibrational mode</b>                | <b>32</b> |
| 2.1 The Anderson-Holstein (AH) model . . . . .   | 32        |
| 2.1.1 Out of equilibrium Born-Oppenheimer approximation: infinite mass<br>(static) case . . . . .  | 33        |
| 2.1.2 Dynamical (finite mass) corrections to static case: setting Langevin<br>equation for the oscillator . . . . .                      | 35        |
| 2.1.3 Numerical solution of Langevin equation: <i>electronic</i> observables and<br>limits of the stochastic approach . . . . .          | 38        |
| 2.2 The two-site SSH model . . . . .   | 46        |
| 2.2.1 Out of equilibrium Born-Oppenheimer approximation: infinite mass<br>(static) case . . . . .  | 48        |
| 2.2.2 Adiabatic Approximation: calculation of damping and fluctuating term   | 51        |
| 2.2.3 Analysis of Numerical results . . . . .  | 52        |
| <b>3 Electronic transport through a nanomechanical resonator acting as elec-<br/>tronic transistor in the presence of nearby antenna</b> | <b>57</b> |
| 3.1 Introduction . . . . .   | 57        |
| 3.2 Model and method . . . . .   | 60        |
| 3.3 Langevin equation for the oscillator . . . . .   | 60        |
| 3.4 Results . . . . .  | 62        |

|          |   |            |
|----------|---|------------|
| 3.4.1    | Nonlinear regime of oscillator's dynamics . . . . .   | 63         |
| 3.5      | Introduction of a transverse Magnetic field . . . . .   | 65         |
| 3.5.1    | Model . . . . .   | 66         |
| 3.5.2    | Adiabatic approximation . . . . .   | 68         |
| 3.5.3    | Mechanical and electronic characteristics of the device . . . . .   | 76         |
| 3.5.4    | Discussion . . . . .  | 84         |
| <b>4</b> | <b>Electronic transport through a strongly correlated molecular junction: coupling with a high frequency vibrational mode</b> | <b>86</b>  |
| 4.1      | Introduction . . . . .  | 86         |
| 4.2      | Hamiltonian of a Quantum Shuttle . . . . .  | 87         |
| 4.3      | Alternative method for calculating conductance through a region with interaction . . . . .                                    | 89         |
| 4.3.1    | Folding Transformation: ``even`` and ``odd`` cases . . . . .  | 89         |
| 4.4      | Numerical Results . . . . .   | 91         |
| 4.4.1    | Scaling analysis of the current in absence of electron-phonon interaction   | 91         |
| 4.5      | Behavior of the electronic current including the phonon effects . . . . .   | 93         |
| 4.6      | Static and dynamical properties of the shuttle mode for $\lambda = 0$ . . . . .   | 94         |
| <b>5</b> | <b>Conclusions</b>  | <b>98</b>  |
| <b>A</b> | <b>Non-Equilibrium contour-ordered Green Functions</b>  | <b>102</b> |
| A.1      | Introduction . . . . .  | 102        |
| A.2      | Equilibrium Green's functions . . . . .   | 102        |
| A.2.1    | Dyson's and Keldysh's equations . . . . .   | 106        |
| <b>B</b> | <b>Capacitive coupling vs Anderson-Holstein model</b>   | <b>109</b> |
| <b>C</b> | <b>Current-current and Current-density fluctuation</b>  | <b>111</b> |
| <b>D</b> | <b>The Density Matrix Renormalization Group</b>   | <b>118</b> |
| D.1      | The DMRG algorithm . . . . .  | 118        |
| D.1.1    | DMRG-projection . . . . .   | 119        |
| D.1.2    | Infinite-system DMRG . . . . .  | 122        |
| D.1.3    | Finite-system DMRG . . . . .  | 123        |
| D.2      | Dynamical correlation functions using DMRG . . . . .  | 124        |
| D.2.1    | Correction Vector . . . . .   | 125        |
| <b>E</b> | <b>Magnetic field correction to the hopping matrix element for a particle in a tight-binding ring</b>                         | <b>127</b> |
|          | <b>Bibliography</b>   | <b>128</b> |
|          | <b>Acknowledgments</b>  | <b>137</b> |

# List of Figures

|     |  |    |
|-----|--|----|
| 1.1 | Simple picture of elastic and inelastic tunneling processes. . . . .   | 14 |
| 1.2 | Conductance measurement with STM. The current and its higher derivatives are recorded while sweeping the bias voltage for (1) tip over molecule and (2) tip over bare substrate. The relevant signal is the background subtracted difference (1-2). Data are shown for an acetylene molecule $C_2H_2$ (adapted from [15] ). The minute conductance increase around $358mV$ indicates the opening of an inelastic channel. . . . .  | 15 |
| 1.3 | $I(V)$ characteristics taken on two different parts of an octanethiolate molecule adsorbed on a Pt chain, as indicated by the blue dot and the red triangle in the STM image of panel A (Figure taken from Ref.[16]). Panel B shows a detailed view of the voltage window from 0 to $0.4V$ where current against voltage curve is linear. . . . .  | 16 |
| 1.4 | $I-V$ characteristic of the $C_{60}$ molecule (adapted from [19]). The device is clearly acting as a transistor where the gate voltage controls the current between source and drain. The series of steps in the current are known as Frank Condon steps caused by vibrational excitations. . . . .  | 17 |
| 1.5 | Conductance measurement of the hydrogen molecule between platinum contacts adapted from [22]. The symmetric decrease seen around $63.5mV$ was interpreted as related to excitation of the center-of-mass motion of the $H_2$ -molecule shown in the inset. . . . .   | 18 |
| 1.6 | NDR of a junction based on monolayer of 2'-amino-4-ethynylphenyl-4'-ethynylphenyl-5'-nitro-1-benzenethiolate embedded between gold wires at $60K$ . Shown on the left is the reported $I-V$ characteristic with NDR peak to valley ratio 1030 : 1. The temperature dependence of the current and voltage values at the peak is shown on the right. (From Ref [23]). . . . .  | 18 |
| 1.7 | Current-voltage measurements on individual BPDN molecules by STM with BPDN embedded into $C_{11}$ alkane matrix (a) and cross-wire tunneling junction (c) are presented in Figs. (b) and (d) respectively. (From Ref [7]). . . . .   | 19 |
| 1.8 | Mechanistic turnover from tunneling to hopping in short strand duplex DNA. The curve on the left shows tunneling through the AT segment, resulting in exponential decay of conductance with length. The segment on the right is for poly GC where transport occurs by hopping and the conductance scales like the inverse length (as it must for diffusion). From Ref. [25]. . . . .   | 20 |
| 1.9 | Onset of activated transport in a non-conjugated molecule. At low temperatures, quantum mechanical tunneling is seen, and the current is independent of temperature. As room temperature is approached, the transport becomes activated. The argument made by the authors is that the small activation energies describe the overlap of the Gaussian spectral density tail with the Fermi occupation tail. From Ref. [35]. . . . . | 21 |

|      |  |    |
|------|--|----|
| 1.10 | General properties and device parameters for a single-walled CNT. This Table was taken from Ref. [48]. . . . .   | 24 |
| 1.11 | Detecting the CNT's motion using the rectification technique. A CNT is doubly clamped between a source and a drain electrode suspended above a gate electrode. The CNT is driven by a high-frequency signal applied to an antenna at approximately 2 cm from the CNT. The single-electron tunnel current through the CNT quantum dot contains information on the oscillation of the CNT at DC due to a rectification effect from Coulomb blockade. . . .   | 25 |
| 1.12 | Top: Coulomb oscillations of the current through a CNT quantum dot; in Coulomb blockade current is zero and the indicated (negative) number of electrons on the CNT is fixed. Between charge states a single-electron tunneling current is visible as Coulomb peaks. Bottom: Gate dependence of resonance frequency (from [11]); the features are indicated by the encircled numbers: (1) a slope caused by tension at fixed charge, (2) a frequency offset caused by a tension difference between charge states, and (3) frequency dips caused by single-electron tunneling. This Fig. was taken from Ref. [11]. . .  | 26 |
| 1.13 | Left: Electronic current vs. antenna frequency at high antenna amplitude for increasing temperature from top to bottom. Right: Electronic current vs. antenna frequency at low temperature for increasing antenna amplitudes from top to bottom. This Fig. was taken from Ref. [12]. . . . .   | 27 |
| 1.14 | The main results of two important experiments reporting the observation of the Kondo effect in QDs: Left panel taken from Ref. [66] and right panel taken from Ref. [55] . . . . .   | 28 |
| 1.15 | Panel(a): $dI/dV$ for a device investigate in [63] at $T = 1.6K$ showing satellite peaks near $\pm 33mV$ . Left inset: Schematic of the $H_g(1)$ intracage vibrational mode. Right inset: $dI/dV$ for another device at $T = 1.6K$ . Panels(b),(c): $d^2I/dV^2$ as a function of bias voltage and electrode spacing for devices investigate in panel (a) at $T = 1.6K$ . Panel (d): $dI/dV$ traces of a device at various electrode spacings for $T = 1.6K$ . $x_0 \simeq 1nm$ is the initial gap between the leads. This figure is taken from Ref. [63]. . . . .  | 30 |
| 2.1  | Spatial dependence of the dimensionless generalized static potential $\bar{U}(\bar{x})$ (panels A,B), friction coefficient $\bar{A}(\bar{x})$ (panels C,D), fluctuating term $\bar{D}(\bar{x})$ (panels E,F) for symmetric $E_g \sim E_p$ and asymmetric $E_g < E_p$ minima for different values of bias, $V_{bias} = 0$ (solid (black) curve), $V_{bias} = 2$ (dashed (red) curve), $V_{bias} = 4$ (dashed dot (green) curve). The potential is expressed in $\hbar\Gamma$ units ( $\bar{U} = U/\hbar\Gamma$ ), the friction coefficient in $m\omega_0$ units ( $\bar{A} = A/m\omega_0$ ), the fluctuating term in $\lambda^2/\omega_0$ units, ( $\bar{D} = D/(\lambda^2/\omega_0)$ ). $V_{bias}$ values are expressed in $\hbar\Gamma/e$ units, where $e$ is the electron charge. The dimensionless position variable $\bar{x}$ is defined as $\bar{x} = x/x_0$ with $x_0 = \frac{\lambda}{m\omega_0^2}$ . . . . . | 34 |
| 2.2  | Panel A: Solution of the Langevin equation Eq. 2.25 in the extremely strong coupling regime $E_p \gg \hbar\Gamma \gg \hbar\omega_0$ ( $\omega_0/\Gamma = 10^{-3}$ ) for $\hbar\Gamma/2E_p = 0.08$ , $E_g = E_p$ and $eV_{Bias} = 0.1$ . Panel B: Current ( $e\Gamma$ units) voltage ( $eV_{bias}$ in $2E_p$ units) characteristic for the same value of $\hbar\Gamma/2E_p$ as above. Solid (red) curve is drown from Ref[28], square line indicates my dynamic simulation and dashed line indicates static I-V. Panel C: Dimensionless position distribution probability for the same values of parameters as in Panel A. The dimensionless position $\bar{x}$ , time $\bar{t}$ and distribution function $\bar{P}$ are defined as $\bar{x} = x/x_0$ , $\bar{t} = t/t_0$ , $\bar{P} = P/(1/x_0)$ , with $x_0 = \frac{\lambda}{m\omega_0^2}$ and $t_0 = 1/\omega_0$ , respectively. . . . .                           | 40 |

|      |  |    |
|------|--|----|
| 2.3  | Panel A: log-plot of <i>dimensionless</i> velocity probability distribution function vs. $v^2$ , at different adiabatic ratios (the values of $\omega_0$ shown in the figure are in $\Gamma$ units), fixed bias voltage $V_{bias} = 0.1$ and different gate voltages and EOC strengths (not shown in the graph). The dotted (red) lines indicate that curves have a good linear fit. Panels B–C–D: log-plot of velocity probability distribution function vs. $v^2$ for $V_{bias} = 0.1$ , $V_{bias} = 1.1$ , $V_{bias} = 2.1$ , respectively. The dashed (red) line indicates linear fitting. Dotted (green) and dash dotted (blue) lines indicate polynomial fitting of 2nd and 4th degree. $V_{bias}$ values are expressed in $\hbar\Gamma/e$ units. The dimensionless distribution function is defined as $\bar{P} = P/(m\omega_0/\lambda)$ , while $v^2$ is expressed in $(\lambda/m\omega_0)^2$ units. . . . . | 41 |
| 2.4  | Main: plot of average kinetic energy $\langle E_{Kin} \rangle$ as function of the bias voltage at fixed adiabatic ratio $\omega_0/\Gamma = 0.1$ and gate voltage $E_g = 0$ , for different interaction strengths $E_p$ : $E_p = 0.1$ square (black) curve, $E_p = 1.0$ circle (red) curve, $E_p = 2.0$ triangle (green) curve, $E_p = 3.0$ star (blue) curve. Two constant energy lines $E = \hbar\omega_0/2\hbar\Gamma = 0.05$ (dashed) and $E = \hbar\Gamma = 1$ (dotted) are also plotted. Inset: Average kinetic energy $\langle E_{Kin} \rangle$ for low bias voltages for the same parameter values of the main plot. The dotted (magenta) line indicates the linear approximation $eV_{bias}/8$ derived in Ref.[27] (I choose a broadening $\hbar\Gamma$ half than used in Ref.[27]). All the quantities ( $\langle E_{Kin} \rangle$ , $E_p$ , $E_g$ and $eV_{bias}$ ) are in unit $\hbar\Gamma$ . . . . .    | 42 |
| 2.5  | Phase diagram at fixed adiabatic ratio $\omega_0/\Gamma = 0.05$ (the value of $\omega_0$ shown in the figure is in $\Gamma$ units). The dashed (black) line indicates the QR boundary for $E_g = 0$ and $E_g = 1$ . The dotted (red) and dashed dotted (green) lines refer to the CAR boundary for $E_g = 0$ and $E_g = 1$ , respectively. $E_p$ , $E_g$ and $eV_{bias}$ are expressed in unit $\hbar\Gamma$ . . . . .   | 42 |
| 2.6  | Phase diagram at fixed gate voltage $E_g = 0$ (asymmetric static potential) for different adiabatic ratios $\omega_0/\Gamma = 0.01 - 0.05 - 0.1 - 0.25$ (the values of $\omega_0$ shown in the figure are in $\Gamma$ units). $E_p$ , $E_g$ and $eV_{bias}$ are in $\hbar\Gamma$ units. . . .  | 43 |
| 2.7  | Panel A: Conductance (in units $G_0 = \frac{e^2}{h}$ ) in the static approximation as function of bias voltages, for $\omega_0/\Gamma = 0.05$ , $E_g = 0$ at different interaction strengths $E_p = 0.05, 0.5, 1.0, 2.0, 3.0$ . Panel B: Dynamical correction to the conductance for the same parameter values of panel A. The value of $\omega_0$ shown in the figure is in $\Gamma$ units while all other quantities ( $E_g$ , $E_p$ and $eV_{bias}$ ) are expressed in $\hbar\Gamma$ units. . . . .   | 44 |
| 2.8  | Panel A: Electronic occupation as function of bias voltages, for $E_g = 0$ , $E_p = 2$ at different adiabatic ratios $\omega_0/\Gamma = 0.05, 0.25, 0.5, 1.0$ . Panel B: Current voltage characteristic for the same value of the parameters of panel A. The values of $\omega_0$ shown in the figure are in $\Gamma$ units while all other quantities ( $E_g$ , $E_p$ and $eV_{bias}$ ) are expressed in $\hbar\Gamma$ units. . . . .   | 45 |
| 2.9  | Panel A: Current as function of gate voltages, for $\omega_0/\Gamma = 0.05$ , $E_p = 0.25$ at different bias voltages $V_{bias} = 0.1, 1.0, 2.0$ . Panel B: Plot of average kinetic energy as function of the gate for $V_{bias} = 0.1, 1.0, 2.0$ . The value of $\omega_0$ shown in the figure is in $\Gamma$ units, while $E_g$ and $E_p$ are expressed in $\hbar\Gamma$ units. $V_{bias}$ is expressed in $\hbar\Gamma/e$ units. . . . .  | 45 |
| 2.10 | Sketch of junction within the SSH model in an energy scale. . . . .  | 47 |

- 2.11 Panel A: Spatial dependence of the dimensionless generalized static potential  $\bar{V}_{SSH}(\bar{x})$  at  $\omega_0/\Gamma = 0.1$ ,  $E_p = 0.2$ , gate voltage  $E_g = 0$ , intermolecular hopping  $t = 2.0$ , for different values of the bias voltage:  $V_{bias} = 0.0$  (solid (black) curve),  $V_{bias} = 3.5$  (dashed (red) curve),  $V_{bias} = 4.0$  (dotted (green) curve),  $V_{bias} = 6.0$  (dashed dotted (blue) curve). The vertical lines indicate the position of the minima of the potential. Panel B: Same as above for  $\omega_0/\Gamma = 0.1$ ,  $E_p = 1.4$ ,  $t = 0.2$ , gate voltage  $E_g = 2$  and different values of the bias voltage:  $V_{bias} = 0$  (solid (black) curve),  $V_{bias} = 4$  (dashed (red) curve),  $V_{bias} = 8$  (dotted (green) curve). The potential is expressed in  $\hbar\Gamma$  units ( $\bar{V}_{SSH} = V_{SSH}/\hbar\Gamma$ ).  $V_{bias}$  values are expressed in  $\hbar\Gamma/e$  units, where  $e$  is the electron charge.  $E_g$ ,  $E_p$  and  $t$  are expressed in  $\hbar\Gamma$  units. The dimensionless position variable  $\bar{x}$  is defined as  $\bar{x} = x/x_0$  with  $x_0 = \frac{\lambda}{m\omega_0^2}$ . . . . . 50
- 2.12 Panels A-B: Spatial dependence of the dimensionless friction coefficient  $\bar{A}(\bar{x})$  and fluctuating term  $\bar{D}(\bar{x})$  at  $\omega_0/\Gamma = 0.1$ ,  $E_p = 0.2$ , gate voltage  $E_g = 0$ , intermolecular hopping  $t = 2.0$ , for different values of the bias voltage:  $V_{bias} = 0.0$  (solid (black) curve),  $V_{bias} = 3.5$  (dashed (red) curve),  $V_{bias} = 4.0$  (dotted (green) curve),  $V_{bias} = 6.0$  (dashed dotted (blue) curve). Panels C-D: Same as above for  $\omega_0/\Gamma = 0.1$ ,  $E_p = 1.4$ ,  $t = 0.2$ , gate voltage  $E_g = 2$  and different values of the bias voltage:  $V_{bias} = 0$  (solid (black) curve),  $V_{bias} = 4$  (dashed (red) curve),  $V_{bias} = 8$  (dotted (green) curve). The friction coefficient in  $m\omega_0$  units ( $\bar{A} = A/m\omega_0$ ) and the fluctuating term in  $\lambda^2/\omega_0$  units, ( $\bar{D} = D/(\lambda^2/\omega_0)$ ).  $V_{bias}$  values are expressed in  $\hbar\Gamma/e$  units, where  $e$  is the electron charge.  $E_g$ ,  $E_p$  and  $t$  are expressed in  $\hbar\Gamma$  units. The dimensionless position variable  $\bar{x}$  is defined as  $\bar{x} = x/x_0$  with  $x_0 = \frac{\lambda}{m\omega_0^2}$ . . . . . 51
- 2.13 Phase diagram at fixed adiabatic ratio  $\omega_0/\Gamma = 0.1$ ,  $E_g = 0$ , for different intermolecular hopping  $t = 0.2 - 0.6 - 1.0 - 2.0$ . The value of  $\omega_0$  shown in the figure is in  $\Gamma$  units, while all other quantities ( $E_g$ ,  $E_p$ ,  $t$  and  $eV_{bias}$ ) are expressed in  $\hbar\Gamma$  units. . . . . 53
- 2.14 Panel A: Average potential energy as function of the bias for different intermolecular hopping  $t = 0.2 - 0.6 - 1.0 - 2.0$ . Panel B: Average kinetic energy as function of the bias for values of intermolecular hopping as in Panel A. I note that the introduction of new energy scale makes the overall energy  $\langle E \rangle$  a decreasing function of the voltage the for intermediate values. The value of  $\omega_0$  shown in the figure is in  $\Gamma$  units, while all other quantities ( $E_g$ ,  $E_p$ ,  $\langle E_{Kin} \rangle$ ,  $\langle E_{pot} \rangle$ ,  $k_B T$ ,  $t$  and  $eV_{bias}$ ) are expressed in  $\hbar\Gamma$  units. . . . . 54
- 2.15 Panel A-D: Conductance as function of the bias at  $\omega_0/\Gamma = 0.1$ ,  $E_g = 0.0$ , interaction strength  $E_p = 0.2$ , for different values of intermolecular hopping  $t = 0.2 - 0.6 - 1.0 - 2.0$ . The solid (black) line indicates Non Interacting curve. The dashed (red) line and the square (green) lines refer to the static and the dynamical approximation, respectively. The value of  $\omega_0$  shown in the figure is in  $\Gamma$  units, while all other quantities ( $E_g$ ,  $E_p$ ,  $t$  and  $eV_{bias}$ ) are expressed in  $\hbar\Gamma$  units. . . . . 56

- 2.16 Panel A: Current-Voltage characteristic in the static approximation for  $\omega_0/\Gamma = 0.1$ ,  $E_g = 2$  and strong coupling  $E_p = 1.4$  for different values of intermolecular hopping ( $t = 0.15$  dashed (black),  $t = 0.2$  dashed dotted (red),  $t = 0.25$  short dashed dotted (blue)). The non interacting quantities ( $t = 0.15$  solid (black),  $t = 0.2$  dotted (red),  $t = 0.25$  short dotted (blue)) are also shown. Panel B: Current-Voltage characteristic in the dynamical approximation for the same value of panel A. The value of  $\omega_0$  shown in the figure is in  $\Gamma$  units, while all other quantities ( $E_g$ ,  $E_p$ ,  $t$  and  $eV_{bias}$ ) are expressed in  $\hbar\Gamma$  units. . . . . 56
- 3.1 (Color online) Panel(a): Normalized current change ( $\Delta I/I_0$ ) in a low current-carrying state ( $V_{gate}^{eff} = -4\hbar\Gamma$ ) as function of the external frequency ( $\omega_{ext}/\omega_0$ ) for different antenna amplitudes:  $A_{ext} = 10^{-5}$  solid thin line (red online),  $A_{ext} = 10^{-4.5}$  normal thickness line (green online),  $A_{ext} = 10^{-3.5}$  thick line (blue online). Panel (b):  $\Delta I/I_0$  against  $\omega_{ext}/\omega_0$  in a high current-carrying state ( $V_{gate}^{eff} = E_p$ ) for different antenna amplitudes:  $A_{ext} = 10^{-3.5}$  solid thin line (red online),  $A_{ext} = 10^{-3}$  normal thickness line (green online),  $A_{ext} = 10^{-2.5}$  thick line (blue online). Insets: solid line (black online) is a distribution  $P(x)$  out of mechanical resonance. Dotted line (blue online) is a distribution obtained at mechanical resonance for the larger value of antenna amplitude considered in main plots of panels (a,b). Short-dashed line (magenta online) represents current as function of position  $I(x)$ . In this plot  $eV_{bias}^{eff} = 0.5\hbar\Gamma$ ,  $\omega_0/\Gamma = 0.004$  and  $E_p/\hbar\Gamma = k_B T/\hbar\Gamma = 0.04$ . . . . . 62
- 3.2 (Color online)  $\Delta I/I_0$  against  $\omega_{ext}/\omega_0$  in a low current-carrying state ( $V_{gate}^{eff} = -1.75\hbar\Gamma$ ) when the resonator is driven by a strong external antenna amplitude  $A_{ext} = 10^{-3.5}$ : panel (a)  $k_B T = 0.05\hbar\Gamma$ , panel (b)  $k_B T = 0.375\hbar\Gamma$ , panel (c)  $k_B T = \hbar\Gamma$ . In panel (c) a Lorentzian fit is also drawn with  $Q = 10^4$  ( $Q$  is defined in the main text). Inset of panel (a): intrinsic quality factor  $Q$  as function of temperature. I use as energy unit  $\hbar\Gamma = 125\mu eV$ . In this plot  $eV_{bias}^{eff} = 0.5\hbar\Gamma$ ,  $\omega_0/\Gamma = 0.005$  and  $E_p/\hbar\Gamma = 0.05$ . . . . . 64
- 3.3 (Color online) Resonator frequency at resonance against effective gate voltage (shifted of  $E_p$ ) for different bias voltages:  $eV_{bias} = 0.1\hbar\Gamma$  curve (1),  $eV_{bias} = 0.5\hbar\Gamma$  curve (2),  $eV_{bias} = 1.0\hbar\Gamma$  curve (3),  $eV_{bias} = 1.5\hbar\Gamma$  curve (4). Solid (red online) and short-dashed (blue online) portions of each curve indicate resonance frequency values with positive and negative current change  $\Delta I$ , respectively. Inset: electronic occupation at resonance frequency against effective gate voltage (shifted of  $E_p$ ) for  $eV_{bias} = 0.1\hbar\Gamma$  (curve (1)) and  $eV_{bias} = 1.5\hbar\Gamma$  (curve (4)). In this plot  $A_{ext} = 10^{-3}$ ,  $\omega_0/\Gamma = 0.01$  and  $E_p/\hbar\Gamma = k_B T/\hbar\Gamma = 0.1$ . . . . . 64
- 3.4 A carbon nanotube (CNT) subject to an external magnetic field  $H$  suspended between two normal metal leads biased by a voltage  $eV_{bias}$ . . . . . 67
- 3.5 (Color online) Panel(a): minimum of the effective potential (coming from the force Eq.3.38) affecting the CNT-resonator as a function of the magnetic field at low bias  $eV_{bias} = 0.1\hbar\Gamma$  ( $V_{bias} = 20\mu V$  in my units). Solid (black) line indicates  $V_g = 0$ , dashed (red) line  $V_g = 0.45$  ( $V_{bias} = 90\mu V$  in my units), dotted (green) line  $V_g = 1.0$  ( $V_{bias} = 200\mu V$  in my units). Panel(b): same as above at large bias  $eV_{bias} = 1.5\hbar\Gamma$  ( $V_{bias} = 300\mu V$  in my units). Solid (black) line indicates  $V_g = 0$ , dashed (red) line  $V_g = 0.75$  ( $V_{bias} = 150\mu V$  in my units), dotted (green) line  $V_g = 1.5$  ( $V_{bias} = 300\mu V$  in my units). . . . . 71



|      |   |    |
|------|---|----|
| 3.6  | (Color online) Spatial dependence of the dimensionless damping coefficient $A(x)$ at low bias (Panels(a-b-c)) and at large bias voltage applied (Panels(d-e-f)). See main text for discussion. . . . .  | 73 |
| 3.7  | (Color online) Spatial dependence of the dimensionless diffusive coefficient $D(x)$ at large bias voltage applied (Panels(a-b-c)). See main text for discussion. . . . .  | 74 |
| 3.8  | (Color online) Device quality factor as a function the gate voltage $V_{gate}$ for different magnetic field strengths at low (Panel (a)) and large (Panel (b)) bias voltage. Panels(c-d) Same as above for the average total damping $\langle A(x) \rangle$ of the system. Panel(a-c): solid thick line $B = 0.0$ , solid normal-thickness line $B = 1.5$ , and solid thin line $B = 3.0$ . Panel(b-d): solid thick line $B = 0.0$ , solid normal-thickness line $B = 0.2$ , and solid thin line $B = 0.4$ . . . . .  | 77 |
| 3.9  | (Color online) Device quality factor as a function the magnetic field strength $B$ for different bias voltages (Solid thick line $eV_{bias} = 0.1$ , solid normal-thickness line $eV_{bias} = 0.75$ , and solid thin line $eV_{bias} = 1.5$ ) at low (Panel (a)) and high (Panel (b)) conducting states. Panels(c-d) Device quality factor as a function the bias voltage $eV_{bias}$ for different magnetic field strengths at low (Panel (c)) and high (Panel (d)) conducting states. Panel(c): solid thick line $B = 0.0$ , solid normal-thickness line $B = 0.05$ , and solid thin line $B = 0.1$ . Panel(d): solid thick line $B = 0.0$ , solid normal-thickness line $B = 0.25$ , and solid thin line $B = 0.5$ . . . . .   | 79 |
| 3.10 | (Color online) Device quality factor as a function the magnetic field strength. Squares represent experimental values obtained in Ref.[136] at $T = 25mK$ , $V_{bias} = 0.3mV$ and distance from the current peak $V_{gate} = -90mV$ . Solid (red) line is calculated $Q$ at $k_B T = 0.01$ , $eV_{bias} = 0.1$ and $V_{gate} = 0.45$ . . . . .   | 80 |
| 3.11 | (Color online) Panel (a): Resonator frequency against effective gate voltage calculated as minimum of the effective potential in the static approximation at small bias $eV_{bias} = 0.1\hbar\Gamma$ for different magnetic field values: Solid thick line $B = 0.0$ , solid normal line $B = 1.5$ , solid thin line $B = 3.0$ . Panel (c): same as Panel (a) at large bias $eV_{bias} = 1.5\hbar\Gamma$ for different magnetic field values: From thicker to thinner line $B = 0.0 - 0.1 - 0.2 - 0.3 - 0.4$ . Panel (b-d): Resonator frequency calculated using an external antenna (with $A_{ext} = 10^{-3}$ ) at mechanical resonance against effective gate voltage for same parameters of Panel (a-c), respectively. Dashed (red online) and solid (blue online) portions of each curve indicate resonance frequency values with positive and negative current change $\Delta I$ , respectively. In Panel (d), only curves referring to magnetic field strengths $B = 0.0 - 0.2 - 0.4$ are reported. . . . . | 81 |
| 3.12 | (Color online) Panel (a) Average electronic current flowing through the CNT level at low bias ( $eV_{bias} = 0.1$ ) as function of the gate voltage for different values of the magnetic field and in the presence of a external antenna applied to the device at fixed frequency $\omega_{ext} = 0.9975$ and amplitude: solid (black) line $A_{ext} = 10^{-3}$ , (dashed (red) line $B = 1.0$ $A_{ext} = 10^{-2.5}$ , dotted (green) line $B = 1.5$ $A_{ext} = 10^{-2.0}$ , dashed-dotted (blue) line $B = 1.0$ $A_{ext} = 10^{-2.5}$ ). Panel (b) Average electronic density on the CNT level for the same parameter values as in Panel(a). See the main text for detailed discussion. . . . .  | 82 |
| 4.1  | A schematic of the system studied in this Chap.. The molecule can oscillate between the two leads, thus modulating the tunneling barriers. . . . .  | 88 |
| 4.2  | A schematic illustration of the folding transformation applied to the $N_{tot} = "even"$ and $N_{tot} = "odd"$ cases. . . . .   | 90 |

|     |   |     |
|-----|---|-----|
| 4.3 | Panel (a): Persistent current as function of the flux for different leads' density of states at $L_{tot} = 96$ . Scaling analysis (square line (black on line) $L_{tot} = 48$ , circle line (red on line) $L_{tot} = 72$ , up-triangle line (green on line) $L_{tot} = 96$ , rumbles line (blue on line) $L_{tot} = 120$ ) of the current as function of $V_G$ for Normal (panel (b)), Cosine (panel (c)) and Wilson (panel (d)) density of states. | 92  |
| 4.4 | Persistent current flowing through the ring (length $L_{tot} = 96$ ) as function of $V_G$ for different values of $\alpha$ (here $\lambda = 0$ ).   | 93  |
| 4.5 | Persistent current at the particle-hole symmetric point ( $V_G = -1/2$ , length $L_{tot} = 96$ ) as function of $\alpha$ for different number of phonons $N_{ph}$ kept to describe the phonon Hilbert space. The crosses curve represents the results obtained for an optimized phonon basis.   | 95  |
| 4.6 | Static properties of the phononic mode at the particle-hole symmetric point ( $V_G = -1/2$ , length $L_{tot} = 96$ ) as function of $\alpha$ for $\lambda = 0$ . Panels (a,b) describe $\langle x \rangle$ and $\alpha \langle \Delta x \rangle$ of the phononic mode with optimized phonon basis. Panels (c,d) describe same quantities as before with optimized phonon basis and <i>shaked</i> density matrix.                                    | 95  |
| 4.7 | Distribution probability of the phononic mode at the particle-hole symmetric point ( $V_G = -1/2$ , length $L_{tot} = 96$ ) as function of $\alpha$ for $\lambda = 0$ . The distribution becomes bimodal for $\alpha \simeq 0.38$ .   | 96  |
| 4.8 | Imaginary part of the phononic spectral function at the particle-hole symmetric point ( $V_G = -1/2$ , length $L_{tot} = 96$ ) for different values of $\alpha$ for $\lambda = 0$ . A low frequency peak corresponding to the distortion of the $P(x)$ in bimodal shape appears for $\alpha \simeq 0.38$ .  | 97  |
| D.1 | Schematic plot of the real-space renormalization.   | 119 |
| D.2 | Two blocks A are connected to form the compound block AA. The dashed lines are the lowest energy eigenstates of the separate blocks A, the solid line sketches the lowest energy eigenstate of the compound block AA.   | 120 |
| D.3 | Step-by-step illustration of the block-growing scheme in the infinite-size DMRG algorithm: After obtaining the new blocks from the previous step (a), I add a new site to each block (b), I build the superblock and obtain the ground-state (c), and I calculate the reduced density-matrix, and rotate to the basis of the eigenvectors with m largest eigenvalues to build the new blocks for the next step (d).                                 | 123 |
| D.4 | Schematic illustration of the finite-size DMRG algorithm: The infinite-size iteration stops when I reach the desired system size. Then, I start sweeping from left to right, and right to left. During the sweeping iterations, one block grows, and the other one "shrinks". The shrinking block is retrieved from the blocks obtained in the previous sweep in the opposite direction, which are stored in memory or disk.                        | 124 |

# Abstract

The emerging field of molecular electronics, in which individual molecules play the role of active devices, is receiving great amount of attention due to its possible technological impact. Recent advances in nanoscale fabrication and engineering techniques have made possible to study the transport properties of devices on the molecular scale. At this level, one inherently probes the quantum mechanical nature of matter which manifests a number of effects not well understood yet. One such effect is the mutual interaction between electrical current and molecular vibrations. The coupling between mechanical and electronic degrees of freedom in nanoscale devices is also at the heart of NanoElectroMechanical Systems (NEMS) physics. Potential applications of these systems include ultrasensitive motion detection, mass sensing, bio-molecular studies and quantum enabled technologies.

In the first part of thesis, I focused my investigation on electronic transport properties of very short molecules connected between metallic leads taking into account electron-vibration interaction inside the device with a single vibrational mode. Within two models widely used in the literature, I implemented a computational scheme for the dynamics of the oscillator mode coupled with an out-of-equilibrium molecular junction providing also a novel and more physically sounding derivation. I concentrated my attention on the physical regime where the vibrational motion of the oscillator is 'slow' with respect to all electronic energy scales and can be considered "classical". I exploited the Keldysh formalism within Non Equilibrium Green's Function theory (NEGF) for the electronic subsystem together with stochastic dynamics for the vibrational degrees of freedom. As main result, the inclusion of dynamical effects of the oscillator motion strongly modifies the physical scenario which would be obtained by a static description, even if the oscillator dynamics is much slower than the electron tunneling rate.

Motivated by recent experiments on single-electron-transistor made of a single suspended carbon nanotubes, I have further investigated the renormalization effects of the bending mode oscillation frequency of the nanotube as function of the external charge injection (due to the applied bias and gate voltages). I also included in the model the effects of an external antenna driving the oscillations of the nanotube. Interestingly, simulations of the stochastic Langevin equation for the vibrational degree of freedom developed in the first part of the thesis, including the effect of the external antenna, reproduce semi-quantitatively the experimental results. I have also shown that, even in the presence of a magnetic field applied perpendicular to the nanotube device, the nanotube dynamics can be fruitfully described by a Langevin equation. In this case, the main result is that the magnetic field provides an additional damping mechanism to the resonator mechanical motion.

In the last part of the thesis, I studied electron transport through molecular systems at high injected carrier densities, where the presence of the electron-electron interactions is not negligible. I have also considered the effect of the interaction with a high frequency molecular mode (center of mass motion of the molecule) inside the device, which cannot be treated semiclassically anymore. In order to investigate systems with strong electron-phonon and electron-electron interactions, I have used an approximation-free numerical technique, suitable for non-equilibrium quantum many-body systems: the Density Matrix Renormalization Group (DMRG). I numerically investigated with DMRG the electronic transport properties of a nanomechanical shuttling device in the Kondo regime. Nanomechanical shuttling systems (NMSS) and NEMS in general offer a unique platform for design of an electron transistor in which spin and charge transfer can be controlled mechanically. My study is motivated by recent contrasting experimental results found in the conductance measured through  $C_{60}$  junctions in the low temperature and low bias regime, where very small or relatively large conductance values are detected. I focused on the effects of tunneling barrier

modulation on the electronic conductance and on the static and dynamical properties of the center of mass phononic mode, clarifying the nature of a *dip* found in the conductance at particle-hole symmetric point.

# Chapter 1

## Introduction

The rapid progress of nanotechnology has been of the utmost importance in modern Physics. Nanotechnology has an important role in the development of new electronic devices able to perform difficult tasks in increasingly short time, making it possible to realize faster and more sensitive detectors at larger scales. Additionally, the high quality of the nano-fabricated samples together with modern cooling techniques allows us to realize setups in which quantum mechanics can be used as a resource for performing specific tasks, therefore opening the field of quantum technology. In this latter spirit, nanodevices can also be regarded as a test-bed for quantum physics.

In probing the physics of nanodevices, an important role is played by transport measurements. Electric currents can now be generated and detected with very high accuracy and sensitivity. Moreover, fluctuations due to finite temperature can be reduced enough so that current and voltage fluctuations across a nanodevice can be used as a probe of the physical mechanisms controlling the device. Beside dc signals, alternate currents and voltages can be used to drive a device so that with transport one can also perform spectroscopic measurements.

In view of such new possibilities, in the present thesis I have studied two different types of nanodevices that have been attracting a great amount of attention in the research community in the last few years because of their importance in both quantum technologies and fundamental physics: molecular[1] and NanoElectroMechanical systems[2] (referred to as NEMS). The probe employed in this study are currents, namely I study properties that can be inferred by measuring current-voltage characteristic curves or their derivatives in particular circumstances, giving a physical interpretation of the results.

### 1.1 Towards molecular electronics

The first class of nanodevices focused on is that of molecular systems. The possibility of producing such devices is due to progress witnessed in nanolithographic technologies that dates back to the 1980's. Conventional lithography based semiconductor electronics has over the last decades rapidly evolved towards increasingly smaller and faster devices. This development is characterized in Moore's Law [3] which states that semiconductor performance doubles roughly every two years while the cost to manufacture semiconductors increases at an even greater rate. Today's microelectronic devices have a minimum feature size of about 100nm but this is in fact not very far away from fundamental limits of optical lithography, i.e. such as related to the wavelength of the light. Although the semiconductor industry sees a way for at least the next decade for making ever-smaller solid-state silicon devices by introducing new short wavelength lithography techniques, the cost of the manufacturing

systems needed to make the chips is enormous and will grow worse with each new generation [4].

Just as the transistor replaced the vacuum tube during the 1950s, and as integrated circuits superseded individual transistors during the 1960s, one promising candidate to take the place of the semiconductor technology is the so-called **molecular electronics** in which individual molecules play the role of the active devices. The obvious advantage is the possibility of ultra-dense electronics since individual molecules are hundreds of times smaller than the smallest features conceivably attainable by semiconductor technology. Where optical lithography based circuits are fundamentally limited to designs on the submicron level, single molecules may take us even as far as to the nanometer scale. Such chips could be extremely more powerful than today's state-of-the-art. Moreover, individual molecules are easily made exactly the same in incomprehensibly huge numbers  $\gg 10^{23}$  in the chemist's laboratory. The dramatic reduction in size and the enormity of numbers in manufacture are the fundamental potentials of molecular electronics.

Molecular electronics was effectively founded by Aviram and Ratner [5] in 1974 when they suggested a molecular structure that could act as a diode, and further described the theory that explained why this was reasonable. But at that time with the given experimental techniques available it was not possible to realize. It was not until the 1990s where the first measurements on single molecules were performed, that the field of molecular electronics received a great amount of attention. In 1997 Reed et al. [6] succeeded to measure the conductance of a molecular junction of gold-sulphur-aryl-sulphur-gold at room temperature using a mechanically controllable break junction (MCBJ), and they argued that the number of active molecules in the junction might have been as few as one. This demonstration towards single molecule measurements was for sure an important achievement, but without knowledge of the actual microscopic configuration the level of interpretation was rather limited.

Today a number of novel nanoscale devices and circuits based on the intricate effects of quantum mechanics have been proposed, including resonant tunneling diodes and transistors, quantum dots and single electron devices, devices displaying negative differential resistance (NDR)[7], atomic switches [8], logic and memory circuits. Some of these have also been experimentally demonstrated, e.g.[9]. But still many issues have to be resolved if real applications are to be built, for instance the organization and interconnection of individual molecules, room temperature functionality, and stability of the metal-molecule contacts.

The challenges associated with building electronics using molecules will not be overcome without a detailed understanding of the individual components. At the present moment this bottom-up approach is therefore focus for a broad range of scientists around the world. Besides the perspectives of the field it is also stimulating in itself because the discoveries on the molecular level raise many fundamental physical questions as well.

The interest and reported results within the field are too vast and comprehensive to give a complete account of here. For instance, the electrical properties of carbon nanotubes [10] (which could be considered as extremely long molecules) have been extensively studied during the last decade. In section 1.2 of this chapter and in chapter 3, I will show that they could act as very sensitive self-detecting single-electron transistors [11, 12]. Below I will limit myself to mention a number of transport experiments related to inelastic effects on the molecular level which is the topic of this thesis, i.e. to the situation where the interplay between electrical current and the vibrational excitations of the molecular conductors has been found to be essential part of the understanding of the observations.

The construction and operation of molecular devices will certainly rely upon control of inelastic effects. As the current flows through such devices energy of the charge carriers may be transferred into the molecules that form the microscopic structures, or vice versa. This

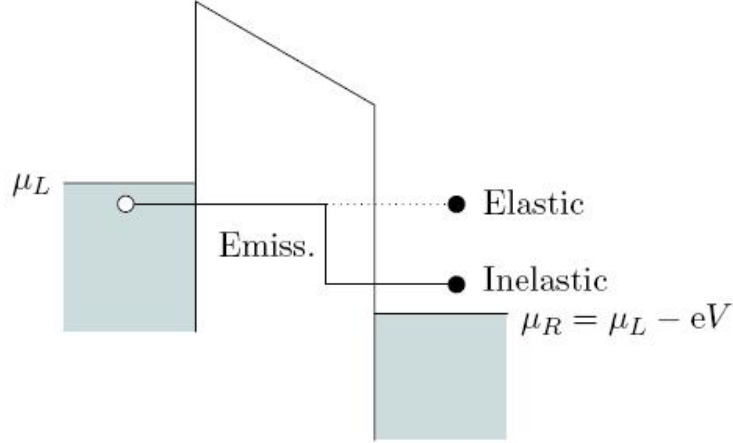


Figure 1.1: Simple picture of elastic and inelastic tunneling processes.

effect is of course always present when a current flows but it is of particular relevance for such minute systems as molecular devices. The consequences of inelastic effects are many: Most important of all is probably that they affect the stability of devices since the energy transfer results in mechanical motion of the atoms which ultimately leads to malfunction or breakdown. On the other hand one can also think of exploiting the influence in a controlled manner to provide certain device properties. One of the main objectives of the present thesis is the study of inelastic effects in electron transport through nanosystems, e.g. single molecules and Nanoelectromechanical systems. A simple picture of elastic and inelastic transport is shown in Fig. 1.1 where scattering of electrons is considered to take place inside a tunneling barrier across which a voltage  $V_{bias}$  is applied.

As indicated, the elastic electron tunneling involves transfer of an electron from filled states on one side of the barrier to adjacent empty states on the other. The incoming electron is accelerated in the electric field and potential energy is thus turned into kinetic energy of the particle. The energy between initial and final states balances, even though the electron may have scattered elastically against static defects and impurities or against other electrons in between. This is in contrast to inelastic tunneling where electrons lose (gain) energy by emission (absorption) of vibrational quanta, i.e. phonons, during the transfer by scattering against lattice vibrations. The inelastic tunneling process is shown on the figure 1.1, where the finite energy drop between initial and final state of the electron indicate that energy has been transferred to the molecular modes of the lattice[13]. The picture given is valid as long as it is reasonable to think in terms of noninteracting (quasi) particles and in the full quantum regime. For sufficiently strong electron-phonon interaction the problem is a true many-particle one in which one cannot conceptually separate elastic and inelastic processes.

In this thesis I will be concerned with interaction of electrons with very low frequency vibrational modes (which can be considered as a "continuum" of phonon excitations) so that multiple scattering processes can take place. I will see that interaction between an incoming electron and a very low frequency vibrational mode can be fruitfully described in a semiclassical way. In this case, the molecular mode can be described as a classical harmonic oscillator whose deformation is coupled to the *average* electron density on the molecule. In chapter 2, I will show that the inelastic tunneling of the electrons can be viewed as a dissipative contribution to the oscillator harmonic motion. Eventually, the non-equilibrium quantum flow of discrete electrons through the junction can be seen as a

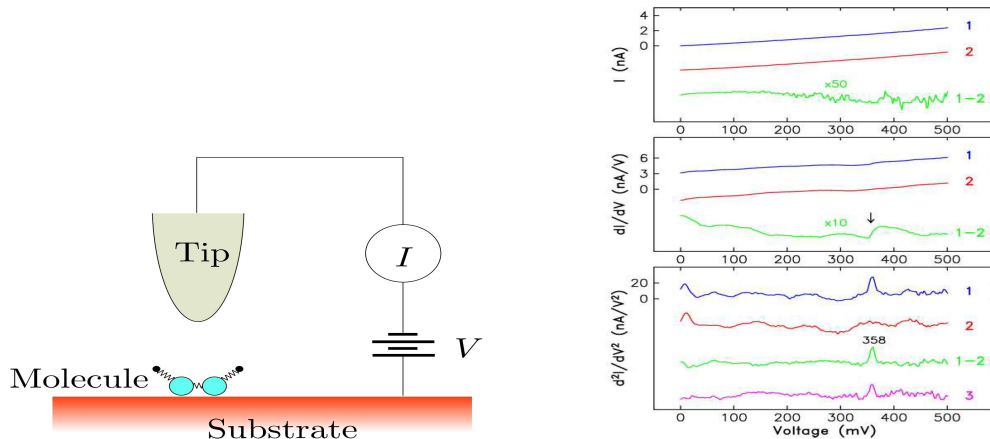


Figure 1.2: Conductance measurement with STM. The current and its higher derivatives are recorded while sweeping the bias voltage for (1) tip over molecule and (2) tip over bare substrate. The relevant signal is the background subtracted difference (1-2). Data are shown for an acetylene molecule  $C_2H_2$  (adapted from [15]). The minute conductance increase around  $358\text{mV}$  indicates the opening of an inelastic channel.

*stochastic* perturbation to the oscillator dynamics, which acquires a diffusive character. If the vibrational motion of the mechanical mode is 'slow' with respect to all electronic energy scales, the molecular junction can be described (from the point of view of the mode) as a mass attached to a classical spring in embedded viscous fluid. Indeed, if the bias voltage applied to the junction is not too large, the electronic non-equilibrium quantum environment behaves as conventional thermal bath at an effective temperature (proportional to the bias voltage).

### 1.1.1 Conductance of single molecules

The main experimental difficulty of measuring the transport properties of single molecules is to establish the situation where one for sure has only one molecule bridging the contacts in a two-terminal configuration. Since the late 1990s a number of different techniques have been demonstrated.

#### Scanning tunneling microscope

One way to probe the conducting properties is to use a scanning tunneling microscope (STM) which can create images of surfaces with atomic resolution utilizing tunneling currents. By positioning the STM tip over an adsorbed molecule on a conducting surface one can directly measure various properties of the molecule by sweeping the bias voltage, e.g. the local density of states. The standard setup is illustrated in Fig. 1.2. Measuring detailed conductance spectra with the STM requires extreme mechanical stability because even the slightest variations of the tunneling gap change the current exponentially. For example, a stability of  $0.01\text{\AA}$  is required to keep the conductance stable to within 2% [15]. In Ref. [15], the authors successfully demonstrated for the first time the use of STM for inelastic spectroscopy (IETS-STM inelastic electron tunneling spectroscopy with STM). With their STM they studied an isolated acetylene  $C_2H_2$  molecule adsorbed on a copper (100) surface. They found the signature of a single vibrational excitation by the tunneling electrons, and measured a conductance increase of the order of several percent at the threshold voltage



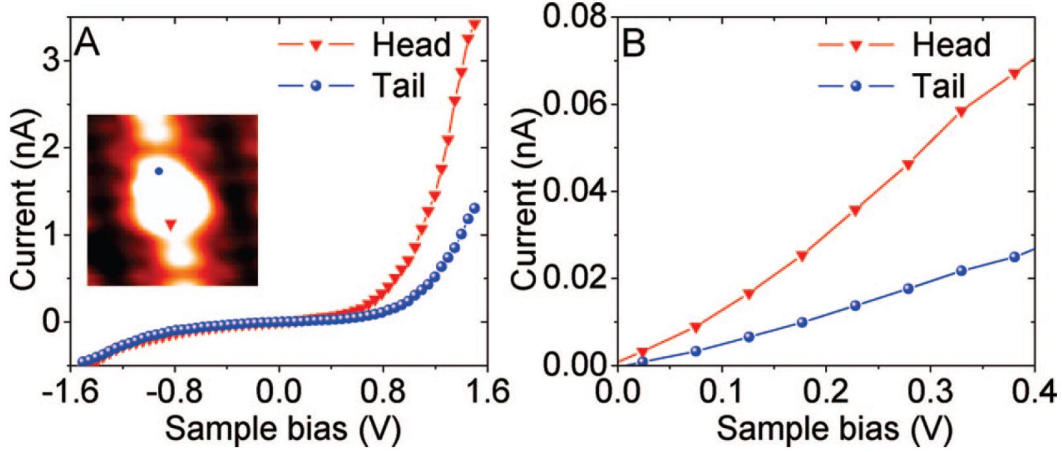


Figure 1.3:  $I(V)$  characteristics taken on two different parts of an octanethiolate molecule adsorbed on a Pt chain, as indicated by the blue dot and the red triangle in the STM image of panel A (Figure taken from Ref.[16]). Panel B shows a detailed view of the voltage window from 0 to 0.4V where current against voltage curve is linear.

corresponding to the  $C-H$  stretch mode. Their measurements are shown in Fig. 1.2.

As example of STM application, one can cite a beautiful experiment conducted recently by Kockmann *et al.* [16], where Octanethiol molecules adsorbed on Pt chains are studied at 77K. As shown in Fig.1.3, current-voltage shapes depend on tip position onto the molecule (in Panel A of Fig. 1.3, red curve refers to head position while blue refers to tail) while for small bias voltage applied (Panel B) a linear current-voltage characteristic is observed.

Even though conductance experiments on single molecules through tunneling gaps yield valuable information as in the IETS-STM, it is also desirable to study the situation in which a molecule is directly connected to two terminals.

## Break junctions

Single molecules may also be contacted with the use of mechanically controllable break junctions (MCBJ) or break junctions formed by electromigration (BJE). In the first method an adjustable tunneling gap is formed by breaking a conducting layer on a flexible substrate in two [17]. In the latter method the gap is formed by applying a large voltage over the terminals, thereby initiating a burn off, until only a tunneling current is monitored [18]. In 2000 Park *et al.* [19] measured the transport via a single  $C_{60}$ -molecule by a BJE technique at cryogenic temperatures. A current-voltage (I-V) curve from their paper is shown in Fig. 1.4. The general pattern observed here is understood within a Coulomb blockade model for quantum dot transport, where the conductance gap is a consequence of the finite energy associated with either adding or removing one electron on  $C_{60}$ . The fine structures reveal information about a quantized excitation with an energy of approximately 5meV, which in turn provide evidence for a coupling between the center-of-mass motion of the fullerene and the transfer of single electrons. The strong correlation between electron transfer and oscillator motion in Park *et al.*'s experiment has also been considered a possible realization of shuttling transport in which an integer number of electrons are transferred per center-of-mass oscillation. This issue will be dealt with thoroughly in the last chapter of this thesis.

However, it seems to be an unresolved issue whether or not a true shuttling regime exists for the  $C_{60}$  in this setup, see e.g. [21]. In 2002 Smit *et al.* [22] measured the conductance of a hydrogen molecule using a MCBJ with Pt contacts at cryogenic temperatures. Only

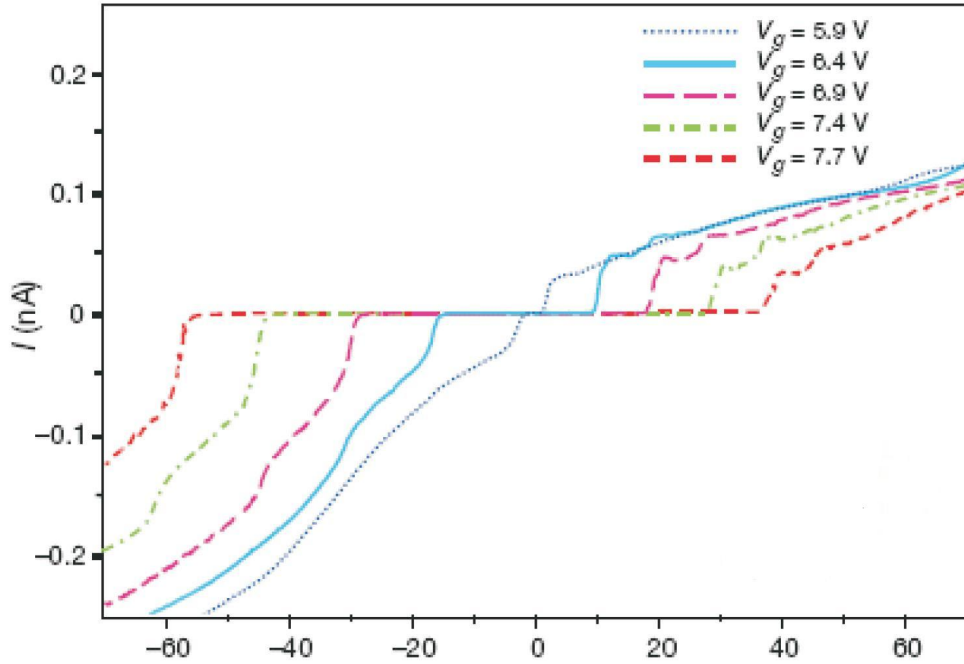


Figure 1.4: I-V characteristic of the  $C_{60}$  molecule (adapted from [19]). The device is clearly acting as a transistor where the gate voltage controls the current between source and drain. The series of steps in the current are known as Frank Condon steps caused by vibrational excitations.

with a small quantity of hydrogen gas in the vacuum chamber they found a frequently occurring stable configuration with a conductance very close to the quantum unit. The differential conductance observed for this configuration is shown in Fig. 1.5 and exhibits a single dominant resonance around 63.5mV that was interpreted as an excitation of the center-of-mass motion of the  $H_2$ -molecule.

### 1.1.2 NDR and Hysteresis in molecular junctions

Here I address the possible consequences of a strong electron-phonon coupling, where charging of the molecular bridge (stabilized by this interaction) can lead to non linear transport behavior. Indeed, "stabilization of molecular charging" may often appear as modification of molecular geometry and can therefore give rise to substantial and sometimes striking effects of negative differential resistance, multistability and hysteresis phenomena. Such structural changes are characteristic of molecular entities, and will therefore be of major importance in the ongoing investigation of molecular, as opposed to solid state or mesoscopic, transport structures.

Examples of such behaviors are shown in Figures 1.6-1.7. Figure 1.6 shows negative differential resistance[23], while in Fig. 1.7 one can observe hysteresis in different molecular junctions [7]. The molecules involved in these junctions are characterized by the presence of redox centers, i.e. centers that support long-living excess electron states. Such "redox molecules" have been implicated in several other observations of multiple conduction states and non-linear response in molecular junctions operating in a polar (aqueous) environment.[24, 25] This suggests the possibility of polaron formation on the molecule as a possible factor. Indeed, as I will see in chapter 2, the Anderson-Holstein model has a positive feedback character: the energy of the resonant level shifts by polaron formation that

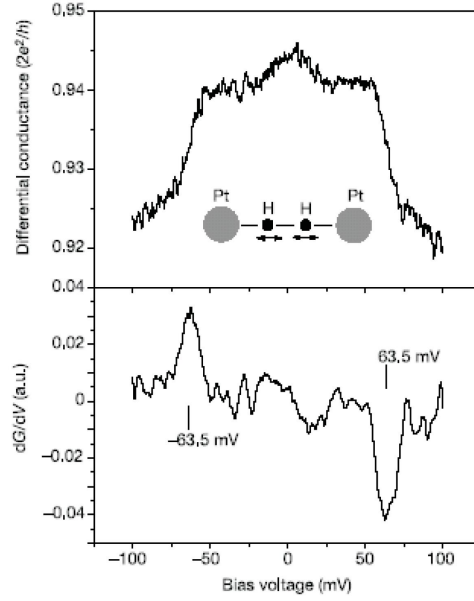


Figure 1.5: Conductance measurement of the hydrogen molecule between platinum contacts adapted from [22]. The symmetric decrease seen around 63.5mV was interpreted as related to excitation of the center-of-mass motion of the  $H_2$ -molecule shown in the inset.

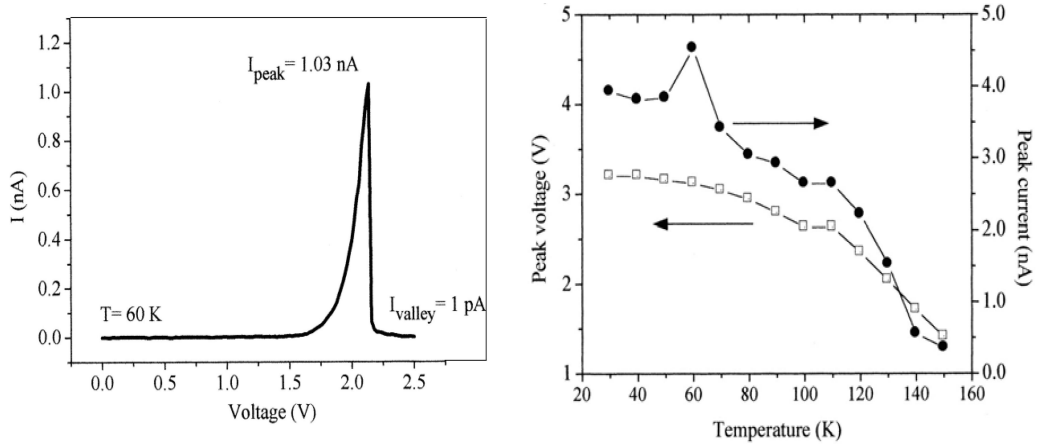


Figure 1.6: NDR of a junction based on monolayer of 2'-amino-4-ethynylphenyl-4'-ethynylphenyl-5'-nitro-1-benzenethiolate embedded between gold wires at 60K. Shown on the left is the reported I-V characteristic with NDR peak to valley ratio 1030 : 1. The temperature dependence of the current and voltage values at the peak is shown on the right. (From Ref [23]).

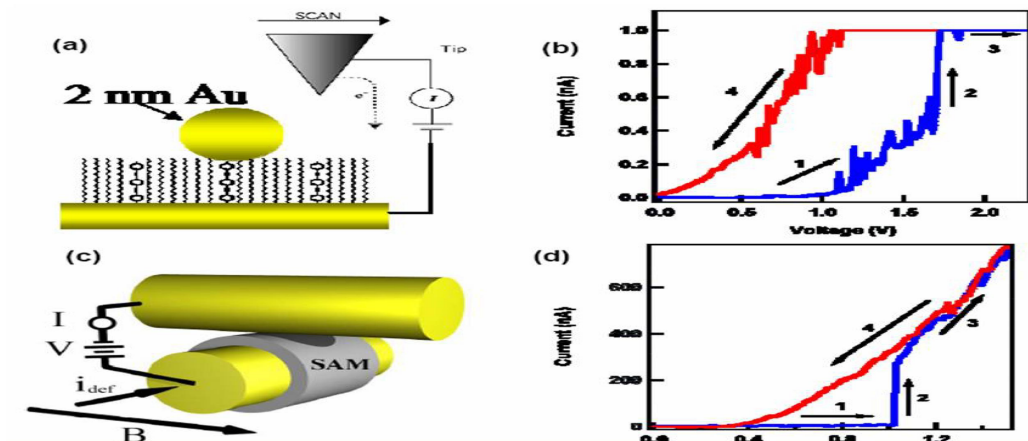


Figure 1.7: Current-voltage measurements on individual BPDN molecules by STM with BPDN embedded into  $C_{11}$  alkane matrix (a) and cross-wire tunneling junction (c) are presented in Figs. (b) and (d) respectively. (From Ref [7]).

depends on the electronic occupation of that level. The latter, in turn, depends on the level energy. Ref.[26] is a study of the nature and possible consequences of this feedback character on the conduction behavior of such junctions, using the reduced one bridge level/ one bridge (primary) oscillator version of the Anderson-Holstein model. This study invokes a mean field approximation akin to the Born-Oppenheimer approximation, which is based on the assumption that the primary vibrational mode is slow relative to the rate at which electrons enter and leave the bridge. In this case the oscillator responds only to the average bridge occupation. This approach predicts multistability and even hysteresis in the I-V curves [26].

The dynamical consequences of this multistability are still under discussion. Whether they can lead to hysteresis behavior and memory effect as suggested in [26] or to intermittent noise associated with transitions between two locally stable states as discussed in [27, 28] is an issue of relative timescales, the observation time vs. the rate of transitions between locally stable states. An interesting possibility that such a mechanism can be the cause of observed negative differential conduction phenomena has also been pointed out,[26] and may again depend on relative timescales [27]. Interestingly, in chapter 2, I will show that the inclusion of dynamical effects of oscillator motion *at lowest order*, rules out any possibility of having hysteresis in molecular junctions if one considers a single site Anderson-Holstein model [29].

On the other hand, a recent experimental study of hysteretic conductance in gated molecular junctions based on the redox molecule bipyridyl-dinitro oligophenylene-ethynylene dithiols (BPDN-DT)[30] indicates that the observed behavior is not sensitive to the gate potential (in contrast to the  $\epsilon_0$  dependence in [31]), suggesting that at least in this system the actual mechanism may go beyond the simple picture described above.

### 1.1.3 Incoherent vs coherent transport

Two very important consequences of the electron interaction with mechanical degrees of freedom in molecular junctions are the crossovers from tunneling to activated transport and from coherent to incoherent transmission under appropriate conditions. While these effects are not identical (e.g. thermal electron transfer from lead to molecule can be followed by coherent propagation along the molecule), energy and timescale considerations indicate that they occur under similar conditions: when activated transport dominates it is likely that

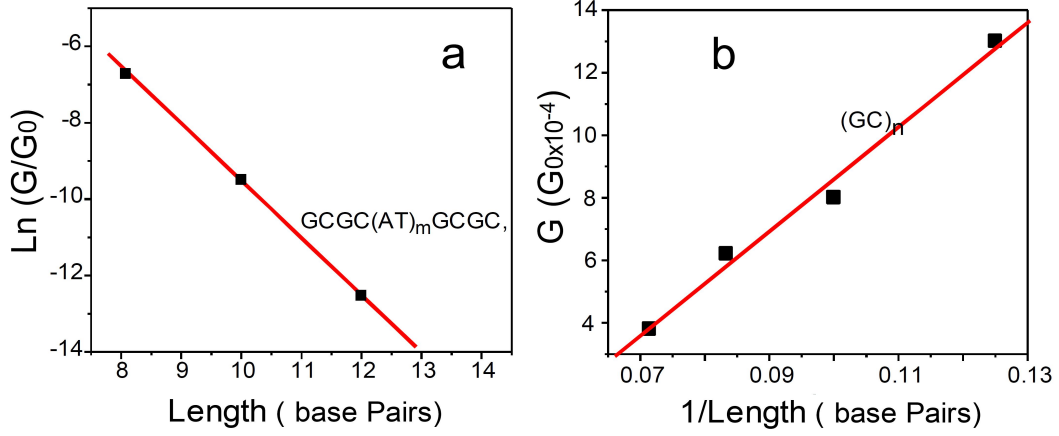


Figure 1.8: Mechanistic turnover from tunneling to hopping in short strand duplex DNA. The curve on the left shows tunneling through the AT segment, resulting in exponential decay of conductance with length. The segment on the right is for poly GC where transport occurs by hopping and the conductance scales like the inverse length (as it must for diffusion). From Ref. [25].

decoherence within the molecular bridge will be effective. The predicted experimental manifestations of these changes in the nature of the conduction process are, first, a transition from temperature independent to activated transport upon temperature increase, and second, an exponential drop with molecular chain length in the tunneling regime becoming an ohmic  $1/\text{length}$  dependence for activated hopping conduction.

In Fig.1.8, one can observe the transition between an exponential length dependence of tunneling through a DNA segment with a large injection gap and an inverse length dependence in the small gap regime, near resonance case [25].

Temperature-dependent transport measurements[32, 33, 34] form a useful tool to distinguish between different transport mechanisms. For example, experiments on ensembles of alkanethiols[32] have shown temperature-independent electron transport indicative of a tunneling mechanism. Selzer *et al.*[33] report on a crossover from temperature-independent transport at low temperature to an exponential dependence at temperatures above 100K. They attribute this crossover to a change of conduction mechanism from tunneling at low temperatures to incoherent hopping transport at high temperatures induced by a coupling to vibrational states. In another interesting paper, Poot *et al.*[35] report on the temperature dependence of three-terminal molecular junctions based on sulfur end-functionalized tercyclohexylidenes (see Fig. 1.9). For low bias voltages, they observe temperature-independent transport at low temperatures and above a crossover temperature of about 150K the current increases exponentially with the inverse temperature. They suggest that a toy model based on transport through one non-interacting molecular level provides a good fit to the data at all bias and gate voltages. With some variation in details, similar predictions are reached by invoking the finite temperature Fermi distribution of electrons in the leads without adhering to dynamical relaxation effects, see e.g. Ref. [36].

Anyway, a further investigation on the effects of electron-phonon interaction on temperature dependence of transport properties of molecular junctions is highly demanded.

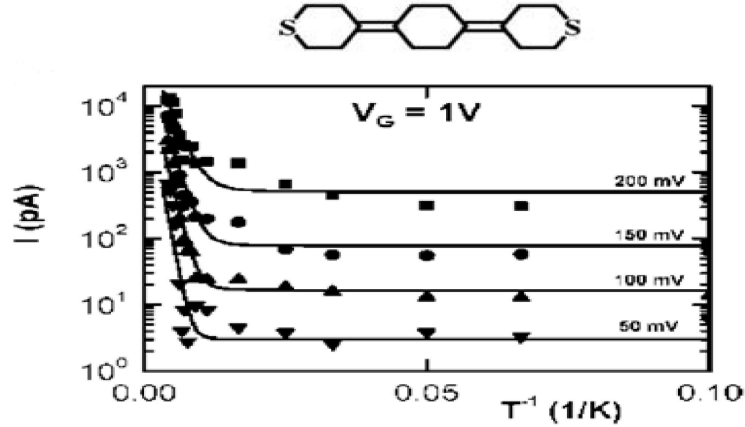


Figure 1.9: Onset of activated transport in a non-conjugated molecule. At low temperatures, quantum mechanical tunneling is seen, and the current is independent of temperature. As room temperature is approached, the transport becomes activated. The argument made by the authors is that the small activation energies describe the overlap of the Gaussian spectral density tail with the Fermi occupation tail. From Ref. [35].

## 1.2 Nanoelectromechanical Systems

The second class of nanodevices studied in this thesis is that of nanoelectromechanical systems (NEMS). NEMS comprise nanometer to micrometer scale mechanical oscillators coupled to electronic devices of comparable dimensions. The motion of such an oscillator leaves its signature on the current characteristics of the electronic device and hence the latter may be used as a measurement device for the motion characteristics of the oscillator. The typical dimensions of a NEMS oscillator is a few microns or less and frequencies in the range of a few MHz to a GHz have been achieved [37]. Indeed, potential applications of these systems include ultrasensitive motion detection, mass sensing, bio-molecular studies and quantum enabled technologies.

NEMS have witnessed an enormous amount of research activity in recent times. In a fundamental sense, the unique feature of these systems is the coupling achieved between mechanical and electronic degrees of freedom. There exists a vast literature on NEMS. In 2000, Craighead [38] published a review that surveyed the field at that time. The book of Cleland[39] provides a comprehensive introduction to various aspects of the subject. Blick and co-workers [40] review experimental methods in NEMS while Blencowe[2] presents a more recent survey. I now turn to some specific applications of NEMS in the next section.

### 1.2.1 Applications of NEMS

Among the most spectacular applications of NEMS is motion sensing. For instance, in 2003, Knobel and Cleland[41] reported nanometer scale displacement sensing using an electronic device known as the single electron transistor (SET). The resonator in their experiment was a  $3\mu\text{m}$  long  $\times$  250nm wide  $\times$  200 nm thick doubly clamped beam of single-crystal GaAs, capacitively coupled to an aluminum SET, located 250nm from the beam. A displacement sensitivity of  $2.0 \times 10^{-15} \text{ m Hz}^{-1/2}$  at 116.7MHz resonant frequency of the beam was reported. In another remarkable experiment in 2004, LaHaye and coworkers [42] reported an experiment in which they used a vibrating nanobeam about a hundredth of a millimeter long as a displacement sensor. The beam had a frequency of 20 million cycles per second (20 MHz),

was cooled in the experiment to about 60 millikelvins and had a measured displacement sensitivity of  $10^{-5}$  nanometers. This displacement sensitivity corresponds to about 1/1000 the diameter of a single hydrogen atom.

Another area of application is mass sensing. Ekinici and coworkers [43] reported an experiment in which a modulated flux of atoms was adsorbed onto the surface of a nanomechanical resonator in an ultrahigh-vacuum environment. The mass-induced resonance frequency shifts of the resonator due to the adsorption process was measured to report a mass sensitivity of  $2.53 \times 10^{-18}g$ . In the area of charge sensing, Cleland and Roukes [44] reported a NEMS based charge detector that achieved a charge sensitivity of  $0.1e$ , where  $e$  is the unit electron charge.

It is clear from my discussion thus far that NEMS have revolutionized sensing technology. However, the utility of these devices is not restricted to practical applications and NEMS have implications for fundamental physics. I now turn to a discussion of those implications.

From a theoretical point of view, NEMS straddle the classical and the quantum worlds since while the oscillator is a macroscopic object, the processes that take place in the electronic device are essentially quantum mechanical [45]. On the one hand, despite quantum mechanics having been formulated almost 75 years ago, fundamental questions regarding the interface between the classical and quantum regimes of mechanics remain yet unanswered. On the other hand, questions in quantum measurement (the interaction of a microscopic system with a macroscopic measurement apparatus) and quantum control (could one control the evolution of a quantum system from a given state to a desired one?) have profound implications for futuristic technologies such as the design of truly nanodevices and, on further extrapolation, for the fantastic possibilities perceived by quantum computation. The point of all this is that, owing to the scale at which they function, NEMS provide a rich arena for research in all of the above areas both as a test bed for the validation of practical ideas as well as to lead theoretical efforts. If classical physics is a faithful approximation of quantum physics at the macroscopic scale, then, in principle, one should be able to observe quantum phenomena in the motion of macroscopic objects. Precisely, one should be able to validate the Heisenberg uncertainty principle in the macroscopic domain. Let us consider the motion of a nanomechanical oscillator. Due to its extremely small size, the oscillator is to be considered as executing thermal Brownian motion under the influence of stochastic atmospheric forces and defects in its own structure. This motion is dictated by the laws of statistical mechanics and it follows that, if cooled sufficiently under controlled conditions, the amplitude of this motion will tend to vanish. The temperature that defines this threshold is determined by the resonant frequency of the oscillator. If the laws of quantum physics are valid, what remains when the Brownian motion subsides is the quantum zero point fluctuation of the oscillator in its lowest energy state. The key point is that, as a consequence of the uncertainty principle, this zero point state is not the state of absolute rest. In other words, the laws of quantum physics prohibit the oscillator from being in a state of total rest. It is now straightforward to see how NEMS experiments can play a crucial role in validating the uncertainty principle for macroscopic systems. If displacement measurements can be made on the beam, at temperatures that guarantee the absence of Brownian motion, then those measurements can be compared to the zero point displacements predicted by quantum physics. It is important to note here that in their experiment with the 20 MHz beam, LaHaye and co-workers [42] reported a measured displacement sensitivity within an astonishing factor of 10 of the zero point amplitude predicted by the uncertainty principle for their system. Hence it is fair to conclude that the state-of-the-art in this enterprise stands on the threshold of actually testing the laws of quantum mechanics in a macroscopic system. In this context, I also note here that the quantum measurement aspect is a significant contributor to the importance of cooling effects in NEMS [47].



Recent research has led to the development of high-frequency top-down fabricated mechanical resonators with high quality factors  $Q$ . Indeed, high  $Q$ -values combined with high resonance frequencies are an important prerequisite for applications such as single-atom mass sensing and fundamental studies of the quantum limit of mechanical motion[42]. However, when miniaturizing mechanical resonators to make them lighter and to increase their resonance frequency, the quality factor tends to decrease significantly from surface effects. Interestingly, it has been recently demonstrated that single-wall carbon nanotubes present a potentially defect-free nanomechanical system with extraordinary mechanical properties which should result in quality factors of the order of  $2 \times 10^5$ . Below I describe two experiments [11, 12] where the authors were able to detect carbon nanotube mechanical motion with extremely high quality factors.

### 1.2.2 Carbon nanotubes: Nonlinear high- $Q$ nanomechanical resonators

A carbon nanotube (CNT) is a remarkable material, which consists of only carbon atoms and can be thought of as a graphene sheet rolled up into a cylinder with the ends capped off with a buckyball sliced in half. This is called a singlewalled CNT and, depending on how the graphene sheet is rolled up, CNTs are either semiconducting or metallic. At low temperatures, CNTs contacted by two electrodes become quantum dots, and Coulomb blockade and single-electron tunneling occurs. When more graphene sheets are wrapped up concentrically a multiwalled CNT is formed. A suspended CNT resonator can be fabricated without defects, thus reducing damping which results in quality factors for the flexural modes above 100,000. Having a radius that can be as small as a nanometer and lengths of several micrometers, CNTs have aspect ratios in the thousands, on a scale and purity that is difficult to achieve in resonators fabricated top-down from silicon, SiN, or other materials. The enormous aspect ratio makes it easy to excite the CNT such that the displacement of the flexural mode is similar in magnitude to the radius; the CNT thus behaves as a thin, narrow beam resonator. The combination of low damping and high aspect ratio paves the way for nonlinear effects. There are two other remarkable properties of CNTs: Their Young's modulus of 1.3TPa makes them an incredibly stiff material, and combining this with a density of only  $1350 \text{ kg/m}^3$ , CNT resonators reach frequencies of several hundreds of megahertz and even gigahertz. At millikelvin temperatures, with  $\hbar\omega_0 \gg k_B T$ , thermal phonons can no longer excite the flexural motion. This makes CNTs perfect candidates to observe quantum (nonlinear) effects in mechanical resonators. In this thesis I'm interested in the opposite regime  $\hbar\omega_0 \ll k_B T$  where the nanotube's motion can be fruitfully described in a classical way. In the next subsection I will describe different ways of detecting the motion of CNT resonators. Next, I show how single-electron tunneling gives rise to frequency softening and damping as well as Duffing-like nonlinearities. Table 1.10 gives an overview of the symbols used in this section for variables and constants along with typical values and example device parameters.

#### Detecting the motion of single walled Carbon Nanotubes

In this subsection, I discuss different ways to detect the flexural motion of CNT resonators suspended between two macroscopic electrodes. Other vibrational modes such as breathing and stretching modes are also present in CNT resonators, but non-flexural modes are difficult to actuate and detect. They are therefore not discussed in this thesis. Because a CNT is easily perturbed, detection has a large influence on its motion. When discussing the nonlinear dynamics of CNT resonators, it is therefore important to have an overview of



| General properties of single-walled CNTs |                 |                        |
|--|-----------------|------------------------|
| $E$                                      | Young's modulus | 1.3 TPa                |
| $\rho$                                   | mass density    | 1350 kg/m <sup>3</sup> |

| Example CNT     |                          |                     |
|-----------------|--------------------------|---------------------|
| $L$             | length                   | 800 nm              |
| $r$             | radius                   | 1.5 nm              |
| $h_g$           | distance to gate         | 230 nm              |
| $C_g$           | capacitance to gate      | 10 aF               |
| $C_{tot}$       | total capacitance        | 20 aF               |
| $Q$             | quality factor           | 100,000             |
| $\omega_0/2\pi$ | resonance frequency      | 140 MHz             |
| $I$             | second moment of inertia | 4.0 nm <sup>4</sup> |
| $A$             | cross-sectional area     | 7.1 nm <sup>2</sup> |

| Variables        |                           |   |
|------------------|---------------------------|---|
| $u(z, t)$        | displacement              | - |
| $\mathcal{A}(t)$ | slowly-changing amplitude | - |
| $\xi(z)$         | mode shape                | - |

Figure 1.10: General properties and device parameters for a single-walled CNT. This Table was taken from Ref. [48].

the different detection methods. Optical detection, which is used frequently in top-down devices, is not an option because of the small cross-section of a CNT. Until now, detection has therefore been done through microscopy or electronically. I summarize five different methods to observe its motion: scanning force microscopy, transmission electron microscopy, field emission microscopy, the mixing technique, which involves frequency down-mixing the flexural motion from several hundreds of megahertz to several kilohertz, and the rectification technique, where the amplitude of the flexural motion is obtained by measuring the dc current flowing through the CNT. The last two (electronic) methods are self-detecting because the CNT is both the object studied and the detector.

In the mixing technique, a frequency-modulated voltage is applied to the source electrode. The frequency modulation of the source voltage causes sidebands in the spectrum around the drive frequency. They both mix with the mechanical resonance and result in a signal at the modulation frequency. In this case no signal needs to be applied to the gate as the CNT is actuated by setting the carrier frequency of the source voltage to the mechanical resonance frequency.

In this thesis I'm concerned with the rectification technique used in a beautiful experiment described in [11, 12]. The advantage of this technique is that the amplitude of the mechanical motion is given by a change in the dc current flowing through the CNT. As with the mixing technique, the use of the rectification technique avoids the difficulty of getting small, high-frequency signals out of a setup at millikelvin temperatures and minimizing the cross-talk from the actuation onto the measurement signal. With the rectification technique, the working principle is as follows. The CNT is suspended between source and drain electrodes above a gate electrode. At low temperatures, the CNT acts as a suspended quantum dot in which charging effects dominate transport. It is actuated using a nearby antenna, which sends out an oscillating electric field. When the CNT oscillates, the distance to the gate changes, and therefore the capacitance changes as well due to CNT motion (see Fig. 1.11). This variation can be *measured* in the average dc electronic current flowing through the three-terminal device and can induce very interesting features. Indeed, because of their high quality factor and therefore narrow linewidths, ultraclean CNT resonators allow for the detection of small changes in resonance frequency. In this sense, the electronic current through the device can be used as a very sensitive spectroscopic measurement.

Figure 1.12 shows Coulomb oscillations (top), and the change in resonance frequency

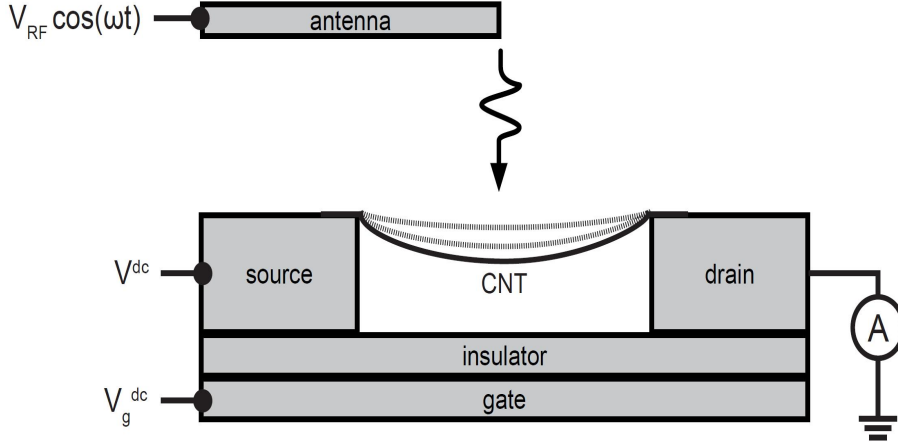


Figure 1.11: Detecting the CNT's motion using the rectification technique. A CNT is doubly clamped between a source and a drain electrode suspended above a gate electrode. The CNT is driven by a high-frequency signal applied to an antenna at approximately 2 cm from the CNT. The single-electron tunnel current through the CNT quantum dot contains information on the oscillation of the CNT at DC due to a rectification effect from Coulomb blockade.

with gate voltage (bottom) at small bias voltages. Three features are worth mentioning: i) in Coulomb blockade, there is a fixed charge on the CNT and the resonance frequency-gate voltage curve approaches a linear dependence, denoted by the dashed lines; ii) from one charge state to the next, there is an offset between the sloped lines; and iii) at the position of Coulomb peaks corresponding to a transition between charge states, there are resonance frequency dips arising from a softening-spring behavior. The slope in resonance frequency is explained as follows: in Coulomb blockade the charge on the CNT quantum dot is constant. If a more negative gate voltage is applied, the force acting on the CNT increases, which pulls the CNT more towards the gate. The tension caused by this pulling leads to the first feature: the resonance frequency increases with gate voltage. As the gate voltage becomes more negative, more and more electrons are extracted from the CNT quantum dot, leaving behind holes. From one charge state to the next, there is a difference in charge of one electron. The tension arising from an extra electron causes the resonance frequency to change in a discrete manner, leading to the second feature: an offset in resonance frequency between two charge states. Figure 1.12 shows a frequency offset of 0.5MHz, which is more than 100 times the linewidth. As I will show in chapter 3, the frequency dips arise from tunneling of single electrons through the device. Figure 1.12 shows that single-electron tunneling can lead to a dip in the resonance frequency by as much as 2MHz. The change in resonant frequency due to single-electron tunneling over this small gate range is an order of magnitude larger than that from the gate induced mechanical tension [48]. Recent experiment performed on the same setup has found a double dip structure in the mechanical resonance-frequency curves as one increase the bias voltages. As I will see in chapter 3, my model has correctly predicted this feature [49].

### 1.2.3 Nonlinear effects in Carbon Nanotube resonators

In this section I describe how the measured lineshape in the electronic current vs. antenna frequency curves changes as the drive power is increased considering also the effect of the temperature. In right panel of Fig. 1.13 one can see that, as the antenna power is increased, the current-frequency curves turn from a Lorentzian to a characteristic triangular shape.

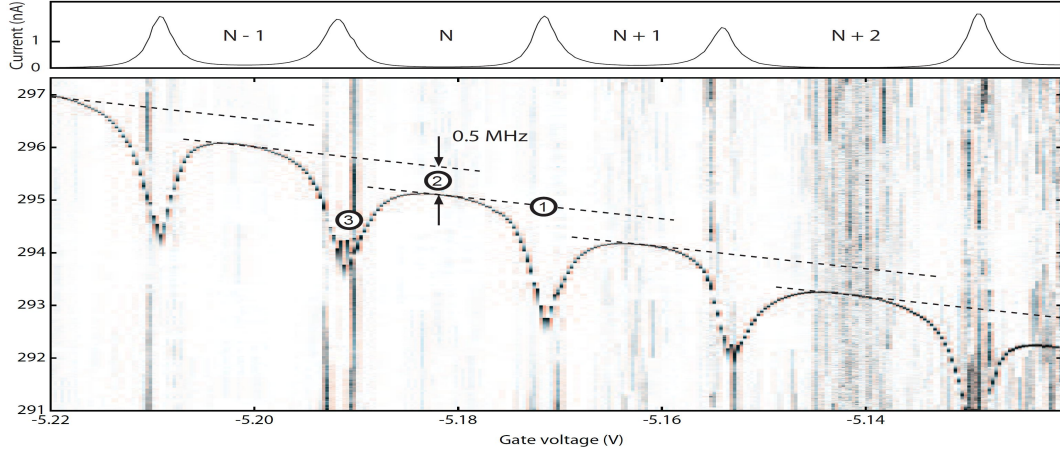


Figure 1.12: Top: Coulomb oscillations of the current through a CNT quantum dot; in Coulomb blockade current is zero and the indicated (negative) number of electrons on the CNT is fixed. Between charge states a single-electron tunneling current is visible as Coulomb peaks. Bottom: Gate dependence of resonance frequency (from [11]); the features are indicated by the encircled numbers: (1) a slope caused by tension at fixed charge, (2) a frequency offset caused by a tension difference between charge states, and (3) frequency dips caused by single-electron tunneling. This Fig. was taken from Ref. [11].

This behavior can be interpreted in terms of the nonlinear correction terms to the force acting on the nanotube induced by the current flow. Indeed, when an elastic object is brought out of its equilibrium position, the restoring force is usually linearly dependent on the displacement. As the applied force and resulting displacement increase (in my case due to application of the antenna), Hooke's Law is no longer valid and nonlinear effects become important. As I will see in chapter 3, these nonlinear terms are due to the intrinsic electron-oscillator interaction. In Ref.[11], they have also studied the nonlinear regime as a function of the temperature. In left panel of Fig.1.13 one can see that, increasing the temperature, the current-frequency curves turn from a triangular to a Lorentzian shape characteristic of the linear response regime. This could be interpreted in terms of a decrease of the quality factor as function of temperature. I will show, in chapter 3, that these features can be qualitatively reproduced using a single site Anderson-Holstein model.

## 1.3 Electronic correlation in transport through Nanostructures

### 1.3.1 The Kondo Effect in Nanostructures

In many nanostructures, such as single-molecule conductors and quantum dots, the system consists basically of a central interacting region, usually the dot or molecule, weakly coupled to ideal noninteracting leads. Due to the confined nature of the nanostructures, the energy spectrum is discrete with several energy levels or quasilocal states. The hybridization of these levels with the continuum states of the leads gives the levels a finite width which is proportional to the rate of electron escape to the leads. A rough model of the dot, for example, is a quantum well separated from the leads by two tunnel barriers. The position of the dot energy levels can be controlled by applying a voltage in the gate electrode. The conductance of the dot is suppressed except when one of the levels crosses the Fermi level of

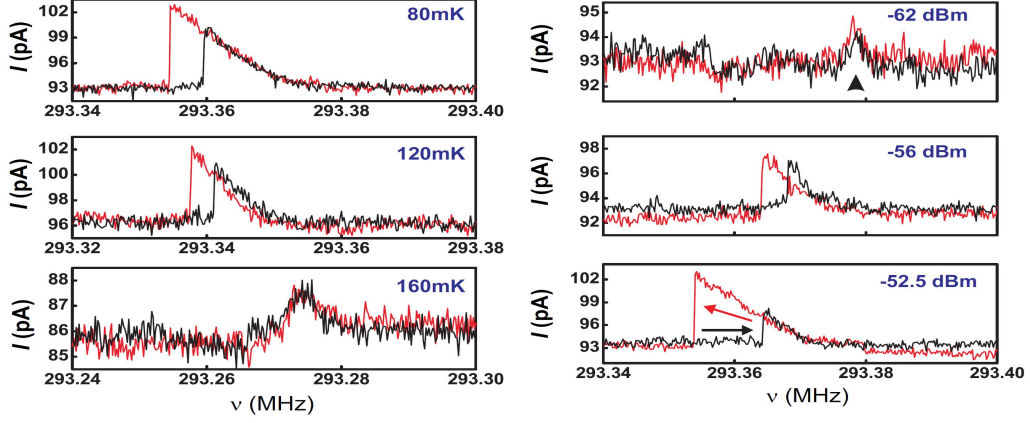


Figure 1.13: Left: Electronic current vs. antenna frequency at high antenna amplitude for increasing temperature from top to bottom. Right: Electronic current vs. antenna frequency at low temperature for increasing antenna amplitudes from top to bottom. This Fig. was taken from Ref. [12].

the leads. In other words, the conductance versus gate voltage shows a collection of peaks each corresponding to a state on the dot crossing the Fermi level. The width of these peaks is proportional to the width of the levels. This is known as resonant tunneling. In this thesis, only one energy level is assumed to be relevant. The other levels are assumed to be of either too high or too low energy to contribute to transport. In addition to the discrete spectrum, in many nanosystems, the Coulombic interaction is dominant. This causes the dot to have a well defined number of electrons. Adding an electron to the dot is prevented by this strong interaction. By changing the gate voltage, the energy of the dot with  $N$  electrons changes. At specific degeneracy points, the dot states having  $N$  and  $N + 1$  electrons are degenerate. This allows for charge fluctuations and, thus, electron transport. The conductance versus gate voltage shows a very low conductance except at charge degeneracy points. This is known as the *Coulomb blockade*.

Molecules or quantum dots (QDs) can act as local magnetic moments and exhibit also the Kondo effect. The Kondo problem originates back in 1930s where it was discovered that the resistivity of metal with dilute concentration of magnetic impurities starts to increase at low temperatures if the temperature is further decreased. A hand waving explanation of the effect is that magnetic moments have spin degrees of freedom which must be frozen at low temperatures in order that the entropy at zero temperature vanishes. As described in Chapter 4 within the Anderson impurity model, this so called screening proceeds by binding the impurity spin into singlet with the spin density of the conduction electrons and is efficient only at temperatures below a certain low-energy scale of the problem, called the Kondo temperature. Because of this binding the impurity density of states at the Fermi energy increases. The conduction electrons, which would pass if the impurity was not there, thus scatter and the resistivity is increased. The Kondo effect is involved also in the formation of heavy fermions in intermetallic compounds based especially upon rare earth elements like Ce, Pr, and Yt and actinide elements like uranium [51]. In these materials, the Kondo effect leads to quasi-electrons with masses up to thousands times the free electron mass, i.e., the electrons are dramatically slowed by the interactions. Another manifestation of the Kondo effect is the unusual metallic  $\delta$ -phase of plutonium [52, 53].

In the nanoscopies the impurity can be imitated by a QD or a molecule embedded in the bath of noninteracting electrons originating from the metallic electrodes. The Coulomb

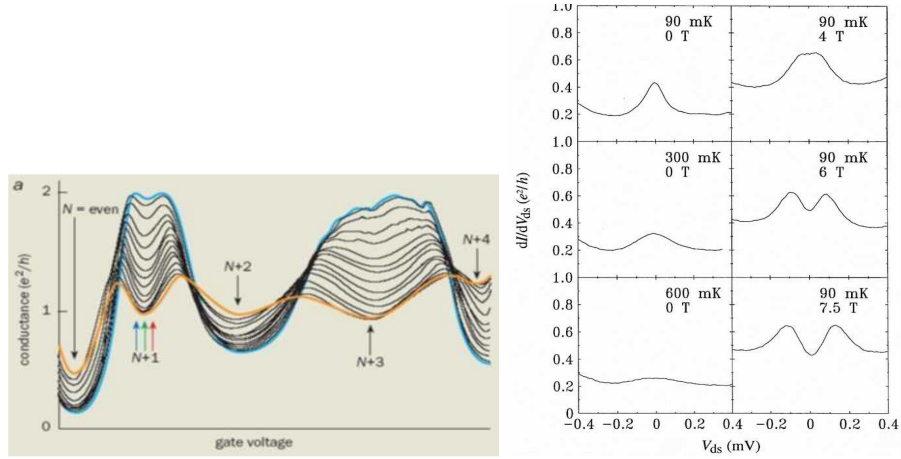


Figure 1.14: The main results of two important experiments reporting the observation of the Kondo effect in QDs: Left panel taken from Ref. [66] and right panel taken from Ref. [55]

interaction which is negligible in the contacts due to the screening by electron-hole pairs is large in the molecular orbital. The spin of the electron there acts as the local moment. Somewhat counterintuitively, in nanoscopic systems the Kondo effect produces the opposite behavior to that of a bulk metal: it increased the conductance. This is because the electrons have to travel through the device, as there is no electrical path around it [54]. The transfer of electrons and thereby the conductance is enhanced at low temperatures when the density of states at the device is increased due to the Kondo effect. Such behavior has been observed in measurements of transport through QDs [55, 56] and molecules [57, 58, 59, 60, 61]. The Kondo effect can be probed also by observing magnetic adatoms at the metallic surfaces using the STM (scanning-tunneling microscope) [64, 65] and could account for the 0.7 anomaly [67] observed in quantum point contacts [68].

### 1.3.2 Key experiments on correlated nanotransport

In this section I review some recent experimental results about Kondo effect in QDs and molecular junctions.

The left panel of Fig. 1.14 shows the conductance through a quantum dot as function of gate voltage at different temperatures. At high temperature, the results show Coulomb blockade behavior (orange line). As temperature is decreased, the conductance in the even occupation regimes is suppressed (due to the suppression of thermal fluctuations), while in the odd occupation regimes, the conductance is enhanced due to the Kondo effect until it reaches the unitary limit  $2e^2/h$  for low enough temperatures (in this thesis I will consider  $G_0 = e^2/h$ ). This was the first experiment to report the unitary conductance limit in the Kondo regime [66]. The right panel shows the differential conductance versus bias voltage for different temperatures and magnetic fields. As the temperature is lowered, a peak is observed at zero bias (zero-bias anomaly). This peak is split upon the application of a magnetic field due to Zeeman effect confirming the prediction of Meir *et al.* [69]. This experiment was the first observation of the Kondo effect in a QD [55].

As already outlined above, Kondo effect has been observed in several molecular junctions [57, 58, 59, 60, 61, 62]. Recent experiments [19, 63] have shown that conduction through molecular systems in this regime is strongly dependent on the molecule-electrode coupling. In Fig. 1.15 the authors of Ref. [63] have shown that both the Kondo temperature  $T_K$  and the magnitude of the zero-bias conductance signal associated with the Kondo resonance are

modified by varying the electrode spacing. The same devices can also exhibit finite-bias inelastic Kondo features at an energy that corresponds to the lowest-energy intracage vibrational mode of  $C_{60}$  (see Fig. 1.15). This study suggests that the motion of the molecule between the leads can modify the relative coupling of the molecule to the two electrodes.

In Ref.[19], the authors report transport measurements of single- $C_{60}$  molecular transistors providing evidence for coupling between the center-of-mass motion of  $C_{60}$  and single-electron hopping, a novel conduction mechanism that has not been observed in previous quantum-dot studies. When an electron hops onto the  $C_{60}$ , the "spring" is compressed as the charge of the additional electron draws the molecule closer to the, say, left contact lead. When the electron hops off the  $C_{60}$ , the spring is released. In this manner, electron-hopping causes the molecule to oscillate between the two contacts as a "shuttle" for electrons.

Recently, several efforts have focused on the "shuttle effect", both in the classical[70] and quantum regimes [71, 72, 73, 74, 75, 76, 77]. Indeed, the first successful experimental implementation of a NMSS[70] was reported in [76, 77] and was most focused on the large bias non-equilibrium regime.

In this thesis I want to address the low temperature low bias regime where a strong interplay between the Kondo physics and vibrational degrees of freedom is expected [156, 159]. Indeed, there are contrasting experimental results in this regime: Park *et al.*[19] performed measurements in  $Au - C_{60} - Au$  junctions where the conductance at low bias was found to be largely suppressed and the current-voltage characteristics were dominated by the Coulomb blockade phenomenon. A related transport experiment through a single  $C_{60}$  molecule[63] showed a much higher low-bias conductance (of the order of  $0.1G_0$  with  $G_0 = e^2/h$ ), which was attributed to the appearance of Kondo physics.

I believe that for the interpretation of the experimental results a better understanding of the interaction effects of the center of mass motion of the molecule onto the electronic hopping by means of a simple theoretical model is necessary.

In Chap.4, I numerically investigate with Density Matrix Renormalization Group (DMRG) the electronic transport properties of a nanomechanical shuttling device in the Kondo regime. I model the system by means of the Anderson impurity model with noninteracting (tight-binding) leads. The molecule (impurity site of the chain) is allowed to oscillate between the two metallic contacts. I focus on the effects of tunneling barrier modulation (encoded in a coupling constant  $\alpha$ ) on the electronic conductance and on the static and dynamical properties of the phononic mode. The results show an interesting and unexpected conductance cancellation for a sufficiently large value of  $\alpha$  when an odd number of electrons occupy the molecule. This results agree with the conductance suppression in the low temperature and bias regime observed in Ref. [19].

At the end of this section I want to give an approximate estimate of the parameter  $\alpha$  using experimental parameters given in Ref. [19]. The dependence of the hopping integral  $t$  on the electrode- $C_{60}$  distance  $z$  can be modeled as  $t(z) = t_0 e^{-z/l_0}$ , where  $l_0$  is the distance from the center of  $C_{60}$  to the electrode. Moreover, the experiment indicates that an additional electron on  $C_{60}$  results in the shortening of the  $C_{60}$ -lead distance by  $\delta \simeq 4$  pm, but it does not significantly change the vibrational frequency. Using the formula  $t' = t(\delta) = t(0)(1 - \alpha\delta)$ , is easy to show that  $\alpha \simeq 0.99/\delta \simeq 0.249\text{pm}^{-1}$ . Using a simple theoretical estimate based on van der Waals and electrostatic interactions between  $C_{60}$  and the leads, the authors in Ref.[19] estimate  $k \simeq 70\text{N/m}$  and  $\omega_0 \simeq 1.2\text{THz}$ , corresponding to the characteristic energy of 5meV describing the step-like jumps measured in the electronic current for large bias voltages. Expressing lengths in terms of the zero-point motion  $x_0 = \sqrt{\hbar\omega_0/2k}$  of the oscillating  $C_{60}$  molecule  $x_0 \simeq 2.4\text{pm}$ , one has approximatively  $\alpha \simeq 0.6$ .



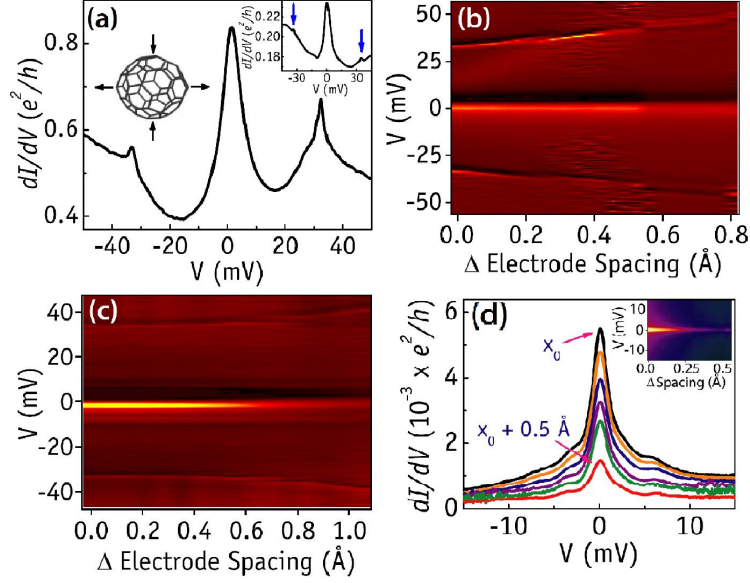


Figure 1.15: Panel(a):  $dI/dV$  for a device investigate in [63] at  $T = 1.6K$  showing satellite peaks near  $\pm 33mV$ . Left inset: Schematic of the  $H_g(1)$  intracage vibrational mode. Right inset:  $dI/dV$  for another device at  $T = 1.6K$ . Panels(b),(c):  $d^2I/dV^2$  as a function of bias voltage and electrode spacing for devices investigate in panel (a) at  $T = 1.6K$ . Panel (d):  $dI/dV$  traces of a device at various electrode spacings for  $T = 1.6K$ .  $x_0 \simeq 1nm$  is the initial gap between the leads. This figure is taken from Ref. [63].

## 1.4 Theoretical methods

The previous sections discussed a number of recent transport experiments on various nanoscale systems. It was found that electron-vibration interaction played an essential part for understanding the properties of the systems scrutinized.

From an analytical stand point, in order to build a transport theory that include these effects it is necessary to go beyond the Landauer-Buttiker[78] and Kubo[79] formalisms. The former approach is limited to non-interacting cases, that is electrons in the central system (molecule) and in the leads are free particles in their quantum states. Within Kubo formalism, also known as linear response theory, one allows for the presence of interactions but one extracts information about electron transport by solving the equilibrium problem by standard many-particle theory. Since the method is limited to the linear regime it cannot be used to model the highly nonlinear device characteristics usually observed.

A complete quantum kinetic description of electron transport under any bias condition can be constructed by the use of nonequilibrium Green's functions (NEGF)[80, 81]. This method has proven to be very successful for a wide range of systems and the generality makes it a strong analytical technique. For these reasons it has also been chosen as the framework for the first part of the present work.

In the last part of the thesis I investigate low-dimensional highly correlated molecular systems, where the strength of the interactions prevents for analytical techniques based on perturbation theory of being used. In particular, I will use an approximation-free numerical technique, suitable for non-equilibrium quantum many-body systems: the Density Matrix Renormalization Group (DMRG)[83, 85]. DMRG is one of the most accurate numerical approaches for treating strongly correlated systems described by lattice Hamiltonians in one spatial dimension. The method consists of a very efficient iterative procedure and allows for the investigation of ground-state (equilibrium) properties of strongly correlated systems

with several hundred to several thousand lattice sites with low computational cost (for an introduction to the DMRG see Appendix D).

DMRG can be considered as a variational method, even if relies heavily on exact diagonalization and numerical renormalization group (NRG [82]) ideas. It was introduced by S. White in 1992 as a development of Wilson NRG's. It is variational because the proposed solution has the very peculiar form of a "matrix-product state" [86]. However, no a priori assumptions are made about the form of the coefficients, or the underlying physics. The power of the method is precisely that it is smart enough to be able to find for us the best possible wave function of that form, without any external bias. Even though the accuracy is finite, it is totally under control, and one can obtain results that are essentially exact. Another ingredient is the block decimation process, similar to the one introduced by Wilson. Recently [87, 88], the algorithm has been extended to time dependent cases, allowing to calculate time-dependent correlation functions of out-of-equilibrium systems with high accuracy. Moreover, the method has been mostly applied to study non-equilibrium quantum transport for electronic systems [89, 90].

In Chap. 4, I will extend the application of this technique to the case where also electron-phonon interaction is present within a Quantum Shuttle model in the low bias quasi-equilibrium regime.

## 1.5 Outline of the thesis

The present thesis is organized as follows. This chapter provided an introduction to the field of molecular electronics and NEMS. I have discussed a number of recent experiments on transport through single molecules in which inelastic effects were observed and on NEMS application of carbon nanotubes as self-detecting single-electron transistors.

In Chap. 2, I develop a very accurate computational scheme for the dynamics of single oscillator mode coupled with an out-of-equilibrium molecular junction. I concentrate my attention on the physical regime where the vibrational motion of the oscillator is 'slow' with respect to all electronic energy scales and can be considered "classical". I exploit the Keldysh formalism within Non Equilibrium Green's Function theory (NEGF) for the electronic subsystem together with stochastic dynamics for the vibrational degrees of freedom.

In Chap. 3, I further investigate the renormalization effects of the bending mode frequency of a suspended nanotube NEMS as a function of the external charge injection (due to the applied bias and gate voltages). I also include in the model the effects of an external antenna driving the oscillations of the nanotube. At the end of the Chap., I show that my approach can be extended to the case where an external magnetic field perpendicular to the oscillator motion is introduced.

In Chap. 4, I numerically investigate with DMRG the electronic transport properties of a nanomechanical shuttling device in the Kondo regime.

Finally, I provide a summary of the thesis and an outlook for future work.



# Chapter 2

## Electronic transport through an interacting molecular junction: coupling to a low frequency vibrational mode

In this chapter I propose a very accurate computational scheme for the dynamics of a classical oscillator coupled to a molecular junction driven by a finite bias, including the finite mass effect. I focus on two models widely used in the literature for the molecular junction: Anderson-Holstein (AH) and two-site Su-Schrieffer-Heeger (SSH) models. As concerns the oscillator dynamics, I'm able to recover a Langevin equation confirming what found by other authors with different approaches and assessing that quantum effects come from the electronic subsystem only. Solving numerically the stochastic equation, I study the position and velocity distribution probabilities of the oscillator and the electronic transport properties at arbitrary values of electron-oscillator interaction, gate and bias voltages. The range of validity of the adiabatic approximation is established in a systematic way by analyzing the behavior of the kinetic energy of the oscillator. Due to the dynamical fluctuations, at intermediate bias voltages, the velocity distributions deviate from a gaussian shape and the average kinetic energy shows a non monotonic behavior. In this same regime of parameters, the dynamical effects favor the conduction far from electronic resonances where small currents are observed in the infinite mass approximation. These effects are enhanced in the two-site SSH model due to the presence of the intermolecular hopping  $t$ . Remarkably, for sufficiently large hopping with respect to tunneling on the molecule, small interaction strengths and at intermediate bias (non gaussian regime), I point out a correspondence between the minima of the kinetic energy and the maxima of the dynamical conductance.

### 2.1 The Anderson-Holstein (AH) model

The spinless Anderson-Holstein model is the simplest model of a molecular junction including the effect of electron-phonon interaction. The molecule is modeled as a single electronic level interacting locally with a single vibrational mode. The electronic system is described by the standard junction Hamiltonian  $\hat{\mathcal{H}}_{el} = \hat{H}_{mol} + \hat{H}_{tun} + \hat{H}_{leads}$ , with

$$\hat{H}_{mol} = E_g \hat{d}^\dagger \hat{d}, \quad (2.1)$$

$$\hat{H}_{tun} = \sum_{k,\alpha} (V_{k,\alpha} \hat{c}_{k,\alpha}^\dagger \hat{d} + h.c.), \quad (2.2)$$

$$\hat{H}_{leads} = \sum_{k,\alpha} \varepsilon_{k,\alpha} \hat{c}_{k,\alpha}^\dagger \hat{c}_{k,\alpha}. \quad (2.3)$$

The molecular electronic level has energy  $E_g$  and creation (annihilation) operators  $\hat{d}^\dagger(\hat{d})$ . The operators  $\hat{c}_{k,\alpha}^\dagger(\hat{c}_{k,\alpha})$  create (annihilate) electrons with momentum  $k$  and energy  $\varepsilon_{k,\alpha} = \xi_{k,\alpha} - \mu_\alpha$  in the left ( $\alpha = L$ ) or right ( $\alpha = R$ ) free metallic leads. The chemical potentials in the leads  $\mu_L$  and  $\mu_R$  are assumed to be biased by an external voltage  $eV_{bias} = \mu_L - \mu_R$ . Electronic tunneling between the molecular dot and a state in the lead has amplitude  $V_{k,\alpha}$ . I consider the oscillator dynamics ‘classical’ from the beginning and described by the position and momentum variables  $x, p$ .

The Hamiltonian of the oscillator is given by

$$H_{osc} = \frac{p^2}{2m} + \frac{1}{2}m\omega_0^2 x^2, \quad (2.4)$$

characterized by the frequency  $\omega_0$  and the effective mass  $m$ . The interaction (typically of electrostatic origin, see Appendix B) is provided by a simple linear coupling between the electron occupation on the molecule,  $\hat{d}^\dagger \hat{d}$ , and the displacement of the oscillator

$$\hat{H}_{int} = \lambda x \hat{d}^\dagger \hat{d}, \quad (2.5)$$

where  $\lambda$  is the electron-oscillator coupling (EOC) strength. The overall Hamiltonian is therefore given by  $\hat{\mathcal{H}} = \hat{\mathcal{H}}_{el} + H_{osc} + \hat{H}_{int}$ .

In the following, the coupling between the electron and the vibrational mode will be often described in terms of the electron-phonon coupling energy  $E_p = \lambda^2/(2m\omega_0^2)$  and the coupling to the leads by the tunneling rate  $\Gamma_{k,\alpha} = 2\pi\rho_\alpha|V_{k,\alpha}|^2/\hbar$  (the full hybridization width of the molecular orbital is then  $\hbar\Gamma_k = \hbar\Gamma_{k,L} + \hbar\Gamma_{k,R}$ ), where  $\rho_\alpha$  is the density of states in the lead  $\alpha$ . For the sake of simplicity, I will suppose flat density of states for the leads within the wide-band approximation ( $\Gamma_{k,\alpha} \mapsto \Gamma_\alpha$ ). In this chapter we will measure length in units of  $x_0 = \frac{\lambda}{m\omega_0^2}$  and energy in units of  $\hbar\Gamma$ . Finally, the leads will be considered as zero temperature thermostats.

In the next subsections, I will first analyze the coupled electron-oscillator problem in the limit of infinite mass for the oscillator (sec. 2.1.1). I will then indicate (sec. 2.1.2) how to construct the stochastic Langevin equation for the dynamics of the oscillator including the finite mass effect. In the subsection (2.1.3) I will solve numerically the stochastic equation and analyze the effects of the oscillator dynamics on the electronic observables inherent to the transport problem (I-V characteristic and conductance).

### 2.1.1 Out of equilibrium Born-Oppenheimer approximation: infinite mass (static) case

When the vibrational motion of the oscillator is slow with respect to all electronic energy scales, it is possible to decouple oscillator and electronic dynamics. In the spirit of Born-Oppenheimer approximation, I consider the limit  $m \mapsto \infty$  in the full Hamiltonian disregarding the kinetic energy of the oscillator. The electronic dynamics is therefore equivalent to a non-interacting resonant single level problem with energy level renormalized by the ‘polaronic’ shift  $E_g \mapsto E_g + \lambda x$ . The retarded (advanced) Green functions  $G^{r(a)}(\omega, x)$  and the lesser (greater) Green functions  $G^{<(>)}(\omega, x)$  in stationary non-equilibrium conditions (see Appendix A for a definition of these Green’s functions) can be derived within the Keldysh formalism (through the Dyson and Keldysh equations)[81, 80] and depend parametrically on the displacement coordinate  $x$ . Starting from the force exerted on the oscillator

$$F = -m\omega_0^2 x + \lambda \langle \hat{n}_{el} \rangle(x), \quad (2.6)$$

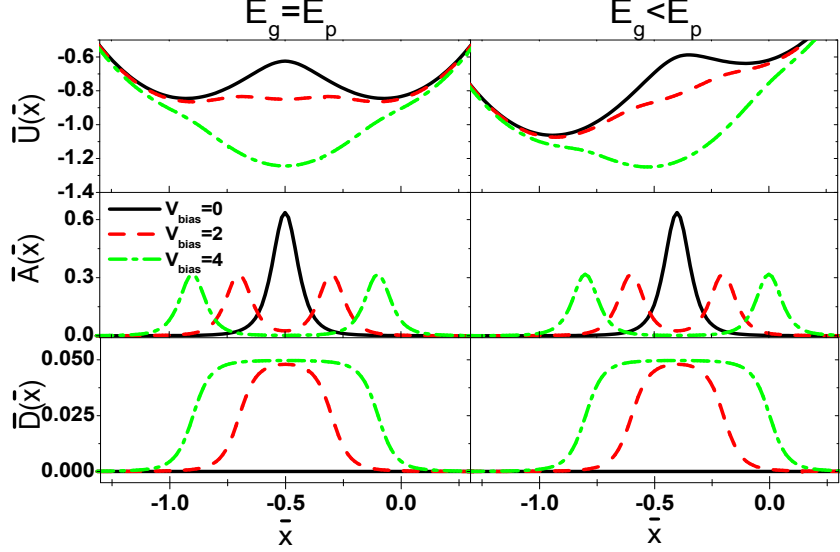


Figure 2.1: Spatial dependence of the dimensionless generalized static potential  $\bar{U}(\bar{x})$  (panels A,B), friction coefficient  $\bar{A}(\bar{x})$  (panels C,D), fluctuating term  $\bar{D}(\bar{x})$  (panels E,F) for symmetric  $E_g \sim E_p$  and asymmetric  $E_g < E_p$  minima for different values of bias,  $V_{bias} = 0$  (solid (black) curve),  $V_{bias} = 2$  (dashed (red) curve),  $V_{bias} = 4$  (dashed dot (green) curve). The potential is expressed in  $\hbar\Gamma$  units ( $\bar{U} = U/\hbar\Gamma$ ), the friction coefficient in  $m\omega_0$  units ( $\bar{A} = A/m\omega_0$ ), the fluctuating term in  $\lambda^2/\omega_0$  units, ( $\bar{D} = D/(\lambda^2/\omega_0)$ ).  $V_{bias}$  values are expressed in  $\hbar\Gamma/e$  units, where  $e$  is the electron charge. The dimensionless position variable  $\bar{x}$  is defined as  $\bar{x} = x/x_0$  with  $x_0 = \frac{\lambda}{m\omega_0^2}$ .

where (see Eq. of Appendix A for a definition of density)

$$\langle \hat{n}_{el} \rangle(x) = \sum_{\alpha=L,R} \hbar^2 \Gamma_{\alpha} \int \frac{d\omega}{2\pi} f_{\alpha}(\omega) |G^r(\omega, x)|^2, \quad (2.7)$$

with  $f_{\alpha}(\omega)$  Fermi function of the lead  $\alpha = R, L$ , one can therefore straightforwardly compute the expression of the generalized potential in non-equilibrium conditions (obtained applying symmetric bias unbalance  $\mu_R = -eV_{bias}/2$ ,  $\mu_L = eV_{bias}/2$ )

$$U(x) = \frac{1}{2} m\omega_0^2 x^2 + \frac{\lambda x}{2} - \sum_{\alpha=L,R} \left[ \frac{\mu_{\alpha} - E_g - \lambda x}{2\pi} \arctan \left( \frac{\mu_{\alpha} - E_g - \lambda x}{\hbar\Gamma/2} \right) - \frac{\hbar\Gamma}{8\pi} \ln[4(\mu_{\alpha} - E_g - \lambda x)^2 + (\hbar\Gamma)^2] \right]. \quad (2.8)$$

This generalized oscillator potential depends parametrically by the spring constant  $m\omega_0^2 = k$ , the EOC strength  $\lambda$ , the energy of the electron level  $E_g$  (which can be considered a gate potential), the coupling to the leads  $\Gamma$  and finally by the bias  $V_{bias}$ . In Fig.2.1 (panels A,B), I present some features of the generalized potential  $U(x)$  in the strong coupling regime ( $E_p > \hbar\Gamma$ ), where the potential shows several minima. For  $E_g \sim E_p$  and not too high bias (panel A, Fig.2.1), the potential develops two symmetric minima near  $x \simeq 0$  (corresponding to  $\langle \hat{n}_{el} \rangle \simeq 0$ ) and  $x \simeq -1$  (corresponding to  $\langle \hat{n}_{el} \rangle \simeq 1$ ) separated by a barrier whose height is roughly proportional to  $E_p$ . This bistable regime corresponds to the physical situation where the bare electron level  $E_g$  is above the chemical potential of both leads, while the

renormalized charged level  $E_g - 2E_p$  is below them. The molecule can stay in one minimum or in the other. If one increases the bias  $V_{bias}$ , the potential  $U(x)$  shows a third minimum corresponding to average electron occupation on the molecule  $\langle \hat{n}_{el} \rangle \simeq 1/2$  and, for sufficiently large  $V_{bias}$ , only this minimum remains. If  $E_g < E_p$  the potential also shows two or more minima but they are asymmetric (panel B, Fig.2.1). For sufficiently high bias, the common feature is the existence of a single minimum corresponding to occupation  $\langle \hat{n}_{el} \rangle \simeq 1/2$ .

In the above analysis the displacement  $x$  has been used as a free parameter. Actually, the only  $x$  values relevant for the electronic properties in the static approximation are those which solve the Eq.  $F(x) = 0$ . These solutions depend parametrically by all the parameters of the theory (in particular by the bias  $V_{bias}$ ). This may yield transitions between different local minima in the potential, determining in the electronic current-voltage characteristic the onset of interesting non linear phenomena like hysteresis, switching and Negative Differential Resistance (NDR).[26] Indeed, the authors of Ref. [26] proposed a polaron mechanism within the AH model to explain such phenomena, effectively observed in transport experiments on molecular devices. However, the results of the static approximation can be strongly modified by dynamical effects. Indeed, corrections due to the finite (though large) mass of the oscillator are expected to be important.[27, 28, 123] As I shall see in the next sections, the inclusion of the finite mass effect on the oscillator dynamics gives rise to a stochastic Langevin equation with a position dependent dissipation term and white noise force. The stochastic fluctuations of the oscillator motion will strongly modify the current-voltage characteristics obtained in the infinite mass approximation.

### 2.1.2 Dynamical (finite mass) corrections to static case: setting Langevin equation for the oscillator

Within the static approximation (infinite mass), the main effect of the non-equilibrium fast electronic environment is the modification of the force (Eq. 2.6) experienced by the mechanical oscillator. In this section I show how to include the finite mass effects on the oscillator dynamics.

First of all, one should include the effect of time dependence of the oscillator dynamics on the Hamiltonian of the electronic problem, which results therefore explicitly time dependent ( $\hat{\mathcal{H}} \mapsto \hat{\mathcal{H}}(x(t))$ ). Using the extension of the Keldysh formalism to time dependent cases,[80] one can solve the Dyson and Keldysh equations for the electron Green functions which now depends on times  $t$  and  $t'$  separately. In absence of electron-electron interactions, the retarded molecular Green function can be nevertheless obtained analitically (with  $E_g(t) = E_g + \lambda x(t)$ )

$$G^r(t, t') = -\frac{i}{\hbar} \theta(t - t') e^{-i \int_{t'}^t dt_1 (\frac{E_g(t_1)}{\hbar} - i\Gamma/2)}, \quad (2.9)$$

and depends in non linear way by the entire dynamics  $x(t)$  of the oscillator. In order to overcome this difficulty, I resort to an adiabatic approximation of the electronic Green function. One assumes a slow time dependence of  $x(t)$  and calculates a truncated electron Green function which acquires a 'slow' time dependence and a linear correction in the oscillator velocity.

#### Adiabatic Approximation

In this section, I show how the adiabatic approximation on the electronic Green function works.

Before implementing the adiabatic approximation, it is convenient to rewrite the Dyson equation for the molecular retarded Green function Eq. 2.9

$$G^r(t, t') = g^r(t, t') + \int dt_1 \int dt_2 G^r(t, t_1) \Sigma_{el-ph}^r(t_1, t_2) g^r(t_2, t'), \quad (2.10)$$

where the Green function  $g^r(t, t')$  already takes into account the coupling with the leads,

$$g^r(t, t') = -\frac{i}{\hbar} \theta(t - t') e^{-i(\frac{\varepsilon_0}{\hbar} - i\Gamma/2)(t - t')}. \quad (2.11)$$

Now, I reparametrize the retarded electron-oscillator self-energy separating slow and fast times scales (in the following, for sake of simplicity, I drop the label  $el-ph$  from the self-energy)

$$\Sigma^r(t_1, t_2) \mapsto \Sigma^r\left(\frac{t_1 + t_2}{2}, t_1 - t_2\right). \quad (2.12)$$

According to the approach used in Ref.[105], I expand Eq. 2.12 with respect to the slow mean time  $\frac{t_1 + t_2}{2}$  about a generic time  $t_0$  belonging to the interval  $[t, t']$

$$\Sigma^r\left(\frac{t_1 + t_2}{2}, t_1 - t_2\right) \simeq \Sigma_0^r(t_0, t_1 - t_2) + \Sigma_1^r(t_0, \frac{t_1 + t_2}{2}, t_1 - t_2), \quad (2.13)$$

with

$$\Sigma_0^r(t_0, t_1 - t_2) = \lambda x(t_0) \delta(t_1 - t_2) \quad (2.14)$$

$$\Sigma_1^r(t_0, \frac{t_1 + t_2}{2}, t_1 - t_2) = \left(\frac{t_1 + t_2}{2} - t_0\right) \lambda \dot{x}(t_0) \delta(t_1 - t_2). \quad (2.15)$$

The adiabatic expansion  $G^r(t, t') \mapsto G_0^r(t_0, t - t') + G_1^r(t_0, t - t')$  for the Green function follows from that for the self-energy via the Dyson equation Eq. 2.10. I can now introduce the Fourier transforms  $G_{0/1}^r(t_0, \omega) = \int d(t - t') e^{i\omega(t - t')/\hbar} G_{0/1}^r(t_0, t - t')$ . Since my goal is an adiabatic expansion of the electronic observables at time  $t$ , from now on I choose  $t_0 = t$ . One can easily show that  $t_0 = t$  is the only choice able to recover the fluctuation-dissipation theorem at vanishing bias voltage (equilibrium condition) for the Langevin equation I will derive below. From the Dyson equation Eq. 2.10, taking into account Eq. 2.14 and Eq. 2.15, I thus find

$$G_0^r(t, \omega) = \frac{1}{\hbar\omega - E_g(t) + i\hbar\Gamma/2}, \quad (2.16)$$

$$G_1^r(t, \omega) = i\hbar \frac{\partial E_g}{\partial t} \frac{\partial G_0^r(t, \omega)}{\partial \hbar\omega} G_0^r(t, \omega). \quad (2.17)$$

obtaining a correction which is linear in the velocity of the oscillator  $\frac{\partial E_g}{\partial t} = \lambda \frac{\partial x}{\partial t}$ .

### Adiabatic Approximation: calculation of damping and fluctuating term

Both in equilibrium and in out-of equilibrium conditions, the interaction with the leads introduces a dissipative correction term to the force (Eq. 2.6) exerted on the oscillator. Actually, in order to estimate such a dissipative term, I have to calculate the adiabatic corrections to the lesser-Green function that is directly related to the occupation

$$\langle \hat{n} \rangle(t) = -i\hbar G^<(t, t) = \sum_{\alpha=L,R} \hbar\Gamma_\alpha \int \frac{d\hbar\omega}{2\pi} f_\alpha(\omega) |G^r(\omega, t)|^2, \quad (2.18)$$

where  $G^r(\omega, t)$  is given by

$$G^r(\omega, t) = \int d\tau G^r(t, \tau) e^{i\omega\tau}. \quad (2.19)$$

From Eq. 2.16, one obtains for the occupation at zero-order an expression of the same form of the static limit (Eq. 2.7) with the substitution  $E_g \leftrightarrow E_g(t)$ , acquiring a weak time dependence through the slow variable  $t$ . Adding the first order correction Eq. 2.17 into the Eq. 2.18, and neglecting terms proportional the square velocity of the oscillator, I obtain for the occupation

$$\langle \hat{n} \rangle(t) \simeq \sum_{\alpha=L,R} \hbar \Gamma_{\alpha} \int \frac{d\hbar\omega}{2\pi} f_{\alpha}(\omega) \left( 1 + \frac{\hbar\Gamma}{2} \frac{\partial E_g}{\partial t} |G_0^r(\omega, t)|^2 \frac{\partial}{\partial \omega} \right) |G_0^r(\omega, t)|^2. \quad (2.20)$$

Therefore, the force Eq. 2.6 modifies to

$$F(x) \mapsto F'(x, v) = F(x) - A(x)v, \quad (2.21)$$

where  $v = \dot{x}$  is the velocity of the oscillator.

In order to include the effect of a ‘fast’ electronic environment on the oscillator motion, I propose to take into account the fluctuations of the force[112] acting on the oscillator. These are induced by the intrinsic ‘quantum’ fluctuations of the electronic subsystem. I add to the *average* force contribution Eq.2.6, suitable corrected by the damping term, Eq.2.21, a stochastic fluctuating term that is able to take into account the effect of the electronic quantum fluctuations on the classical dynamics of the oscillator. I estimate the noise strength evaluating the *average* of the square fluctuation of the force over the electronic steady state. This fluctuating term is directly related to the fluctuation of the electron occupation

$$\langle \delta \hat{F}(t) \delta \hat{F}(t') \rangle = \lambda^2 \langle \delta \hat{n}(t) \delta \hat{n}(t') \rangle = \lambda^2 \left( \langle \hat{n}(t) \hat{n}(t') \rangle - \langle \hat{n}(t) \rangle \langle \hat{n}(t') \rangle \right). \quad (2.22)$$

Decoupling the term  $\langle \hat{n}(t) \hat{n}(t') \rangle$  with the Wick theorem, one obtains

$$\langle \delta \hat{F}(t) \delta \hat{F}(t') \rangle = \lambda^2 \hbar^2 G^<(t' - t) G^>(t - t') = \lambda^2 \hbar^2 G_0^<(t' - t) G_0^>(t - t'), \quad (2.23)$$

where I have used zero-order time-dependent Green functions (as in Eq. 2.16) in order to take only first order corrections in the adiabatic ratio  $\frac{\omega_0}{\Gamma}$ . At this level of approximation, I have obtained a multiplicative colored noise. According to the adiabatic approximation, I can further simplify the fluctuating term retaining only the zero-frequency component of the noise

$$\langle \delta \hat{F}(t) \delta \hat{F}(t') \rangle = \lambda^2 \hbar^2 \int d\varepsilon e^{i\varepsilon(t-t')} \int \frac{d\omega}{2\pi} G_0^<(\omega + \varepsilon) G_0^>(\omega) \simeq D(x) \delta(t - t'), \quad (2.24)$$

corresponding to electronic times scales comparable with that of the oscillator. I have therefore obtained a multiplicative white noise in the equation of motion of the oscillator. The resulting Langevin equation for the oscillator dynamics becomes

$$\begin{aligned} m\ddot{x} + A(x)\dot{x} &= F(x) + \sqrt{D(x)}\xi(t), \\ \langle \xi(t) \rangle &= 0, \quad \langle \xi(t)\xi(t') \rangle = \delta(t - t'), \end{aligned} \quad (2.25)$$

where  $\xi(t)$  is a standard white noise term. Explicitly, the damping term  $A(x)$  is given by (from Eq. 2.20)

$$A(x) = \frac{4m\omega_0}{\pi} \frac{\hbar\omega_0}{\hbar\Gamma} \frac{E_p}{\hbar\Gamma} \sum_{\alpha=R,L} \left( \frac{1}{[(\frac{\mu_{\alpha}-E_g-\lambda x}{\hbar\Gamma})^2 + 1]^2} \right), \quad (2.26)$$

while the fluctuating term is (from Eq. 2.24)

$$D(x) = \frac{m\omega_0 E_p}{\pi} \frac{\hbar\omega_0}{\hbar\Gamma} \sum_{\alpha=L,-R} \left( \arctan\left(\frac{\mu_\alpha - E_g - \lambda x}{\hbar\Gamma}\right) + \frac{\frac{\mu_\alpha - E_g - \lambda x}{\hbar\Gamma}}{[(\frac{\mu_\alpha - E_g - \lambda x}{\hbar\Gamma})^2 + 1]} \right), \quad (2.27)$$

where it is understood that  $\sum_{\alpha=L,-R} K(\alpha) = K(L) - K(R)$ , for a generic function  $K(\alpha)$ . I note that Eqs. 2.25, 2.26 and 2.27 are identical to that obtained in Ref.[27, 28]. Introducing a natural temporal unit  $t_0 = 1/\omega_0$ , the dimensionless damping  $\bar{A}(\bar{x})$  and fluctuating  $\bar{D}(\bar{x})$  coefficients result proportional to the adiabatic ratio  $\omega_0/\Gamma$ . Regarding the spatial dependence of the damping term, one can note in Fig. 2.1 (panels C-D) that it is almost localized on the position of the local minima of the static potential. The fluctuating coefficient, as shown in Fig. 2.1 (solid (black) line in panels E-F), vanishes at equilibrium (bias voltage  $V_{bias} = 0$ ). Only applying finite bias it becomes different from zero. In Fig. 2.1 (dashed (red) and dashed dotted (green) lines in panels E-F), I show that its spatial extension increases as the bias increases.

### 2.1.3 Numerical solution of Langevin equation: *electronic* observables and limits of the stochastic approach

From the Langevin equation Eq. 2.25 it is possible to derive the distribution probabilities  $P(x)$  and  $P(v)$  of the position and velocities variables of the oscillator. I have evaluated them solving the second order stochastic differential equation with the 4-order stochastic Runge-Kutta algorithm developed by R. L. Honeycutt.[113, 114] First of all, as suggested in Ref.[115], in order to solve my second order ordinary differential equation with multiplicative white noise, I decompose the problem in a set of three first order differential equations

$$\begin{aligned} \dot{x} &= v \\ m\dot{v} &= F(x) - A(x)v + \sqrt{D(x)}\xi(t), \\ \dot{\xi}(t) &= -\zeta\xi(t) + \eta(t), \end{aligned} \quad (2.28)$$

where the auxiliary variable  $\xi(t)$  is able to mimic a white noise uncorrelated variable<sup>1</sup>. The third equation takes into account the effect of spatial dependence of the noise involving a non multiplicative noise term  $\eta(t)$ . For my simulations I have fixed a time step  $t_s = 0.1\tau$  ( $\tau = 1/\omega_0$ ) and set long simulation times up to  $T = 10^9 t_s$ . Within this settings, the algorithm shows an excellent stability in the whole range of model parameters. In order to construct my histograms, I have sampled the values of  $x(t)$  and  $v(t)$  every 100 time steps. I have therefore obtained the distribution probabilities of the stationary state of the oscillator.

Given the assumption about the separation between the slow ionic (vibrational) and fast electronic (tunneling) timescales, the problem of evaluating a generic observable (electronic or not) of the system reduces to the evaluation of that quantity for a fixed position  $x$  and velocity  $v$  of the oscillator, with the consequent averaging over the stationary probability distributions,  $P(x)$  and  $P(v)$ . Therefore, for a generic observable which depends only by position,  $O(x)$ , the averaged quantity is

$$\langle O(x) \rangle = \int dx P(x) O(x), \quad (2.29)$$

---

<sup>1</sup>In order to be sure of simulate a standard white noise with the variable  $\xi(t)$ , I've chosen  $\zeta$  such that its reciprocal is much smaller than the time step used to simulate dynamics  $1/\zeta \ll \tau$ .

while, for an observable which depends on velocity variable only, one has

$$\langle O(v) \rangle = \int dv P(v) O(v). \quad (2.30)$$

The current, the spectral function and the electronic occupation depend only on the position variable

$$I(x) = \frac{e\hbar}{2\pi} \int_{\mu_R}^{\mu_L} d\omega \frac{\Gamma_L \Gamma_R}{\Gamma} A(\omega, x), \quad (2.31)$$

$$A(\omega, x) = \frac{\hbar\Gamma}{(\hbar\omega - E_g - \lambda x)^2 + \hbar^2\Gamma^2/4}, \quad (2.32)$$

$$\langle \hat{n} \rangle(x) = \frac{1}{2} + \frac{1}{2\pi} \sum_{\alpha=R,L} \arctan \left[ \frac{\mu_\alpha - E_g - \lambda x}{\hbar\Gamma/2} \right]. \quad (2.33)$$

The position distribution probabilities  $P(x)$  have been already discussed by authors of Ref.[28] in the extremely strong coupling regime  $E_p \gg \hbar\Gamma \gg \hbar\omega_0$ . They analyze the case where the static potential shows two symmetric or asymmetric wells separated by a very high barrier. In this regime, solving numerically the Fokker-Plank equation of the problem, they estimate the switching-rates by evaluating the escape times from each well of the generalized potential. Indeed, this point is interesting for clarifying the role of electron-phonon interaction in the appearance of a bistable behavior in single molecule tunneling devices. One of the results of this thesis is that the multistability and hysteretic behavior in the current-voltage characteristic disappear if the dynamical effects of the oscillator motion are taken into account. To clarify this point, I focus here the case (already considered in Ref.[28]) where the switching times between different oscillator potential wells are very long, and the oscillator jumps between two states (see panel A of Fig. 2.2) corresponding to very small electronic currents. In order to explore the same regime of parameters, very long simulation times as  $T = 10^9 t_s$  are necessary for sampling the entire phase space experienced during the dynamics. Nevertheless, as shown in Panel B of Fig. 2.2, I get an excellent agreement with Pistolesi *et al.*[28] results. It is interesting to note that in Ref.[28], the authors consider a broadening  $\Gamma$  which is twice the values I consider in this thesis (I show in the caption of Fig. 2.2 the comparison between the simulations taking correctly into account of this factor). In the small bias regime, a strong suppression of the current can be observed. The oscillator spends a long time in each potential well, suddenly jumps into the other and then come back in the same way (see panel A in Fig. 2.2). For clarity I show in panel C of Fig. 2.2 the corresponding position distribution probability  $P(x)$ . The maxima of  $P(x)$  correspond to two low current carrying states: the position of the molecular energy level is far above ( $E_g \sim E_p$ ) or below ( $E_g \sim -E_p$ ) the chemical potential of the leads. For sufficiently high bias voltage, as discussed in subsection 2.1.1, appears a third minimum in the static potential. This minimum corresponds to a high-current carrying state determining a continuous enhancement of the current, against the abrupt discontinuity (or hysteresis) which would be obtained in the static approximation (dashed line in panel B of Fig. 2.2).

## Non gaussian features of $P(v)$ and study of the average kinetic energy of the oscillator

In this section I focus my attention on the oscillator observables  $O(v)$  which depend on the velocity  $v$ . I remark that the oscillator is coupled to the electronic bath only through the



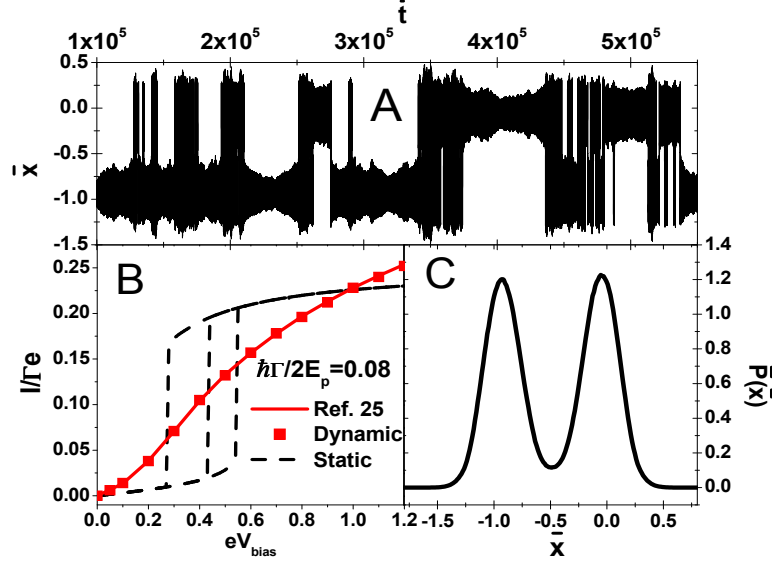


Figure 2.2: Panel A: Solution of the Langevin equation Eq. 2.25 in the extremely strong coupling regime  $E_p \gg \hbar\Gamma \gg \hbar\omega_0$  ( $\omega_0/\Gamma = 10^{-3}$ ) for  $\hbar\Gamma/2E_p = 0.08$ ,  $E_g = E_p$  and  $eV_{Bias} = 0.1$ . Panel B: Current ( $e\Gamma$  units) voltage ( $eV_{bias}$  in  $2E_p$  units) characteristic for the same value of  $\hbar\Gamma/2E_p$  as above. Solid (red) curve is drawn from Ref[28], square line indicates my dynamic simulation and dashed line indicates static I-V. Panel C: Dimensionless position distribution probability for the same values of parameters as in Panel A. The dimensionless position  $\bar{x}$ , time  $\bar{t}$  and distribution function  $\bar{P}$  are defined as  $\bar{x} = x/x_0$ ,  $\bar{t} = t/t_0$ ,  $\bar{P} = P/(1/x_0)$ , with  $x_0 = \frac{\lambda}{m\omega_0^2}$  and  $t_0 = 1/\omega_0$ , respectively.

interaction term  $\hat{H}_{int}$ , Eq. 2.5. As the bias voltage increases, this bath is strongly driven out of equilibrium. It is therefore important to analyze the effect of the electronic subsystem on the oscillator distribution probability  $P(v)$  as a function of the bias voltage. In the small bias regime, regardless the value of the gate voltages  $E_g$  and the coupling  $E_p$ , as shown in Fig. 2.3 (panel A) for different adiabatic ratios (from  $\omega_0 = 10^{-3}$  to  $\omega_0 = 0.25$ ), the velocity distribution probabilities  $P(v)$  are gaussian. In this regime, the non-equilibrium electronic bath behaves like a conventional bath for the oscillator with an ‘effective’ temperature linearly proportional to the bias voltage. As described in the inset of Fig. 2.4, at arbitrary  $E_p$  and gate voltages the kinetic energy curves show a common linear trend at low bias with a slope  $V_{bias}/4$  in agreement with Mozyrsky *et al.* (I get  $V_{bias}/8$  because I choose a broadening  $\hbar\Gamma$  half than used in Ref.[27]). As one increases the bias voltage, the  $(\log P(v) \text{ vs. } v^2)$  plot starts to deviate from a linear trend, as shown in Fig. 2.3, panels B – C – D. This behavior indicates that the oscillator dynamics cannot be simply reduced to an effective temperature in this regime, pointing to a very significant role of the dynamical effects.

In the adiabatic approximation, the average kinetic energy of the oscillator has an important role. It describes the effect of the ‘back-action’ of the non-equilibrium electronic bath on the oscillator dynamics and can be used, as shown below, as a tool to assess the validity of the adiabatic approximation. I show in Fig. 2.4 the behavior of the kinetic energy  $\langle E_{kin} \rangle$  for different interaction strengths  $E_p$  as function of the bias voltage. First of all, I note that, regardless the values of  $E_p$ , for  $V_{bias} = 0$  all kinetic energy curves show  $\langle E_{kin} \rangle = 0$ . At equilibrium, the oscillator ‘thermalizes’ to the temperature of the electronic bath ( $T_{el} = 0$ ). I have also plotted two constant energy lines that specify the range of validity of my approximation,  $E = \hbar\omega_0/2 \sim k_B T_D/2$  and  $E = \hbar\Gamma$ . At intermediate bias values, the curves

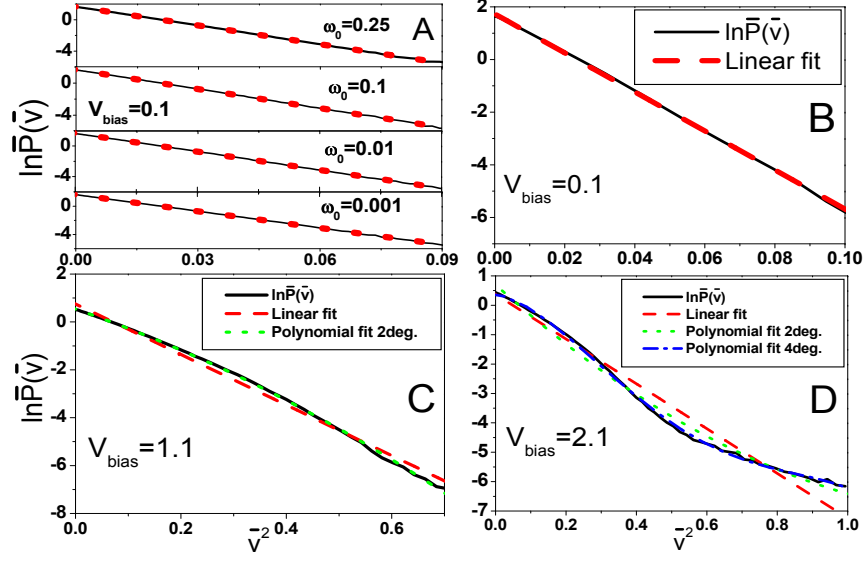


Figure 2.3: Panel A: log-plot of *dimensionless* velocity probability distribution function vs.  $v^2$ , at different adiabatic ratios (the values of  $\omega_0$  shown in the figure are in  $\Gamma$  units), fixed bias voltage  $V_{bias} = 0.1$  and different gate voltages and EOC strengths (not shown in the graph). The dotted (red) lines indicate that curves have a good linear fit. Panels B – C – D: log-plot of velocity probability distribution function vs.  $v^2$  for  $V_{bias} = 0.1$ ,  $V_{bias} = 1.1$ ,  $V_{bias} = 2.1$ , respectively. The dashed (red) line indicates linear fitting. Dotted (green) and dash dotted (blue) lines indicate polynomial fitting of 2nd and 4th degree.  $V_{bias}$  values are expressed in  $\hbar\Gamma/e$  units. The dimensionless distribution function is defined as  $\bar{P} = P/(m\omega_0/\lambda)$ , while  $v^2$  is expressed in  $(\lambda/m\omega_0)^2$  units.

show a departure from the common linear behavior observed in the small bias regime, more evident as the interaction strength increases. The kinetic energy curves corresponding to  $E_p = 2.0$  and  $E_p = 3.0$  show an interesting plateau at intermediate bias where increasing the bias does not produce an increase of the average kinetic energy. Actually, at  $E_p = 3.0$ , I find even a very slight decrease. I also note, in the same regime, that the distribution velocity probabilities are not gaussian.

### Limits of the adiabatic approach

As mentioned, I can use the average kinetic energy of the oscillator to fix the range of validity of the adiabatic approximation. If this energy is lower than the characteristic Debye temperature of the oscillator  $\langle E_{Kin} \rangle < \hbar\omega_0/2 \sim k_B T_D/2$ , I actually explore a region, as discussed in Ref.[116], where quantum correlation effects can not be disregarded. I call this region Non Classical or Quantum Region (QR). If  $k_B T_D/2 < \langle E_{Kin} \rangle < \hbar\Gamma$ , that is the kinetic energy is lesser than the characteristic energy scale of the electronic degrees of freedom and simultaneously greater than characteristic Debye temperature, a huge number of vibrational quanta (phonons) are present in the system. I call this region Classical Adiabatic (CAR). When the dynamical kinetic energy of the oscillator exceeds the characteristic energy scale of the electron dynamics  $\langle E_{Kin} \rangle > \hbar\Gamma$ , I'm clearly going beyond the limit of adiabatic approximation I start with. I define this region Classical Non Adiabatic (CNAR). I expect that in the CAR my approximation is very accurate. By using this data, I'm now able to build up a phase diagram in the plane  $(E_p - V_{bias})$  for different values of gate voltages (Fig. 2.5) and different adiabatic ratios (Fig. 2.6). It is interesting to note that, in Fig. 2.5,

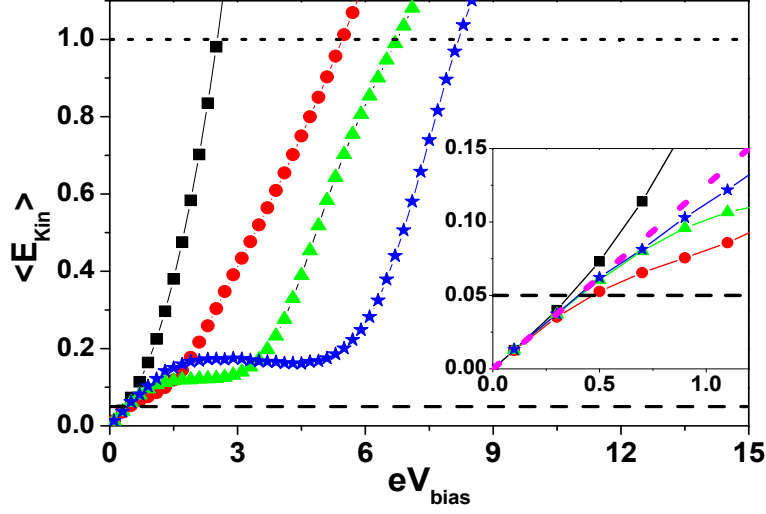


Figure 2.4: Main: plot of average kinetic energy  $\langle E_{Kin} \rangle$  as function of the bias voltage at fixed adiabatic ratio  $\omega_0/\Gamma = 0.1$  and gate voltage  $E_g = 0$ , for different interaction strengths  $E_p$ :  $E_p = 0.1$  square (black) curve,  $E_p = 1.0$  circle (red) curve,  $E_p = 2.0$  triangle (green) curve,  $E_p = 3.0$  star (blue) curve. Two constant energy lines  $E = \hbar\omega_0/2\hbar\Gamma = 0.05$  (dashed) and  $E = \hbar\Gamma = 1$  (dotted) are also plotted. Inset: Average kinetic energy  $\langle E_{Kin} \rangle$  for low bias voltages for the same parameter values of the main plot. The dotted (magenta) line indicates the linear approximation  $eV_{bias}/8$  derived in Ref.[27] (I choose a broadening  $\hbar\Gamma$  half than used in Ref.[27]). All the quantities ( $\langle E_{Kin} \rangle$ ,  $E_p$ ,  $E_g$  and  $eV_{bias}$ ) are in unit  $\hbar\Gamma$ .

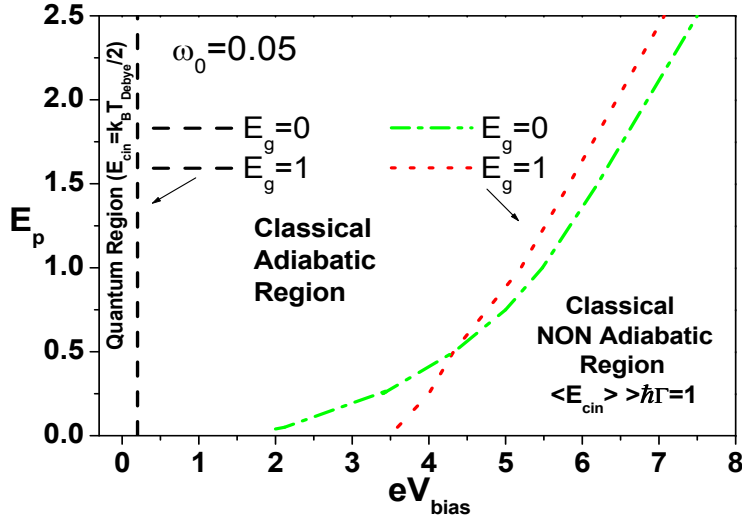


Figure 2.5: Phase diagram at fixed adiabatic ratio  $\omega_0/\Gamma = 0.05$  (the value of  $\omega_0$  shown in the figure is in  $\Gamma$  units). The dashed (black) line indicates the QR boundary for  $E_g = 0$  and  $E_g = 1$ . The dotted (red) and dashed dotted (green) lines refer to the CAR boundary for  $E_g = 0$  and  $E_g = 1$ , respectively.  $E_p$ ,  $E_g$  and  $eV_{bias}$  are expressed in unit  $\hbar\Gamma$ .

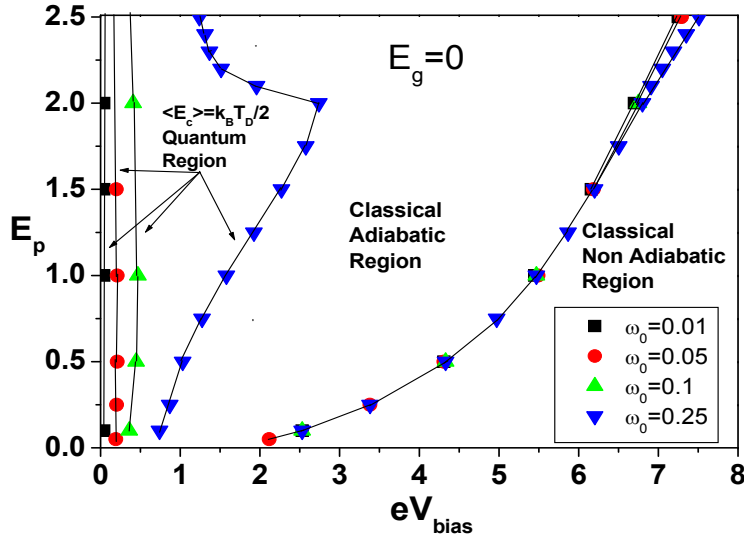


Figure 2.6: Phase diagram at fixed gate voltage  $E_g = 0$  (asymmetric static potential) for different adiabatic ratios  $\omega_0/\Gamma = 0.01 - 0.05 - 0.1 - 0.25$  (the values of  $\omega_0$  shown in the figure are in  $\Gamma$  units).  $E_p$ ,  $E_g$  and  $eV_{bias}$  are in  $\hbar\Gamma$  units.

the QR-CAR boundary is almost independent from the gate voltage in the limit of small adiabatic ratio. The CAR-CNAR boundary is slightly dependent from the gate voltage showing an enlargement of the CAR with  $E_g$ . Globally, one can note that, apart for the QR (small bias), the CAR enlarges as one increases the electron oscillator coupling.

As expected, as I increase the adiabatic ratio, the QR expands reaching great values of bias voltage  $V_{bias}$ , Fig. 2.6. In particular, in the down-triangle (blue) curve (adiabatic ratio  $\omega_0/\Gamma = 0.25$ ) one notes that the QR-CAR boundary reach a ‘‘maximum’’ in correspondence of  $E_p \simeq 2$  and  $V_{bias} \simeq 2.8$ . For  $E_p < 2$ , the bias values identifying the QR-CAR boundary increase as the voltage increases. For couplings  $E_p > 2$ , one can note an inversion of this behavior: the CAR starts to extend for a very large area of the phase diagram except for a narrow region at small bias (QR) and for a region at bigger bias values (CNAR). This means that, even for intermediate adiabatic ratios, I need sufficiently strong couplings  $E_p$  in order to obtain a predominant CAR in the phase diagram. Moreover, this is due to the fact that the node between kinetic energy curves and the Debye line occurs in the non monotonic intermediate bias region (see Fig. 2.4). On the other hand, the CAR-CNAR boundary is almost independent from the adiabatic ratio (for not too high interaction strength). This is what is expected from physical grounds and constitutes a self-consistent check of the approximation used.

## Electronic transport properties

I can now analyze the electronic transport properties resulting from the average over the dynamical fluctuations of the oscillator motion. I first study the conductance-voltage curves as function of the EOC strength (Fig.2.7), then I show how the dynamical fluctuations strongly renormalize the infinite mass approximation results studying the I-V curves for different adiabatic ratios (Fig. 2.8). Finally, I investigate the dependence of the kinetic energy and of the I-V characteristic as function of gate voltage studying the properties of the junction as function of a transversal electric field (Fig. 2.9).

In Fig. 2.7 I show several conductance curves for different interaction strength,  $E_p =$

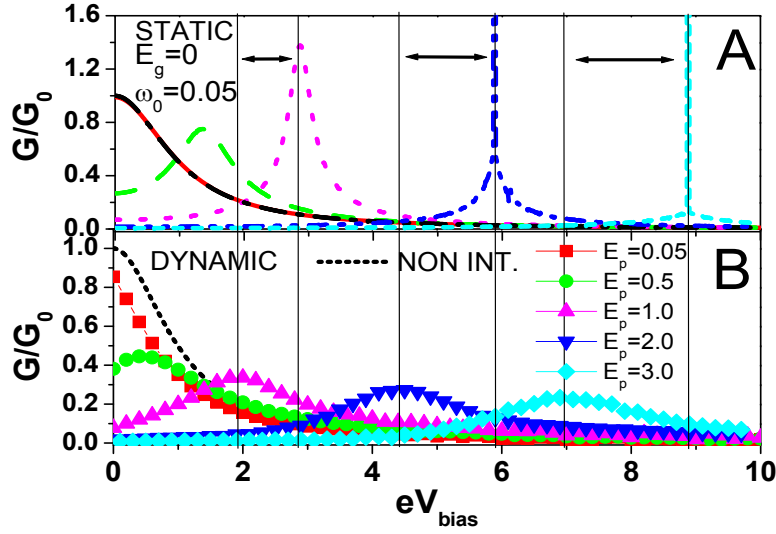


Figure 2.7: Panel A: Conductance (in units  $G_0 = \frac{e^2}{h}$ ) in the static approximation as function of bias voltages, for  $\omega_0/\Gamma = 0.05$ ,  $E_g = 0$  at different interaction strengths  $E_p = 0.05, 0.5, 1.0, 2.0, 3.0$ . Panel B: Dynamical correction to the conductance for the same parameter values of panel A. The value of  $\omega_0$  shown in the figure is in  $\Gamma$  units while all other quantities ( $E_g$ ,  $E_p$  and  $eV_{bias}$ ) are expressed in  $\hbar\Gamma$  units.

0.05 – 3, for  $\omega_0/\Gamma = 0.05$  and  $E_g = 0$ . The comparison between static (panel A) and dynamical (panel B) approximation is very interesting. The static solution shifts the non interacting resonance by a quantity proportional to the polaronic energy  $E_p$  (panel A). As one can see, this effect strongly reduces the low bias conductance. The dynamical correction, on the other hand, reduces the polaronic shift compared to the static curves and also broadens (as a result of the very broad non-equilibrium distribution probabilities  $P(x)$ ) the electronic resonance. In the intermediate bias regime, I note a strong enhancement of the conduction far from the electronic resonance where a very small current is observed in the static approximation. Moreover, including the dynamical fluctuations, the reduction of the small bias conductance is less pronounced. I note also that my dynamical approximation is close to the static solution in the small bias regime, while is substantially different in intermediate one. The dynamical correction strongly renormalizes the static results even for small adiabatic ratios.

I analyze in Fig.2.8 the behavior of the electronic occupation (panel A) and current voltage characteristic (panel B) at strong coupling  $E_p = 2$ , for different adiabatic ratios  $\omega_0/\Gamma = 0.01, 0.1, 0.25$  and at  $E_g = 0$ . In the low bias regime, as a result of strong electron-oscillator interaction, the molecular level renormalizes itself far below the chemical potential of the leads. I note a large difference between the non interacting occupation value ( $\langle \hat{n} \rangle \simeq 0.5$ ) and the interacting one ( $\langle \hat{n} \rangle \simeq 1$ ). As one increases the bias voltage, many charges are pumped out the molecular ‘dot’. In the large bias regime the stationary charge quantity in the molecular ‘dot’ reduces approaching the non interacting value ( $\langle \hat{n} \rangle \simeq 0.5$ ). The non-equilibrium broadening of the distribution probabilities  $P(x)$ , then, induces a strong reduction of the conduction threshold with respect to the static solution (solid magenta curve in Fig. 2.8 panel B). I note a small variation of physical properties with respect to the adiabatic ratio at intermediate voltages, in the CAR in correspondence to non Gaussian regime of the distribution probabilities.

In many molecular transport experiments, one records the current or the conductance

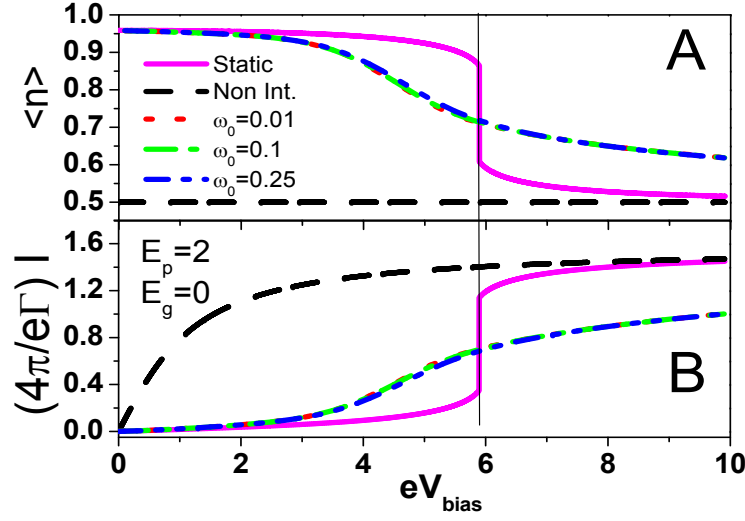


Figure 2.8: Panel A: Electronic occupation as function of bias voltages, for  $E_g = 0$ ,  $E_p = 2$  at different adiabatic ratios  $\omega_0/\Gamma = 0.05, 0.25, 0.5, 1.0$ . Panel B: Current voltage characteristic for the same value of the parameters of panel A. The values of  $\omega_0$  shown in the figure are in  $\Gamma$  units while all other quantities ( $E_g$ ,  $E_p$  and  $eV_{bias}$ ) are expressed in  $\hbar\Gamma$  units.

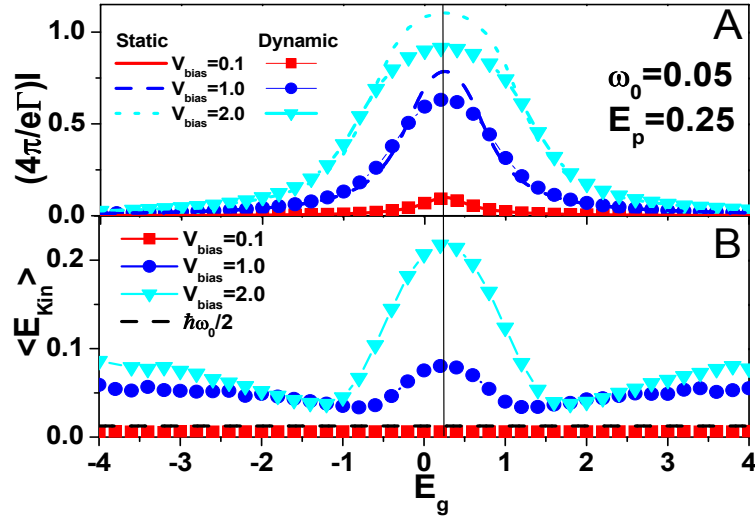


Figure 2.9: Panel A: Current as function of gate voltages, for  $\omega_0/\Gamma = 0.05$ ,  $E_p = 0.25$  at different bias voltages  $V_{bias} = 0.1, 1.0, 2.0$ . Panel B: Plot of average kinetic energy as function of the gate for  $V_{bias} = 0.1, 1.0, 2.0$ . The value of  $\omega_0$  shown in the figure is in  $\Gamma$  units, while  $E_g$  and  $E_p$  are expressed in  $\hbar\Gamma$  units.  $V_{bias}$  is expressed in  $\hbar\Gamma/e$  units.

varying the transverse electric field on the molecule at fixed source-drain voltage. For this reason, in the panel A of Fig. 2.9, it is shown the current for different bias voltages at moderately low electron-oscillator coupling ( $E_p = 0.25$ ) as function of gate voltage. In this regime no bistability is observed ( $E_p < \hbar\Gamma$ ). The static and dynamical approximations agree in the small bias regime (solid and square lines in panel A of Fig.2.9). Increasing the bias voltage, the dynamical correction becomes more important showing a suppression of the current at low  $E_g$ . This is caused by the spectral weight broadening due to the average over the position distribution probabilities  $P(x)$ . From panel B of Fig. 2.9 (square (red) line), one can learn that, in the small bias regime, the kinetic energy is independent of the gate voltage, while, as the voltage increases, it shows a symmetric drop with respect to polaronic energy  $E_g = E_p$ , corresponding to the symmetric regime. The I-V curve also shares this symmetry. This effect can be explained observing that, when the ‘bare’ molecular level and the renormalized one are both in the bias window, the energy associated to the electronic current flow is more efficiently transferred to the oscillator. When the electronic resonance is far above or below the chemical potential of the leads there is a less effective coupling between the oscillator and the electronic subsystem.

## 2.2 The two-site SSH model

The first step towards a more realistic description of a molecular junction is to consider a model Hamiltonian composed by two sites connected by an internal hopping  $t$ . In particular dimer molecules[59], this hopping can be controlled by a vibrational mode which assists the electron tunneling through the two molecular sites. In this case, a guess for the molecular Hamiltonian is given by

$$\hat{H}_{Mol}^{SSH} = E_g(\hat{d}_1^\dagger \hat{d}_1 + \hat{d}_2^\dagger \hat{d}_2) - t(x)(\hat{d}_1^\dagger \hat{d}_2 + h.c.), \quad (2.34)$$

where I consider, as in the SSH model, an electron hopping

$$t(x) = t - \alpha x \quad (2.35)$$

depending linearly on the lattice displacement  $x$  associated with the intermolecular vibrational mode. The molecular sites have a common energy  $E_g$  and are described in terms of creation (annihilation) operators  $\hat{d}_i^\dagger(\hat{d}_i)$ ,  $i = 1, 2$ . The SSH model was introduced to describe the transport properties of conducting polymers (e.g. polyacetylene [108]) and the two site case represents the shortest version of a molecular wire[109]. A generalization of this two site model was proposed in Ref.[111] for the study the electron transport of dimer molecules interacting with a single internal vibrational mode.

Most of the molecular devices studied experimentally so far[95, 96, 59] have been weakly coupled to the leads. This corresponds to the bare tunnel broadening  $\hbar\Gamma$  of molecular electronic levels smaller than the energy required to excite one oscillator quantum (phonon)  $\hbar\omega_0$ . In the strong-coupling regime, when the electron-oscillator interaction energy  $E_p$  exceeds  $\hbar\omega_0$ , the physics is governed by the Franck-Condon effect[101, 102, 103], i.e. the tunneling of an electron onto the molecule with the simultaneous emission or absorption of several phonons is more probable than elastic tunneling. The current as the function of voltage exhibits steps separated by  $\hbar\omega_0/e$ , [20] and the conductance show phonon sidebands[111].

As in the AH model, I study here the case of slow phonons at strong coupling,  $\omega_0 \ll \Gamma$  and  $eV_{bias} > \hbar\omega_0$ , considering the dynamics of the vibrational mode ‘‘classical’’. Moreover, because of the direct coupling of the electron-oscillator interaction to the inter-molecular

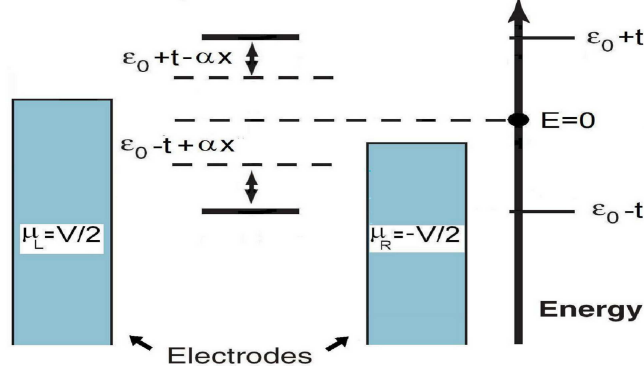


Figure 2.10: Sketch of junction within the SSH model in an energy scale.

hopping  $t$ , one expects that the role of the dynamical fluctuations becomes crucial to determine the physical scenario described by the model. The total Hamiltonian is

$$\hat{\mathcal{H}}_{TOT} = \hat{\mathcal{H}}_{el-SSH} + H_{osc}, \quad (2.36)$$

where

$$\hat{\mathcal{H}}_{el-SSH} = \hat{H}_{Mol}^{SSH} + \hat{H}_{Tun} + \hat{H}_{leads}, \quad (2.37)$$

with  $\hat{H}_{leads}$  and  $\hat{H}_{osc}$  given by Eq. 2.3 and Eq. 2.4, respectively. The tunneling Hamiltonian  $\hat{H}_{Tun}$  is given by

$$\hat{H}_{Tun} = \sum_{k,L} (V_{k,L} \hat{c}_{k,L}^\dagger \hat{d}_1 + h.c.) + \sum_{k,R} (V_{k,R} \hat{c}_{k,R}^\dagger \hat{d}_2 + h.c.), \quad (2.38)$$

indicating that the left (right) lead is coupled only to the molecular site 1(2). In real space, the molecular Hamiltonian  $\hat{H}_{Mol}^{SSH}$  is not diagonal. I therefore perform a transformation which diagonalizes the molecular isolated problem

$$\begin{aligned} \hat{c}_{\gamma_1}^\dagger &= \frac{\hat{d}_1^\dagger + \hat{d}_2^\dagger}{\sqrt{2}}, \\ \hat{c}_{\gamma_2}^\dagger &= \frac{\hat{d}_1^\dagger - \hat{d}_2^\dagger}{\sqrt{2}}, \end{aligned} \quad (2.39)$$

with the same transformation for corresponding annihilation operators. This transformation leaves invariant  $\hat{H}_{leads}$  but changes  $\hat{H}_{Mol}^{SSH}$  and  $\hat{H}_{Tun}$ . Explicitly I have

$$\hat{H}_{Mol}^{SSH} = \varepsilon_{\gamma_1}(x) \hat{c}_{\gamma_1}^\dagger \hat{c}_{\gamma_1} + \varepsilon_{\gamma_2}(x) \hat{c}_{\gamma_2}^\dagger \hat{c}_{\gamma_2} \quad (2.40)$$

$$\hat{H}_{Tun} = \sum_{i=1,2} \left[ \sum_k \left( \frac{V_{k,L}}{\sqrt{2}} \hat{c}_{k,L}^\dagger \hat{c}_{\gamma_i} + h.c. \right) + (-1)^{i-1} \sum_k \left( \frac{V_{k,R}}{\sqrt{2}} \hat{c}_{k,R}^\dagger \hat{c}_{\gamma_i} + h.c. \right) \right], \quad (2.41)$$



where

$$\begin{aligned}\varepsilon_{\gamma_1}(x) &= \varepsilon + (t - \alpha x), \\ \varepsilon_{\gamma_2}(x) &= \varepsilon - (t - \alpha x).\end{aligned}\tag{2.42}$$

As one can see, the above transformation allows us to take into account exactly of the intermolecular hopping's effect. The molecular Hamiltonian  $\hat{H}_{Mol}^{SSH}$  (Eq. 2.40) is equivalent to that of a non interacting two level system. In Fig. 2.10 a schematic picture of the junction in an energy representation is shown. I observe that there are two electronic resonances, corresponding to a 'bonding' and 'anti-bonding' states whose position is renormalized by the electron-oscillator interaction. From now on I work in the energy space for convenience.

In the following, I will (subsection 2.2.1) first analyze the coupled electron-oscillator problem within the SSH model in the limit of infinite mass for the oscillator. Then, I will construct, as done in AH model, the stochastic Langevin equation for the dynamics of the oscillator (sec. 2.2.2). In the subsection 2.2.3 I will describe the numerical results.

### 2.2.1 Out of equilibrium Born-Oppenheimer approximation: infinite mass (static) case

As in AH model, performing the limit  $m \mapsto \infty$ , at zero-order static approximation, I neglect the kinetic energy of the oscillator. The electronic dynamics, with the oscillator displacement  $x$  as a free parameter, is therefore equivalent in the energy space to a non-interacting two level problem with energy levels renormalized by the 'polaronic' shift  $-\alpha x$ , Eq. 2.42. In what follows, I consider the case of symmetric coupling of the molecule to the leads  $\hbar\Gamma_L = \hbar\Gamma_R$  in the wide-band approximation. Here, I briefly show how calculate the generalized potential of the oscillator coupled to the double 'dot' molecular junction.

Within the Keldysh formalism, I use the equation of motion approach to calculate the molecular Green functions in stationary non-equilibrium conditions. In the zero order static approximation, I have the following equation of motion for the molecular retarded Green function

$$\begin{aligned}& \left( \begin{array}{cc} i\hbar\frac{\partial}{\partial t} - \varepsilon_{\gamma_1}(x) + i\frac{\hbar\Gamma_L + \hbar\Gamma_R}{4} & i\frac{\hbar\Gamma_L - \hbar\Gamma_R}{4} \\ i\frac{\hbar\Gamma_L - \hbar\Gamma_R}{4} & i\hbar\frac{\partial}{\partial t} - \varepsilon_{\gamma_2}(x) + i\frac{\hbar\Gamma_L + \hbar\Gamma_R}{4} \end{array} \right) \\ & \times \begin{pmatrix} G_{1,1}^r(t, t') & G_{1,2}^r(t, t') \\ G_{2,1}^r(t, t') & G_{2,2}^r(t, t') \end{pmatrix} = \delta(t - t') \begin{pmatrix} 1 & 0 \\ 0 & 1 \end{pmatrix},\end{aligned}\tag{2.43}$$

which acquires a  $2 \times 2$  matrix structure. A similar equation is valid also for the advanced Green function. In the hypothesis of symmetric coupling with the leads, one obtains two separate problems for the molecular energy levels  $\varepsilon_{\gamma_1}(x)$  and  $\varepsilon_{\gamma_2}(x)$ , respectively. The diagonal elements of the retarded (advanced) Green function in Fourier space are

$$G_{j,j}^{r(a)}(\omega, x) = \frac{1}{\hbar\omega - \varepsilon_{\gamma_j}(x) + (-)i\left(\frac{\hbar\Gamma_L + \hbar\Gamma_R}{4}\right)}, \quad j = 1, 2\tag{2.44}$$

while the non diagonal terms are zero.

The lesser matrix Green function is instead given by

$$G^<(\omega, x) = i\frac{\hbar\Gamma}{4} \begin{pmatrix} (n_L + n_R)|G_{1,1}^r|^2 & (n_L - n_R)G_{1,1}^r G_{2,2}^a \\ (n_L - n_R)G_{2,2}^r G_{1,1}^a & (n_L + n_R)|G_{2,2}^r|^2 \end{pmatrix}$$

where, for sake of simplicity, I have dropped the frequency  $\omega$  and the displacement  $x$  dependence. The diagonal terms of the lesser Green function are directly related to the electron ``densities'' (these obviously not correspond to the densities in real space)

$$\langle \hat{n}_{\gamma_i} \rangle(x) = \frac{1}{2} + \frac{1}{2\pi} \sum_{\alpha=R,L} \arctan \left[ \frac{\mu_\alpha - \varepsilon_{\gamma_i}(x)}{\hbar\Gamma/4} \right], \quad i = 1, 2.$$

For sake of clarity, I show here that the population in real space of the left and right molecular sites are expressed in terms of lesser Green functions (Eq. 2.45)

$$\langle \hat{n}_i \rangle(x) = \frac{1}{2} \int \frac{d\omega}{2\pi i} \left( G_{1,1}^< + G_{2,2}^< + (-1)^{i+1} (G_{1,2}^< + G_{2,1}^<) \right), \quad (2.45)$$

where  $i = 1, 2$ .

The force exerted on the oscillator is given by

$$F_{SSH} = -kx + \alpha(\langle \hat{n}_{\gamma_1} \rangle - \langle \hat{n}_{\gamma_2} \rangle)(x). \quad (2.46)$$

Taking care of Eq. 2.45 and Eq. 2.46, one can straightforwardly compute the expression of the generalized potential in non-equilibrium conditions ( $\mu_R = -eV_{bias}/2$ ,  $\mu_L = eV_{bias}/2$ )

$$\begin{aligned} V_{SSH}(x) = & \frac{1}{2}kx^2 - \sum_{\alpha=L,R} \sum_{i=1,2} \left[ \frac{\mu_\alpha - \varepsilon_{\gamma_i}(x)}{2\pi} \arctan \left( \frac{\mu_\alpha - \varepsilon_{\gamma_i}(x)}{\hbar\Gamma/4} \right) \right. \\ & \left. - \frac{\hbar\Gamma}{16\pi} \ln[16(\mu_\alpha - \varepsilon_{\gamma_i}(x))^2 + (\hbar\Gamma)^2] \right]. \end{aligned} \quad (2.47)$$

This generalized oscillator potential depends parametrically on the new electronic energy scale introduced in the problem: the intermolecular hopping  $t$  ``hidden'' in  $\varepsilon_{\gamma_i}(x)$ , see Eq. 2.42. Furthermore, it depends on the polaron energy,  $E_p$ , the gate voltage  $E_g$ , and the bias  $V_{bias}$ .

In Fig. 2.11 I present some features of the generalized potential  $V_{SSH}(x)$  which will allow us to understand the effect of the non-equilibrium electronic system on the ``static'' stretching of the oscillator (solutions of the equation  $F_{SSH} = 0$ ). Moreover, this will help us to clarify the role of the dynamical effects in the transport properties that I will show later.

I focus here on the weak coupling ( $E_p/\hbar\Gamma \ll 1$ ) regime where moreover the intermolecular hopping  $t$  is larger than the coupling  $\hbar\Gamma$  of the molecule with the leads. In the panel A, I show the generalized potential of the SSH model at fixed EOC strength,  $E_p = 0.2$ , intermolecular hopping  $t = 2.0$ , as function of the bias voltage  $V_{bias}$ . One can observe that, as the bias increases, the position of generalized potential minimum goes from  $x \simeq -1$  (corresponding to  $\langle n_{\gamma_1} \rangle - \langle n_{\gamma_2} \rangle \simeq -1$ ) to  $x \simeq 0$  (corresponding to  $\langle n_{\gamma_1} \rangle - \langle n_{\gamma_2} \rangle \simeq 0$ ). The oscillator switches from a full stretching configuration ( $x \simeq -1$ ) to a no-stretching one ( $x \simeq 0$ ). At equilibrium, I have a physical situation where the renormalized anti-bonding electron level  $\varepsilon_{\gamma_1}(x)$  is above the chemical potential of both leads, while the bonding one  $\varepsilon_{\gamma_2}(x)$  is below them. The classical ``spring'' is fully compressed ( $x \simeq -1$ ) and this corresponds in real space to molecular sites half-filled ( $\langle n_1 \rangle \simeq \langle n_2 \rangle \simeq 0.5$ ). Studying the electronic populations of left (1) and right (2) molecular sites (Eq. 2.45), one can observe that, if one increases the bias voltage, the left site starts to empty, while the right one populates, reaching, for  $eV_{bias}^*/2 \simeq t - \alpha x(V_{bias}^*)$  (hopping value properly renormalized), a small difference of population roughly equal to  $\langle n_1 \rangle - \langle n_2 \rangle \simeq -0.1$ . For sufficiently high bias, the molecular level

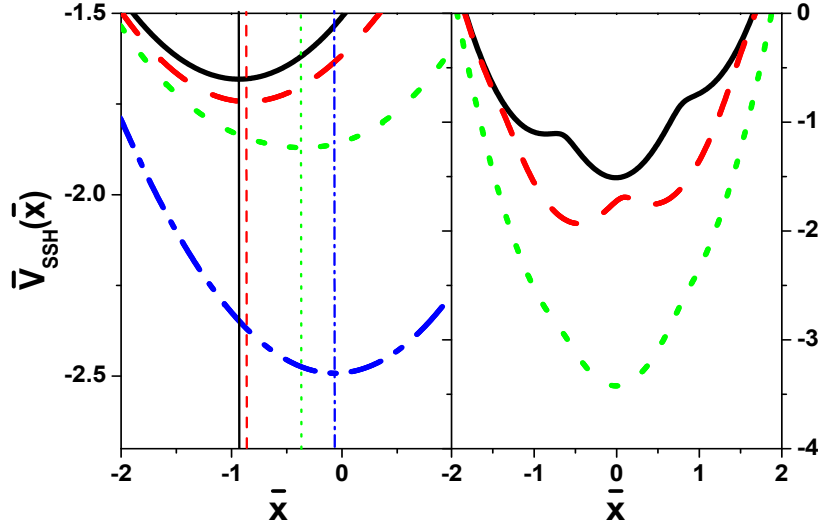


Figure 2.11: Panel A: Spatial dependence of the dimensionless generalized static potential  $\bar{V}_{SSH}(\bar{x})$  at  $\omega_0/\Gamma = 0.1$ ,  $E_p = 0.2$ , gate voltage  $E_g = 0$ , intermolecular hopping  $t = 2.0$ , for different values of the bias voltage:  $V_{bias} = 0.0$  (solid (black) curve),  $V_{bias} = 3.5$  (dashed (red) curve),  $V_{bias} = 4.0$  (dotted (green) curve),  $V_{bias} = 6.0$  (dashed dotted (blue) curve). The vertical lines indicate the position of the minima of the potential. Panel B: Same as above for  $\omega_0/\Gamma = 0.1$ ,  $E_p = 1.4$ ,  $t = 0.2$ , gate voltage  $E_g = 2$  and different values of the bias voltage:  $V_{bias} = 0$  (solid (black) curve),  $V_{bias} = 4$  (dashed (red) curve),  $V_{bias} = 8$  (dotted (green) curve). The potential is expressed in  $\hbar\Gamma$  units ( $\bar{V}_{SSH} = V_{SSH}/\hbar\Gamma$ ).  $V_{bias}$  values are expressed in  $\hbar\Gamma/e$  units, where  $e$  is the electron charge.  $E_g$ ,  $E_p$  and  $t$  are expressed in  $\hbar\Gamma$  units. The dimensionless position variable  $\bar{x}$  is defined as  $\bar{x} = x/x_0$  with  $x_0 = \frac{\lambda}{m\omega_0^2}$ .

populations tend again to the common value 0.5. As I shall see in next section, the inclusion of the dynamical effects allows to clarify the physical picture arising from the above description, in terms of an energy balance between the electronic and oscillator subsystems.

At static level, it is also interesting to discuss the extremely strong coupling regime  $E_p > \hbar\Gamma > t$ , for gate voltage  $E_g = 2.0$  (panel B). In this case, at equilibrium, I'm describing a physical situation where the renormalized bonding and anti-bonding electron levels are both above the chemical potential ( $V_{bias} = 0$ ). The molecular sites in real space are both almost empty ( $\langle n_1 \rangle \simeq \langle n_2 \rangle \simeq 0$ ), and the oscillator is in a no-stretching configuration  $x \simeq 0$  (solid (black) curve). Increasing the bias voltage, the generalized potential develops different minima. At intermediate bias, the minimum corresponding to  $x \simeq -0.5$  prevails (dashed (red) curve). In this regime, the non-interacting real space populations  $\langle n_1 \rangle$  and  $\langle n_2 \rangle$  starts to increases asymmetrically going to the asymptotic values  $\langle n_1 \rangle \simeq 0.8$ ,  $\langle n_2 \rangle \simeq 0.2$ . Instead, the interacting real space populations go to the same value  $\langle n_1 \rangle \simeq \langle n_2 \rangle \simeq 0.25$ , corresponding to a very high current-carrying configuration. In this regime, the generalized potential develops two asymmetric minima near  $x \simeq -0.5$  and  $x \simeq 0.5$  separated by a barrier. For sufficiently large bias voltage only the minimum  $x \simeq 0$  corresponding to a low-current-carrying configuration survives. In this case, including the interaction effects, the left site is almost filled  $\langle n_1 \rangle \simeq 0.9$ , while the right one is almost empty  $\langle n_2 \rangle \simeq 0.1$ , showing that, as result of the strong electron-phonon interaction, the bias voltage does not manage to deplete both molecular sites. As I shall see later, the features of the static potential obtained in this case determine the possibility to observe in the I-V a strong Negative Differential Resistance,

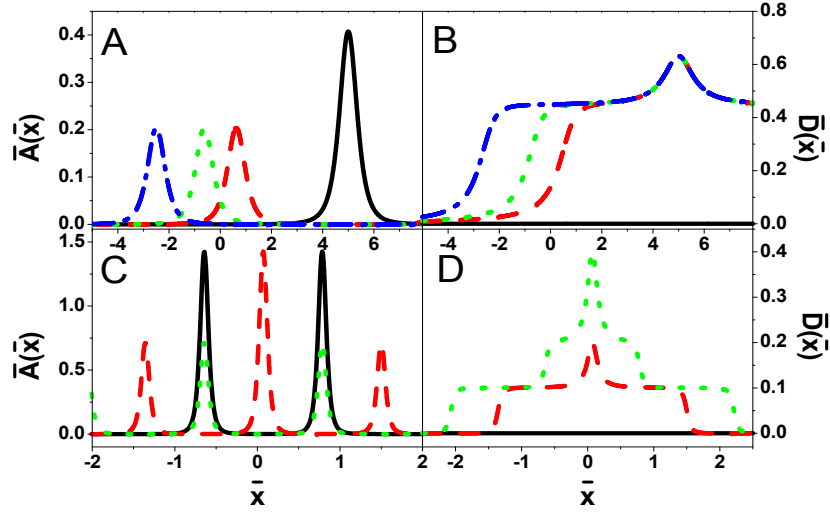


Figure 2.12: Panels A-B: Spatial dependence of the dimensionless friction coefficient  $\bar{A}(\bar{x})$  and fluctuating term  $\bar{D}(\bar{x})$  at  $\omega_0/\Gamma = 0.1$ ,  $E_p = 0.2$ , gate voltage  $E_g = 0$ , intermolecular hopping  $t = 2.0$ , for different values of the bias voltage:  $V_{bias} = 0.0$  (solid (black) curve),  $V_{bias} = 3.5$  (dashed (red) curve),  $V_{bias} = 4.0$  (dotted (green) curve),  $V_{bias} = 6.0$  (dashed dotted (blue) curve). Panels C-D: Same as above for  $\omega_0/\Gamma = 0.1$ ,  $E_p = 1.4$ ,  $t = 0.2$ , gate voltage  $E_g = 2$  and different values of the bias voltage:  $V_{bias} = 0$  (solid (black) curve),  $V_{bias} = 4$  (dashed (red) curve),  $V_{bias} = 8$  (dotted (green) curve). The friction coefficient in  $m\omega_0$  units ( $\bar{A} = A/m\omega_0$ ) and the fluctuating term in  $\lambda^2/\omega_0$  units, ( $\bar{D} = D/(\lambda^2/\omega_0)$ ).  $V_{bias}$  values are expressed in  $\hbar\Gamma/e$  units, where  $e$  is the electron charge.  $E_g$ ,  $E_p$  and  $t$  are expressed in  $\hbar\Gamma$  units. The dimensionless position variable  $\bar{x}$  is defined as  $\bar{x} = x/x_0$  with  $x_0 = \frac{\lambda}{m\omega_0^2}$ .

when the dynamical effects of the oscillator are neglected.

### 2.2.2 Adiabatic Approximation: calculation of damping and fluctuating term

As I have discussed after the Eq. 2.43, the assumption of symmetric coupling to the leads allows to disentangle in the energy space the problem for the molecular bonding and anti-bonding levels  $\varepsilon_{\gamma_i}(x)$ . Repeating site-by-site the construction introduced in the previous section for AH model, I can straightforwardly set for my two site SSH model a Langevin equation for the oscillator dynamics, very similar to that derived in AH model. The new coefficients,  $F(x)$ ,  $A(x)$  and  $D(x)$  are given by

$$F(x) = -kx + \lambda \frac{1}{2\pi} \sum_{\alpha=R,L} \sum_{i=1,2} \arctan \left[ \frac{\mu_{\alpha} - \varepsilon_{\gamma_i}(x)}{\hbar\Gamma/4} \right], \quad (2.48)$$

$$A(x) = \frac{16\hbar k E_p}{\pi \hbar^2 \Gamma^2} \sum_{\alpha=R,L} \sum_{i=1,2} \left( \frac{1}{\left[ \left( \frac{\mu_{\alpha} - \varepsilon_{\gamma_i}(x)}{\hbar\Gamma/4} \right)^2 + 1 \right]^2} \right), \quad (2.49)$$

$$\begin{aligned}
D(x) &= \frac{kE_p}{\pi} \int d\omega \left[ G_{1,1}^< G_{1,1}^> + G_{2,2}^< G_{2,2}^> + 2G_{1,2}^< G_{2,1}^> \right] = \\
&= \frac{2kE_p}{\pi\Gamma} \sum_{\alpha=L,-R} \sum_{i=1,2} \left\{ \left( \arctan\left(\frac{\mu_\alpha - \varepsilon_{\gamma_i}(x)}{\hbar\Gamma/4}\right) \right. \right. \\
&\quad \left. \left. + \frac{\frac{\mu_\alpha - \varepsilon_{\gamma_i}(x)}{\hbar\Gamma/4}}{\left[\left(\frac{\mu_\alpha - \varepsilon_{\gamma_i}(x)}{\hbar\Gamma/4}\right)^2 + 1\right]} \right) + 4 \left( \frac{1}{\left(\frac{\varepsilon_{\gamma_1}(x) - \varepsilon_{\gamma_2}(x)}{\hbar\Gamma/4}\right)^2 + 4} \right) \times \right. \\
&\quad \left[ \arctan\left(\frac{\mu_\alpha - \varepsilon_{\gamma_i}(x)}{\hbar\Gamma/4}\right) + \frac{(-1)^i}{\left(\frac{\varepsilon_{\gamma_1}(x) - \varepsilon_{\gamma_2}(x)}{\hbar\Gamma/4}\right)} \times \right. \\
&\quad \left. \left. \ln \left( 1 + \left( \frac{\mu_\alpha - \varepsilon_{\gamma_i}(x)}{\hbar\Gamma/4} \right)^2 \right) \right] \right\}, \tag{2.50}
\end{aligned}$$

where in the last expression I have dropped the frequency  $\omega$  and the displacement  $x$  dependence in the Green functions. I end this section briefly discussing some of the peculiarities of the damping function  $A(x)$  and of the fluctuating term  $D(x)$ . As regards the damping term (panel A and C in Fig. 2.12), one can observe that is located in suitable points and is strongly space dependent. It is interesting to note that, as in the AH model case, it survives also for  $V_{bias} = 0$  (solid (black) curves in Panels A-C). In this case, one can also note that for  $E_p \ll t$  (panel A),  $A(x)$  is almost zero in the interval mostly explored in the dynamics ( $-2 < x < 2$ ), while, for  $E_p \gg t$  (panel C), shows two pronounced peaks in that interval. As one can see, the position of  $A(x)$ 's maxima is strongly bias dependent.

As concerns the fluctuating term (Panels B and D in Fig. 2.12), one can note that, as in the AH model, is identically zero at equilibrium. When the bias increases, it becomes almost different from zero in the region mostly explored in the dynamics ( $-2 < x < 2$ ). In Panel B of Fig. 2.12 one can observe that the spatial extension of the fluctuating term increases as the bias increases, while, in Panel D, in the interesting strong coupling regime ( $E_p \gg t$ ), it shows a maximum for  $x = 0$ , the no-stretching equilibrium state of the oscillator. It is important to re-stress here that the space dependence of these terms determines the non-gaussian character of the distribution probabilities  $P(x)$  and  $P(v)$  of the oscillator.

### 2.2.3 Analysis of Numerical results

As done for the AH model, I here show the results arising from the numerical simulation of the Langevin equation of the SSH model. I evaluate the fundamental ingredients of the Adiabatic approximation: the distribution probabilities of the oscillator. These allows us to calculate the dynamical properties of the oscillator (average kinetic and potential energy) as well as the electronic transport properties of the molecular junction.

#### Study of the average kinetic energy of the oscillator and limits of the Adiabatic approach

First of all, I study the behavior of velocity distribution probabilities  $P(v)$  resulting from the solution of the Langevin equation associated to the SSH model. As in AH model, I have verified that in the small bias regime, regardless the value of the gate voltages  $E_g$ , the polaronic coupling  $E_p$  and the hopping  $t$ , the *dimensionless* velocity distribution probabilities  $P(v)$  are gaussian. The introduction of a new energy scale in the problem does not much modifies the physical picture I obtained in AH model in the small bias regime: the non-equilibrium electronic bath behaves like a conventional bath for the oscillator with an effective

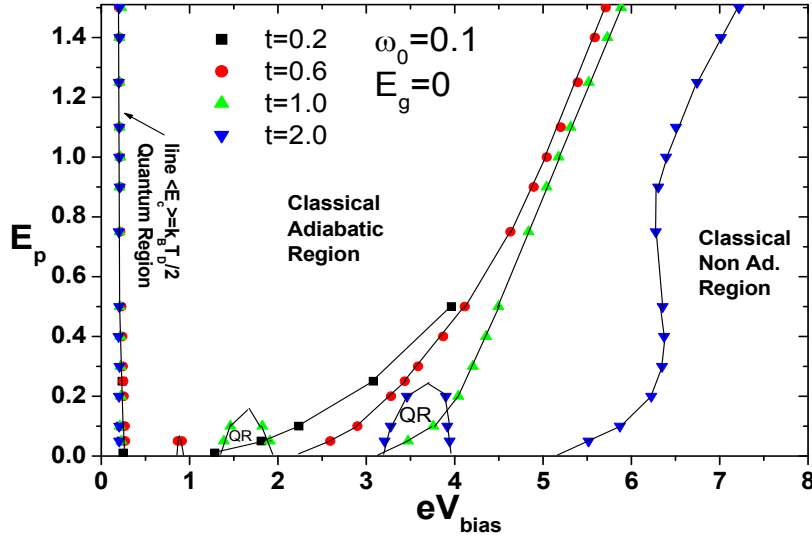


Figure 2.13: Phase diagram at fixed adiabatic ratio  $\omega_0/\Gamma = 0.1$ ,  $E_g = 0$ , for different intermolecular hopping  $t = 0.2 - 0.6 - 1.0 - 2.0$ . The value of  $\omega_0$  shown in the figure is in  $\Gamma$  units, while all other quantities ( $E_g$ ,  $E_p$ ,  $t$  and  $eV_{bias}$ ) are expressed in  $\hbar\Gamma$  units.

temperature linearly proportional to the bias voltage. In particular, in the SSH model case, it is worth noticing that the average kinetic energy exhibits a slope twice that found in the AH model. This is a consequence of the transformation Eq. 2.39 I have applied on the total Hamiltonian, that renormalized the tunneling amplitudes with the leads,  $V_{k,\alpha} \mapsto V_{k,\alpha}/\sqrt{2}$ . From the physical point of view, I find that the two electronic *channels* independently contribute to the oscillator effective temperature, showing that the problem is equivalent to the *sum* of two single-site junctions.

As one increases the bias voltage, the  $(\log(P(v)) \text{ vs. } v^2)$  plot starts to deviate from a linear trend, so that, even in SSH case, the oscillator dynamics cannot be simply reduced to an effective temperature in the intermediate bias regime.

I also find that, up to very large values of the bias voltage, the average kinetic energy shows a behavior qualitatively similar to that of AH model (Fig. 2.4) for moderate values of the ratio  $0 < t/E_p < 1$ . In this regime, I can conclude that the dynamical fluctuations of the oscillator motion does not ‘see’ the double ‘dot’ structure of the electronic molecular junction. If  $t/E_p \gg 1$ , as I will discuss later, the average kinetic energy show an interesting non monotonic behavior in the intermediate bias regime (see below, Fig. 2.14).

The systematic analysis of the average kinetic energy allows us to build up a phase diagram in the plane  $(E_p - V_{bias})$  for different intermolecular hoppings  $t$  and at fixed adiabatic ratio and gate voltage, assessing the range of validity of the adiabatic approximation as done for AH model (Fig. 2.13). It is interesting to note that QR-CAR boundary is almost independent from the intermolecular hopping in the limit of small adiabatic ratio. Joining together the results obtained for the AH phase diagrams (Fig. 2.5 and Fig. 2.6), I can conclude that, in the limit of very small adiabatic ratios, the QR-CAR boundary is completely independent by the other energy scales considered in the problem. The CAR-CNAR boundary is instead slightly dependent on  $t$  showing the expansion of the CAR. As the intermolecular hopping  $t$  increases, bigger values of bias voltage are needed to get average kinetic energy values greater than energy coupling to the leads,  $\langle E_{Kin} \rangle > \hbar\Gamma$ . In this case, the intermolecular hopping  $t$  plays the same role as the gate in AH model (see, Fig. 2.5).

A new feature which was not observed in the AH model is the appearance of small QR for

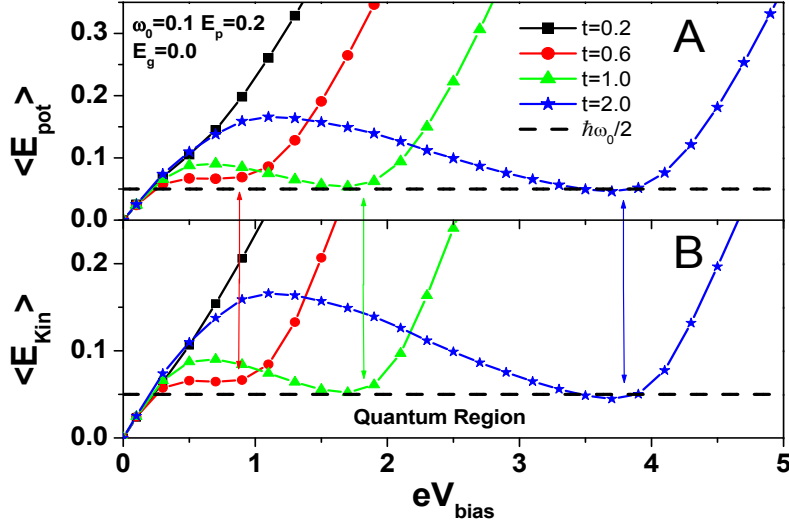


Figure 2.14: Panel A: Average potential energy as function of the bias for different intermolecular hopping  $t = 0.2 - 0.6 - 1.0 - 2.0$ . Panel B: Average kinetic energy as function of the bias for values of intermolecular hopping as in Panel A. I note that the introduction of new energy scale makes the overall energy  $\langle E \rangle$  a decreasing function of the voltage for intermediate values. The value of  $\omega_0$  shown in the figure is in  $\Gamma$  units, while all other quantities ( $E_g$ ,  $E_p$ ,  $\langle E_{kin} \rangle$ ,  $\langle E_{pot} \rangle$ ,  $k_B T$ ,  $t$  and  $eV_{bias}$ ) are expressed in  $\hbar\Gamma$  units.

sufficiently small coupling  $E_p$ , at intermediate bias voltages (Fig. 2.13). For strong enough electron-phonon coupling  $E_p$ , these regions disappear. This feature can be understood analyzing the behavior the average kinetic energy  $\langle E_{kin} \rangle$  for the parameters characterizing the QR observed at intermediate bias. As it is clear from Fig. 2.14,  $\langle E_{kin} \rangle$  can decrease significantly at intermediate  $V_{bias}$ . The effect becomes less and less evident decreasing the intermolecular hopping and disappears at  $t = 0.2$ . It is interesting to note that the potential energy curves show almost the same trend (see Fig. 2.14, panel A). Therefore, for sufficiently high  $t$  and low  $E_p$ , the oscillator overall energy decreases as a function of bias voltage.

The behavior of the average energy of the oscillator as function of bias voltage is determined by net balance of energy exchanged by the junction: after an increasing trend in the low bias regime, where the energy pumped by the bias exceeds that ceased to the electrons by the oscillator, the decreasing behavior in the intermediate bias regime is due to the opposite physical mechanism: the energy ceased to the electron system by the oscillator exceeds that pumped by the bias.

This ‘‘transition’’ occurs for that particular range of bias voltages where the molecular energy levels are going through the bias window, with a resulting strong current enhancement (electronic *resonance*). In particular, when the electron molecular levels enter the bias window completely, in the case of symmetric bias unbalance and for  $E_g = 0$ , I expect that the electronic conductance reaches its maximum. Remarkably, comparing Fig. 2.15 and Fig. 2.14, one can observe that the conductance maxima corresponds to kinetic energy minima, shifted by a quantity close to the EOC strength  $\alpha$ . Physically, as a consequence of the SSH coupling with the oscillator, the current enhancement is followed by a strong effective absorption of energy of the electron system from the oscillator.

## Electronic transport properties

In order to evaluate the current through the molecular system in SSH model, I use the Meir-Wingreen formula[91] for non interacting molecular levels, specialized to a two-level system

$$I(x) = \frac{e}{\hbar} \int \frac{d\omega}{2\pi} (f_L(\omega) - f_R(\omega)) \text{Tr}\{\mathbf{G}^a \mathbf{\Gamma}_L \mathbf{G}^r \mathbf{\Gamma}_R\}, \quad (2.51)$$

where the matrices  $\mathbf{\Gamma}_{L/R}$  are given by

$$\mathbf{\Gamma}_L = \frac{\hbar\Gamma}{4} \begin{pmatrix} 1 & 1 \\ 1 & 1 \end{pmatrix}, \quad \mathbf{\Gamma}_R = \frac{\hbar\Gamma}{4} \begin{pmatrix} 1 & -1 \\ -1 & 1 \end{pmatrix}, \quad (2.52)$$

and bold  $\mathbf{G}^{r,a}$  indicate retarded (advanced) matrix green functions (Eq. 2.44). I have explicitly indicated that the current depends on the deformation  $x$  of the oscillator, so that it has to be averaged over the probability distribution function  $P(x)$ .

Here, I focus on two particular physical regimes, previously discussed in the analysis of the static approximation: the weak coupling ( $E_p \ll \hbar\Gamma$ ) and the strong coupling ( $\hbar\Gamma \ll E_p$ ) limits, varying arbitrarily the intermolecular energy scale  $t$ . As I shall see, in both regimes, the direct coupling of the electron-oscillator interaction to the inter-molecular hopping makes the role of the dynamical fluctuations so much important to determine correct results.

In the weak coupling regime, it is interesting to observe that, as in the AH model, the dynamical corrections renormalize and broaden the electronic resonances (Fig. 2.15) with respect to the static solution. In particular, in panel A of Fig. 2.15, I note that the static approximation exceeds the maximum value of non interacting conductance and shows a region of negative conductance at intermediate bias. However, when the dynamical contributions are included (square (green) curve), the effect on the conductance is dramatic washing out all the structures observed in the static approximation. More interesting are the cases of panels B-C-D of Fig. 2.15, where again the static approximation shows the spurious result of conductance greater than  $2G_0$ , while the dynamical approximation renormalizes and broadens the peak of conductance to bias values where the static approximation shows small electric conduction. Even in the weak coupling regime, the inclusion of the dynamical fluctuations is crucial to obtain correct results for the electronic conduction.

Finally, I examine the electronic transport properties in the strong coupling regime, where moreover  $\hbar\Gamma \gg t$ . In this case, I expect strongly non linear behavior of I-Vs in the infinite mass (static) limit for the oscillator. In Fig. 2.16 I show the current voltage characteristic for strong interaction,  $E_p = 1.4$ , at fixed adiabatic ratio  $\omega_0/\Gamma = 0.1$ , gate voltage  $E_g = 2.0$  and for different small intermolecular hoppings  $t \ll \hbar\Gamma$  ( $t = 0.15$  (black) dashed,  $t = 0.2$  (red) dashed dotted,  $t = 0.25$  (blue) short dashed dotted line). In panel A, I show a comparison between the non interacting and static approximation. The static approximation shows an interesting region of Negative Differential Resistance (NDR), as a consequence of the rich structure of the minima of the generalized potential described in the previous subsection (see also Fig. 2.11, Panel B). At intermediate bias voltage, a strong current currying region appears. This corresponds to  $x \sim \langle n_{\gamma_1} \rangle - \langle n_{\gamma_2} \rangle \simeq -0.5$  for which the electronic levels renormalize in the bias window with an effective energy larger than the ‘bare’ value. Then, for sufficiently large bias, the minimum corresponding to  $x \simeq 0$  prevails, determining a strong current reduction due the drop of the hoppings to their non interacting ‘bare’ values. As in the case described above, one can note (panel B) that the dynamical corrections wash out almost all the features of the static approximation. There is a very low conduction threshold after which one can not observe NDR features. Again, I observe that the inclusion of dynamical corrections are crucial for a correct description of the SSH model while the static approximation can easily lead to erroneous conclusions.



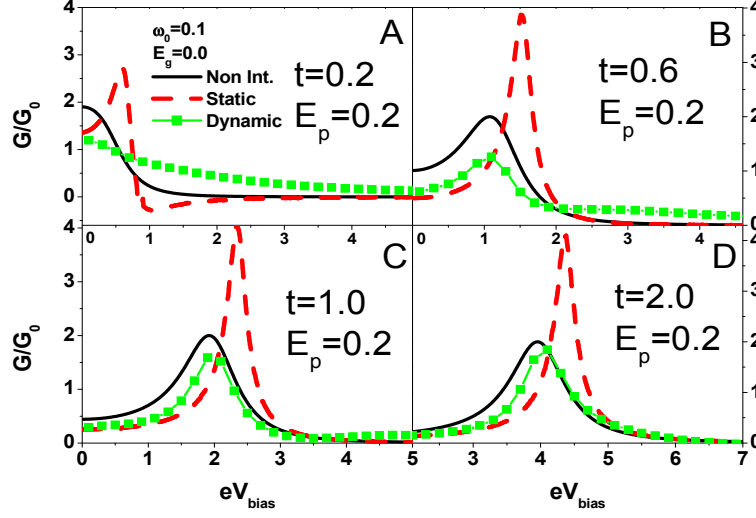


Figure 2.15: Panel A-D: Conductance as function of the bias at  $\omega_0/\Gamma = 0.1$ ,  $E_g = 0.0$ , interaction strength  $E_p = 0.2$ , for different values of intermolecular hopping  $t = 0.2 - 0.6 - 1.0 - 2.0$ . The solid (black) line indicates Non Interacting curve. The dashed (red) line and the square (green) lines refer to the static and the dynamical approximation, respectively. The value of  $\omega_0$  shown in the figure is in  $\Gamma$  units, while all other quantities ( $E_g$ ,  $E_p$ ,  $t$  and  $eV_{bias}$ ) are expressed in  $\hbar\Gamma$  units.

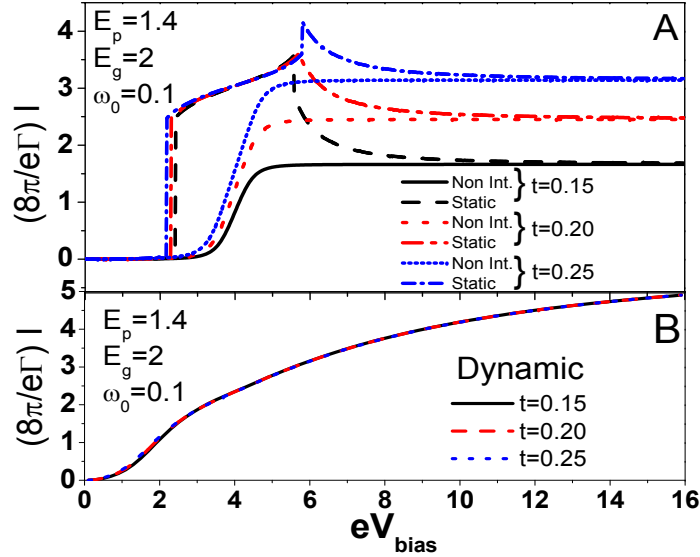


Figure 2.16: Panel A: Current-Voltage characteristic in the static approximation for  $\omega_0/\Gamma = 0.1$ ,  $E_g = 2$  and strong coupling  $E_p = 1.4$  for different values of intermolecular hopping ( $t = 0.15$  dashed (black),  $t = 0.2$  dashed dotted (red),  $t = 0.25$  short dashed dotted (blue)). The non interacting quantities ( $t = 0.15$  solid (black),  $t = 0.2$  dotted (red),  $t = 0.25$  short dotted (blue)) are also shown. Panel B: Current-Voltage characteristic in the dynamical approximation for the same value of panel A. The value of  $\omega_0$  shown in the figure is in  $\Gamma$  units, while all other quantities ( $E_g$ ,  $E_p$ ,  $t$  and  $eV_{bias}$ ) are expressed in  $\hbar\Gamma$  units.

## Chapter 3

# Electronic transport through a nanomechanical resonator acting as electronic transistor in the presence of nearby antenna

In this chapter, I study a general model describing a self-detecting single electron transistor realized by a suspended carbon nanotube (CNT) actuated by a nearby antenna. The main features of the device, recently observed in a number of experiments, are accurately reproduced. When the device is in a low current-carrying state, a peak in the current signals a mechanical resonance. On the contrary, a dip in the current is found in high current-carrying states. In the nonlinear vibration regime of the resonator, I'm able to reproduce quantitatively the characteristic asymmetric shape of the current-frequency curves. I show that the nonlinear effects coming out at high values of the antenna amplitude are related to the effective nonlinear force induced by the electronic flow. The interplay between electronic and mechanical degrees of freedom is understood in terms of an unifying model including in an intrinsic way the nonlinear effects driven by the external probe. I also include in the model the presence of a transverse magnetic field applied to the device. As a main result, the magnetic field modifies the bending mode CNT dynamics giving an enhanced damping as well as a noise term originating from the electronic phase fluctuations induced by the CNT displacements. In particular, a quadratic dependence of the device quality factor  $Q$  on external magnetic field strength, in quantitative agreement with recent experiments, emerges as a result of a back-action of quantum electronic current-flow fluctuations on the bending mode dynamics. I also show that, when the device is driven far from equilibrium, one can tune with the external magnetic field the mechanical properties of the resonator such as quality factors and resonance frequencies.

### 3.1 Introduction

It has been recently shown that carbon nanotubes can act simultaneously as single electron transistors [138] (SET) and as nanoelectromechanical systems (NEMS) [38, 43]. The idea is to use a single carbon nanotube placed between two metal contacts in a suspended configuration as a self-detecting SET. Due to the extreme properties of carbon nanotubes (ideal for NEMS applications, because they have a low mass and a high Young's modulus), the electronic current flowing through the device results very sensitive to the dynamics of the nanotube itself.

Although the main effort has been focused on detecting the quantum regime of mechanical resonators [42, 44, 118], recently, G. A. Steele *et al.*[11] and A. K. Huttel *et al.*[12] were able to fabricate a carbon nanotube electromechanical device working in the semiclassical regime (resonator frequencies in MHz range compared to an electronic hopping frequency of the order of tens of GHz) with an extremely large quality factor ( $Q > 10^5$ ). By measuring the variations of the electronic current flowing through the nanotube as function of the frequency of a nearby antenna actuating its motion, they were able to detect very well defined resonances corresponding to the bending mode of the nanotube itself. The possibility of using currents to probe nanomechanical resonances is strongly related to the extremely large quality factor obtained. In particular, when the SET is in a low current-carrying state (far from electronic resonance), a peak in the current signals a mechanical resonance, while a dip is observed in a high current-carrying state (SET in electronic resonance). Moreover, by adjusting the antenna power, the nanotube resonator can easily be tuned into the nonlinear vibration regime. For small antenna amplitudes, the current-frequency curves are very well fitted by a Lorentzian, while a characteristic triangular shape or even hysteresis for large antenna amplitudes is obtained. Interestingly, the operating temperature can affect the nonlinearity and the quality factor of the resonator in a non expected way: the nonlinear effects in current-frequency curves are washed out increasing the temperature <sup>1</sup>. A detailed analysis of a single frequency resonance dip has also shown that a broadening can be obtained increasing the source-drain voltage [11]. In Ref. [11], the authors were able to provide an explanation of some of the observed effects in terms of a model in which the gate voltage acquires an assigned time dependence. Within this phenomenological model, the back-action of the nanotube motion on detected current is understood neglecting completely the dynamics of the resonator and analyzing the problem directly at mechanical resonance conditions only in the limit of small external antenna amplitudes (linear response regime).

In my approach, I do not consider a priori assumptions on the resonator (nanotube) dynamics. Actually, in the device investigated in Ref. [11, 12], the chemical potentials of the leads, to which the nanotube is anchored, differ by the value of the applied transport voltage  $eV_{bias}$  (where  $e$  is the electron charge), and thus the environment that the nanotube experiences cannot be considered at equilibrium since the voltages applied in the experiment are typically greater than the temperature,  $eV_{bias} \gg k_B T$  ( $k_B$  being Boltzmann constant). Therefore, in order to understand the behavior of the device under such conditions, one needs to determine self-consistently the influence of electrical current and of the external antenna on the resonator dynamics, and vice versa, the influence of nonthermal nanotube vibrations driven by the antenna on the electronic current <sup>2</sup>. As rigorously demonstrated by Mozyrsky *et al.* [27], and reobtained by us in a different way in the previous Chap.[29], in absence of the external antenna, the vibrational dynamics of the nanotube can be described, employing a separation between slow vibrational and fast electronic time scales [29, 105, 119, 120], by a Langevin equation [28, 123, 122, 119, 120, 121]. This equation is ruled by an effective force as well as a damping and diffusive terms stemming from the interaction of the resonator with the electronic bath consisting of both the nanotube itself (that can be described by a single electronic level [121]) and the out-of-equilibrium environment given by the macroscopic leads. By including the external antenna effects through a forcing term in the Langevin equation, I provide such a self-consistent description of vibrational and electronic dynamics as argued above.

A theoretical treatment of the nanotube based device investigated in [11, 12], including

---

<sup>1</sup>Usually, increasing the temperature, one would expect to access the region far away the potential minimum, where nonlinear effects could be present.

<sup>2</sup>For the sake of simplicity, back-actions effects of the vibrating resonator on the electromagnetic field of the antenna are disregarded.

the external antenna effects, has been already considered by G. Labadze and Ya. M. Blanter [124]. In Ref. [124], the authors use a Fokker-Plank equation for the resonator distribution probability based on master equations[128, 126, 127, 125, 129]. This approach implicitly assumes that the energy scale of the applied voltages is much larger than the electronic tunneling energy scale  $\hbar\Gamma$ ,  $eV_{bias} \gg \hbar\Gamma$ . Moreover, tunneling is considered in the *sequential* regime and quantum effects in the electronic dynamics such as *cotunneling* are disregarded<sup>3</sup>. I point out that these effects can be important to interpret the experimental results obtained by G. A. Steele *et al.* [11] and A. K. Huttel *et al.* [12] since, as already emphasized by G. Weick *et al.*[121], the temperature is much smaller than  $\hbar\Gamma$  and the bias voltage *effectively* applied to the electronic level of the nanotube can be less than or of the same order of magnitude of the electronic tunneling energy,  $k_B T \ll eV_{bias}^{eff} \leq \hbar\Gamma$ . My approach, based on an adiabatic expansion of the time-dependent electronic Green function on the Keldysh contour in the small parameter  $\omega_0/\Gamma$  [29, 105, 119, 120], takes into account from the beginning of all higher order terms in the tunneling matrix element between the leads and the nanotube (so sequential tunneling and cotunneling regimes are described in a unified way).

The inclusion of the external antenna effects in the effective Langevin equation for the resonator has allowed us to explore also the nonlinear response regime in a nonperturbative way. I point out that, even describing the vibrational dynamics of the nanotube as a single *harmonic* vibrational mode, I'm able to reproduce all the main features observed in Ref. [11, 12] including the nonlinear effects. Indeed, in the nonlinear vibration regime of the resonator, I'm able to reproduce quantitatively the characteristic asymmetric shape of the current-frequency curves. The observed nonlinearity is due to the intrinsic nonlinear terms of the effective force stemming from the strong interaction between electron and resonator dynamics [27, 28, 123, 122, 29]. These terms are completely neglected in Ref. [124], loosing any possibility to describe renormalization frequency effects and to explore the nonlinear response regime for the resonator. I show that nonlinear effects can be highlighted *only dynamically* by applying large external antenna amplitudes. In this sense, my approach is different from other theoretical studies where nonlinear terms are discussed only statically [11] or are added from the beginning assuming that the resonator is characterized by anharmonic terms.[129, 121, 130]

Within my approach, the experimental results obtained in Ref. [11, 12] in the linear response regime are also reproduced, as well as the broadening of the mechanical resonance dip as function of the applied bias voltage. Furthermore, I'm able to predict, in the limit of large bias, the onset of a fine double dip structure that could be experimentally observed (these features were effectively found in Ref.[139] and I will discuss them in detail in Sec. 3.5).

The chapter is organized as follows: In Sec. 3.2, I present the model able to describe the electronic transistor consisting of the vibrating nanotube. Then (Sec. 3.3), the equation of motion describing the resonator dynamics including the external antenna effects is discussed. In Sec. 3.4, I present numerical results. In Sec. 3.5, I show that my approach can be extended to the case where an external magnetic field perpendicular to the nanotube device is introduced.

---

<sup>3</sup>In sequential tunneling regime,  $\hbar\Gamma \ll \min[eV_{bias}, k_B T]$ , the tunneling events between the leads and the molecule are energy-conserving, with the rates determined by Fermi's golden rule at the lowest order in perturbation theory in the tunneling Hamiltonian  $\hat{H}_{tun} = \sum_{k,\alpha} (V_{k,\alpha} \hat{c}_{k,\alpha}^\dagger \hat{d} + h.c.)$ . In the cotunneling regime,  $eV_{bias} < \hbar\Gamma < k_B T$  or  $k_B T < \hbar\Gamma < eV_{bias}$  or  $\max[eV_{bias}, k_B T] < \hbar\Gamma$ , higher-order tunneling events become dominant.

## 3.2 Model and method

I describe the suspended carbon nanotube with a single impurity Holstein model [131], which was already studied in the previous chapter. As I show below, this model is able to catch the main physical ingredients of the experiments in Ref. [11, 12]. For the sake of clarity, I here point out that the model used in [11, 12] and in other papers in the literature [124, 126, 127, 125, 129, 132], based on on a capacitive coupling of the nanotube (dot) to the gate electrode, is equivalent to a Holstein-like coupling between the occupation on the dot and the vibrational degree of freedom (see Appendix B).

As suggested by Weick *et al.* [129], in the small energy window of interest for a single dip feature, the electronic part of the device is modeled as a single electronic level coupled to the leads through standard tunneling terms. The electronic Hamiltonian is given by  $\hat{\mathcal{H}}_{el} = \hat{H}_{mol} + \hat{H}_{tun} + \hat{H}_{leads}$ , where  $\hat{H}_{mol}$ ,  $\hat{H}_{tun}$  and  $\hat{H}_{leads}$  were given in Eqs. 2.1, 2.2 and 2.3 of previous Chap., respectively. Nanotube's electronic level has energy  $V_{gate}^{eff}$  with creation (annihilation) operators  $\hat{d}^\dagger$  ( $\hat{d}$ ) (Eq. 2.1). The operators  $\hat{c}_{k,\alpha}^\dagger$  ( $\hat{c}_{k,\alpha}$ ) create (annihilate) electrons with momentum  $k$  and energy  $\varepsilon_{k,\alpha} = E_{k,\alpha} - \mu_\alpha$  in the left ( $\alpha = L$ ) or right ( $\alpha = R$ ) free metallic leads (Eq. 2.3), while the electronic tunneling between the molecular level and a state in the lead has amplitude  $V_{k,\alpha}$  (Eq. 2.2). The chemical potentials in the leads  $\mu_L$  and  $\mu_R$  are assumed to be biased by an external voltage  $eV_{bias}^{eff} = \mu_L - \mu_R$ . The coupling to the leads is described by the tunneling rate  $\Gamma_{\alpha,k} = 2\pi\rho_\alpha|V_{k,\alpha}|^2/\hbar$ , where  $\rho_\alpha$  is the density of states in the lead  $\alpha$ . I will suppose symmetric coupling ( $\Gamma_{L,k} = \Gamma_{R,k}$ ) and a flat density of states for the leads, considered as thermostats at finite temperature, within the wide-band approximation ( $\Gamma_{\alpha,k} \mapsto \Gamma_\alpha$ ,  $\alpha = L, R$ ) [129, 121].

The Hamiltonian of the mechanical degree of freedom is given by  $\hat{H}_{osc} = \frac{\hat{p}^2}{2m} + \frac{1}{2}m\omega_0^2\hat{x}^2$ , characterized by the frequency  $\omega_0$  and the effective mass  $m$  ( $k = m\omega_0^2$ ). The interaction is provided by  $\hat{H}_{int} = \lambda\hat{x}\hat{N}_{el}$  [129, 128], where  $\lambda$  is the electron-oscillator coupling strength and  $\hat{N}_{el} = \hat{d}^\dagger\hat{d}$  represents the electronic occupation on the nanotube (see also Appendix B). Definitely, the overall Hamiltonian is

$$\hat{\mathcal{H}} = \hat{\mathcal{H}}_{el} + \hat{H}_{osc} + \hat{H}_{int}. \quad (3.1)$$

In this chapter, I will measure lengths in units of  $x_0 = \frac{\lambda}{k}$  and energies in units of  $\hbar\Gamma$ .

The experimental values of the resonance frequencies of the vibrating nanotube (120-300 MHz range) suggest that the vibrational motion is very slow compared to the electronic tunneling rate on the nanotube itself (adiabatic limit):  $\omega_0/\Gamma \ll 1$ . Moreover, it was estimated in Ref.[129] that for the experiment in consideration the coupling energy describing electron-phonon interaction,  $E_p = \frac{\lambda^2}{2k} \simeq 5\mu eV$ , implying a strong coupling between the electronic and vibrational degrees of freedom ( $E_p/\hbar\omega_0 = 10$ ). Summarizing, the regime of the relevant parameters is  $\hbar\omega_0 \ll E_p(\sim k_B T) \ll eV_{bias}^{eff} \leq \hbar\Gamma$ <sup>4</sup>.

## 3.3 Langevin equation for the oscillator

As discussed in the previous Chap.[29] and in Ref.[116], when  $eV_{bias}^{eff} \gg \hbar\omega_0$  and  $k_B T > \hbar\omega_0$ , the semi-classical treatment of the oscillator dynamics is well justified. Within a non-equilibrium adiabatic approximation [27, 28, 123, 29, 105], the vibrational dynamics of the

---

<sup>4</sup>It is very difficult to infer the actual values of the effective source-drain bias  $eV_{bias}^{eff}$  and the gate voltage  $V_{gate}^{eff}$  applied to the device from the experimental setup. Due to the capacitive coupling between the carbon nanotube and the surrounding electrodes and to the length (400 – 1100nm) of the nanotube itself, only a fraction of the applied bias and gate voltage acts effectively onto the nanotube level interested in the transport [11, 12].

nanotube can be described by a *nonstandard Langevin equation* controlled by a self-consistent effective *anharmonic* force as well as by damping and diffusive terms depending explicitly on the resonator displacement  $x$ . In the presence of the antenna, I here propose that the oscillator dynamics can be obtained by solving numerically the following equation

$$m\ddot{x} + A(x)\dot{x} = F(x) + \xi(t) + A_{ext}\cos(\omega_{ext}t), \quad (3.2)$$

where  $A_{ext}$  and  $\omega_{ext}$  represent the amplitude and the external antenna frequency, respectively. Furthermore, in Eq. 3.2, the position-dependent force  $F(x)$ , damping  $A(x)$ , and the intensity of the noise  $D(x)$ ,  $\langle \xi(t)\xi(t') \rangle = D(x)\delta(t-t')$  (where  $\xi(t)$  is a standard white noise term), are related to the electronic Green's functions on the Keldysh contour [27, 28, 123, 29]. For the sake of exposition clarity, I here list some of the results of the previous Chap.

$$F(x) = -kx + \lambda \langle \hat{N}_{el} \rangle(x), \quad (3.3)$$

$$\langle \hat{N}_{el} \rangle(x) = \int \frac{d\hbar\omega}{2\pi i} G^<(\omega, x) \quad (3.4)$$

$$A(x) = \lambda^2 \hbar \int \frac{d\hbar\omega}{2\pi} G^<(\omega, x) \partial_{\hbar\omega} G^>(\omega, x), \quad (3.5)$$

$$D(x) = \lambda^2 \hbar \int \frac{d\hbar\omega}{2\pi} G^<(\omega, x) G^>(\omega, x). \quad (3.6)$$

The lesser  $G^<$  and greater  $G^>$  Green's functions at finite temperature are given by

$$G^<(\omega, x) = \frac{i\hbar\Gamma}{2} \frac{f_L(\omega) + f_R(\omega)}{(\hbar\omega - V_{gate}^{eff} - \lambda x)^2 + (\hbar\Gamma/2)^2}, \quad (3.7)$$

$$G^>(\omega, x) = \frac{-i\hbar\Gamma}{2} \frac{2 - f_L(\omega) - f_R(\omega)}{(\hbar\omega - V_{gate}^{eff} - \lambda x)^2 + (\hbar\Gamma/2)^2}, \quad (3.8)$$

where  $f_{L,R}(\omega)$  are the Fermi functions of the leads and I have assumed that  $\hbar\Gamma_L = \hbar\Gamma_R = \hbar\Gamma/2$ . At low temperatures,  $k_B T \ll \hbar\Gamma$ , the Fermi function  $f_\alpha(\omega)$  can be replaced by the step function  $\Theta(\hbar\omega - \mu_\alpha)$  ( $\alpha = L, R$ ), obtaining

$$\langle N_{el} \rangle(x) = \frac{1}{2\pi} \sum_{\alpha=L,R} \left( \arctan \left( \frac{\mu_\alpha - V_{gate}^{eff} - \lambda x}{\hbar\Gamma/2} \right) + \frac{\pi}{2} \right), \quad (3.9)$$

$$A(x) = \frac{4m\omega_0}{\pi} \frac{\hbar\omega_0}{\hbar\Gamma} \frac{E_p}{\hbar\Gamma} \sum_{\alpha=R,L} \frac{1}{\left[ \left( \frac{\mu_\alpha - V_{gate}^{eff} - \lambda x}{\hbar\Gamma/2} \right)^2 + 1 \right]^2}, \quad (3.10)$$

$$D(x) = \frac{m\omega_0 E_p}{\pi} \frac{\hbar\omega_0}{\hbar\Gamma} \left\{ \arctan \left( \frac{\mu_\alpha - V_{gate}^{eff} - \lambda x}{\hbar\Gamma/2} \right) + \frac{\frac{\mu_\alpha - V_{gate}^{eff} - \lambda x}{\hbar\Gamma/2}}{\left[ \left( \frac{\mu_\alpha - V_{gate}^{eff} - \lambda x}{\hbar\Gamma/2} \right)^2 + 1 \right]} \right\}_{\alpha=R}^{\alpha=L}. \quad (3.11)$$

As also stressed in the previous Chap., the linear elastic force exerted on the oscillator is modified by a relevant *nonlinear* correction term proportional to the electronic occupation Eq. 3.9. The strength of the damping  $A(x)$  and diffusive  $D(x)$  terms result proportional to the adiabatic ratio  $\omega_0/\Gamma$  and therefore one can safely neglect their spatial dependence. Anyway, I point out that the diffusive term  $D(x)$  vanishes at equilibrium (bias voltage  $V_{bias}^{eff} = 0$ ). Only on application of finite bias it becomes different from zero. In the regime

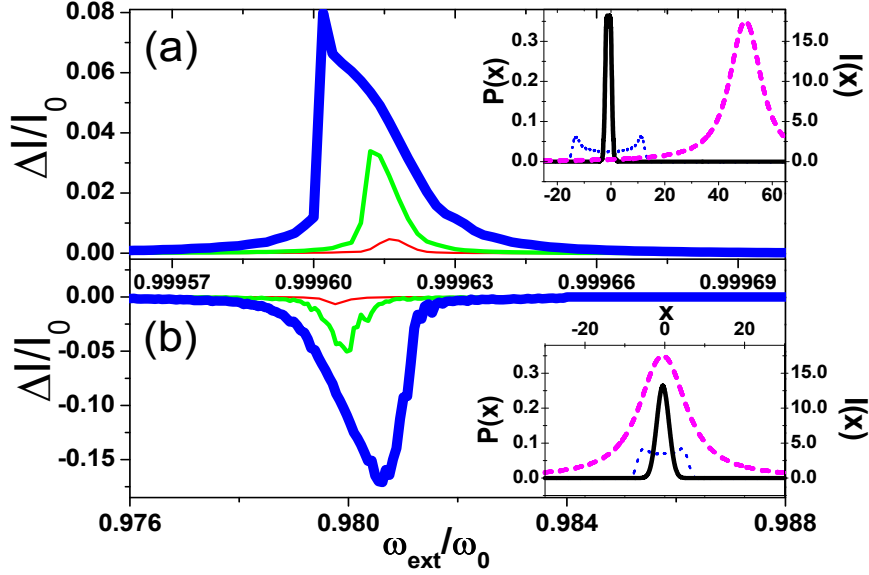


Figure 3.1: (Color online) Panel(a): Normalized current change ( $\Delta I/I_0$ ) in a low current-carrying state ( $V_{gate}^{eff} = -4\hbar\Gamma$ ) as function of the external frequency ( $\omega_{ext}/\omega_0$ ) for different antenna amplitudes:  $A_{ext} = 10^{-5}$  solid thin line (red online),  $A_{ext} = 10^{-4.5}$  normal thickness line (green online),  $A_{ext} = 10^{-3.5}$  thick line (blue online). Panel (b):  $\Delta I/I_0$  against  $\omega_{ext}/\omega_0$  in a high current-carrying state ( $V_{gate}^{eff} = E_p$ ) for different antenna amplitudes:  $A_{ext} = 10^{-3.5}$  solid thin line (red online),  $A_{ext} = 10^{-3}$  normal thickness line (green online),  $A_{ext} = 10^{-2.5}$  thick line (blue online). Insets: solid line (black online) is a distribution  $P(x)$  out of mechanical resonance. Dotted line (blue online) is a distribution obtained at mechanical resonance for the larger value of antenna amplitude considered in main plots of panels (a,b). Short-dashed line (magenta online) represents current as function of position  $I(x)$ . In this plot  $eV_{bias}^{eff} = 0.5\hbar\Gamma$ ,  $\omega_0/\Gamma = 0.004$  and  $E_p/\hbar\Gamma = k_B T/\hbar\Gamma = 0.04$ .

of experimental parameters explored in Refs. [11, 12],  $\hbar\omega_0 \ll E_p(\sim k_B T) \ll eV_{bias}^{eff} \leq \hbar\Gamma$ , the effect of the electronic bath on the resonator dynamics can be described by an effective temperature proportional to the bias voltage  $k_B T_{eff} \simeq eV_{bias}^{eff}/8$  [27, 29].

In Eq. 3.2, I consider the parameter  $A_{ext}$  expressed in terms of the natural force unit  $\lambda = \omega_0 \sqrt{2mE_p}$ . Assuming a nanotube mass of  $m \sim 10^{-23} kg$ , an oscillation frequency of 120 MHz,  $\lambda$  is of the order of  $10^{-16} N$ , while the effective spring constant is  $k = 10^{-6} N/m$ . By solving the second order stochastic differential equation 3.2 with the procedure outlined in the previous Chap.[29], I'm able to obtain the distribution probabilities of the displacement  $P(x)$ . This allows us to calculate any system property as an average over the distribution probability  $P(x)$ . In particular, in order to make contact with experimental results, I have calculated the average electronic current  $\langle I \rangle$  flowing through the nanotube as  $\langle I \rangle = \int_{-\infty}^{+\infty} dx I(x) P(x)$ , where  $I(x)$  is the current at a particular resonator displacement.

### 3.4 Results

One of the main results of Ref. [11, 12] is the observation of the electronic current changes at fixed gate voltage as function of the external antenna frequency and amplitude. My model accurately reproduces the experimental results both in a low current-carrying state, where a peak in the current signals a mechanical resonance (Fig.3.1a), and in a high current-carrying state, where a dip is observed (Fig.3.1b).

These two behaviors (peak and dip) can be understood considering that the oscillator explores wider regions in configuration space when the external antenna amplitude increases (see the distribution probabilities  $P(x)$  shown in the insets of Fig. 3.1). When the electronic device is in a low current-carrying state (Fig.3.1a),  $P(x)$  is concentrated at  $x$  values far from the configurations where the device carries the maximum current (inset of Fig.3.1a). By increasing the external antenna amplitude, the resonator is able to explore larger regions which carry more and more current obtaining a positive contribution in the normalized electronic current change  $\Delta I/I_0$  with respect to the background value  $I_0$ . On the contrary, when the device is in a high current-carrying state, the distribution probabilities and the current are centered at the same position (inset of Fig.3.1b). In this case, the effect of the external antenna is to give a negative contribution in the normalized electronic current change  $\Delta I/I_0$  (Fig 3.1b) since, the resonator explores regions of phase space which carry less and less current (inset of Fig. 3.1b).

### 3.4.1 Nonlinear regime of oscillator's dynamics

The results shown in Fig.3.1 allow also to characterize the behavior of the resonator in the nonlinear regime. Interestingly, (see Fig.3.1a), increasing the amplitude of the external forcing, the shape of the current-frequency curves changes. For small antenna amplitudes, a characteristic Lorentzian shape is observed. This is expected for an harmonic oscillator driven by a periodic forcing in the absence of external noise. In fact, even if in mechanical resonance, the oscillator explores only small regions around the stationary point and nonlinear corrections terms of the force  $F(x)$  (eq. (3.3)) do not come into play. At mechanical resonance, only when the amplitude of the external antenna increases, the oscillator explores a larger region in phase space, where the nonlinear terms of the force acting on the oscillator cannot be neglected.

Within my approach, for large antenna amplitudes and in the presence of noise, the current-frequency profiles assume the experimentally observed characteristic triangular shape [12]. Furthermore, a softening is observed when the device is in a low current-carrying state (Fig. 3.1a), while an hardening in a high current-carrying state is obtained (Fig. 3.1b). This nonlinear behavior can be understood by analyzing the properties of the force  $F(x)$  (eq. 3.3) around the stationary point. Softening and hardening behavior of the resonance frequency are usually related to the sign of the cubic nonlinear term [135]. When the device is in a low current-carrying state, indeed, the sign of this term is positive, giving a net softening effect. In a high current-carrying state ( $V_{gate}^{eff} = E_p$ ) and for bias values sufficiently small, the sign of the cubic nonlinear term is negative providing an hardening.

The temperature dependence of the current-frequency profiles, observed in the experiments, exhibits a nontrivial behavior that supports my model. As shown in Fig.3.2a, for very small temperatures, a triangular shape is found as discussed above. On the other hand, for sufficiently large temperatures, the current-frequency profile turns into Lorentzian shape, characteristic of the linear response regime (Fig.3.2c). This counterintuitive behavior is determined by a significative reduction of the intrinsic nonlinear terms in the effective force  $F(x)$  on the resonator as function of the temperature. Actually, the correction term due the average electronic occupation (eq. (3.9)) tends to become independent of the resonator displacement  $x$ . Furthermore, the broadening of the current-frequency profiles as function of the temperature is produced not only by this effect but also by the growth of the intrinsic damping coefficient  $A(x)$  in the Langevin equation Eq.(3.2). Indeed, with increasing temperatures,  $A(x)$  increases where resonator dynamics occurs. The temperature dependence of the intrinsic damping  $A(x)$  is also responsible for the behavior of the resonator quality factor  $Q$ , defined as  $I_0/\Delta I_{half-high}$ . In the regime where the current-frequency profiles exhibit a



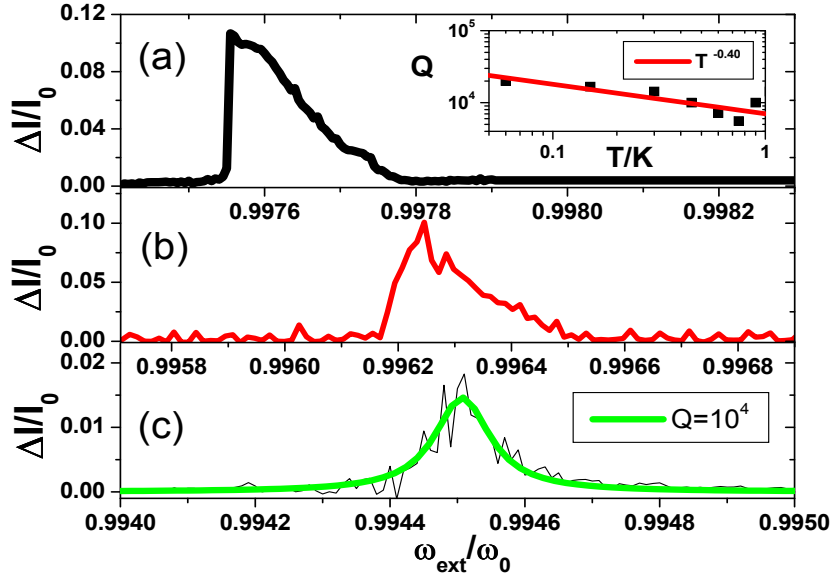


Figure 3.2: (Color online)  $\Delta I/I_0$  against  $\omega_{ext}/\omega_0$  in a low current-carrying state ( $V_{gate}^{eff} = -1.75\hbar\Gamma$ ) when the resonator is driven by a strong external antenna amplitude  $A_{ext} = 10^{-3.5}$ : panel (a)  $k_B T = 0.05\hbar\Gamma$ , panel (b)  $k_B T = 0.375\hbar\Gamma$ , panel (c)  $k_B T = \hbar\Gamma$ . In panel (c) a Lorentzian fit is also drawn with  $Q = 10^4$  ( $Q$  is defined in the main text). Inset of panel (a): intrinsic quality factor  $Q$  as function of temperature. I use as energy unit  $\hbar\Gamma = 125\mu eV$ . In this plot  $eV_{bias}^{eff} = 0.5\hbar\Gamma$ ,  $\omega_0/\Gamma = 0.005$  and  $E_p/\hbar\Gamma = 0.05$ .

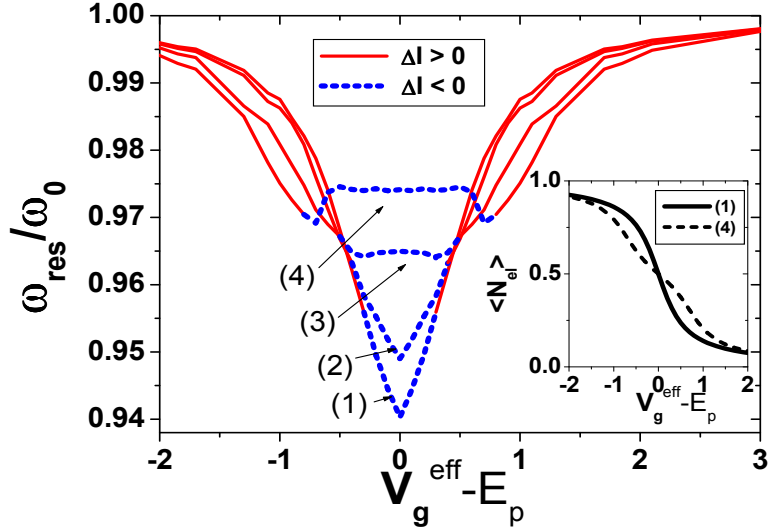


Figure 3.3: (Color online) Resonator frequency at resonance against effective gate voltage (shifted of  $E_p$ ) for different bias voltages:  $eV_{bias} = 0.1\hbar\Gamma$  curve (1),  $eV_{bias} = 0.5\hbar\Gamma$  curve (2),  $eV_{bias} = 1.0\hbar\Gamma$  curve (3),  $eV_{bias} = 1.5\hbar\Gamma$  curve (4). Solid (red online) and short-dashed (blue online) portions of each curve indicate resonance frequency values with positive and negative current change  $\Delta I$ , respectively. Inset: electronic occupation at resonance frequency against effective gate voltage (shifted of  $E_p$ ) for  $eV_{bias} = 0.1\hbar\Gamma$  (curve (1)) and  $eV_{bias} = 1.5\hbar\Gamma$  (curve (4)). In this plot  $A_{ext} = 10^{-3}$ ,  $\omega_0/\Gamma = 0.01$  and  $E_p/\hbar\Gamma = k_B T/\hbar\Gamma = 0.1$ .

Lorentzian shape, I find a power-law of the kind  $T^{-0.40}$ <sup>5</sup> that is quite close to that found in the experiment ( $T^{-0.36}$ ). However, it is important to point out that this exponent depends on the gate voltage effectively applied to the device.

Finally, I have analyzed all the traces of current variations as function of the antenna frequency, obtained tuning the effective gate voltage. Going from a low to a high current-carrying state, the characteristic dip of the resonance frequency as function of the effective gate voltage is obtained in excellent agreement with experiments (curve (1) of Fig.3.3). The observed renormalization of the resonance frequency can be related to strong variations of the electronic occupation eq.(3.9) as function of the gate voltage (see solid line in the inset of Fig.3.3). When the device is in a low current-carrying state ( $|V_{gate}^{eff} - E_p| > 1.5\hbar\Gamma$ ), the average electronic occupation is not sensitive to gate voltage variations. Instead, in a high current-carrying state ( $|V_{gate}^{eff} - E_p| < 1.5\hbar\Gamma$ ), the electronic occupation shows a strong variation, providing the softening of the resonance frequencies. Increasing the bias voltage to values closer to  $\hbar\Gamma$  or larger (line (3) and (4) of Fig. 3.3), one obtains a broadening of the resonance frequency dip, owing to a wider conduction window with respect to the broadening ( $\sim \hbar\Gamma$ ) of the electronic energy level. Actually, with increasing the bias, the electronic contribution to the effective spring constant increases, producing a nontrivial renormalization of the resonance frequency as function of the gate. I note that for  $eV_{bias}^{eff} = 1.5\hbar\Gamma$  (line (4) of Fig. 3.3), a fine structure represented by two very small dips appears. When the bias window, whose extension is proportional to  $eV_{bias}^{eff}$ , becomes larger than the broadening of the level, one could tune the electronic device into a region of conducting states where the variations of the occupation are smaller than that obtained at the boundary of the conduction window itself (see dashed line in the inset of Fig.3.3). When the electronic device goes through states with different conducting character, the maximum renormalization of the resonance frequency occurs, providing two dips in the resonance frequency of the nanotube. This feature could be experimentally observed[139] with a larger resolution in the applied gate voltage, when a very large bias is applied to the nanotube.

### 3.5 Introduction of a transverse Magnetic field

In this section I introduce, in the same model investigated above, the presence of an external magnetic field perpendicular to the suspended carbon-nanotube device[50]. As a main result, I find that the magnetic field provides an additional damping mechanism to the resonator mechanical motion. In particular, a quadratic decrease of the quality factor  $Q$  as a function of the external magnetic field strength, in quantitative agreement with the experiment performed in Ref.[136], emerges.

As concerns the physical mechanism triggered by the magnetic field, I show that the application of a field perpendicular to the current flux modifies all the terms describing the CNT-resonator dynamics. Actually, the coupling with a transverse magnetic field introduces an electronic tunneling phase which depends on the mechanical displacement of the CNT-resonator itself. This modifies the effective force acting on the resonator by a pure nonequilibrium correction term proportional to the magnetic field as well as to the electronic current flowing through the CNT. Moreover, even at zero bias voltage, damping and diffusive terms are both modified by quantum electronic current-current and density-current fluctuations corrections whose strengths are quadratic and linear in magnetic field, respectively. Finally, I further show that, at zero bias, displacement-charge and magnetic field mediated

---

<sup>5</sup>I have verified that, in the range of temperature investigated ( $0.05 < k_B T / \hbar\Gamma < 1 \rightarrow 60mK < T < 1.2K$ ), the widths of current frequency profiles are independent on the external antenna amplitude applied to tune the resonator in the linear response regime.

electron-oscillator couplings cooperate behaving as a whole as a standard thermal bath at leads' temperature.

As concerns the mechanical properties of the CNT-resonator, I'm able to reproduce, in the absence of magnetic field, all results experimentally observed[139] on a similar CNT-resonator device: when bias voltages are smaller than the broadening due to tunnel coupling, the resonance frequency and quality factor show a single dip as a function of gate voltage. At bias voltages that exceed the broadening due to tunnel coupling, the resonance frequency and quality factor show a double dip structure. Actually, in this regime, the onset of a double dip structure in the resonance frequency against gate voltage curve was already predicted by us in the previous Sec. (Ref.[49]).

Introducing the external magnetic field, the scenario outlined above modifies as follows. At low bias, the single dip feature in the CNT-resonator resonance frequency gets distorted and acquires, in the limit of large magnetic field, a dip-peak structure that could be experimentally observed. As concerns the quality factor against gate voltage, it preserves a single dip feature but with a global reduction with respect to zero magnetic field. Remarkably, when the device is in a low-conducting state, I find a  $Q$  against magnetic field curve in quantitative agreement to the experiment performed in Ref.[136]. At large bias voltages, the double dip feature in both CNT-resonator resonance frequency and in quality factor get distorted with the introduction of the field. The former acquires a dip-peak structure while the latter becomes single-dip shaped in the limit of large magnetic field.

The chapter ends with a study of the device response when the CNT-resonator motion is actuated by an external antenna at fixed frequency and amplitude. In this case, the device current-gate voltage characteristic is modified by fine structure features any time the mechanical resonance with the proper nanotube oscillation frequency occurs. These structures can be tuned as a function of the external field and could be experimentally observed.

The following subsections are organized as follows: In sec.3.5.1 I present the model able to describe the electronic transistor consisting of the vibrating CNT including the effect of a transverse magnetic field. In sec.3.5.2 I will construct, by means of the adiabatic approximation, the stochastic Langevin equation for the dynamics of the oscillator including magnetic field and, eventually, the external antenna effects. In sec.3.5.3 I present numerical results.

### 3.5.1 Model

I consider the system sketched in Fig.3.4, which shows a single-wall carbon nanotube (CNT) suspended between two normal metal leads. An external magnetic field  $H$  is applied perpendicular to the nanotube. As in the previous section, I also restrict the nanotube mechanical degrees of freedom to the fundamental bending mode and model it as a harmonic oscillator with frequency  $\omega_0$ .

The electronic part of the device is modeled as in the previous section (see section 3.2).

In the presence of an external transverse magnetic field, the electronic tunneling between the CNT level and a state in the lead has a time dependent amplitude  $V_{k,\alpha}^H(x)$ , where  $x$  is the mechanical CNT displacement from its equilibrium configuration. When the external magnetic field values are sufficiently small, such as the Zeeman splitting is negligible compared to broadening due to tunnel coupling, I can neglect the effect of the electronic spin degrees of freedom (this issue will be considered elsewhere [150]). In the presence of a magnetic field, the phases of the tunneling amplitudes with the leads depend on the CNT displacement

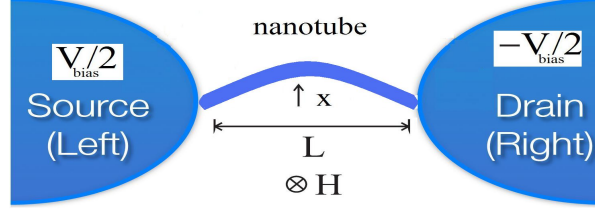


Figure 3.4: A carbon nanotube (CNT) subject to an external magnetic field  $H$  suspended between two normal metal leads biased by a voltage  $eV_{bias}$ .

$x$ , [148, 149]

$$\begin{aligned} V_{k,L}^H &= V_{k,L} e^{-ipx}, \\ V_{k,R}^H &= V_{k,R} e^{ipx}, \end{aligned} \quad (3.12)$$

where  $p = \delta eHL/2\hbar$  gives the CNT momentum change induced by the Lorentz force when an electron tunnels from the CNT to a lead, and  $\delta \simeq 1$  is a numerical factor determined by the spacial profile of the fundamental mode [151]. Above,  $e$  is the modulus of the electron charge,  $\hbar$  is the Plank constant and  $L$  is the CNT length.

For the sake of simplicity, I will suppose symmetric coupling  $V_{k,L} = V_{k,R}$  and a flat density of states for the leads  $\rho_{k,\alpha} \mapsto \rho_\alpha$ , considered as thermostats at finite temperature  $T$ , within the wide-band approximation ( $V_{k,\alpha} \mapsto V_\alpha$ ,  $\alpha = L, R$ ) [129, 121].

Definitely, the total tunneling rate is  $\hbar\Gamma = \sum_{\alpha=L,R} \hbar\Gamma_\alpha$ , with  $\Gamma_\alpha = 2\pi\rho_\alpha|V_{k,\alpha}|^2/\hbar$ .

The Hamiltonian of the mechanical degree of freedom is given by

$$\hat{H}_{osc} = \frac{\hat{p}^2}{2m} + \frac{1}{2}m\omega_0^2\hat{x}^2, \quad (3.13)$$

characterized by the frequency  $\omega_0$  and the effective mass  $m$  ( $k = m\omega_0^2$ ). The electron-oscillator interaction is provided by [129, 128]

$$\hat{H}_{int} = \lambda\hat{x}\hat{n}, \quad (3.14)$$

where  $\lambda$  is the electron-oscillator coupling strength and  $\hat{n} = \hat{d}^\dagger\hat{d}$  represents the electronic occupation on the CNT. Definitely, the overall Hamiltonian is

$$\hat{\mathcal{H}} = \hat{\mathcal{H}}_{el} + \hat{H}_{osc} + \hat{H}_{int}. \quad (3.15)$$

For the experiment discussed in Ref. [136], one has a strong separation between vibrational ( $\omega_0 \simeq 500 \text{ MHz} \simeq 2\mu\text{eV}$ ) and electronic time scales ( $\Gamma \simeq 50\text{GHz}$ ) so that I can solve the model in the adiabatic limit,  $\omega_0/\Gamma \ll 1$ . The experimental values of bias voltages and temperatures allow also a semi-classical treatment of the oscillator dynamics [29, 27, 28]. In this Sec., I will measure lengths in units of  $x_0 = r$ , where  $r$  is a small fraction of CNT radius ( $r = 60\text{pm}$ ) appropriate to resolve the CNT bending dynamics at relatively small temperatures ( $T \simeq 25\text{mK}$ ). For the sake of simplicity, I will indicate dimensionless displacement variable with  $x$ . Energies are measured in units of  $\hbar\Gamma = 200\mu\text{eV}$ , and times in units of  $t_0 = 1/\omega_0$ . In terms of these units, the dimensionless spring constant is  $k/m\omega_0^2 \simeq 1$ , since, following Ref. [136], the effective mass of the nanotube is  $m = 1.3 \times 10^{-21}\text{kg}$ . Definitely, the adiabatic ratio is  $\omega_0/\Gamma = 0.01$ , while the dimensionless temperature  $k_B T = 0.01$ . Magnetic fields are measured in terms of the quantity  $B = \frac{H}{H_0}$  where the magnetic field unit is  $H_0 = 2\hbar/eLr \simeq 16.6T$ , since the CNT length is  $L \simeq 700\text{nm}$ . Throughout this Sec., I keep fixed the dimensionless

electron-oscillator coupling  $\lambda = 0.1$  (the force unit is  $\hbar\Gamma/r$ ), corresponding to an estimate  $E_p = \lambda^2/2k \simeq 1\mu eV$ , implying a moderate coupling between the electronic and vibrational degrees of freedom ( $E_p/\hbar\omega_0 = 0.5$ ). Summarizing, the regime of the parameters relevant for the experiment in Ref.[136] is  $\hbar\omega_0 \simeq E_p \simeq k_B T \ll eV_{bias}^{eff} \leq \hbar\Gamma$ .

In the next section, I show how adiabatic approximation works on the coupled electron-oscillator problem in the presence of a transverse magnetic field.

### 3.5.2 Adiabatic approximation

As analyzed in the previous section, I work in the physical regime where the vibrational motion of the CNT-resonator is 'slow' with respect to all electronic energy scales and can be considered "classical":  $\omega_0 \ll \Gamma$ . This regime of the parameters leads to the adiabatic approximation for the electronic problem. In contrast to previous works that treated the adiabatic approximation in the absence of a magnetic field[29, 105, 119], I here investigate the effect of a transverse magnetic field on the electronic problem described by the Hamiltonian Eq.3.15. I remark that the adiabatic approximation has been used to describe larger systems[144, 145] for the study of spectral and transport properties of organic semiconductors[144, 145, 146, 147].

#### Adiabatic approximation for the electron problem in the presence of a magnetic field

In this subsection, I show how the adiabatic approximation on the electronic CNT level Green function works in the presence of a transverse magnetic field.

Assuming a slow time dependence of electronic Green functions on the resonator displacement  $x$ , I'm able to calculate truncated expressions for the CNT level Green functions which acquire a 'slow' time dependence and, at first order, a linear correction in the oscillator velocity. As a result of the adiabatic approximation, the truncated CNT level Green functions will depend on the instantaneous value of the position and velocity of the resonator  $G^{r,a,<,>}(\omega, x, v)$ .

The adiabatic expansion of the Fourier transformed retarded CNT level Green function is

$$G^r(\omega, x, v) = G_{(0)}^r(\omega, x) + G_{(1)}^r(\omega, x, v), \quad (3.16)$$

where the expression of  $G_{(0)}^r(\omega, x)$  is

$$G_{(0)}^r(\omega, x) = \frac{1}{\hbar\omega - V_{gate}(x) + i\Gamma/2}, \quad (3.17)$$

and that of  $G_{(1)}^r(\omega, x, v)$  is

$$G_{(1)}^r(\omega, x, v) = -i\hbar\dot{V}_{gate}(x)G_{(0)}^r(\omega, x)\frac{\partial G_{(0)}^r(\omega, x)}{\partial \hbar\omega}. \quad (3.18)$$

Above,  $V_{gate}(x) = V_{gate} + \lambda x$  and the dot indicates the time derivative  $\dot{V}_{gate} = \lambda \frac{\partial x}{\partial t} = \lambda v$ .

Using the adiabatic approximation[149]  $x(t_1) - x(t_2) \simeq \dot{x}(t_0)(t_1 - t_2)$ , I obtain for the lesser and greater components in Fourier space

$$\Sigma_{leads}^<(\omega, v) \simeq \Sigma_{leads,(0)}^<(\omega) + \Sigma_{leads,(1)}^<(\omega, v) \quad (3.19)$$

where the expression of  $\Sigma_{leads,(0)}^<(\omega)$  is

$$\Sigma_{leads,(0)}^<(\omega) = i[\hbar\Gamma_L f_L(\omega) + \hbar\Gamma_R f_R(\omega)], \quad (3.20)$$

and that of  $\Sigma_{leads,(1)}(\omega, v)$  is

$$\Sigma_{leads,(1)}(\omega, v) = -ie\tilde{H} \left( \frac{\partial[\hbar\Gamma_L f_L(\omega) + \hbar\Gamma_R f_R(\omega)]}{\partial[eV_{bias}]} \right) v. \quad (3.21)$$

Above, I have defined  $\tilde{H} = 2p\hbar/e$ . Definitely, for the CNT level occupation I get

$$\langle \hat{n} \rangle(x, v) \simeq \langle \hat{n} \rangle_{(0)}(x) + \langle \hat{n} \rangle_{(1)}(x, v), \quad (3.22)$$

where

$$\begin{aligned} \langle \hat{n} \rangle_{(0)}(x) &= \int \frac{d\hbar\omega}{2\pi i} |G_{(0)}^r(\omega, x)|^2 \Sigma_{leads,(0)}^<(\omega) \\ &= \int \frac{d\hbar\omega}{2\pi} \frac{\hbar\Gamma_L f_L(\omega) + \hbar\Gamma_R f_R(\omega)}{(\hbar\omega - V_{gate}(x))^2 + [\hbar\Gamma]^2/4}, \end{aligned} \quad (3.23)$$

with linear corrections in the oscillator velocity

$$\langle \hat{n} \rangle_{(1)}(x, v) = v[R_{(1)}(x) + R_{(2)}(x)], \quad (3.24)$$

$$\begin{aligned} R_{(1)}(x) &= \int \frac{d\hbar\omega}{2\pi i v} 2\Re[G_{(0)}^r(\omega, x)G_{(1)}^a(\omega, x, v)]\Sigma_{leads,(0)}^<(\omega) \\ &= \frac{\hbar\lambda}{2} \int \frac{d\hbar\omega}{2\pi} g^{(0)}(\omega) \frac{\hbar\Gamma_L + \hbar\Gamma_R}{[(\hbar\omega - V_{gate}(x))^2 + [\hbar\Gamma]^2/4]^2}, \end{aligned} \quad (3.25)$$

$$\begin{aligned} R_{(2)}(x) &= \int \frac{d\hbar\omega}{2\pi i v} |G_{(0)}^r(\omega, x)|^2 \Sigma_{leads,(1)}(\omega, v) \\ &= e\tilde{H} \int \frac{d\hbar\omega}{2\pi} g^{(1)}(\omega) \frac{1}{(\hbar\omega - V_{gate}(x))^2 + [\hbar\Gamma]^2/4}, \end{aligned} \quad (3.26)$$

where

$$g^{(0)}(\omega) = -\frac{\partial[\hbar\Gamma_L f_L(\omega) + \hbar\Gamma_R f_R(\omega)]}{\partial\hbar\omega}, \quad (3.27)$$

$$g^{(1)}(\omega) = -\frac{\partial[\hbar\Gamma_L f_L(\omega) + \hbar\Gamma_R f_R(\omega)]}{\partial[eV_{bias}]}. \quad (3.28)$$

Finally, in the hypothesis of symmetric coupling to the leads  $\Gamma_L = \Gamma_R$ , one can calculate the adiabatic expansion for the symmetrized current  $\langle \hat{I} \rangle = [\langle \hat{I}_L \rangle - \langle \hat{I}_R \rangle]/2$

$$\begin{aligned} \langle \hat{I} \rangle(x, v) &= \frac{e}{\hbar} \int \frac{d\hbar\omega}{2\pi} |G^r(\omega, x)|^2 (\Sigma^{R,>}(\omega, v) \Sigma^{L,<}(\omega, v) \\ &\quad - \Sigma^{L,>}(\omega, v) \Sigma^{R,<}(\omega, v)). \end{aligned} \quad (3.29)$$

Using Eqs 3.16, 3.19, I get

$$\langle \hat{I} \rangle(x, v) \simeq \langle \hat{I} \rangle_{(0)}(x) + \langle \hat{I} \rangle_{(1)}(x, v), \quad (3.30)$$

where

$$\begin{aligned}
\langle \hat{I} \rangle_{(0)}(x) &= \frac{e}{\hbar} \int \frac{d\hbar\omega}{2\pi} |G_{(0)}^r(\omega, x)|^2 (\Sigma_{(0)}^{R,>}(\omega) \Sigma_{(0)}^{L,<}(\omega) \\
&\quad - \Sigma_{(0)}^{L,>}(\omega) \Sigma_{(0)}^{R,<}(\omega)) \\
&= \frac{e}{\hbar} \int \frac{d\hbar\omega}{2\pi} \frac{\hbar\Gamma_L \hbar\Gamma_R (f_L(\omega) - f_R(\omega))}{(\hbar\omega - V_{gate}(x))^2 + [\hbar\Gamma]^2/4},
\end{aligned} \tag{3.31}$$

with linear corrections in the oscillator velocity

$$\langle \hat{I} \rangle_{(1)}(x, v) = v[U_{(1)}(x) + U_{(2)}(x)], \tag{3.32}$$

$$\begin{aligned}
U_{(1)}(x) &= \frac{e}{\hbar v} \int \frac{d\hbar\omega}{2\pi} 2\Re[G_{(0)}^r(\omega, x) G_{(1)}^a(\omega, x, v)] \times \\
&\quad \times (\Sigma_{(0)}^{R,>}(\omega) \Sigma_{(0)}^{L,<}(\omega) - \Sigma_{(0)}^{L,>}(\omega) \Sigma_{(0)}^{R,<}(\omega)) \\
&= -\frac{e\lambda\hbar\Gamma}{2} \int \frac{d\hbar\omega}{2\pi} \frac{\hbar\Gamma_L \hbar\Gamma_R}{[(\hbar\omega - V_{gate}(x))^2 + [\hbar\Gamma]^2/4]^2} \times \\
&\quad \frac{\partial(f_L(\omega) - f_R(\omega))}{\partial\hbar\omega},
\end{aligned} \tag{3.33}$$

$$\begin{aligned}
U_{(2)}(x) &= \frac{e}{\hbar v} \int \frac{d\hbar\omega}{2\pi} |G_{(0)}^r(\omega, x)|^2 [\Sigma_{L,(1)}(\omega, v) (\Sigma_{(0)}^{R,>}(\omega) + \\
&\quad - \Sigma_{(0)}^{R,<}(\omega)) + \Sigma_{R,(1)}(\omega, v) (\Sigma_{(0)}^{L,<}(\omega) - \Sigma_{(0)}^{L,>}(\omega))] \\
&= \frac{e^2}{\hbar} \tilde{H} \int \frac{d\hbar\omega}{2\pi} \frac{\hbar\Gamma_L \hbar\Gamma_R}{(\hbar\omega - V_{gate}(x))^2 + [\hbar\Gamma]^2/4} \times \\
&\quad \frac{\partial[f_R(\omega) - f_L(\omega)]}{\partial[eV_{bias}]}.
\end{aligned} \tag{3.34}$$

In next subsection, I show that, even in the presence of a transverse magnetic field, the dynamics of the CNT-resonator can be accurately described by a stochastic Langevin equation.

### Langevin equation for the oscillator

In the absence of a magnetic field, as seen in the previous Chap., the effect of the electron bath and the electron-resonator coupling on the oscillator dynamics gives rise to a stochastic Langevin equation with a position dependent dissipation term and white noise force [29]. As in Ref.[49], the equation for the oscillator dynamics can be written as follows

$$\begin{aligned}
m\ddot{x} + A(x)\dot{x} &= F_{(0)}(x) + \sqrt{D(x)}\xi(t) + A_{ext} \cos(\omega_{ext}t), \\
\langle \xi(t) \rangle &= 0, \quad \langle \xi(t)\xi(t') \rangle = \delta(t - t'),
\end{aligned} \tag{3.35}$$

where  $\xi(t)$  is a standard white noise term. I have included in the schematization the effect of an external antenna exciting the motion of the CNT, where  $A_{ext}, \omega_{ext}$  represent the amplitude and the external antenna frequency, respectively. In this section, I describe how all the terms appearing in above equation modify in the presence of an external transverse magnetic field.

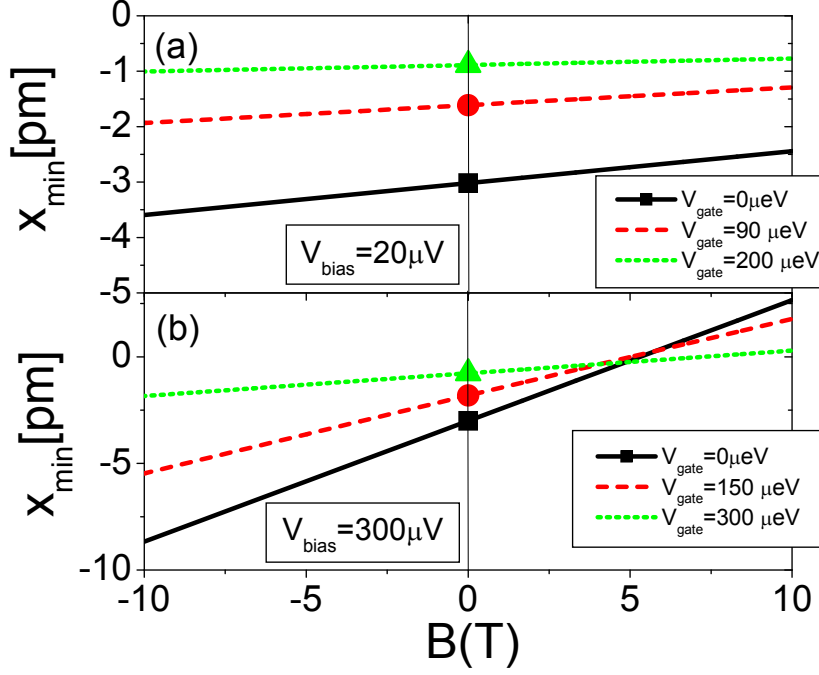


Figure 3.5: (Color online) Panel(a): minimum of the effective potential (coming from the force Eq.3.38) affecting the CNT-resonator as a function of the magnetic field at low bias  $eV_{bias} = 0.1\hbar\Gamma$  ( $V_{bias} = 20\mu V$  in my units). Solid (black) line indicates  $V_g = 0$ , dashed (red) line  $V_g = 0.45$  ( $V_{bias} = 90\mu V$  in my units), dotted (green) line  $V_g = 1.0$  ( $V_{bias} = 200\mu V$  in my units). Panel(b): same as above at large bias  $eV_{bias} = 1.5\hbar\Gamma$  ( $V_{bias} = 300\mu V$  in my units). Solid (black) line indicates  $V_g = 0$ , dashed (red) line  $V_g = 0.75$  ( $V_{bias} = 150\mu V$  in my units), dotted (green) line  $V_g = 1.5$  ( $V_{bias} = 300\mu V$  in my units).

The total force acting on the CNT-resonator is

$$F = -kx - \lambda\langle\hat{n}\rangle(x, v) + \tilde{H}\langle\hat{I}\rangle(x, v). \quad (3.36)$$

The linear elastic force exerted on the oscillator is modified by two relevant *nonlinear* correction terms: the former is proportional to the electronic density on the CNT level Eq.(3.23), while the latter to the electronic current Eq.(3.31). The first term, due to the density-displacement interaction on CNT-resonator and proportional to  $\lambda$  was already discussed in Refs.[49, 11]. Far from equilibrium and in the presence of a magnetic field, a magnetomotive coupling between the CNT-resonator displacement and the electronic flow through the device comes into play. Actually, the transverse magnetic field introduces a phase in the electronic tunneling that is proportional to the displacement of the CNT resonator as well as on the field strength. This originates a Lorentz-like additive correction, linear in the magnetic field strength and in the electronic current, to the average force acting on the resonator.

In the limit of the adiabatic approximation, the force Eq.3.36 can be decomposed in different expansion terms. It explicitly depends on the oscillator position  $x$  through  $V_{gate}(x) = V_{gate} + \lambda x$  and velocity  $v$ . The force is

$$F(x, v) = F_{(0)}(x) + F_{(1)}(x, v), \quad (3.37)$$

where

$$F_{(0)}(x) = -kx - \lambda\langle\hat{n}\rangle_{(0)}(x) + \tilde{H}\langle\hat{I}\rangle_{(0)}(x), \quad (3.38)$$



and

$$\begin{aligned} F_{(1)}(x, v) &= -\lambda \langle \hat{n} \rangle_{(1)}(x, v) + \tilde{H} \langle \hat{I} \rangle_{(1)}(x, v) \\ &= -A(x)v. \end{aligned} \quad (3.39)$$

The total damping term  $A(x)$  is given by three contributions

$$A(x) = A^\lambda(x) + A^H(x) + A^{H,\lambda}(x), \quad (3.40)$$

where both

$$A^\lambda(x) = \lambda R_{(1)}(x), \quad (3.41)$$

coming from the electron-oscillator coupling, and

$$A^H(x) = -\tilde{H}U_{(2)}(x), \quad (3.42)$$

due to magnetic field coupling, are positive definite. The function  $A^{H,\lambda}(x)$  is proportional to both electron-oscillator coupling  $\lambda$  and magnetic field  $H$

$$A^{H,\lambda}(x) = \lambda R_{(2)}(x) - \tilde{H}U_{(1)}(x), \quad (3.43)$$

and is not positive definite. Remarkably, I have verified that the whole sum appearing in Eq.3.40 is positive definite in all parameter regime of the model. This shows that, using a spinless fermionic model in the presence of normal (not ferromagnetic) electronic leads, the CNT-resonator experiences no negative damping regions. This is in contrast to results of Ref.[149], where the authors use a normal and a ferromagnetic lead and observe negative damping and consequent nano-electromechanical self-excitations of the CNT-resonator system.

A fluctuating term has to be included to take correctly into account the effect of the bath degrees of freedom. When a magnetic field is present, the force-force fluctuations are given by three contributions (see appendix A)

$$\begin{aligned} \langle \delta \hat{F}(t) \delta \hat{F}(t') \rangle &= \lambda^2 \langle \delta \hat{n}(t) \delta \hat{n}(t') \rangle + \\ &- \tilde{H} \lambda [\langle \delta \hat{n}(t) \delta \hat{I}(t') \rangle + \langle \delta \hat{I}(t) \delta \hat{n}(t') \rangle] + \\ &+ \tilde{H}^2 \langle \delta \hat{I}(t) \delta \hat{I}(t') \rangle, \end{aligned} \quad (3.44)$$

where I get a mixed current-density fluctuation contribution  $[\langle \delta \hat{n}(t) \delta \hat{I}(t') \rangle + \langle \delta \hat{I}(t) \delta \hat{n}(t') \rangle]$ , and a current-current fluctuation contribution  $\langle \delta I_\alpha(t) \delta I(t') \rangle$  to the noise.

In the adiabatic limit, exploiting the effect of the 'fast' electronic environment on the oscillator motion, one derives

$$\langle \delta \hat{F}(t) \delta \hat{F}(t') \rangle = D(x) \delta(t - t'), \quad (3.45)$$

where in the presence of a magnetic field I have

$$D(x) = D^\lambda(x) + D^H(x) + D^{H,\lambda}(x), \quad (3.46)$$

with

$$\begin{aligned} D^\lambda(x) &= \lambda^2 \hbar \int \frac{d\hbar\omega}{2\pi} G_{(0)}^<(\omega, x) G_{(0)}^>(\omega, x) = \\ &= \lambda^2 \hbar \int \frac{d\hbar\omega}{2\pi} \frac{\hbar \Gamma_L f_L(\omega) + \hbar \Gamma_R f_R(\omega)}{((\hbar\omega - V_{gate}(x))^2 + [\hbar\Gamma]^2/4)^2} \times \\ &\times (\hbar \Gamma_L (1 - f_L(\omega)) + \hbar \Gamma_R (1 - f_R(\omega))) \end{aligned} \quad (3.47)$$

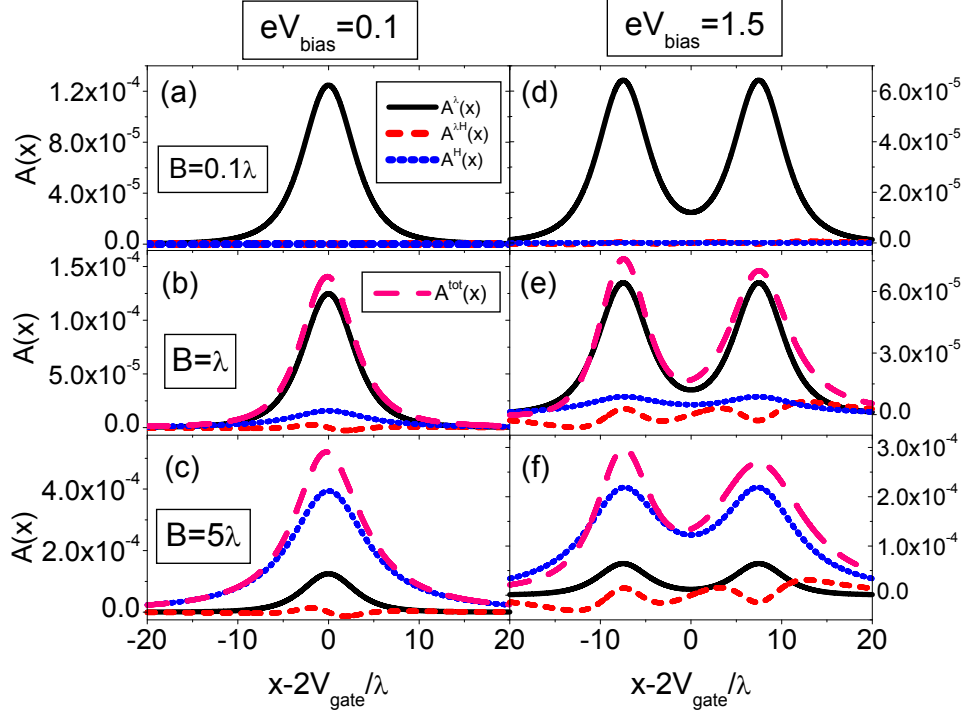


Figure 3.6: (Color online) Spatial dependence of the dimensionless damping coefficient  $A(x)$  at low bias (Panels(a-b-c)) and at large bias voltage applied (Panels(d-e-f)). See main text for discussion.

and

$$\begin{aligned}
D^{H\lambda}(x) &= \frac{e\tilde{H}}{2}\lambda \int \frac{d\hbar\omega}{2\pi} |G_{(0)}^r(\omega, x)|^2 B(\omega, x) \times \\
&\times (\Sigma_{(0)}^{L,>}(\omega)\Sigma_{(0)}^{L,<}(\omega) - \Sigma_{(0)}^{R,<}(\omega)\Sigma_{(0)}^{R,>}(\omega)) = \\
&= e\lambda\tilde{H} \int \frac{d\omega}{2\pi} \frac{\hbar\Gamma_L + \hbar\Gamma_R}{[(\hbar\omega - V_{gate}(x))^2 + [\hbar\Gamma]^2/4]^2} \times \\
&\times \left\{ [\hbar\Gamma_L]^2 f_L(\omega)(1 - f_L(\omega)) - [\hbar\Gamma_R]^2 f_R(\omega)(1 - f_R(\omega)) \right\}
\end{aligned} \tag{3.48}$$

where  $B(\omega, x) = -2\Im G_{(0)}^r(\omega, x)$  is the electronic spectral function of the electronic level. The noise strength contribution coming from current-current fluctuations is

$$\begin{aligned}
D^H(x) &= \tilde{H}^2\hbar \int \frac{d\hbar\omega}{2\pi} [f_L(\omega) - f_R(\omega)]^2 T(\omega, x) \times \\
&\times (1 - T(\omega, x)) + \left\{ f_L(\omega)(1 - f_L(\omega)) + \right. \\
&\left. + f_R(\omega)(1 - f_R(\omega)) \right\} T(\omega, x),
\end{aligned} \tag{3.49}$$

where

$$T(\omega, x) = \frac{\hbar\Gamma_L\hbar\Gamma_R}{[(\hbar\omega - V_{gate}(x))^2 + [\hbar\Gamma]^2/4]}. \tag{3.50}$$

In the absence of electron bias voltage, one has  $D(x) = 2k_B T A(x)$ , that is the fluctuation-dissipation condition is verified for each fixed position  $x$ . Moreover, it is possible to show

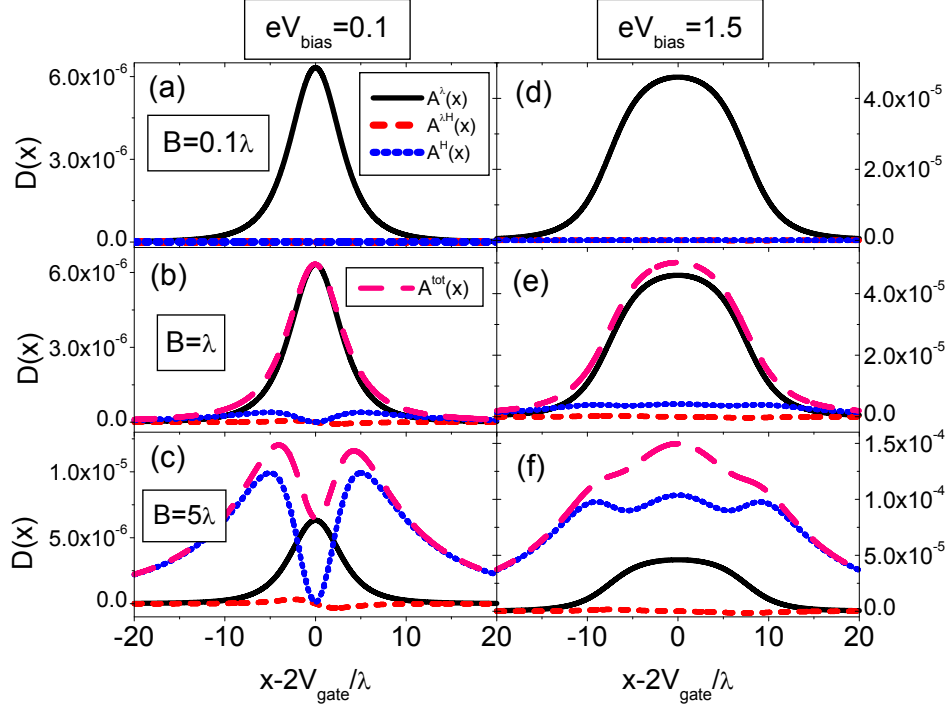


Figure 3.7: (Color online) Spatial dependence of the dimensionless diffusive coefficient  $D(x)$  at large bias voltage applied (Panels(a-b-c)). See main text for discussion.

that in the units chosen, the dimensionless damping  $A(x)$  (Eq.3.40) and diffusive term  $D(x)$  (Eq.3.46) result proportional to the adiabatic ratio  $\omega_0/\Gamma$ .

It is important to point out that, when there is no intrinsic electron-oscillator coupling  $\lambda = 0$ , in the absence of the antenna effects and at zero bias ( $V_{bias} = 0$ ), the oscillator is still governed by a Langevin equation

$$m\ddot{x} + A^H(x)\dot{x} = kx + \sqrt{D^H(x)}\xi(t), \quad (3.51)$$

with a harmonic force  $F_{(0)}(x) = kx$ , an intrinsic positive-definite dissipative term  $A^H(x)$ , and a diffusive term  $D^H(x)$  proportional to the thermal current-current noise. Looking at Eqs. 3.42 and 3.49, one can clearly see that a natural quadratic dependence of damping and diffusive strength on the magnetic field emerges. This can be explained observing that, even at zero bias voltage, the electronic tunneling events, whose phase is dependent linearly on the CNT displacements as well as on the magnetic field strength, perturb the CNT mechanical motion with a force with zero average (due to  $\langle \hat{I} \rangle = 0$ ,  $\tilde{H}$  can be also different from zero) and square mean proportional to the magnetic field square. Definitely, even in the absence of external bias voltage  $V_{bias}$ , the magnetic field applied perpendicular to the CNT couples to the bending mode dynamics behaving as a surrounding thermal bath at leads temperature  $k_B T$ .

I end this section with a systematic study of the spatial dependence of the total force, the damping (see Fig.3.6) and diffusive terms (see Fig.3.7) as a function of the bias voltage as well as on the magnetic field.

As concerns the total force acting on the CNT resonator, I point out that, for the magnetic field strengths investigated in this Sec., the effective potential preserves its parabolic shape with a displaced minimum and renormalized curvature. For instance, when a left-to-right current flows through the device (see the sketch in Fig.3.4) in the presence of a

positive magnetic field (outgoing from the sketch reported in Fig.3.4), the CNT-resonator effective potential minimum is displaced towards positive displacements  $x$  with respect to the minimum set by the density-displacement interaction (see Panel (a-b) of Fig.3.5). In Fig.3.5, one can observe that, the minimum of the effective potential acting on the resonator depends linearly on the magnetic field strength. This comes from the linear dependence on the magnetic field of the Lorentz-like correction term to the force Eq.3.38. In particular, as shown in Panel(a) in Fig.3.5, in the low bias regime for the device (small compared to the broadening of the CNT level), the larger is the gate voltage, the smaller is the displacement of the potential minimum as a function of the external magnetic field with respect to the shift produced by the charge-displacement interaction on the CNT (whose position is indicated by a (black) square for  $V_g = 0$ , a (red) circle for  $V_g = 0.45$  ( $V_{bias} = 90\mu V$  in my units), and a (green) triangle  $V_g = 1.0$  ( $V_{bias} = 200\mu V$  in my units)). This can be explained observing that in the low conducting regime of the device the resonator is less effectively coupled with the electronic subsystem. In the large bias regime (Panel(b) of Fig.3.5), a smaller magnetic field is sufficient to displace the potential minimum of the same quantity produced by the sole charge-displacement interaction on the CNT. Again, the larger is the gate voltage, the smaller is the displacement of the potential minimum as a function of the external magnetic field with respect to the shift produced by the charge-displacement interaction on the CNT.

The renormalization of the effective potential curvature, that is of the resonance frequency of the resonator, will be discussed in subsection B of next section.

In this section, I limit myself to discuss the damping term  $A(x)$ , since for the diffusive term  $D(x)$ , unless explicitly stated, a similar analysis can be done. As shown above (see Eq.3.40), I can distinguish between three contributions to the friction affected by the oscillator: a *pure* electron-oscillator contribution  $A^\lambda(x)$ , depicted in Fig.3.6 with a solid (black) line, already discussed in Ref.[29, 123]; a damping contribution due to current-current fluctuations  $A^H(x)$ , depicted in Fig.3.6 with a dotted (blue) line; a mixed damping term due to current-density fluctuations (not positive definite), indicated by  $A^{\lambda H}(x)$  and depicted in Fig.3.6 with a short-dashed (red) line. The total damping  $A(x)$  is depicted with a dashed (pink) line. As one can observe in Panel(a), at low bias voltage, when the external magnetic field strength is smaller than electron-oscillator coupling  $\lambda$ , the damping contributions coming from the current-current  $A^H(x)$  and current-density  $A^{\lambda H}(x)$  fluctuations are negligible with respect to that generated by the *pure* electron-oscillator contribution  $A^\lambda(x)$ . In Panel (a),  $A^\lambda(x)$  and  $A^H(x)$  have a single peak structure centered at  $x - 2V_{gate}/\lambda \simeq 0$ , while  $A^{\lambda H}(x)$  is an odd symmetric function with respect to this point. I point out that these peculiar structures emerge only at larger values of magnetic field (Panels(b-c) of Fig.3.6). The total damping affecting the resonator is peaked at configurations where large density variations take place  $|x - 2V_{gate}/\lambda| < \hbar\Gamma/\lambda$ . Indeed, the density of the CNT level goes from a region  $x - 2V_{gate}/\lambda < -\hbar\Gamma/\lambda$  corresponding to almost completely filled states ( $\langle n \rangle \sim 1$ ) to a region  $x - 2V_{gate}/\lambda > \hbar\Gamma/\lambda$  corresponding to completely empty states ( $\langle \hat{n} \rangle \sim 0$ ). Definitely, the CNT level experiences an unit charge variation across the  $|x - 2V_{gate}/\lambda| < \hbar\Gamma/\lambda$  region[49, 139].

At large bias voltages applied (Panel (b)),  $A^\lambda(x)$  has two peaks centered at  $x - 2V_{gate}/\lambda \simeq eV_{bias}/2\lambda$  and  $x - 2V_{gate}/\lambda \simeq -eV_{bias}/2\lambda$ , respectively.  $A^H(x)$  shows the same behavior, while  $A^{\lambda H}(x)$  is an odd symmetric function with respect to these two points. As in Panel (a),  $A^H(x)$  and  $A^{\lambda H}(x)$  are negligible with respect to  $A^\lambda(x)$ . The total damping affecting the resonator is peaked at configurations where the CNT level experiences a half-unit charge variation across the  $|x - 2V_{gate}/\lambda \pm eV_{bias}/2\lambda| < \hbar\Gamma/\lambda$  regions[49, 139].

When the external magnetic field is turned on, an enhanced damping as well as as noise strength emerges with a quadratic dependence on the magnetic field intensity Eqs.3.40-3.46. In Panels(b-e) of Fig.3.6, one can observe that, as the dimensionless ratio  $B/\lambda$  is equal to one, the total damping affecting the resonator is only slightly perturbed by the application

of the magnetic field. At low bias,  $A(x)$  preserves its single peak structure with an enhanced strength (dashed (pink) curve in Panel (b) of Fig.3.6). At large bias, the strength of the two peaks becomes asymmetric, with an enhanced damping of the peak at  $x - 2V_{gate}/\lambda \simeq -eV_{bias}/2$ . This effect can be explained as follows: when a magnetic field is applied to the device, the resonator starts to feel even the variations of the electronic current flowing through the CNT as a function of the gate voltage (see Eq.3.38). These current variations are positive for  $x - 2V_{gate}/\lambda < 0$  and negative otherwise. At  $x - 2V_{gate}/\lambda \simeq -eV_{bias}/2$ , large negative variations of the electronic density and positive variations of the electronic current cooperate giving an enhanced damping.

I intend now to study the regime realized when the external magnetic field strength is larger than electron-oscillator coupling  $\lambda$ . In this case, the contribution to the damping coming from the current-current fluctuations  $A^H(x)$  are dominant with respect to those corresponding to density-density  $A^\lambda(x)$  and density-current  $A^{\lambda H}(x)$  fluctuations. In the low bias regime, the total damping term preserves its single peak structure which, due to the intrinsic asymmetry of the current-density term  $A^{\lambda H}(x)$ , is slightly distorted. For the same reason, in the large bias regime, the double dip structure of the total damping term is preserved with an enhanced asymmetry. In the large magnetic field regime, it is important to point out the particular spatial dependence of the noise strength  $D(x)$  (Panels (c-f) of Fig.3.7). Here, the noise contribution due to the current-current fluctuations ( $D^H(x)$ ) emerges with the characteristic double peak structure even at low bias regime (dotted (blue curve in Panel (c) of Fig.3.7)). Comparing the dashed (pink) curves in Panel (c) of Figs.3.6-3.7, one can observe that, even at low bias voltage, the application of a large magnetic field drive the CNT-resonator far out of equilibrium, breaking the validity of the Einstein relation  $D(x) = 2k_B T_{eff} A(x)$  with an effective temperature. Far from equilibrium, this relation is strictly valid only at very low bias voltages[29, 27].

In the next section, I study numerical results of the model concerning mechanical properties of CNT-resonator (resonance frequency and quality factor) as well as the electronic observables inherent to the transport problem (I-V characteristic).

### 3.5.3 Mechanical and electronic characteristics of the device

Given the assumption about the separation between the slow vibrational and fast electronic (tunneling) timescales, the problem of evaluating a generic observable (electronic or not) of the system reduces to the evaluation of that quantity for a fixed position  $x$  and velocity  $v$  of the oscillator, with the consequent averaging over the stationary probability distribution  $P(x, v)$ . From the solution of the Langevin equation Eq.3.35, one can determine the distribution  $P(x, v)$  which allows to calculate all the electronic observables  $O$ :

$$\langle O \rangle = \int dx dv P(x, v) O(x, v). \quad (3.52)$$

I analyze in the next section the effects of the magnetic field on the mechanical as well as electronic properties of the device.

#### Device Quality factors

One of the main results of Ref.[136] is the observation of a quadratic dependence of the device quality factor  $Q$  on external magnetic field strength. Within my model, as also stressed in the previous sections, such a quadratic dependence on  $B$  emerges naturally. In this Sec., in order to include back-actions effects of the out of equilibrium electronic bath on the resonator, I

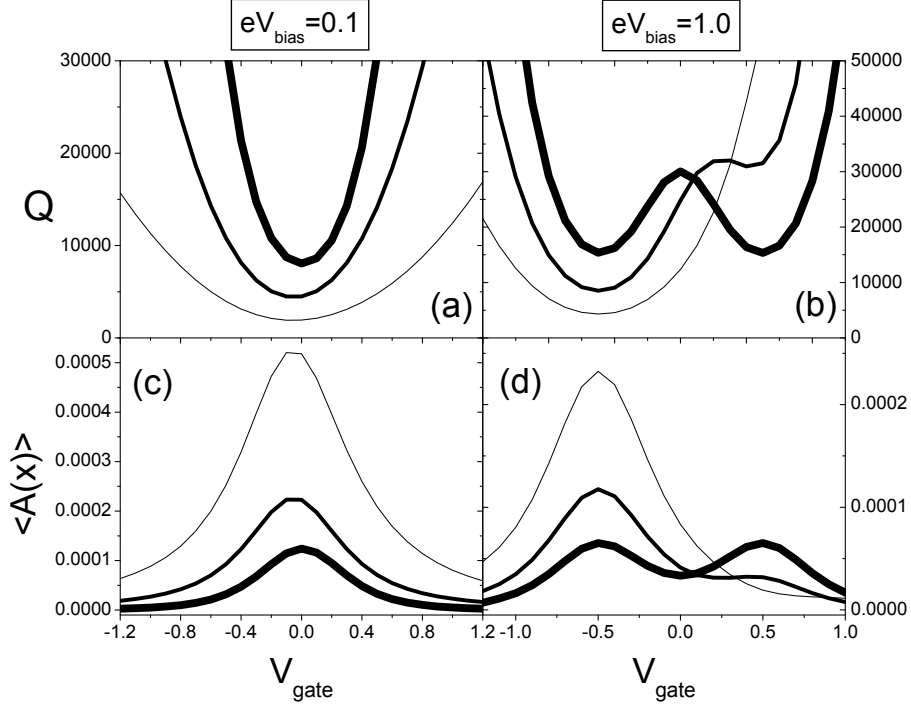


Figure 3.8: (Color online) Device quality factor as a function the gate voltage  $V_{gate}$  for different magnetic field strengths at low (Panel (a)) and large (Panel (b)) bias voltage. Panels(c-d) Same as above for the average total damping  $\langle A(x) \rangle$  of the system. Panel(a-c): solid thick line  $B = 0.0$ , solid normal-thickness line  $B = 1.5$ , and solid thin line  $B = 3.0$ . Panel(b-d): solid thick line  $B = 0.0$ , solid normal-thickness line  $B = 0.2$ , and solid thin line  $B = 0.4$ .

have calculated the average device quality factor as

$$Q = \int_{-\infty}^{\infty} dx \frac{1}{A(x)} P(x), \quad (3.53)$$

where  $A(x)$  is the total damping at a particular resonator displacement  $x$  and  $P(x)$  is the reduced displacement distribution probability of the CNT-resonator. I have verified that this particular way of extracting quality factors is completely equivalent to measure the width at half-high in the current-frequency curves obtained in the linear response to an external antenna exciting the nanotube motion[49].

Motivated by the experiment performed in Ref.[136] and by recent experimental study on a similar CNT device[139], I here performed a systematic study of the quality calculated from my model as a function of the bias, gate voltage as well as on the magnetic field. In Panels (a-b) of Fig.3.8, I investigate the device quality factor  $Q$  as a function of gate voltage in the low and large bias voltage regime, respectively. In the absence of a transverse magnetic field, I reproduce the qualitative behavior obtained in the experiment of Ref.[139]. When bias voltages are smaller than the broadening due to tunnel coupling, the quality factor shows a single dip as a function of gate voltage (solid (black) thick line in Panel (a) of Fig.3.8). At bias voltages that exceed (or are equal to) the broadening due to tunnel coupling, the quality factor shows a double dip structure (solid (black) thick line in Panel (b) of Fig.3.8). This behavior, already addressed in Refs. [49, 139], can be easily explained looking at the average charge and dissipation of the CNT-resonator through the system. As also discussed referring to total damping affecting the CNT-resonator in the previous

section, at low bias voltage and in the absence of magnetic field, the total average damping affecting the resonator is peaked at electronic configurations where the the CNT level experiences an unit charge variation across the region where the small conduction window is placed  $|V_{gate}| < \hbar\Gamma$  (solid (black) thick line in Panel (c) of Fig.3.8). At large bias voltages, the conduction window, whose extension is proportional to  $eV_{bias}$ , becomes larger than the broadening of the CNT level, so that the total average damping affecting the resonator is peaked at electronic configurations where the CNT level experiences a half-unit charge variation, that is at  $|V_{gate} - eV_{bias}/2| < \hbar\Gamma$  and  $|V_{gate} + eV_{bias}/2| < \hbar\Gamma$ . When the transverse magnetic field is turned on, the above scenario modifies as follows. At low bias voltages, the total damping affected by the CNT-resonator increases quadratically with the field at every point in the configuration space of the oscillator. Moreover, the CNT-resonator distribution probabilities  $P(x)$  depend slightly on the magnetic field as well as on the gate voltages and are actually centered at configurations close to the harmonic potential minimum  $x \simeq 0$  in the absence of electron-oscillator interaction. The overall result is an enhanced average total damping as one increases the magnetic field (solid normal ( $B = 1.5$ ) and thin ( $B = 3.0$ ) (black) lines in Panel (c) of Fig.3.8) and a corresponding decrease of the quality factor in all the gate voltage range investigated (solid normal ( $B = 1.5$ ) and thin ( $B = 3.0$ ) (black) lines in Panel (a) of Fig.3.8). At large bias voltage, the  $P(x)$  continues to depend only slightly on the magnetic field but now are very spread on the configuration space. Therefore, the average in Eq.3.53 reproduce the spatial dependence structure of the total damping coefficient reciprocal  $1/A(x)$ . The double peak structure of the average total damping term (solid thick (black) line in Panel (d) of Fig.3.8) is canceled by the magnetic field, giving a single peak at  $V_{gate} = eV_{bias}/2$  where a cooperation between negative density and positive current variations take place (solid normal ( $B = 0.2$ ) and thin ( $B = 0.4$ ) (black) lines in Panel (d) of Fig.3.8). As a consequence, the quality factor loses its double dip structure getting a single dip at  $V_{gate} = -eV_{bias}/2$  (solid normal ( $B = 0.2$ ) and thin ( $B = 0.4$ ) (black) lines in Panel (b) of Fig.3.8).

I intend now to study the device quality factors as a function of the transverse magnetic field  $B$  comparing different conducting states of the device. In Panel (a) of Fig.3.9, one can observe calculated device quality factors as a function of the magnetic field at a low conducting state of the device ( $V_{gate} = 0.45$ ). Different curves, from the thicker to the thinner, refer to increasing bias voltages applied to the device  $eV_{bias} = 0.1 - 0.75 - 1.5$ . At every fixed bias voltage, a clear quadratic dependence of the total average damping on the magnetic field strength is observed (not shown in Fig.3.9), with a Lorentzian shape of the quality factor curves (see Panel (a) of Fig.3.9). It is important to point out that the range of magnetic field strengths experimentally investigated in Ref.[136],  $B = 0 - 3T$ , corresponds to small magnetic fields in my units (I recall that  $H_0 = 16.6T$ ). Remarkably, at low bias and small magnetic fields, a quadratic decrease of the  $Q$  against magnetic field is observed (see solid thick (black) line in Panel (a) of Fig.3.9). In Fig.3.10, I show the quantitative agreement between experimental and calculated quality factors against magnetic field when the device is in a low conducting state, with  $eV_{bias} = 0.1$  and  $V_{gate} = -0.45$ . The slight increase of the quality factor  $Q$  as a function of the field for small magnetic fields, is due to asymmetry introduced by the gate voltage  $V_{gate} = 0.45$  applied to the device (see also Panel (a) of Fig.3.9). For gate voltage equal to zero, that in the high conducting state of the device, the calculated  $Q$  against  $B$  curve is a parabola with a maximum at zero magnetic field applied.

Coming back to Panel (a) of Fig.3.9, one can observe an interesting increase of the quality factor peak as a function of the bias voltage. In particular, for  $eV_{bias} = 1.5$  (thinner line in Panel (a) of Fig.3.9) a quality factor peak at  $B \simeq V_{gate}/2 = 0.225$  occurs. This can be directly related to the average total damping dip, not shown in Fig.3.9. This effect can be

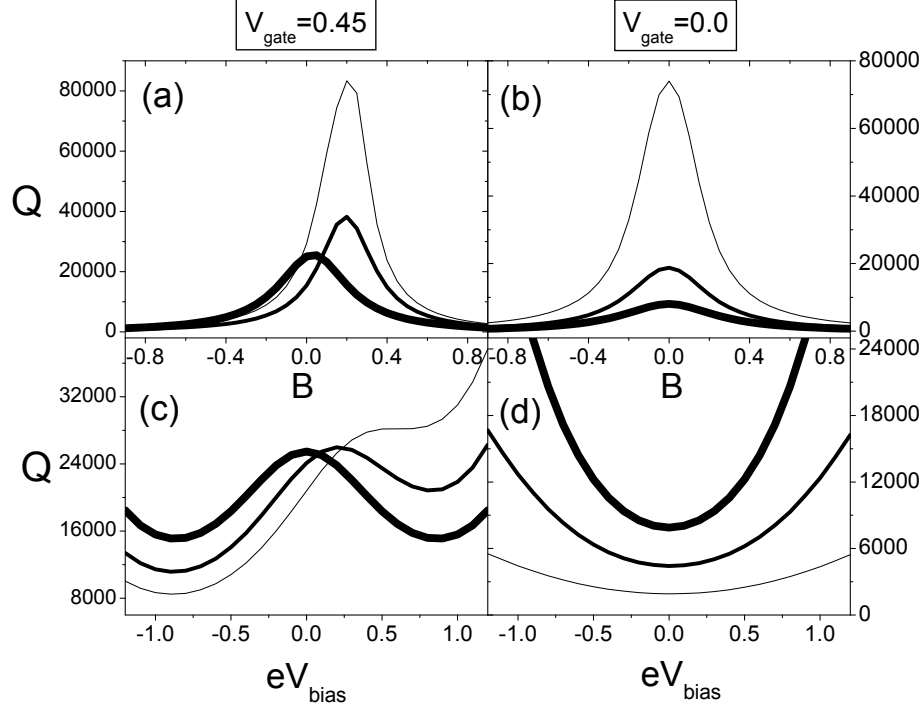


Figure 3.9: (Color online) Device quality factor as a function the magnetic field strength  $B$  for different bias voltages (Solid thick line  $eV_{bias} = 0.1$ , solid normal-thickness line  $eV_{bias} = 0.75$ , and solid thin line  $eV_{bias} = 1.5$ ) at low (Panel (a)) and high (Panel (b)) conducting states. Panels(c-d) Device quality factor as a function the bias voltage  $eV_{bias}$  for different magnetic field strengths at low (Panel (c)) and high (Panel (d)) conducting states. Panel(c): solid thick line  $B = 0.0$ , solid normal-thickness line  $B = 0.05$ , and solid thin line  $B = 0.1$ . Panel(d): solid thick line  $B = 0.0$ , solid normal-thickness line  $B = 0.25$ , and solid thin line  $B = 0.5$ .

explained noting that, when the bias voltage applied to the electronic device is increased, a transition from a single peak to a double peak structure in the *spatial* dependence total damping affected by the CNT-resonator can be observed (compare Panel(a) and (d) of Fig.3.6), while at the same time, the displacement distribution probabilities  $P(x)$  spread on the configuration space remaining centered at configurations close to the harmonic potential minimum  $x \simeq 0$  characteristic of the low bias regime. The overall result is a reduction of the average total damping affecting the CNT-resonator whose minimum is translated by a quantity proportional to the gate voltage applied to the device. This argument becomes even more clear when no gate voltage is applied to the device which is therefore placed in a high conducting state. In this case a perfect symmetry with respect to zero magnetic field is obtained (see Panel (b) of Fig.3.9).

I end this section with a study of the device quality factors as function of the bias voltages and magnetic fields comparing low and high conducting states of the device. In Panel (c) of Fig.3.9, one can observe calculated device quality factors as a function of the bias voltages at a low conducting state of the device ( $V_{gate} = 0.45$ ). Different curves, from the thicker to the thinner, refer to increasing magnetic field applied to the device  $B = 0.0 - 0.05 - 0.1$ . At zero magnetic field, a clear double dip feature in the quality factor  $Q$ , as experimentally observed in Ref.[139], is visible. This can be explained looking at the average total damping and in terms of the average charge in the CNT level. The total average



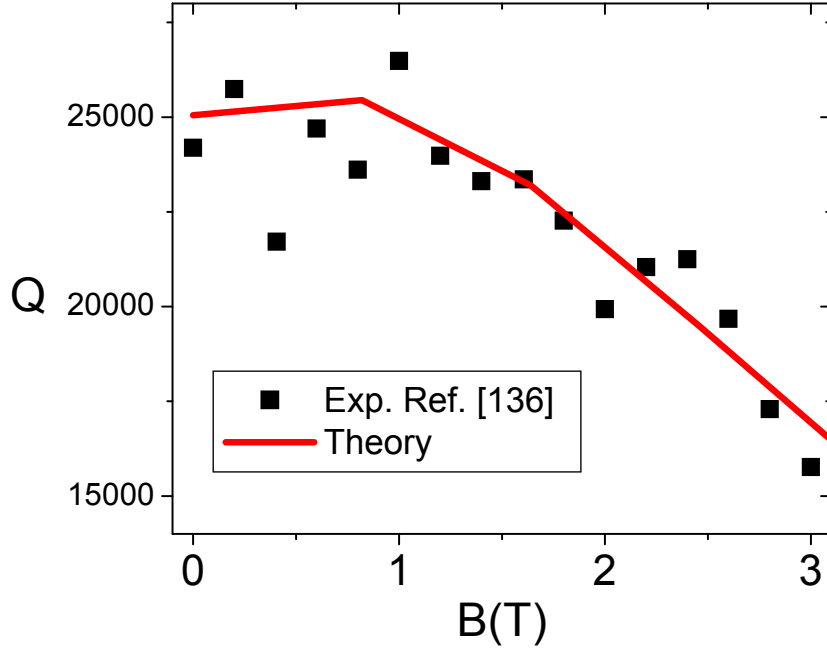


Figure 3.10: (Color online) Device quality factor as a function the magnetic field strength. Squares represent experimental values obtained in Ref.[136] at  $T = 25mK$ ,  $V_{bias} = 0.3mV$  and distance from the current peak  $V_{gate} = -90mV$ . Solid (red) line is calculated  $Q$  at  $k_B T = 0.01$ ,  $eV_{bias} = 0.1$  and  $V_{gate} = 0.45$ .

damping, in the absence of magnetic field, has two peaks at  $eV_{bias} = -2V_{gate} = -0.9$  and at  $eV_{bias} = 2V_{gate} = 0.9$ . Indeed, as also discussed previously, the total average damping is peaked at electronic configurations where the CNT level experiences a half-unit charge variation, that is at  $|V_{gate} - eV_{bias}/2| < \hbar\Gamma$  and  $|V_{gate} + eV_{bias}/2| < \hbar\Gamma$ . Therefore, when the edges of the conduction window (whose width is proportional to  $eV_{bias}$ ) meet the CNT level energy (given by  $V_{gate}$ ), a maximum total average damping (minimum quality factor) is observed. As also discussed in reference of Fig.3.8, the double peak structure of the average total damping term is canceled by the magnetic field, giving a single peak at  $eV_{bias} = -2V_{gate}$  where a cooperation between negative density and positive current variations take place. As a consequence, the quality factor loses its double dip structure getting a single dip at  $eV_{bias} = -2V_{gate}$  (solid normal ( $B = 0.05$ ) and thin ( $B = 0.1$ ) (black) lines in Panel (c) of Fig.3.9).

In Panel (d) of Fig.3.9, I show calculated device quality factors as a function of the bias voltages at a high conducting state of the device ( $V_{gate} = 0.0$ ). Different curves, from the thicker to the thinner, refer to increasing magnetic field applied to the device  $B = 0.0 - 0.25 - 0.5$ . As above, at zero magnetic field, a single dip feature in the quality factor  $Q$ , as experimentally observed in Ref.[139], is visible. This behavior can be discussed with the same argument given for discussing the Panels(a-b) of Fig.3.9, where a reduction of the total average damping as a function of the bias voltage applied to the device was observed. Again, a decrease of the quality factor in all the gate voltage range investigated as a function of the magnetic field is observed (see Panel (d) of Fig.3.9).

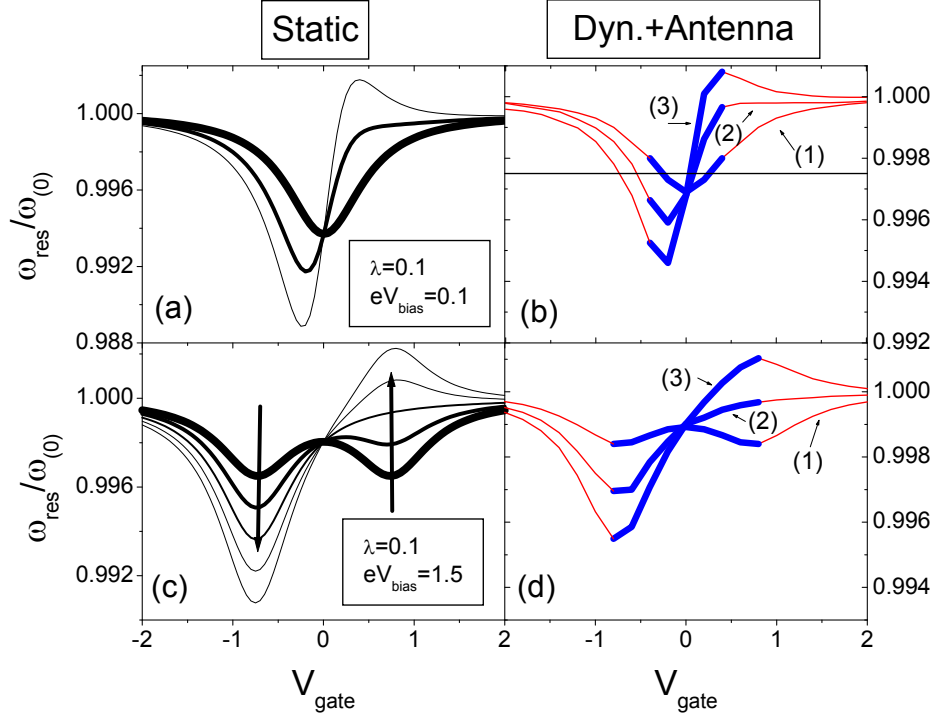


Figure 3.11: (Color online) Panel (a): Resonator frequency against effective gate voltage calculated as minimum of the effective potential in the static approximation at small bias  $eV_{bias} = 0.1\hbar\Gamma$  for different magnetic field values: Solid thick line  $B = 0.0$ , solid normal line  $B = 1.5$ , solid thin line  $B = 3.0$ . Panel (c): same as Panel (a) at large bias  $eV_{bias} = 1.5\hbar\Gamma$  for different magnetic field values: From thicker to thinner line  $B = 0.0 - 0.1 - 0.2 - 0.3 - 0.4$ . Panel (b-d): Resonator frequency calculated using an external antenna (with  $A_{ext} = 10^{-3}$ ) at mechanical resonance against effective gate voltage for same parameters of Panel (a-c), respectively. Dashed (red online) and solid (blue online) portions of each curve indicate resonance frequency values with positive and negative current change  $\Delta I$ , respectively. In Panel (d), only curves referring to magnetic field strengths  $B = 0.0 - 0.2 - 0.4$  are reported.

### Resonance frequency renormalization and current-voltage curves

In this section, I address the magnetic field effects on the renormalization of the CNT-resonator resonance frequencies and its back-action effects on the current voltages curves of the device. In order to study the CNT resonance frequency renormalization as function of the gate voltage, I have compared results coming from two ways of evaluation of the resonance frequencies. In the first method, referred to as *Static*, I evaluate the position of the minima of the static potential arising from the generalized force acting on the resonator (Eq.3.38). In the second method, referred to as *Dynamic+antenna*, I have analyzed, at every fixed value of the gate voltage, all the traces of electronic current as a function of the antenna frequency reporting with a red (blue) dot the resonance frequency values with positive (negative) current change  $\Delta I = I - I_0$  with respect to background value  $I_0$  obtained in the absence of the antenna.

In Fig.3.11, I report the resonance frequencies of the CNT-resonator as a function of the electronic gate voltage comparing the two methods outlined above. I address the low bias regime in Panels (a-b), while the large bias regime is investigated in Panels(c-d). In Panel (a) of Fig.3.11, different curves, from the thicker to the thinner, refer to increasing magnetic field applied to the device  $B = 0.0 - 1.5 - 3.0$ . The same description was done in Panel (c),

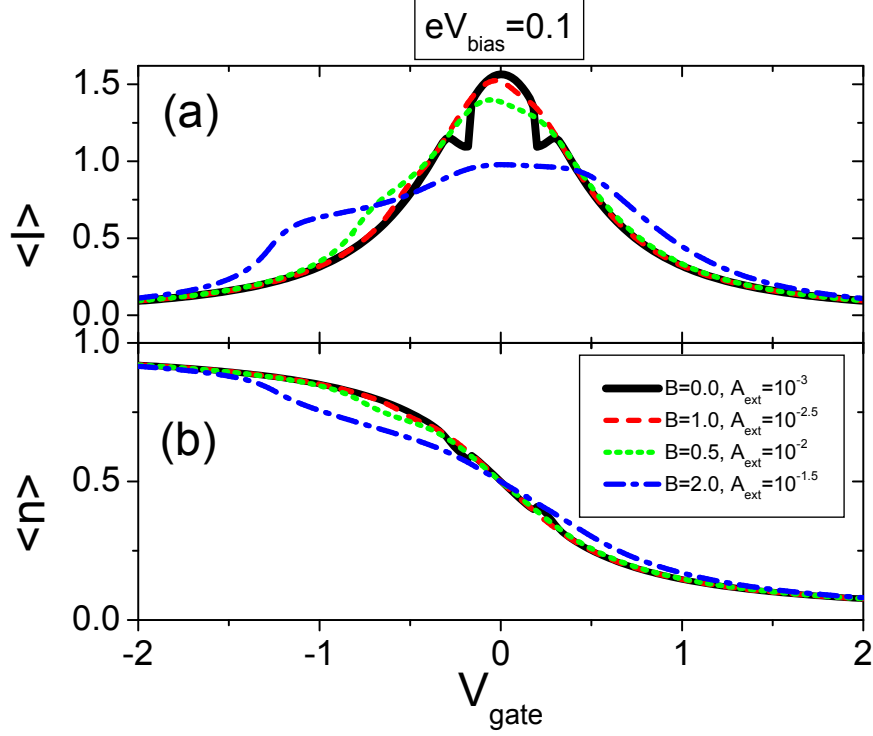


Figure 3.12: (Color online) Panel (a) Average electronic current flowing through the CNT level at low bias ( $eV_{\text{bias}} = 0.1$ ) as function of the gate voltage for different values of the magnetic field and in the presence of a external antenna applied to the device at fixed frequency  $\omega_{\text{ext}} = 0.9975$  and amplitude: solid (black) line  $A_{\text{ext}} = 10^{-3}$ , (dashed (red) line  $B = 1.0$   $A_{\text{ext}} = 10^{-2.5}$ , dotted (green) line  $B = 1.5$   $A_{\text{ext}} = 10^{-2.0}$ , dashed-dotted (blue) line  $B = 1.0$   $A_{\text{ext}} = 10^{-2.5}$ ). Panel (b) Average electronic density on the CNT level for the same parameter values as in Panel(a). See the main text for detailed discussion.

where different curves refer to increasing magnetic field in the range  $B = 0.0 - 0.2 - 0.4$ . The thicker (black) lines in Panels (a) and (c), corresponding to the absence of magnetic field, reproduce qualitatively all results experimentally observed[139] on a similar CNT-resonator device: when bias voltages are smaller than the broadening due to tunnel coupling (Panel (a)), the resonance frequency shows a single dip as a function of gate voltage. At bias voltages that exceed the broadening due to tunnel coupling (Panel (c)), the resonance frequency shows a double dip structure. Actually, in this regime, the onset of a double dip structure was already predicted by us in Ref.[49]. It is important to point out that the resonance frequency renormalization curves obtained in the presence of the external antenna (Panel (b-d) of Fig.3.11) have the same qualitative behavior (as a function of the gate) of those obtained in the static approach. In the presence of an external antenna with a finite amplitude, renormalization effects in the resonance frequencies are less pronounced due to nonlinear softening[11, 49].

As already analyzed in Ref.[11, 49], when the device is in a low current-carrying state, a peak in the current-frequency curve signals the mechanical resonance (whose position is indicated by thin (red) lines in Panels (b-d) of Fig.3.11), while in a high current-carrying state, a dip in the current-frequency curves is observed (whose position is indicated by thick (blue) lines in Panels (b-d) of Fig.3.11). In the presence of a transverse magnetic field, the different character of low and high conducting states, signaled by a peak or a dip in current-frequency curves is preserved (curves (2) and (3) in Panels (b-d) of Fig.3.11).

The peculiar features of CNT-resonator frequency renormalization as a function of the gate can be explained with the same argument used to describe the quality factors behavior in the previous section. Indeed, in the absence of magnetic field, the resonator frequency renormalization is maximum at electronic configurations where the the CNT level experiences the largest density variations against the gate voltage,

$$k_{eff} = k + \lambda \left. \frac{\partial \langle \hat{n} \rangle}{\partial V_{gate}} \right|_{x=x_{min}}. \quad (3.54)$$

Actually, at low bias voltages, an unit charge density variation across the region where the small conduction window is placed  $|V_{gate}| < \hbar\Gamma$  (solid (black) thick line in Panel (a) of Fig.3.11) occurs. At large bias voltages, the CNT frequency renormalization is larger at electronic configurations where the CNT level experiences a half-unit charge variation, that is at  $|V_{gate} - eV_{bias}/2| < \hbar\Gamma$  and at  $|V_{gate} + eV_{bias}/2| < \hbar\Gamma$ .

When the transverse magnetic field is turned on, the above scenario modifies as follows. The resonator frequency renormalization is larger at electronic configurations where the CNT level experiences the largest density *and* current variations against the gate voltage,

$$k_{eff} = k + \lambda \left. \frac{\partial \langle \hat{n} \rangle}{\partial V_{gate}} \right|_{x=x_{min}} - \lambda \tilde{H} \left. \frac{\partial \langle \hat{I} \rangle}{\partial V_{gate}} \right|_{x=x_{min}}. \quad (3.55)$$

At low bias voltage, the single dip feature in the CNT-resonator resonance frequency gets distorted (solid normal-thickness line in Panel(a) of Fig.3.11) and acquires, in the limit of large magnetic field (solid thin line in Panel(a) of Fig.3.11), a dip-peak structure that could be experimentally observed. Actually, the peak observed at  $V_{gate} \simeq 0.3$  corresponds to an hardening of the CNT-resonator resonance frequency. This effect can be explained as follows: when a magnetic field is applied to the device, the resonator starts to feel even the variations of the electronic current flowing through the CNT as a function of the gate voltage (see Eq.3.55). These current variations are positive for  $V_{gate} < 0$  and negative otherwise. At  $V_{gate} \simeq 0.3$ , the positive (due to the positive sign of the magnetic field) variations of the electronic current overcome the negative variation of the electronic density giving a hardening in the CNT resonance frequency. At  $V_{gate} \simeq -0.25$ , one has negative variations of both density and current, obtaining a more pronounced softening in the resonance frequency. The effect outlined above is more pronounced in the large bias regime (see Panel (c) of Fig.3.11). Here, the magnetic field gives an enhanced softening dip at  $V_{gate} \simeq -eV_{bias}/2$  and an hardening peak at  $V_{gate} \simeq eV_{bias}/2$ , where positive variations of the electronic current cooperate with negative variation of the electronic density. In both low and high bias regime, the hardening effect outlined above could be experimentally observed.

The peculiar renormalization frequency effects discussed above have a nontrivial back-action effects on the electronic density and current-gate voltage characteristic of the device. In Fig.3.12, I study the electronic CNT level density and current as a function of the gate voltage in the presence of an external antenna at fixed amplitude and frequency  $\omega_{ext} = 0.9975$  (corresponding to the horizontal line in Panel (b) of Fig.3.11) in the low bias regime of the device<sup>6</sup>. When the external antenna frequency becomes equal to the proper frequency

---

<sup>6</sup>In the large bias regime, features of different origin of those investigated in this thesis can appear in the current-voltages characteristic of the device. These switching effects are experimentally observed in dc-current through the device investigated in Ref.[136], and have been identified as nano-electromechanical self-excitations of the system, where positive feedback from single electron tunneling drives mechanical motion. These features, smeared by the external magnetic field, were predicted by a model introduced in Ref. [126, 127] where energy dependence of electronic tunneling amplitudes was also considered.

of the resonator, I observe a dip structure in both density and current at a gate voltage corresponding to high conducting states of the device (solid (black) line in Panels (a-b) of Fig.3.12). This feature, that could be experimentally observed, is considered as a "dip" with respect to corresponding curves in the absence of antenna or with an antenna frequency far from the range of the proper frequencies of the CNT-resonator (not shown in Fig.3.12).

When a transverse magnetic field is applied to the device, the CNT frequency renormalization profile as a function of the gate voltage changes (see Fig.3.11). Therefore, the mechanical resonance condition between the external antenna frequency and the proper frequency of the resonator occurs at different electronic gate voltages. For sufficiently large magnetic fields, the resonance can occur in correspondence of a low conducting state of the device. As one can observe in Panels (a-b) of Fig.3.12, a dip structure in the electronic density at a more negative gate voltage and corresponding current peak (dotted (green) and dashed-dotted (blue) lines in Panel (a-b) of Fig.3.12) is visible. Actually, the above structures are broadened due the reduction of the quality factor as a function of the magnetic field. In the limit of very large magnetic fields, if I keep fixed the amplitude of the external antenna, the fine structures outlined above are completely washed out due to the decrease of the device quality factors.

### 3.5.4 Discussion

In conclusion, I have studied a CNT-based electronic transistor in the presence of an external magnetic field perpendicular to the current flux[50]. I was able to show that the application of a transverse magnetic field modifies the bending mode CNT dynamics giving an enhanced damping as well as a noise term originating from the electronic phase fluctuations induced by the displacements of CNT itself.

The effective force acting on the resonator is modified by a pure nonequilibrium correction term proportional to the magnetic field as well as to the electronic current flowing through the CNT. Even at zero bias voltage, damping and diffusive terms are both modified by quantum electronic current-current as well as density-current fluctuations corrections whose strengths are quadratic and linear in the magnetic field, respectively.

Within my model, a quadratic dependence of the device quality factor  $Q$  on external magnetic field strength, experimentally observed in Ref.[136], emerges naturally. This behavior is understood in terms of a back-action of quantum electronic current flow fluctuations on the bending mode dynamics. A systematic study of device quality factor as a function of gate and bias voltage in the presence of the magnetic field has also been performed. All results are discussed observing the average charge and electronic current variations with respect to gate voltage applied to the device and can be summarized as follows. At a fixed electronic conducting regime, if negative charge variations and positive current variations occur, one has an enhanced damping reducing the quality factor of the device. Vice-versa, negative charge variations and negative current variations reduce damping with a consequent increase of quality factors.

I also show that, when the device is driven far from equilibrium, one can tune CNT-resonator frequencies by varying the external magnetic field: the peculiar (single or double dip) features in the CNT-resonator resonance frequency, obtained in different conducting regimes for the device, get distorted and acquire, in the limit of large magnetic field, a peculiar dip-peak structure that could be experimentally observed.

Finally, when the device is actuated by an external antenna at fixed frequency and amplitude, the device current-gate voltage response is modified by fine structure features any time the mechanical resonance with the proper nanotube oscillation frequency occurs. These structures can be tuned as a function of the external field and could be experimentally

observed. In this sense, I have shown that, only exciting the CNT motion with application of an external rf-antenna, one can observe a magnetic field dependence of the electronic current.

I point out that throughout this Chap. I do not take into account of a magnetic field with a component longitudinal to the CNT-resonator. This issue has been recently addressed in Ref.[139] and explained in terms of a more sophisticated theoretical schematization of the CNT-resonator electronic structure which has a cylindrical quasi-one dimensional shape.

I end this section noting that it could be of outstanding interest to study the possibility to include quantum corrections as well as electron-electron interaction effects to the oscillator dynamics in the low bias regime. These corrections becomes important when the resonator and electronic time scales are of the same order on magnitude. In this direction, it was shown in Ref.[148] that a magnetic field applied perpendicular to the CNT results in negative magnetoconductance due to quantum vibrations of the tube inducing an Aharonov-Bohm-like effect on the electrons crossing the device. Work in this direction is in progress.

# Chapter 4

## Electronic transport through a strongly correlated molecular junction: coupling with a high frequency vibrational mode

### 4.1 Introduction

In recent years there has been an increasing interest in the study of transport phenomena in nanoscale systems motivated by their potential as electronic devices. Due to their small size, electronic correlations are dominant and lead to interesting many-body effects, such as the Coulomb blockade and Kondo resonance[154]. These effects have been observed experimentally in transport experiments through molecular conductors [19, 63] and other nanostructures[55]. Another interesting property of molecules is their flexible nature. They have an intrinsic spectrum of internal vibrational modes and, when coupled to the electrodes, molecules acquire "external" vibrational modes as well. An important example is the center of mass motion of the molecule coupled between the two leads. The excitation of this mode can modulate the electronic energy levels and tunneling barriers between the electrodes and the molecule itself, thus changing the molecular transport properties. For example, the effects of the interaction between electron tunneling and the center of mass motion of the whole molecule have been observed in a number of recent transport experiments[19, 63, 62, 58] and have been the subject of considerable theoretical investigation[155, 156, 157, 158, 159]. In a different way, studying the interplay of mechanical motion and electronic conduction in nanoscale systems establishes a strong link to the physics of Nanomechanical shuttling systems (NMSS) and NEMS. The shuttle devices are a particular kind of NEMS. The characteristic component that gives the name to these devices is an oscillating object of nanometer size (molecule) that transfers electrons one-by-one between a source and a drain lead.

In this Chap., I want to address the transport properties of a nanomechanical shuttling system in the low temperature low bias regime where a strong interplay between the Kondo physics and vibrational degrees of freedom is expected [156, 159]. Indeed, as already emphasized in Chap. 1, there are contrasting experimental results in this regime: Park et al.[19] performed measurements in  $Au - C_{60} - Au$  junctions where the conductance at low bias was found to be largely suppressed and the current-voltage characteristics were dominated by the Coulomb blockade phenomenon. A related transport experiment through a single  $C_{60}$  molecule[63] showed a much higher low-bias conductance (of the order of  $0.1G_0$

with  $G_0 = e^2/h$ ), which was attributed to the appearance of Kondo physics.

I believe that for the interpretation of the experimental results a better understanding of the interaction effects of the center of mass motion of the molecule onto the electronic hopping by means of a simple theoretical model is necessary.<sup>1</sup>

In the following, I numerically investigate with Density Matrix Renormalization Group (DMRG) the electronic transport properties of a nanomechanical shuttling device in the Kondo regime. I model the system by means of the Anderson impurity model with noninteracting (tight-binding) leads. The molecule (impurity site of the chain) is allowed to oscillate between the two metallic contacts. I focus on the effects of tunneling barrier modulation (encoded in the coupling constant  $\alpha$ ) on the electronic conductance and on the static and dynamical properties of the phononic mode.

I use an alternative method for calculating the conductance through nanoscopic correlated systems based on the calculation of the persistent current of a fictitious auxiliary system threaded by a magnetic flux.[160, 161] As shown in Ref. [162], a DMRG calculation of the ground state energy of this auxiliary system turns out sufficient for calculate the conductance in linear response. A *dip* in the electronic conductance at the particle-hole symmetric point for a finite value of  $\alpha$  is obtained. This result is different from that obtained in the literature[156] where the same dip was found for any value of  $\alpha$  different from zero. K. A. Al-Hassanieh *et al.*[156] justify the *dip* as due to the destructive interference between the purely electronic and phonon-assisted tunneling channels, which are found to carry opposite phases. In [156], conductance is calculated by means of Green functions, within Keldysh formalism, using exact diagonalization supplemented by a Dyson equation embedding procedure (ED + DE)[163]. The cancellation effect cited above is also found by other authors using different numerical techniques.[159] I justify the presence of the dip for a finite  $\alpha$  value by means of a Jahn-Teller distortion, where a natural breaking of the inversion symmetry is obtained. The distribution probability of the phononic mode in real space becomes bimodal for  $\alpha$  equal to the critical value, even if it retains its symmetry with respect to zero displacement configuration. Correspondingly, the average quadratic displacement increases up to the limit physical value  $t'/\alpha$  where the effective hopping between the molecule and one of the leads is equal to zero, giving the conductance cancellation and in particular no current flow through the device. In order to assess even-odd effects, I have further verified that the physical properties of the system (for finite system size) don't depend on the total number of sites of the chain,  $L_{tot}$ , if this quantity is sufficiently large.

## 4.2 Hamiltonian of a Quantum Shuttle

The physical system analyzed in this Chap. is schematically depicted in Figure 4.1. The center-of-mass (c.m.) vibrational mode is treated quantum mechanically and leads to an asymmetric modulation of the molecule-leads tunneling barriers. The vibrational excitation is also coupled to the excess charge on the molecule (Holstein interaction). In fact, an important feature of molecules is that they generally distort upon the addition or the removal of electrons. Moreover, the molecule-electrode bonds can depend in general on the molecule's charge and on the molecule-electrode distance. The electronic part of the system is modeled using the Anderson impurity Hamiltonian. The total Hamiltonian can be written as

$$\hat{H} = \hat{H}_M + \hat{H}_{leads} + \hat{H}_{M-leads}, \quad (4.1)$$

---

<sup>1</sup>The molecular internal vibrational modes have been proposed to account for the side peaks in the nonlinear conductance. Indeed, in Ref. [63], the authors were also able to tune finite-bias Kondo features which appear at the energy of the first  $C_{60}$  intracage vibrational mode (see Fig. 1.15 of Chap. 1).



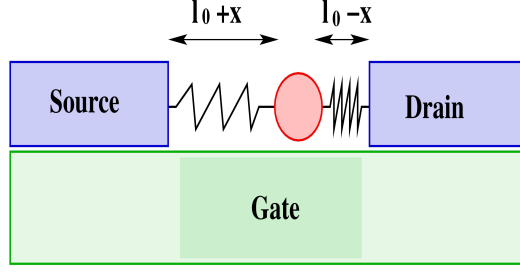


Figure 4.1: A schematic of the system studied in this Chap.. The molecule can oscillate between the two leads, thus modulating the tunneling barriers.

where  $\hat{H}_M$  is the Hamiltonian of the molecule,

$$\hat{H}_M = V_G \hat{n}_d + U \hat{n}_{d\uparrow} \hat{n}_{d\downarrow} + \lambda(1 - \hat{n}_d)(\hat{a} + \hat{a}^\dagger) + \omega_0 \hat{a}^\dagger \hat{a}. \quad (4.2)$$

In the above Hamiltonian, the first term represents the energy of the relevant molecular orbital controlled by the gate voltage  $V_G$ , the second term represents the Coulomb repulsion between the electrons of opposite spins occupying the molecular orbital, the third term couples the vibrational excitation to the net charge on the molecule ( $\hat{a}$  and  $\hat{a}^\dagger$  are the phonon operators) and the fourth term represents the vibrational energy.  $\hat{H}_{leads}$  describes the two leads, modeled here as semi-infinite ideal chains

$$\hat{H}_{leads} = -t \sum_{\sigma, i=1}^{+\infty} \left[ \hat{c}_{L,i,\sigma}^\dagger \hat{c}_{L,i+1,\sigma} + \hat{c}_{R,i,\sigma}^\dagger \hat{c}_{R,i+1,\sigma} + h.c. \right], \quad (4.3)$$

where  $\hat{c}_{Li\sigma}^\dagger$  ( $\hat{c}_{Ri\sigma}^\dagger$ ) creates an electron with spin  $\sigma$  at site  $i$  in the left (right) lead and  $t$  is the hopping amplitude.  $\hat{H}_{M-leads}$  connects the molecule to the leads,

$$\hat{H}_{M-leads} = -t'[1 - \alpha(\hat{a} + \hat{a}^\dagger)] \sum_{\sigma} (\hat{d}_{\sigma}^\dagger \hat{c}_{L,1,\sigma} + h.c.) - t'[1 + \alpha(\hat{a} + \hat{a}^\dagger)] \sum_{\sigma} (\hat{d}_{\sigma}^\dagger \hat{c}_{R,1,\sigma} + h.c.). \quad (4.4)$$

where  $\hat{d}_{\sigma}^\dagger$  creates an electron with spin  $\sigma$  in the molecule,  $t'$  is the hopping parameter between the molecule and the first site of each lead, and  $\alpha$  is a parameter that carries the dependence of  $t'$  on the molecule displacement  $\hat{x}$  from its equilibrium position (note the opposite signs in this dependence for the two leads). This displacement can be written in terms of the phonon operators as  $\hat{x} = \hat{a} + \hat{a}^\dagger$ . For future convenience, it is useful to split the above Hamiltonian term  $\hat{H}_{M-leads}$  in two parts: one independent and the other dependent on the shuttle interaction  $\alpha$

$$\hat{H}_{M-leads}^D = -t' \sum_{\sigma} (\hat{d}_{\sigma}^\dagger \hat{c}_{L,1,\sigma} + h.c.) - t' \sum_{\sigma} (\hat{d}_{\sigma}^\dagger \hat{c}_{R,1,\sigma} + h.c.), \quad (4.5)$$

$$\hat{H}_{M-leads}^\alpha = t' \alpha (\hat{a} + \hat{a}^\dagger) \sum_{\sigma} (\hat{d}_{\sigma}^\dagger \hat{c}_{L,1,\sigma} + h.c.) - t' \alpha (\hat{a} + \hat{a}^\dagger) \sum_{\sigma} (\hat{d}_{\sigma}^\dagger \hat{c}_{R,1,\sigma} + h.c.), \quad (4.6)$$

representing the tunneling terms not assisted ( $H_{M-leads}^D$ , ‘‘direct’’ channel) and assisted ( $H_{M-leads}^\alpha$ , ‘‘phonon’’ channel) by emission or absorption of phonons.

If both  $\lambda = 0$  and  $\alpha = 0$ , the full Hamiltonian  $\hat{H}$  is symmetric with respect to particle-hole (p-h) transformation with  $V_G = -U/2$ , while in the general case with  $\lambda$  and  $\alpha$  different from zero, the Hamiltonian is symmetric with respect to p-h and space inversion ( $\hat{x} \rightarrow -\hat{x}$ ).

### 4.3 Alternative method for calculating conductance through a region with interaction

In this chapter I employ an alternative method for calculating the conductance through nanoscopic correlated systems. The method is applicable only to a certain class of systems, namely to those exhibiting Fermi liquid properties, at zero temperature and in the linear response regime. However, even if its quite restrictive domain of validity, I will see that the method is easier to use than the methods based on the calculation of the impurity Green’s function (Kubo [79] and Keldysh [81] formalism). I can summarize this new approach as follows: as shown by Rejec *et al.*, [160] one can obtain analytically the conductance of a non interacting region by calculating the ground-state energy of an auxiliary system, formed by connecting the leads of the original system into a ring which is threaded by a magnetic flux  $\phi$ . The persistent electronic current flowing through the system  $I = -\frac{e}{h} \frac{\partial E(\phi)}{\partial \phi}$  obtained in this way is proportional to the conductance in the limit of very large systems. This method has been verified only numerically for interacting central regions by comparing with respect to numerically exact results.[160, 161] The main advantage of this new approach is the fact that it is often much easier to calculate the ground-state energy for example, using variational methods than the Green’s function, which is needed in the Kubo and Keldysh approaches. Moreover, from a numerical point of view, Quantum Monte Carlo[167] and Numerical Renormalization Group (NRG)[168] cannot be applied to the case of a (complex) magnetic flux threading the ring, making highly desirable to count with a reliable numerical technique to treat this problem. As shown in Ref.[162], the density matrix renormalization group (DMRG) method could overcome these limitations. However, its efficiency with periodic boundary conditions (PBC) is undermined by the structure of the quantum entanglement in a ring geometry, and its application has been limited to the case of spinless fermions,[161] or to small rings. In order to overcome this difficulty, I revisit a well known canonical transformation that was originally introduced in the context of quantum impurity problems,[169] and referred to as a ‘‘folding’’ transformation,[170] mapping a Hamiltonian with periodic boundary conditions onto an equivalent model with open boundary conditions. This has two important implications: (i) it reduces the entanglement by half, allowing for a more efficient representation in terms of Matrix Product State[171] and (ii) the OBC enable the DMRG algorithm to simulate the problem optimally.

Therefore, in order to calculate the conductance of a system Hamiltonian with OBC, I calculate the persistent current of an auxiliary system with PBC (just ground state calculation with DMRG). In order to reduce the entanglement afflicting DMRG applied to a system with PBC, the ring is further ‘‘folded’’ in a system with OBC.

#### 4.3.1 Folding Transformation: ‘‘even’’ and ‘‘odd’’ cases

Let’s apply to the total Hamiltonian  $\hat{H}$  of my model the folding transformation described above. I introduce a symmetric (+) and antisymmetric (−) combination of operators acting on the left and right leads. This is nothing else but an application of the reflection symmetry,

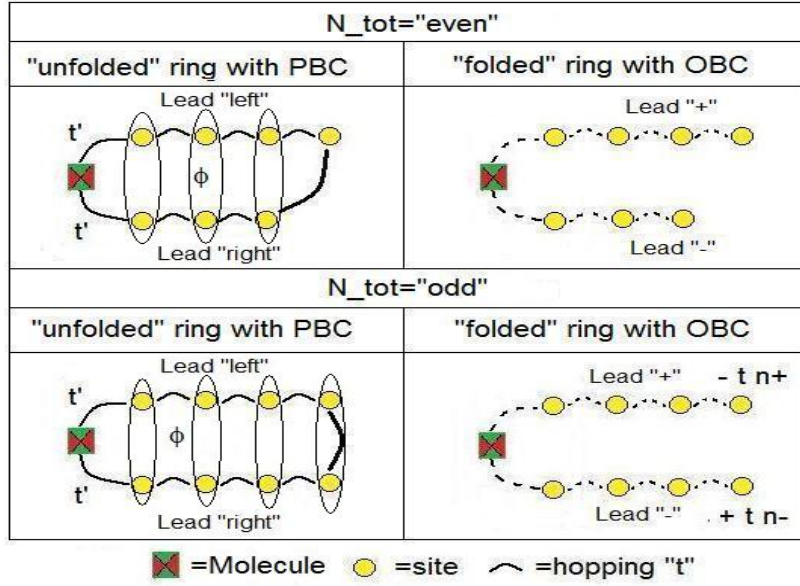


Figure 4.2: A schematic illustration of the folding transformation applied to the  $N_{tot} = \text{"even"}$  and  $N_{tot} = \text{"odd"}$  cases.

yielding new even(+) and odd(-) operators

$$c_{\pm,j,\sigma} = \frac{1}{\sqrt{2}}(c_{L,j,\sigma} \pm c_{R,j,\sigma}). \quad (4.7)$$

I assume that the left and right leads have a finite length  $L_{left}$  and  $L_{right}$ , respectively. Obviously, the total length of the chain is given by  $L_{tot} = L_{left} + L_{right} + 1$ . It is well known that in the Anderson Impurity model with tight binding leads the physical properties of the system for finite system size are different if the total number of sites of the chain  $L_{tot}$  (sum of the number of sites of each lead plus the molecular site) is even or odd. This is easily understood at half-filling and in the case where the Holstein interaction  $\lambda$  and the shuttle interaction coupling constant  $\alpha$  are zero. In fact, if  $L_{tot}$  is even, in the ground state of the system the total spin of the *odd* electrons in the leads ( $S_{tot} = 1/2$ ) screen the spin of the electron of the molecule ( $S_{mol} = 1/2$ ) and one obtains the standard Kondo physics. Otherwise, if  $L_{tot}$  is odd, the previous description is not applicable anymore (the total spin of the *even* electrons in the leads is integer). Anyway, I expect that in thermodynamical limit ( $L_{tot} \rightarrow \infty$ ) the physical properties of the model should be independent on  $L_{tot}$  showing the standard Kondo effect.

The folding transformation is schematically shown in both cases in Figure 4.2. The effect of a magnetic flux  $\phi$  threading the ring is introduced by adding a phase in the hopping matrix element  $t \rightarrow te^{-i\phi/L_{tot}}$  of all the links of the ring. By performing a gauge transformation on the fermionic operators, one has the freedom to move the phase to any link along the ring. In particular, I'm going to move it in between the first site of each lead and the molecular site. The new, transformed Hamiltonians of the ``direct`` and `` $\alpha$ `` channel coupling the leads to the molecular site will now read

$$\hat{H}'_{M-leads}{}^D = -\sqrt{2}t' \cos(\phi) \sum_{\sigma} (\hat{d}_{\sigma}^{\dagger} \hat{c}_{+,1,\sigma} + h.c.) + i\sqrt{2}t' \sin(\phi) \sum_{\sigma} (\hat{d}_{\sigma}^{\dagger} \hat{c}_{-,1,\sigma} + h.c.), \quad (4.8)$$

$$\begin{aligned} \hat{H}'_{M-leads}{}^{\alpha} &= -i\sqrt{2}t' \sin(\phi) \alpha (\hat{a} + \hat{a}^{\dagger}) \sum_{\sigma} (\hat{d}_{\sigma}^{\dagger} \hat{c}_{+,1,\sigma} + h.c.) \\ &+ \sqrt{2}t' \cos(\phi) \alpha (\hat{a} + \hat{a}^{\dagger}) \sum_{\sigma} (\hat{d}_{\sigma}^{\dagger} \hat{c}_{-,1,\sigma} + h.c.). \end{aligned} \quad (4.9)$$

As one can observe in the upper and lower left panel of Fig. 4.2, the folding transformation is applied between couples the sites of the same numeration of the left and right lead. For example, in the  $L_{tot}$  ``even`` case, the transformation is applied to all couples of sites up to the second last of the ``left`` lead coupled with the last site of the ``right`` lead. In this way, one can fold the ring cutting the link joining the last sites of each lead obtaining a renormalized link with hopping  $\sqrt{2}t$  between the last and the second last site of the ``+`` lead

$$\hat{H}'_{Leads, L_{left}, L_{left}-1} = -\sqrt{2}t \sum_{\sigma} (\hat{c}_{(+, L_{left}, \sigma)}^{\dagger} \hat{c}_{(+, L_{left}-1, \sigma)} + h.c.). \quad (4.10)$$

In the  $L_{tot}$  ``odd`` case, the leads have the same number of sites and one can fold the ring obtaining chemical potential terms in each term of the last sites of the transformed ``+`` and ``-`` leads

$$\hat{H}'_{Leads, L_{left}, L_{right}} = -t \sum_{\sigma} (\hat{n}_{(+, L_{left}, \sigma)} - \hat{n}_{(-, L_{right}, \sigma)}). \quad (4.11)$$

## 4.4 Numerical Results

In this section, I present the numerical solution of the ``folded`` Hamiltonian (4.1) obtained in the previous section using the density-matrix renormalization-group (DMRG) technique[83, 85] on finite-size clusters of length  $L_{tot}$  with open boundary conditions (OBCs). This algorithm provides numerically exact results for static properties at zero temperature with a precision which depends on the number  $m$  of states retained. Most of the results here reported were obtained for  $m = 500$ , except otherwise stated, asserting that the integrated weight of discarded states are of order  $10^{-6}$  in the worst case. In order to assess even-odd effects most of the results reported below were obtained by using even and odd chain lengths. Throughout all this chapter, the impurity is located in one of two central sites of the chain when  $L_{tot}$  is even (in the central site when  $L_{tot}$  is odd). I focus on the effects of tunneling barrier modulation (encoded in the coupling constant  $\alpha$ ) on the electronic conductance and on the static and dynamical properties of the phononic mode. In my numerical calculations I use the hopping in the leads  $t$  as the unit of energy. Unless otherwise stated, I will keep the following parameter values:  $U = 1$ ,  $t' = 0.45$  and  $\omega_0 = 0.2$ . The gate voltage  $V_G$ , the Holstein coupling constant  $\lambda$  and the shuttling coupling constant  $\alpha$  were varied.

### 4.4.1 Scaling analysis of the current in absence of electron-phonon interaction

In this section, I neglect the effect of the electron-phonon interaction coupling constants  $\alpha$  and  $\lambda$ . In Fig.4.3 panel (a), I analyze the behavior of the persistent current flowing through the auxiliary system as function of the flux threading the ring. I have considered a ring of length  $L_{tot} = 96$  looking at different density of states for the leads. As shown in [172], in order to obtain the conductance, the values of the full-interacting current  $I_U(\pi/2)$  should be normalized by the value of non interacting current for  $V_G = 0$ ,  $I_{V_G=0}(\pi/2)$ . For this reason in panels (b,c,d) of Fig. 4.3 I show on the `y` axis the quantity  $[I_U(\pi/2)/I_{V_G=0}(\pi/2)]^2 \propto G$ , which is directly proportional to the conductance[172].

I have called ``Normal`` the density of states obtained from the Hamiltonian (4.3). The ``Cosine`` and ``Wilson`` density of states are obtained by the following ansatz on the hopping matrix elements in the leads' Hamiltonian for a finite size chain

$$\begin{aligned} \text{Cosine} &: t \rightarrow t_{n-1,n} = 0.45t \cos(\pi(n-1)/(L_{lead}-1)) + 0.55t, \\ \text{Wilson} &: t \rightarrow t_{n-1,n} = t(0.1)^{(n-1)/(L_{lead}-1)}. \end{aligned}$$

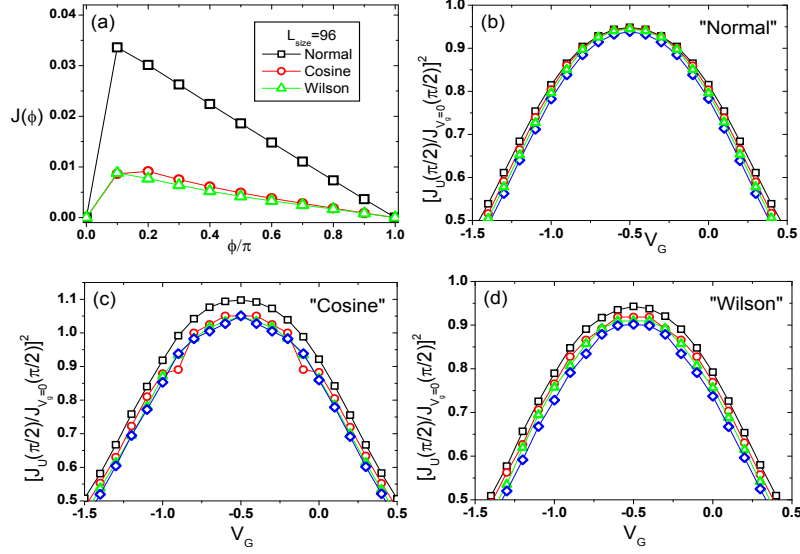


Figure 4.3: Panel (a): Persistent current as function of the flux for different leads' density of states at  $L_{tot} = 96$ . Scaling analysis (square line (black on line)  $L_{tot} = 48$ , circle line (red on line)  $L_{tot} = 72$ , up-triangle line (green on line)  $L_{tot} = 96$ , rumble line (blue on line)  $L_{tot} = 120$ ) of the current as function of  $V_G$  for Normal (panel (b)), Cosine (panel (c)) and Wilson (panel (d)) density of states.

For justifying the introduction of Cosine and Wilson modulation of the hopping in the leads, I need to briefly recapitulate the key idea introduced by Wilson for solving the Kondo problem (Wilson's numerical renormalization-group method (NRG)[82]). In the original NRG formulation, Wilson showed that the contribution from band states exponentially close to the Fermi energy needs to be taken into account in order to capture the correct properties of the ground state of the system. For this reason, standard tight-binding numerical approaches (based on a normal modulation of the leads' hopping) face a formidable challenge in addressing this problem: finite-size effects set a minimum energy scale, the level spacing, below which the calculation cannot capture the crossover to the Kondo state. Wilson proposed a combination of two elements to handle this problem: (i) A discretization procedure of the metallic band, leading to a mapping into an impurity connected to a one-dimensional tight-binding chain with exponentially decaying hoppings. (ii) A non-perturbative renormalization procedure that probes successive energy scales by recursively diagonalizing the Hamiltonian and keeping the relevant states at each scale. In this thesis I borrow the first Wilson's idea considering, in real space, a molecule connected to two tight-binding chains with exponentially decaying hoppings (as done in Ref.[89]). I refer to this as Wilson modulation for the leads' hopping. Another possibility is to consider a smoother decrease of the leads' hopping as one gets farther from the molecule (Cosine modulation).

The current profiles (red circles and green triangles in panel (a)) show that for Cosine and Wilson leads' density of states, for each value for the magnetic flux, a smaller current flows through the system. The panels (b,c,d) of Fig. 4.3 show a scaling analysis of the persistent current in the three cases cited above as function of the gate voltage. In each case, a beautiful Kondo resonance is obtained for  $V_G = -1/2$  as expected. The scaling analysis in the Normal case (panel (b)) shows a convergence of the results for the current for  $L_{tot} = 120$ . In Cosine (panel (c)) and Wilson (panel (d)) cases, the numerical results for the persistent current converge faster (for lower system size) than for Normal leads' density of states. Actually, using Cosine-like and Wilson-like modulation increases the density of

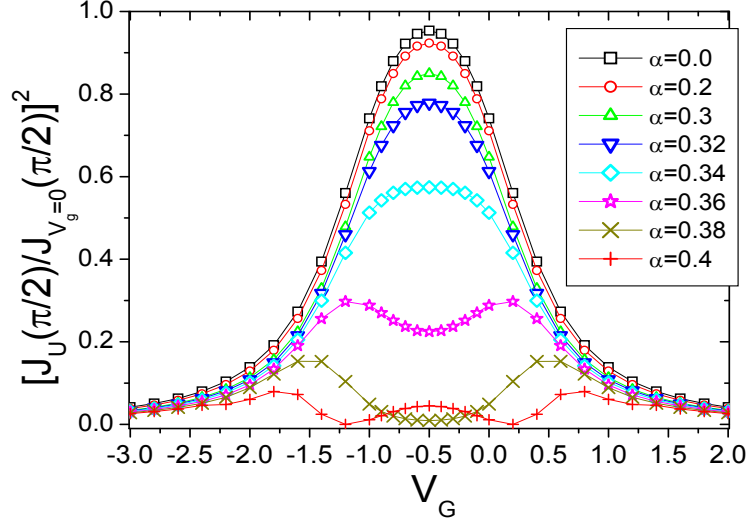


Figure 4.4: Persistent current flowing through the ring (length  $L_{tot} = 96$ ) as function of  $V_G$  for different values of  $\alpha$  (here  $\lambda = 0$ ).

states of the leads close to the fermi level and this helps the DMRG convergence to the Kondo ground state. From now on, in all the successive results I will consider simulations with Wilson-like modulation of the leads.

## 4.5 Behavior of the electronic current including the phonon effects

Before starting to analyze the transport properties of the system in presence of the phonons, I recall that the inclusion of the magnetic flux  $\phi$  threading the auxiliary ring should be carefully carried out because of the dependence of the hopping  $t'(\hat{x})$  connecting the molecule to the leads on the phonon displacement. Actually, as a result of the application of the magnetic flux, it is possible to show (Appendix E) that the shuttling coupling constant  $\alpha$  modifies to a complex constant  $\alpha^* = \alpha + i\phi/L_{tot}$ . With this in mind, I can start to consider the effect of the shuttle interacting coupling constant  $\alpha^*$  analyzing the behavior of the persistent current as function of  $V_G$  for different  $\alpha^*$  values. Actually I have changed the real part  $\alpha$  of the complex constant  $\alpha^*$ . It has also been verified that the imaginary part of  $\alpha^*$  (being proportional to  $L_{tot}$ ) has no effect on the observables of the system, if the length of the chain  $L_{tot}$  is sufficiently large.

In the following analysis, I will assume that the Holstein coupling constant  $\lambda$  is zero. As one can see in Fig. 4.4 the application of DMRG has shown different results with respect to those present in the literature: while K.A. Al-Hassanieh *et al.*[156] obtained a dip at  $V_G = -1/2$  for any small value of  $\alpha$ , now this dip is seen only for  $\alpha$  larger than a critical value  $\alpha_c$ . In order to confirm the presence of the dip, I performed a careful analysis of the numerical results at the p-h symmetric point ( $V_G = -1/2$ ) looking at the current as function of  $\alpha$  for different number of phonon states kept to describe the phonon Hilbert space. Actually, in Fig. 4.5 I have compared results of simulations where the phonon Hilbert space is considered in the bare number basis with respect to a simulation based on an optimized phonon basis.[166] I found that the current values obtained increasing the

number basis dimension converge for  $N_{ph} \sim 8$  to the results obtained with the optimized phonon Hilbert space approach[173] (see next subsection).

### Optimized Phonon Basis

In an electron-phonon lattice model, the number of phonons is not conserved and the Hilbert space is infinite, even for a finite number of sites. Of course, the number of phonons can be artificially constrained, but for strongly coupled systems the number of phonons needed for an accurate treatment may be quite large. This often severely constrains the size of the chains which may be studied. In case of this thesis, I deal with the very simple case of one phonon mode coupled locally on the central site of a tight-binding chain. This is coupled only with the first site of each lead through shuttle-like terms, while the other sites of the leads are not coupled with phonons.

In this section, I present a technique for generating a controlled truncation of the Hilbert space for the molecular site (being the tensor product of the four-dimensional electronic Hilbert space times the truncated Hilbert space for the phonon mode), which allows the use of a very small and optimized local basis without significant loss of accuracy.

The key idea of this approach is identical to the key idea of DMRG: in order to eliminate states from a part of a system without loss of accuracy, one should transform to the basis of eigenvectors of the reduced density matrix, and discard states with low probability. The key difference is that here the subsystem is a single site, rather than varying fractions of the entire system.

Actually I perform a set of DMRG sweeps (in order to get an almost exact result) on a small cluster of sites including the molecular site at the center (typically, three sites on the left, the molecular site and two sites to the right). All of the phonon states are "bare" (I keep typically a lot of phonon states  $N_{ph}$  40-50): they are eigenstates of the single site phonon Hamiltonian, characterized by the frequency  $\omega_0$ . At the end of a couple of DMRG sweeps, I extract the density matrix for the phonon mode of the molecular site tracing out the electronic degrees of freedom. The most probable  $m$  eigenstates of this matrix are the new optimal phonon states. These optimal states are used to construct the basis for the molecular site when applying the DMRG on the main system.

## 4.6 Static and dynamical properties of the shuttle mode for $\lambda = 0$

I have further analyzed the origin of the dip looking at the static and dynamical spectral properties of the phonon mode for  $\lambda = 0$  and  $\lambda \neq 0$ . I started analyzing the case  $\lambda = 0$ . In this case one can readily observe that the average position of the oscillator  $\langle x \rangle$  should be zero for inversion symmetry. However, as described in Fig. 4.6 panel (a), I obtain that for  $\alpha$  larger than  $\alpha_c$ ,  $\langle x \rangle$  starts to increase assuming values different from zero. I interpret this result as the onset of a Jahn-Teller distortion. In fact, the average square displacement  $\langle \Delta x \rangle = \langle (\hat{x} - \langle x \rangle)^2 \rangle^{1/2}$  multiplied by  $\alpha$  increases monotonically with  $\alpha$  reaching a critical value 1 for  $\alpha \simeq \alpha_c$  (Fig. 4.6 panel (b)). I have further studied the renormalization of the phonon propagator by the electron-phonon coupling  $\alpha$ . The dynamical information about oscillator is contained in the displacement Green's function. In Fig. 4.8, I have plotted the phonon displacement spectral function for different values of the shuttling coupling constant  $\alpha$ . For moderate  $\alpha$  values, I observe a softening of the frequency of the oscillator, where the spectral weight is concentrated on a single peak. For  $\alpha$  larger than the  $\alpha_c$ , a peak at very low frequency appears, corresponding to the onset of the

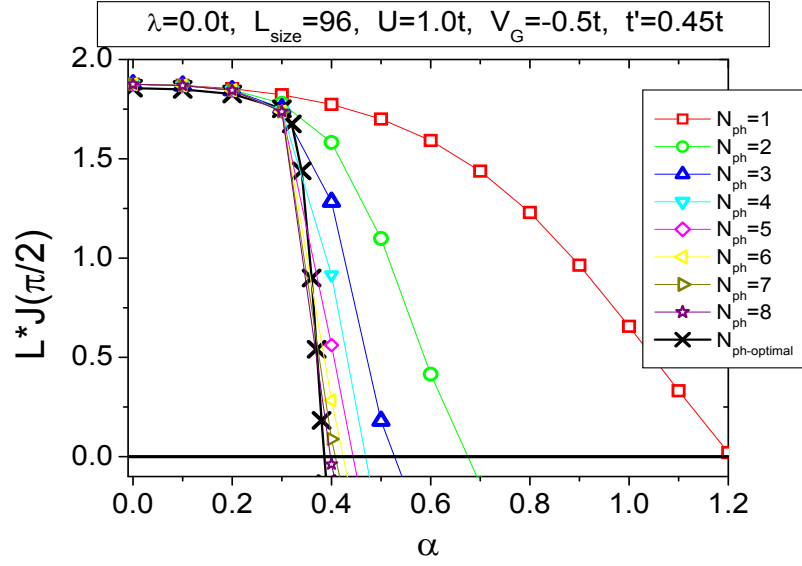


Figure 4.5: Persistent current at the particle-hole symmetric point ( $V_G = -1/2$ , length  $L_{tot} = 96$ ) as function of  $\alpha$  for different number of phonons  $N_{ph}$  kept to describe the phonon Hilbert space. The crosses curve represents the results obtained for an optimized phonon basis.

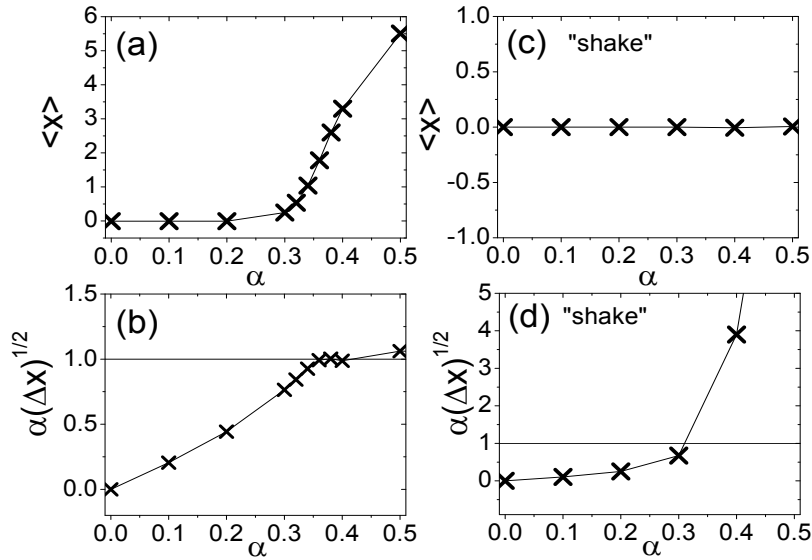


Figure 4.6: Static properties of the phononic mode at the particle-hole symmetric point ( $V_G = -1/2$ , length  $L_{tot} = 96$ ) as function of  $\alpha$  for  $\lambda = 0$ . Panels (a,b) describe  $\langle x \rangle$  and  $\alpha \langle \Delta x \rangle$  of the phononic mode with optimized phonon basis. Panels (c,d) describe same quantities as before with optimized phonon basis and *shaked* density matrix.



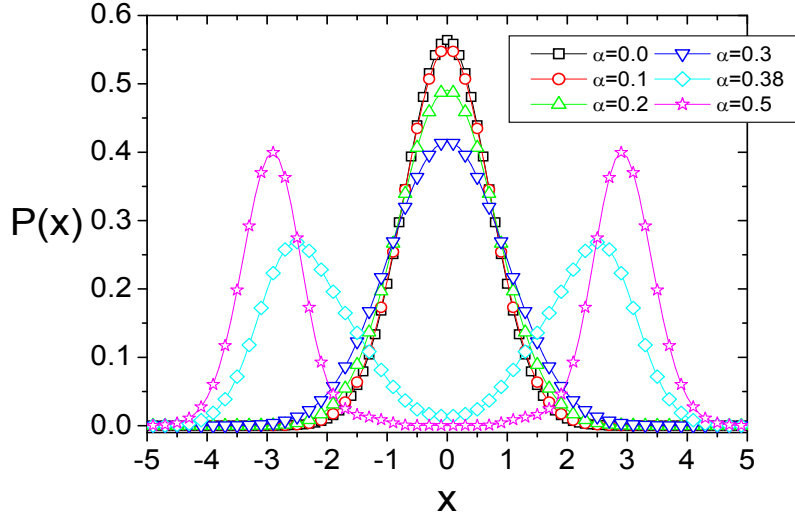


Figure 4.7: Distribution probability of the phononic mode at the particle-hole symmetric point ( $V_G = -1/2$ , length  $L_{tot} = 96$ ) as function of  $\alpha$  for  $\lambda = 0$ . The distribution becomes bimodal for  $\alpha \simeq 0.38$ .

Janh-Teller distortion. The behavior of the displacement spectral function, calculated with a correction vector method[164] (See also Appendix D)

$$A(\omega) = -\frac{1}{\pi} \text{Im} \langle\langle x, x \rangle\rangle_{\omega}, \quad (4.12)$$

can be understood in terms of the evolution of the probability density function of the oscillator in real space. This latter function was obtained using the reduced density matrix of the phonon in the bare phonon Hilbert space

$$P(x) = \langle x | \hat{\rho}_{ph} | x \rangle = \sum_{n,m} \Psi_m^*(x) \rho_{ph}^{m,n} \Psi_n(x), \quad (4.13)$$

where  $\Psi_n(x)$  are the eigenfunctions (Hermite polynomials) of the noninteracting harmonic oscillator. As one can observe in Fig. 4.7, for  $\alpha$  lesser than  $\alpha_c$  the probability density function has a Gaussian shape centered at  $x = 0$  and the phonon displacement spectral function presents a single peak for a frequency close (lesser) than the bare frequency  $\omega_0$ . For  $\alpha$  larger than  $\alpha_c = 0.38$  the probability density function becomes bimodal and symmetric with respect  $x = 0$  where the spectral function (Fig. 4.8) develops two peaks corresponding to the inter-well (very low frequency mode) and intra-well oscillation frequency. In order to clarify the nature of the Janh-Teller distortion, I have evaluated the static quantities in simulations where the density matrix was shaken by a little perturbation [174]. As one can observe in Fig. 4.6 panel (c,d), shaking the density matrix allows the oscillator to better explore its configuration space where positive and negative average displacements are equally probable. This results in an average displacement  $\langle x \rangle$  that is zero for all  $\alpha$  values (panel (c) in Fig. 4.6). Anyway, the average square displacement  $\langle \Delta x \rangle$  increase monotonically with  $\alpha$  reaching a maximum value for  $\alpha \simeq \alpha_c$  as before (panel (d) in Fig. 4.6).

The investigation of this model with the introduction of an Holstein coupling  $\lambda$  is under investigation.

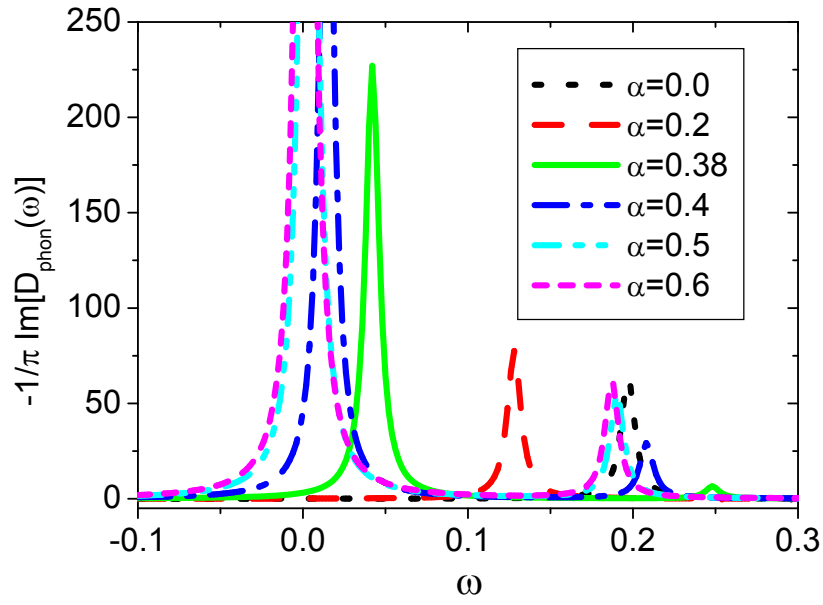


Figure 4.8: Imaginary part of the phononic spectral function at the particle-hole symmetric point ( $V_G = -1/2$ , length  $L_{tot} = 96$ ) for different values of  $\alpha$  for  $\lambda = 0$ . A low frequency peak corresponding to the distortion of the  $P(x)$  in bimodal shape appears for  $\alpha \simeq 0.38$ .

# Chapter 5

## Conclusions

The interaction between electronic and vibrational degrees of freedom is the most important microscopic mechanism at the heart of molecular systems and NEMS physics. In this thesis, I have studied electronic transport through molecular systems and NEMS under typical experimentally investigated conditions: low temperatures, large bias voltages applied and forcing antennas.

I have investigated these devices within Hamiltonian models widely used in the literature, using both semi-analytical (first part of the thesis) and numerical (second part of the thesis) techniques.

In the first part of the thesis, I have derived and studied the stochastic Langevin equation for the dynamics of a single oscillator mode coupled to a voltage-biased molecular junction in the adiabatic limit[29]. Using the generalization of the Keldysh formalism to time dependent cases, I was able to show, in agreement with other approaches, that the oscillator dynamics is controlled by an effective potential as well as by damping and fluctuating terms coming from the time depending electron Green function. Interestingly, I have established the range of validity of the adiabatic approximation underlying the stochastic approach distinguishing between Quantum, Classical-Adiabatic and Classical non Adiabatic regimes studying the average kinetic energy of the oscillator.

I applied my analysis to two simple models of molecules.

For the single site Holstein model, the analysis of the validity of the adiabatic approximation has allowed me to build up a phase diagram showing that the quantum effects are relevant only in a very narrow region if the vibrational energy of the molecular mode is smaller than all other energy scales. Moreover, I have studied the current-voltage characteristic and the conductance, observing a dynamical reduction of the polaronic shift and the broadening of the electronic resonance due to the average on the non-equilibrium position distribution probability of the oscillator. In the Non-Gaussian intermediate bias regime and for sufficiently high interaction strength, the kinetic energy shows an interesting non monotonic behavior. Correspondingly, I observe in the transport properties a strong enhancement of conduction with respect to the infinite mass approximation (static limit).

I have also studied the case of a molecular Hamiltonian composed by a couple of sites interacting with a single vibrational mode in the SSH model. In this case, because of the direct coupling of the electron-oscillator interaction to the inter-molecular hopping, the role of the dynamical fluctuations becomes crucial to determine the physical scenario described by the model. The new inter-molecular electronic hopping energy scale  $t$  introduces a reduction of the Classical adiabatic region in the phase diagram. The new feature is the occurrence of small Quantum regions for sufficiently small electron-oscillator coupling, at intermediate bias voltages. For strong enough electron-oscillator coupling ( $E_p$ ), these regions disappear. In this region of parameters the average dynamical kinetic energy decreases as the bias

voltage increases. Also the potential energy curves show this behavior. Therefore, the oscillator energy decreases as a function of bias voltage. This loss of energy occurs for that particular range of bias voltages where the molecular energy levels enter in the bias window. Correspondingly, as in the single site model case, I have observed in the transport properties an enhancement of conduction with respect to the infinite mass approximation. Remarkably, in the case of small electron-oscillator interaction and in absence of gate voltage, I found that the maxima of conductance correspond to the minima of the kinetic energy, shifted by the electron-oscillator coupling strength  $\alpha$ . Finally, within this model, the dynamical corrections on the transport properties cancel out completely the ‘detailed’ features (like NDR) present in the static case. As main result, I can conclude observing that the inclusion of dynamical effects of the oscillator motion strongly modifies the physical scenario which would be obtained by a static description, even if the oscillator dynamics is much slower than the electron tunneling rate.

I end this discussion regarding semi-analytical approaches noting that it could be of outstanding interest to study the possibility to include the quantum correction to the oscillator dynamics in the low bias regime classified as Quantum Region (QR). In this direction, Millis *et al.*[116] find in the quasi-equilibrium regime  $E_p \gg \omega_0 \gg V_{bias}$  a quantum contribution to the effective temperature of the oscillator in addition to the diffusive one. At finite mass  $m$ , nearby the ‘gaussian fluctuation’ paths involving small excursions (characteristic frequency  $\omega_0$ ) from the minima of the static potential, quantum tunneling processes become important. The inclusion of the quantum corrections in my approach, within the minimal models considered, is under investigation.

I here point out that the technique developed and used in Chap. 2 for the single molecular mode (single mechanical degree of freedom) in interaction with voltage biased molecular junction, has been extended to 3-D systems with  $N$  mechanical degrees of freedom allowing to calculate the spectral, optical, and transport properties of single crystal Organic Field-Effect Transistors (OFET) in the low bias quasi-equilibrium regime [144]. In this thesis I have focused my attention to the case of a single mechanical degree of freedom.

In chapter 3, I have studied a self-detecting electron-transistor realized by a suspended carbon nanotube including, in a non-perturbative way, the effect of the antenna driving the nanotube toward a nonlinear regime. All the qualitative features of the NEMS device, experimentally observed, are accurately reproduced clarifying the origin of the nonlinear effects. The nonlinear behavior is understood without adding *by hand* nonlinear terms to the effective force exerted on the resonator [11, 129, 121, 130], but stems out naturally from the nontrivial non-equilibrium time-dependent electronic occupation controlled by the coupling with the leads. I have shown that, increasing the temperature, the nonlinear effects in the current-frequency response are washed out as a result of the increase of the intrinsic damping of the resonator and of the reduction of the intrinsic nonlinear terms of the effective self-consistent force. Within my approach, a broadening of the frequency dip as function of the bias voltage is reproduced, predicting in the limit of large bias a double dip structure. This double dip feature has found very recently an experimental confirmation [48]. At the end of Chap. 3, I’ve investigated the inclusion of a transverse magnetic field applied to the carbon nanotube-device[136]. As a main result, the magnetic field modifies the bending mode CNT dynamics giving an enhanced damping as well as a noise term originating from the electronic phase fluctuations induced by the CNT displacements[50]. In particular, a quadratic dependence of the device quality factor  $Q$  on external magnetic field strength, in quantitative agreement with recent experiments, emerges as a result of a back-action of quantum electronic current-flow fluctuations on the bending mode dynamics[50]. I’ve also shown that, when the device is driven far from equilibrium, one can tune the mechanical properties of the resonator by varying the external magnetic field: CNT-resonator resonance

frequencies as a function of gate voltage acquire, in the limit of a large magnetic field, a peculiar dip-peak structure that could be experimentally observed. Finally, at a fixed gate, bias voltage and temperature, if charge and current variations of the opposite sign occur, one has an enhanced damping reducing the quality factor of the device. Vice-versa, charge and current variations of the same sign reduce damping with a consequent increase of quality factors.

As possible outlook, it could be very interesting to introduce in my description the effects of electron-electron interactions within a model that includes the spin degrees of freedom. In this case and in the presence of a large magnetic field, the Zeeman effect could modify qualitatively the numerical results.

In the last part of the thesis, I analyzed the electronic transport properties of a molecule oscillating between two electrodes in the Kondo regime, within the Anderson-Impurity model. It is well known that in this regime, the strong electron-electron correlations prevent from using any analytical approach to the problem. I therefore use an approximation-free numerical technique: the DMRG. DMRG is one of the most accurate numerical approaches for treating strongly correlated systems described by lattice Hamiltonians in one spatial dimension. The method consists of a very efficient iterative procedure and allows for the investigation of ground-state (equilibrium) properties of strongly correlated systems with several hundred to several thousand lattice sites with low computational cost.

I have used an alternative method for calculating the conductance through nanoscopic correlated systems based on the calculation of the persistent current of a fictitious auxiliary system threaded by a magnetic flux. I focused on the effects of tunneling barrier modulation (encoded in a coupling constant  $\alpha$ ) on the electronic conductance and on the static and dynamical properties of the phononic mode. The results show an interesting and unexpected conductance cancellation (*dip*) for a sufficiently large value of  $\alpha$  when an odd number of electrons occupy the molecule. I justify the presence of the dip for a finite  $\alpha$  value by means of a Jahn-Teller distortion, where a natural breaking of the inversion symmetry is obtained. Correspondingly, the average quadratic fluctuations of the displacement increase up to the limit physical value  $t'/\alpha$  where the effective hopping between the molecule and one of the leads is equal to zero, giving the conductance cancellation. Additionally, I found that the electron-phonon coupling modifies the shape of the distribution probability in real space affecting the static and dynamic properties of the oscillator. In the absence of Holstein interaction and for moderate  $\alpha$ s, the Gaussian distribution is softened and the frequency of oscillations decreases. For  $\alpha > \alpha_c$ , the phononic distribution becomes bimodal even if it retains its symmetry with respect to zero displacement configuration. In this regime, the phonon propagator consists of a part corresponding to high-frequency oscillations within the peak (well) and another part corresponding to slow tunneling between the degenerate peaks (wells).

The investigation of this model with the introduction of an Holstein coupling is under investigation. I anticipate that in this case the occurrence of the dip in the conductance is suppressed. Indeed, with an Holstein coupling the inversion symmetry of the system is broken from the beginning. For finite  $\lambda$  the degeneracy between the peaks in the distribution probabilities is broken and, again, the average quadratic fluctuations of the displacement increase significantly while the average  $\langle x \rangle$  starts to increase assuming values different from zero. I argue that an even small Holstein interaction could account for the asymmetric configurations of the molecule between the electrodes typically observed experimentally [63].

My study suggests that a careful estimate of the parameter  $\alpha$  of the model, owing to the modification of the electronic hopping integral due to the center of mass motion of a molecule placed between the two leads, is necessary. For a  $C_{60}$  molecular junction investigated in [19] a relatively large value of  $\alpha$  ( $\alpha \simeq 0.6 < 1$ ) can be extracted and this could justify the conduc-

tance suppression in the low temperature and bias regime. Nevertheless, recent experimental studies [63] have shown that relatively large conductance values can be measured through  $C_{60}$  molecular junctions. I believe that more realistic theoretical models taking account of a more complicated molecular level structure and of other internal vibrational modes of the molecule are necessary for a correct interpretation of experimental results.

As a future application of the DMRG, I intend to apply the time-dependent extension of the algorithm[191] to investigate the non-equilibrium response within the minimal model cited above. This will allow to calculate the current-voltage response of the device and a possible comparison with experimental results[63]. As a future project, I'm going to analyze a more realistic two-site two mechanical mode model allowing for the analysis of the interaction between breathing and center of motion modes of the diatomic molecule analyzed.

# Appendix A

## Non-Equilibrium contour-ordered Green Functions

### A.1 Introduction

In many-particle problems the systems are usually described by Hamiltonians which can not be solved exactly, and one has to rely on perturbative methods. In these situations the introduction of second quantization operators and Green's functions prove to be very important techniques. In this chapter, I define equilibrium and nonequilibrium Green's functions limiting to list the key equations used in the main text. I derive Dyson and Keldysh equations describing behavior of nanoscale system in stationary non-equilibrium conditions.

### A.2 Equilibrium Green's functions

In this section, I describe very briefly equilibrium Green functions (there are many excellent treatises on the topic such as [92, 93]).

Let us consider an isolated physical system (at zero temperature) described by an Hamiltonian operator  $\hat{H} = \hat{H}_0 + \hat{V}$ . One can start by defining a time-ordered (also called causal) zero-temperature single-particle Green function

$$G^T(x, t; x', t') = -i \langle \Psi_0 | T \hat{\psi}_{\hat{H}}(x, t) \hat{\psi}_{\hat{H}}^\dagger(x', t') | \Psi_0 \rangle, \quad (\text{A.1})$$

where one can introduce field operators  $\hat{\psi}_{\hat{H}}(x, t)$  in Heisenberg picture:  $\hat{\psi}_{\hat{H}}(t) = e^{i\hat{H}t} \hat{\psi}_{\hat{H}}(t=0) e^{-i\hat{H}t}$ . They are defined introducing a convenient basis in one-particle sector of the Hilbert space (Fock space) as linear combination of creation and annihilation operators

$$\begin{aligned} \hat{\Psi}_H(x, t, \sigma) &\equiv \sum_k \psi_k(x) \hat{c}_{k\sigma}(t), \\ \hat{\Psi}_H^\dagger(x, t, \sigma) &\equiv \sum_k \psi_k^*(x) \hat{c}_{k\sigma}^\dagger(t), \end{aligned} \quad (\text{A.2})$$

where  $\psi_k(x)$  and  $\psi_k^*(x)$  are one-particle wave functions, and  $\hat{c}_{k\sigma}$  ( $\hat{c}_{k\sigma}^\dagger$ ) destroys (creates) a particle in the Fock-state  $|k\sigma\rangle$ . The sum above extends over a complete set of quantum numbers in the one-particle Hilbert space. In the Eq. A.1, the quantum state  $|\Psi_0\rangle$  is the ground state of the interacting system, while  $T\{\dots\}$  is the time-ordering operator.

The definition of the Green function can be generalized to describe an equilibrium system at a finite temperature  $T$  with a chemical potential  $\mu$  (Grand Canonical ensemble):

$$G(x, t; x', t') = -i \text{Tr} \left\{ \hat{\rho} T \hat{\psi}_{\hat{H}}(x, t) \hat{\psi}_{\hat{H}}^\dagger(x', t') \right\}, \quad (\text{A.3})$$

Here  $\hat{\rho}$  is the density matrix operator

$$\hat{\rho} = \frac{e^{-\beta(\hat{H} - \mu \hat{N})}}{\text{Tr}[e^{-\beta(\hat{H} - \mu \hat{N})}]}, \quad \beta \equiv (k_B T)^{-1}, \quad (\text{A.4})$$

where  $\hat{N}$  is the occupation operator and the trace  $\text{Tr}$  is the sum over all diagonal elements of a complete set in the Fock-space. One can also define in an analogous fashion two- and many-particle Green functions.

There are two main reasons to study Green's functions: (1) Experimentally relevant quantities can be extracted from the knowledge of the Green function. (2) The definition A.1 allows the construction of a systematic perturbation theory.

## Examples of Measurable Quantities

The particle density of a many-body system is given by  $\langle \hat{n}(x) \rangle = \langle \hat{\psi}^\dagger(x) \hat{\psi}(x) \rangle$ , but this object is directly related to the Green function

$$\langle \hat{n}(x) \rangle = -i G^T(x, t; x, t^+), \quad (\text{A.5})$$

where  $t^+ (= \lim_{\epsilon \rightarrow 0} (t + \epsilon))$  is infinitesimally larger than  $t$  in order to get the correct time ordering. Note that in equilibrium, and for uniform systems Green functions depend only on differences of variables,  $G(x, t; x', t') = G(x - x', t - t')$ , and it is advantageous to work in Fourier space

$$G(k, \omega) = \int d^3x \int dt e^{i\omega(t-t')} e^{-ik(x-x')} G(x - x', t - t').$$

For future use I also define retarded, advanced, and the "lesser than" (or just "lesser") and "greater than" (or just "greater") Green functions (Furthermore, to lighten the notation I set  $\hbar = 1$ ):

$$\begin{aligned} G^r(x, t; x', t') &\equiv -i\theta(t - t') \langle \{ \hat{\psi}(x, t), \hat{\psi}^\dagger(x', t') \} \rangle, \\ G^a(x, t; x', t') &\equiv i\theta(t' - t) \langle \{ \hat{\psi}(x, t), \hat{\psi}^\dagger(x', t') \} \rangle, \\ G^<(x, t; x', t') &\equiv i \langle \hat{\psi}^\dagger(x', t') \hat{\psi}(x, t) \rangle, \\ G^>(x, t; x', t') &\equiv -i \langle \hat{\psi}(x, t) \hat{\psi}^\dagger(x', t') \rangle. \end{aligned} \quad (\text{A.6})$$

The retarded Green function  $G^r$  differs from zero only for times  $t \geq t'$ , thus this function can be used to calculate the response at time  $t$  to an earlier perturbation of the system at time  $t'$ . The advanced Green function  $G^a$  is only finite for  $t \leq t'$ . Due to the (anti)commutator structure, these two functions again obey an inhomogeneous differential equation as the originally defined time-ordered Green function  $G^T$ . The *lesser* Green function is also called the particle propagator, while the *greater* Green function, in which the order of the creation and annihilation operators are reversed, is called the hole propagator. Importantly, their differential equations do not have the singular inhomogeneous terms. This observation is the precursor of a more fundamental difference between the lesser/greater and retarded/advanced functions; this difference will be accentuated under non-equilibrium conditions. I note that the



time-ordered, the retarded, and the advanced Green functions can be expressed in terms of  $G^>$  and  $G^<$ :

$$G^T(t, t') = \theta(t - t')G^>(t, t') + \theta(t' - t)G^<(t, t') \quad (\text{A.7})$$

$$G^r(t, t') = \theta(t - t')[G^>(t, t') - G^<(t, t')] = G^T - G^< = G^> - G^{\tilde{T}}, \quad (\text{A.8})$$

$$G^a(t, t') = \theta(t' - t)[G^<(t, t') - G^>(t, t')] = G^T - G^> = G^< - G^{\tilde{T}}. \quad (\text{A.9})$$

From the above relations it seems that there are only two independent Green functions  $G^{>,<}$ . The observables can also be expressed in terms of  $G^{>,<}$ ; for example

$$\rho(x, x', t) = [G^<(x, t; x', t')]_{t=t'}. \quad (\text{A.10})$$

Anyway, one can show that in equilibrium all the above Green's functions can be expressed in terms of each other. Indeed one has the following relations

- $G^r - G^a = G^> - G^<;$
- $G^r(x, t; x', t') = [G^a(x', t'; x, t)]^*;$
- $G^>(\omega) = -e^{\beta(\omega - \mu)}G^<(\omega)$ , Fluctuation-Dissipation theorem.

It is easy to show that the first property comes directly from the definition of the Green's function, while the second (that is trivial to check in equilibrium) can be proved to be valid even in stationary non-equilibrium conditions[94]. A proof of the Fluctuation-Dissipation theorem can be found in Haug[80].

## Contour ordered Green's function and perturbation theory

Let us consider a physical system described by a time independent Hamiltonian  $\hat{H} = \hat{H}_0 + \hat{H}^i$ , where  $\hat{H}_0$  is an exactly solvable non-interacting Hamiltonian (at most quadratic in the operators) while  $\hat{H}^i$  describe the interactions among the particles of the system. I suppose that the system is in thermodynamic equilibrium with a heat bath at temperature  $T$  and in contact with a particle reservoir at chemical potential  $\mu$  until a time  $t_0$ , when the system is disconnected from the reservoirs and a time dependent perturbation described by an operator  $\hat{H}'(t)$  is applied to it. The total Hamiltonian is now time-dependent (for sake of simplicity I omit the  $\wedge$  symbol)

$$\mathcal{H} = \hat{H} + \hat{H}'(t), \quad \hat{H}'(t) = 0, \quad t \leq t_0.$$

For a molecular junction, the external perturbation is usually represented by the coupling with two reservoirs with different electro-chemical potentials. In non-equilibrium theory one can define a contour-ordered Green's function defined as

$$G(1, 1') \equiv -i\langle T_c \{ \hat{\psi}_{\mathcal{H}}(1) \hat{\psi}_{\mathcal{H}}^\dagger(1') \} \rangle \quad (\text{A.11})$$

where  $\hat{\psi}_{\mathcal{H}}(1)$  is the field operator in the Heisenberg picture and where the short-hand notation  $1 \equiv (\vec{r}_1, \sigma_1, \tau_1)$  has been introduced. Here the average is evaluated with respect to the unknown non-equilibrium density matrix  $\hat{\rho}(\mathcal{H})$ . The above definition trivially extends the equilibrium definition of Green's function to a generic two-time function on a contour  $c$ . As discussed in the previous paragraph, I introduced also a time-ordering operator  $T_c$  along the contour

$$T_c \{ \hat{\psi}_{\mathcal{H}}(1) \hat{\psi}_{\mathcal{H}}^\dagger(1') \} = \begin{cases} \hat{\psi}_{\mathcal{H}}(1) \hat{\psi}_{\mathcal{H}}^\dagger(1') & \tau_1 >_c \tau_{1'} \\ -\hat{\psi}_{\mathcal{H}}^\dagger(1') \hat{\psi}_{\mathcal{H}}(1) & \tau_{1'} >_c \tau_1. \end{cases} \quad (\text{A.12})$$

with an obvious notation. For instance, if  $\tau_1 >_c \tau_{1'}$ , this means that  $\tau_1$  follows on the contour the variable  $\tau_{1'}$ , independently on the actual numerical value assumed on the contour. As in equilibrium, I can define other Green's functions. For example, for the *G-lesser* and *G-greater* I get

$$G(1, 1') = \begin{cases} G^<(1, 1') & \tau_1 <_c \tau_{1'} \\ G^>(1, 1') & \tau_{1'} <_c \tau_1, \end{cases} \quad (\text{A.13})$$

where the equality is independent on the actual values assumed by  $\tau_1$  and  $\tau_{1'}$  on the real axis. If contour time-position are on the real axis, I recover the correspondent equilibrium Green's functions. One should be careful on the relative positions of the times  $\tau_1$  and  $\tau_{1'}$  on the two branches of the contour  $c$ ,  $c_1$  ( $-\infty \rightarrow +\infty$ ) and  $c_2$  ( $+\infty \rightarrow -\infty$ ). Observing that on  $c_2$  the time-ordering means anti-time-ordering, I point out that the contour ordered Green function  $G(1, 1')$  contains four *real* Green's functions  $((\tau_1, \tau_{1'}) \rightarrow (t_1, t_{1'}))$

$$G(1, 1') = \begin{cases} G^T(1, 1'), & t_1, t_{1'} \in c_1 \\ G^<(1, 1'), & t_1 \in c_1 \quad t_{1'} \in c_2, \\ G^>(1, 1'), & t_1 \in c_2 \quad t_{1'} \in c_1, \\ G^{\tilde{T}}(1, 1'), & t_1, t_{1'} \in c_2, \end{cases} \quad (\text{A.14})$$

where  $G^T$  and  $G^{\tilde{T}}$  are time-ordered and anti-time-ordered Green's functions, respectively. Applying the couple of unitary transformations described in the previous sections to field operator  $\hat{\psi}_{\mathcal{H}}(1)$  and  $\hat{\psi}_{\mathcal{H}}(1')$  in Eq. A.11, I can easily prove that [94]

$$\begin{aligned} G(1, 1') &= -i \langle T_c \{ S'_c S_c^i \hat{\psi}_{\hat{H}_0}(1) \hat{\psi}_{\hat{H}_0}^\dagger(1') \} \rangle_0 \\ &= -i \langle T_c \{ e^{-i \int_c d\tau' [\hat{H}'_{\hat{H}_0}(\tau') + H_{\hat{H}_0}^i(\tau')] } \hat{\psi}_{\hat{H}_0}(1) \hat{\psi}_{\hat{H}_0}^\dagger(1') \} \rangle_0, \end{aligned} \quad (\text{A.15})$$

where I have used the notation  $\langle .. \rangle_0 = Tr(\hat{\rho}_{\hat{H}_0} ..)$ . This is the starting point of a perturbation theory for non-equilibrium Green's functions. I can observe that this approach is not plagued of the *denominator problem* which characterizes the equilibrium theory. The main difference between equilibrium and non-equilibrium theory is the presence of an integration along a contour in the latter. They have the same formal structure: expanding the exponential in the Eq. one obtains at zero-order the noninteracting contour-ordered Green's function

$$G^{(0)}(1, 1') = -i \langle T_c \{ \hat{\psi}_{\hat{H}_0}(1) \hat{\psi}_{\hat{H}_0}^\dagger(1') \} \rangle_0,$$

while at higher orders one gets statistical averages of operators over the noninteracting density matrix  $\hat{\rho}_{\hat{H}_0}$ . One can show that for this average a generalized Wick theorem is valid [94]. Moreover, in the presence of a classical one-particle external field  $U$  and of a two-particle interaction term, the contour-ordered green's function  $G(1, 1')$  satisfies a Dyson equation

$$\begin{aligned} G(1, 1') &= G^{(0)}(1, 1') + \int_c d2 G^{(0)}(1, 2) U(2) G(2, 1') \\ &\quad + \int_c d2 \int_c d3 G^{(0)}(1, 2) \Sigma(2, 3) G(3, 1'), \end{aligned} \quad (\text{A.16})$$

where  $\Sigma[G]$  is the self-energy term describing the particle-particle interaction. I have again introduced a short-end notation

$$\int_c d1 \equiv \sum_{\sigma_1} \int d\vec{r}_1 \int_c d\tau_1. \quad (\text{A.17})$$

The contour integrations are mostly a formal tool since in practical calculations one replaces them by real-time integrations. The procedures for such replacements are known as the Langreth's rules.

## Observation

In non-equilibrium, I can define also retarded and advanced Green's functions and verify that they satisfy properties Eqs. (2.14) (2.15). It is easy to show that they verify also

$$G^r(1, 1') - G^a(1, 1') = G^>(1, 1') - G^<(1, 1'), \quad (\text{A.18})$$

so that even in non-equilibrium situations I have just three independent Green's functions. Moreover, in non-equilibrium stationary conditions, one can show that contour-ordered Green's functions depend only on contour time differences obtaining

$$G^r(1, 1') = [G^a(1', 1)]^*, \quad (\text{A.19})$$

reducing to two independent Green's functions. In stationary conditions one can also work in the frequency domain using Fourier transform, but is not possible to show a fluctuation-dissipation theorem as in equilibrium conditions.

Finally, I point out that in stationary non-equilibrium conditions one just needs two Green's function ( I will be typically concerned with  $G^r$  and  $G^<$ ). In the next section I will show that these two Green's function cannot be determined separately but they satisfy two coupled equations (Dyson's and Keldysh's equations) which are nonlinear algebraic equation in the frequency domain.

### A.2.1 Dyson's and Keldysh's equations

As already discussed in previous section, in steady state the non-equilibrium problem is thus reduced to working with two independent Green's functions. This is what I do in the non-equilibrium situations considered in the present work.

Applying Langreth's theorem[80] to the Dyson's equation A.16 I extract

$$G^{r(a)}(1, 1') = G_{(0)}^{r(a)}(1, 1') + \int_t d2 \int_t d3 G_{(0)}^{r(a)}(1, 2) \Sigma^{r(a)}(2, 3) G^{r(a)}(3, 1'), \quad (\text{A.20})$$

$$\begin{aligned} G^{\lessgtr}(1, 1') &= G_{(0)}^{\lessgtr}(1, 1') + \int_t d2 \int_t d3 \left[ G_{(0)}^r(1, 2) \Sigma^r(2, 3) G^{\lessgtr}(3, 1'), \right. \\ &\quad \left. G_{(0)}^r(1, 2) \Sigma^{\lessgtr}(2, 3) G^a(3, 1') + G_{(0)}^{\lessgtr}(1, 2) \Sigma^a(2, 3) G^a(3, 1') \right], \end{aligned} \quad (\text{A.21})$$

where integrals are evaluated on the real axis with a compact notation

$$\int_t d1 \equiv \sum_{\sigma_1} \int d\vec{r}_1 \int_{-\infty}^{+\infty} dt_1 \quad (\text{A.22})$$

and I've ignored the one-body potential  $U$  which can be absorbed in  $G_0$  by a suitable redefinition  $G_0^{-1} - U \rightarrow G_0^{-1}$ . The *lesser* Green's function A.21 can be rewritten in the following way (this can be carried out similarly for the *greater* component  $G^>$ )

$$G^< = G_0^< + G_0^r \Sigma^r G^< + G_0^r \Sigma^< G^a + G_0^< \Sigma^a G^a. \quad (\text{A.23})$$

I will solve Eq. (2.78) by iteration. At first step I get

$$\begin{aligned} G^< &= (1 + G_0^r \Sigma^r) G_0^< (1 + \Sigma^a G^a) + (G_0^r + G_0^r \Sigma^r G_0^r) \Sigma^< G^a \\ &\quad + G_0^r \Sigma^r G_0^r \Sigma^r G^<. \end{aligned} \quad (\text{A.24})$$

It is easy to convince oneself that iterating the procedure the prefactor of  $\Sigma^< G^a$  reproduces the expansion of the retarded Green's function  $G^r$ , obtaining

$$G^< = (1 + G^r \Sigma^r) G_0^< (1 + \Sigma^a G^a) + G^r \Sigma^< G^a. \quad (\text{A.25})$$

Finally, reintroducing explicitly the time integrations

$$\begin{aligned} G^<(1, 1') &= \int_t d2 \dots \int_t d5 [\delta(1-2)\delta(2-3) + G^r(1, 2)\Sigma^r(2, 3)] \\ &\quad \times G_0^<(3, 4)[\delta(4-5)\delta(5-1') + \Sigma^a(4, 5)G^a(5, 1')] \\ &\quad + \int_t d2 \int_t d3 G^r(1, 2)\Sigma^<(2, 3)G^a(3, 1'), \end{aligned} \quad (\text{A.26})$$

where

$$\delta(1-2) \equiv \delta(\vec{r}_1 - \vec{r}_2)\delta(t_1 - t_2)\delta_{\sigma_1, \sigma_2}. \quad (\text{A.27})$$

Introducing the inverse operator  $\vec{G}_0^{-1}$  defined as

$$\begin{aligned} \int_c d2 \vec{G}_0^{-1}(1, 2) G_0(2, 1') &= \delta(1-1'), \\ \vec{G}_0^{-1}(1, 2) &\equiv (\imath \partial_{t_1} - H_0(1))\delta(1-2), \end{aligned} \quad (\text{A.28})$$

where the arrow indicate which way the operator acts, and using the noninteracting properties

$$\int_c d2 \vec{G}_0^{-1}(1, 2) G^{r(a)}(2, 1') = \delta(1-1') + \int_c d2 \Sigma^{r(a)}(1, 2) G^{r(a)}(2, 1'), \quad (\text{A.29})$$

$$\int_c d2 G^{r(a)}(1, 2) \overleftarrow{G}_0^{-1}(2, 1') = \delta(1-1') + \int_c d2 G^{r(a)}(1, 2) \Sigma^{r(a)}(2, 1'), \quad (\text{A.30})$$

where I have applied the operator  $\vec{G}_0^{-1}$  to the Dyson equation A.16 and to its left-iterated version. Substituting Eqs. (2.84) and (2.85) in Eq. (2.81), I get

$$\begin{aligned} G^<(1, 1') &= \int_t d2 \int_t d3 G^r(1, 2) [\overleftarrow{G}_0^{-1}(2) G_0^<(2, 3) \vec{G}_0^{-1}(3)] G^a(3, 1') \\ &\quad + \int_t d2 \int_t d3 G^r(1, 2) \Sigma^<(2, 3) G^a(3, 1'). \end{aligned} \quad (\text{A.31})$$

One can show that in steady state, where one can use Fourier transform the first line term in Eq. (2.86) is zero. Indeed, this latter contains  $G_0^<$  which has a memory of the correlation of the initial (before introducing interactions and non-equilibrium perturbations) state of the system. One implicitly assumes that the non-equilibrium steady state, if it exists, loses any information of the initial state of the system due to unavoidable irreversible processes in the transient. I will thus consider the stationary Keldysh equation

$$G^<(1, 1') = \int_t d2 \int_t d3 G^r(1, 2) \Sigma^<(2, 3) G^a(3, 1'), \quad (\text{A.32})$$

where the one asks for the unknown *lesser* Green's function  $G^<$  ( $G^>$ ). From this Green's function one can extract the particle density in the presence of interactions in the non-equilibrium steady state.

In equilibrium,  $G^<$  is proportional to the Fermi distribution if one assumes a time independent Hamiltonian and interactions such that the system can be considered a Fermi liquid.

Ultimately, in order to solve for the system dynamics one must be able to solve simultaneously the Dyson's equation A.20 for the retarded component and the Keldysh's equation A.32 for the *lesser* Green's function. Here, the biggest difficulty is given by the functional dependence of the self-energies  $\Sigma^{(r,<)}$  on the unknown Green's functions  $G^{(r,<)}$ .

# Appendix B

## Capacitive coupling vs Anderson-Holstein model

Here, I briefly show that the model Hamiltonian for the vibrating nanotube encapsulated in the eq.(3.15) is equivalent to that used in [11, 12] and in other papers in the literature [124, 126, 127, 125, 129, 132]. Indeed, as clearly discussed in Ref. [133], a single electronic transistor (SET) consists of a metallic dot (represented by a nanotube in the case considered in Ref. [11, 12]) with a large Coulomb-charging energy  $E_C = e^2/2C_{tot}$  ( $C_{tot}$  is the total capacitance of the dot) coupled via tunnel junctions to both a source and a drain metal electrode. The Hamiltonian for the electronic and vibrational degrees of freedom of the dot is given by

$$H_{dot} = E_C(N_{el} - N_{gate})^2 + \frac{1}{2}kx^2, \quad (\text{B.1})$$

comprising a charging-energy term and the harmonic vibrational energy. In eq.(B.1),  $N_{el}$  is the charge on the SET dot and  $N_{gate} = C_{gate}V_{gate}/e$  is the dimensionless electron number associated with a gate voltage  $V_{gate}$  which is coupled to the dot via a capacitance  $C_{gate}$ . In addition, a voltage  $V_{bias}$  is applied between source and drain which drives the tunneling of electrons across the SET. Here,  $C_{tot} = C_{gate} + C_{leads}$ , where  $C_{leads}$  is the sum of the capacitances resulting from the coupling to the leads. When the nanotube is allowed to vibrate, the gate capacitance  $C_{gate}$  assumes a spatial dependence  $C_{gate}(h(x))$ , where  $h$  is the distance between the nanotube and the gate electrode when the nanotube is displaced by a distance  $x$  from its equilibrium position ( $h(x) = h_0 + x$ ). In the limit of small displacements, one can expand  $\hat{H}_{dot}(x)$  around  $x = 0$  obtaining a Holstein-like linear correction term in  $x$ :

$$H_{int} = \lambda N_{el}x, \quad (\text{B.2})$$

where  $\lambda = -2(E_C V_g/e)(dC_g/dx)$ . In the small energy window of interest for a single dip feature investigated in Ref. [11, 12], I can neglect the weak gate and bias voltage dependence of  $\lambda$  that is assumed constant [125, 133, 134]. Moreover, if I choose  $x = 0$  as the position where the Coulomb force for  $N_{el} = 0$  electrons in the island equals the elastic force,  $\lambda$  can be then interpreted as the net force acting on the nanotube when one excess electron is populating the nanotube itself. The terms independent on  $N_{el}$  in the above expansion are usually neglected [133, 134]. One further assumes that the gate voltage is such that only charge states with  $N_{el} = 0$  and 1 are accessible. In this case,  $N_{el}^2 = N_{el}$  and one can incorporate remaining constant terms (independent on  $x$ ) in the above expansion in an effective gate voltage obtaining

$$H_{dot} \simeq V_{gate}^{eff} N_{el} + \lambda N_{el}x + \frac{1}{2}kx^2. \quad (\text{B.3})$$

If I quantize the electronic and vibrational degrees of freedom, eq.(B.2) gives the Holstein coupling discussed in the Chap. 3.

# Appendix C

## Current-current and Current-density fluctuation

Here I illustrate how the calculation of the force fluctuation (Eq. 3.44 of Chap. 3) can be performed with the nonequilibrium Green function approach. I follow faithfully Haug [80].

I recall the expression for the current operator (through the left barrier) [80]

$$I_L = \frac{ie}{\hbar} \sum_k k [V_{L,k} c_k^\dagger d - V_{L,k}^* d^\dagger c_k], \quad (\text{C.1})$$

where I simplify the notation somewhat by suppressing indices which are not relevant to the structure of the theory. I define  $\delta I_L(t) = I_L(t) - \langle I_L \rangle$ , and plan to evaluate the correlation function (I set  $V_{L,k} = V_k$ )

$$\begin{aligned} S(t, t') &= \frac{1}{2} \langle \{ \delta I_L(t), \delta I_L(t') \} \rangle \\ &= \frac{1}{2} \langle \{ I_L(t), I_L(t') \} \rangle - \langle I_L \rangle^2 \\ &= \frac{1}{2} \left( \frac{ie}{\hbar} \right)^2 \sum_{k, k'} \left[ V_k V_{k'} \langle c_k^\dagger(t) d(t) c_{k'}^\dagger(t') d(t') \rangle \right. \\ &\quad - V_k V_{k'}^* \langle c_k^\dagger(t) d(t) d^\dagger(t') c_{k'}(t') \rangle + \\ &\quad - V_k^* V_{k'} \langle d^\dagger(t) c_k(t) c_{k'}^\dagger(t') d(t') \rangle + \\ &\quad \left. + V_k^* V_{k'}^* \langle d^\dagger(t) c_k(t) d^\dagger(t') c_{k'}(t') \rangle \right] + h.c. - \langle I_L \rangle^2, \end{aligned} \quad (\text{C.2})$$

where  $\{A, B\} = AB + BA$  is an anti-commutator. The Fourier transform of  $S$  is called the noise spectrum; in what follows I shall be particularly concerned with its zero-frequency component,  $S(0) = \int d(t-t') S(t-t')$  that is the relevant quantity in the adiabatic expansion. In order to evaluate the (nonequilibrium) expectation values occurring in Eq. C.2 in a systematic way, I first define the following contour-ordered two-particle Green functions

$$\begin{aligned} G_1^{cd}(\tau, \tau') &= i^2 \langle T_C c_k^\dagger(\tau) d(\tau) c_{k'}^\dagger(\tau') d(\tau') \rangle \\ G_2^{cd}(\tau, \tau') &= i^2 \langle T_C c_k^\dagger(\tau) d(\tau) d^\dagger(\tau') c_{k'}(\tau') \rangle \\ G_3^{cd}(\tau, \tau') &= i^2 \langle T_C d^\dagger(\tau) c_k(\tau) c_{k'}^\dagger(\tau') d(\tau') \rangle \\ G_4^{cd}(\tau, \tau') &= i^2 \langle T_C d^\dagger(\tau) c_k(\tau) d^\dagger(\tau') c_{k'}(\tau') \rangle \end{aligned} \quad (\text{C.3})$$



The nonequilibrium noise correlator is then given by

$$\begin{aligned}
S(t, t') = & \frac{1}{2} \left( \frac{e}{\hbar} \right)^2 \sum_{k, k'} \left[ V_k V_{k'} G_1^{cd, >}(t, t') + \right. \\
& - V_k V_{k'}^* G_2^{cd, >}(t, t') - V_k^* V_{k'} G_3^{cd, >}(t, t') + \\
& \left. + V_k^* V_{k'}^* G_4^{cd, >}(t, t') \right] + h.c. - \langle I_L \rangle^2,
\end{aligned} \tag{C.4}$$

where  $G_i^{cd, >}(t, t')$  are the greater than components of the contour-ordered counterparts  $G_i^{cd}(\tau, \tau')$  defined in Eq. C.3. As the first step, I express the Green functions Eq. C.3 in terms of two-particle Green functions which only involve the central region operators. Following Ref. [80], here I use the S-matrix expansion because it appears more systematic. Consider then, as an example, the nonequilibrium Green function  $G_2^{cd}(\tau, \tau')$ , which I treat as follows (the other components are similar, or simpler than the chosen example)

$$\begin{aligned}
G_2^{cd}(\tau, \tau') &= i^2 \langle T_C c_k^\dagger(\tau) d(\tau) d^\dagger(\tau') c_{k'}(\tau') \rangle \\
&= i^2 \langle T_C \tilde{c}_k^\dagger(\tau) \tilde{d}(\tau) \tilde{d}^\dagger(\tau') \tilde{c}_{k'}(\tau') S \rangle,
\end{aligned} \tag{C.5}$$

where tildes denote interaction picture with respect to the tunneling coupling, and the S-matrix is

$$S = \sum_{j=0}^{\infty} \frac{(-i)^j}{j!} \int_C d\tau_1 \dots \int_C d\tau_j \langle T_C \tilde{H}_T(\tau_1) \dots \tilde{H}_T(\tau_j) \rangle \tag{C.6}$$

with the tunneling Hamiltonian

$$H_T = \sum_k \left[ V_k c_k^\dagger d + V_k^* d^\dagger c_k \right]. \tag{C.7}$$

Up to second order in  $H_T$ , the Green function Eq. C.5 becomes

$$\begin{aligned}
G_2^{cd}(\tau, \tau') &= i^2 \langle T_C \tilde{c}_k^\dagger(\tau) \tilde{d}(\tau) \tilde{d}^\dagger(\tau') \tilde{c}_{k'}(\tau') \rangle + \\
& i^2 \frac{(-i)^2}{2!} \left\langle T_C \tilde{c}_k^\dagger(\tau) \tilde{d}(\tau) \tilde{d}^\dagger(\tau') \tilde{c}_{k'}(\tau') \times \right. \\
& \times \int d\tau_1 \int d\tau_2 \sum_{k_1, k_2} \left[ V_{k_1} c_{k_1}^\dagger(\tau_1) d(\tau_1) + V_{k_1}^* d^\dagger(\tau_1) c_{k_1}(\tau_1) \right] \\
& \times \left. \left[ V_{k_2} c_{k_2}^\dagger(\tau_2) d(\tau_2) + V_{k_2}^* d^\dagger(\tau_2) c_{k_2}(\tau_2) \right] \right\rangle + \dots
\end{aligned} \tag{C.8}$$

where the dots represent higher order terms. The expectation values in Eq. C.8 can now be factorized, because in the interaction picture the  $\tilde{c}$  and  $\tilde{d}$  operators are independent. I find (by a change of dummy variables, I see that Eq. C.8 gives rise to two identical terms, thereby canceling the factor  $1/2$ )<sup>1</sup>

$$\begin{aligned}
G_2^{cd}(\tau, \tau') &= -\delta_{k, k'} g_k(\tau', \tau) G^0(\tau, \tau') - \\
& \int d\tau_1 \int d\tau_2 \sum_{k_1, k_2} V_{k_1} V_{k_2}^* \langle T_C \tilde{c}_k^\dagger(\tau) \tilde{c}_{k'}(\tau') \tilde{c}_{k_1}^\dagger(\tau_1) \tilde{c}_{k_2}(\tau_2) \rangle \times \\
& i^2 \langle T_C \tilde{d}(\tau) \tilde{d}^\dagger(\tau') \tilde{d}(\tau_1) \tilde{d}^\dagger(\tau_2) \rangle.
\end{aligned} \tag{C.9}$$

<sup>1</sup>The overall sign of the second term in Eq. C.9 is determined as follows. One requires an even number of permutations (in fact, eight) to bring all  $\tilde{c}$ 's and  $\tilde{d}$ 's adjacent to each other. The minus sign comes from the  $(-i)^2$  of the second-order expansion.

I must next consider the expectation values involving four  $\tilde{c}$ 's and four  $\tilde{d}$ 's. Since the central region may contain interactions, the  $\tilde{d}$ -terms cannot be simplified, while the noninteracting nature of the contacts allows a further factorization:

$$\begin{aligned}
& \langle T_C \tilde{c}_k^\dagger(\tau) \tilde{c}_{k'}(\tau') \tilde{c}_{k_1}^\dagger(\tau_1) \tilde{c}_{k_2}(\tau_2) \rangle = \\
& = \langle T_C \tilde{c}_k^\dagger(\tau) \tilde{c}_{k'}(\tau') \rangle \langle T_C \tilde{c}_{k_1}^\dagger(\tau_1) \tilde{c}_{k_2}(\tau_2) \rangle + \\
& + \langle T_C \tilde{c}_k^\dagger(\tau) \tilde{c}_{k_2}(\tau_2) \rangle \langle T_C \tilde{c}_{k'}(\tau') \tilde{c}_{k_1}^\dagger(\tau_1) \rangle \\
& = -\delta_{k,k'} \delta_{k_1,k_2} g_k(\tau', \tau) g_{k_1}(\tau_2, \tau_1) + \\
& + \delta_{k,k_2} \delta_{k',k_1} g_k(\tau_2, \tau) g_{k'}(\tau', \tau_1).
\end{aligned} \tag{C.10}$$

The first term of Eq. C.9 and the fourth line of Eq. C.10 can be combined:

$$\begin{aligned}
& -\delta_{k,k'} g_k(\tau', \tau) \left[ G^0(\tau, \tau') + \sum_{k_1} \int d\tau_1 \int d\tau_2 |V_{k_1}|^2 \times \right. \\
& \left. g_{k_1}(\tau_2, \tau_1) i^2 \langle T_C \tilde{d}(\tau) \tilde{d}^\dagger(\tau') \tilde{d}(\tau_1) \tilde{d}^\dagger(\tau_2) \rangle \right].
\end{aligned} \tag{C.11}$$

The quantity in square brackets is recognized as the beginning of the series expansion of the full central region Green function,

$$G(\tau, \tau') = -i \langle T_C d(\tau) d^\dagger(\tau') \rangle = -i \langle T_C \tilde{d}(\tau) \tilde{d}^\dagger(\tau') S \rangle. \tag{C.12}$$

It is straightforward to see that the higher order terms in  $H_T$ , which have  $g_k(\tau', \tau)$  as a common factor, term by term reproduce the series expansion for  $G(\tau, \tau')$ . I thus conclude that all these terms sum up to  $-\delta_{k,k'} g_k(\tau', \tau) G(\tau, \tau')$ . A similar analysis can be applied to the second line Eq. C.9. Qualitatively, the term obtained thus far can be written as (suppressing all variables)  $VV^* g^2 \langle dd^\dagger dd^\dagger \rangle$ , which is nothing but the zeroth order term of the series expansion of an interacting two-particle Green function  $G_2^{cd}(\tau, \tau')$  for the central region. Higher order terms in the S-matrix expansion generate the full series for the interacting two-particle Green function, in full analogy of what was found in Eq C.11 (though with slightly more involved combinatorics). Combining the results I have thus obtained

$$\begin{aligned}
G_2^{cd}(\tau, \tau') &= -\delta_{k,k'} g_k(\tau', \tau) G(\tau, \tau') - \\
& \int d\tau_1 \int d\tau_2 V_k^* V_{k'} g_k(\tau_2, \tau) g_{k'}(\tau', \tau_1) G_2^{dd}(\tau, \tau', \tau_1, \tau_2),
\end{aligned} \tag{C.13}$$

where

$$G_2^{dd}(\tau, \tau', \tau_1, \tau_2) = i^2 \langle T d(\tau) d^\dagger(\tau') d(\tau_1) d^\dagger(\tau_2) \rangle. \tag{C.14}$$

Similar calculations for the remaining Green functions in Eq. C.4 yield

$$\begin{aligned}
G_1^{cd}(\tau, \tau') &= -V_k^* V_{k'}^* \int d\tau_1 \int d\tau_2 g_k(\tau_1, \tau) g_{k'}(\tau_2, \tau') \times \\
& \times G_1^{dd}(\tau, \tau', \tau_1, \tau_2),
\end{aligned} \tag{C.15}$$

$$\begin{aligned}
G_3^{cd}(\tau, \tau') &= -\delta_{k,k'} g_k(\tau, \tau') G(\tau', \tau) - \\
& \int d\tau_1 \int d\tau_2 V_k V_{k'}^* g_k(\tau, \tau_1) g_{k'}(\tau_2, \tau') G_3^{dd}(\tau, \tau', \tau_1, \tau_2),
\end{aligned} \tag{C.16}$$

$$\begin{aligned}
G_4^{cd}(\tau, \tau') &= -V_k V_{k'} \int d\tau_1 \int d\tau_2 g_k(\tau, \tau_1) g_{k'}(\tau', \tau_2) \times \\
&\times G_4^{dd}(\tau, \tau', \tau_1, \tau_2),
\end{aligned} \tag{C.17}$$

where

$$\begin{aligned}
G_1^{dd}(\tau, \tau', \tau_1, \tau_2) &= i^2 \langle T d(\tau) d^\dagger(\tau') d(\tau_1) d^\dagger(\tau_2) \rangle, \\
G_3^{dd}(\tau, \tau', \tau_1, \tau_2) &= i^2 \langle T d(\tau) d^\dagger(\tau') d(\tau_1) d^\dagger(\tau_2) \rangle, \\
G_4^{dd}(\tau, \tau', \tau_1, \tau_2) &= i^2 \langle T d(\tau) d^\dagger(\tau') d(\tau_1) d^\dagger(\tau_2) \rangle,
\end{aligned} \tag{C.18}$$

respectively. I have thus far obtained

$$\begin{aligned}
S(\tau, \tau') &= \frac{1}{2} \left( \frac{e}{\hbar} \right)^2 \left\{ \sum_k |V_k|^2 \left[ g_k(\tau', \tau) G(\tau, \tau') + \right. \right. \\
&+ g_k(\tau, \tau') G(\tau', \tau) \Big] + \sum_{k, k'} |V_k|^2 |V_{k'}|^2 \int d\tau_1 \int d\tau_2 \times \\
&\times \left[ -g_k(\tau_1, \tau) g_{k'}(\tau_2, \tau') G_1^{dd}(\tau, \tau', \tau_1, \tau_2) \right. \\
&+ g_k(\tau_2, \tau) g_{k'}(\tau', \tau_1) G_2^{dd}(\tau, \tau', \tau_1, \tau_2) \\
&- g_k(\tau, \tau_1) g_{k'}(\tau_2, \tau') G_3^{dd}(\tau, \tau', \tau_1, \tau_2) \\
&\left. \left. - g_k(\tau, \tau_1) g_{k'}(\tau', \tau_2) G_4^{dd}(\tau, \tau', \tau_1, \tau_2) \right] \right\} + h.c. - \langle I_L \rangle^2
\end{aligned} \tag{C.19}$$

No approximations have been employed in arriving at Eq. C.19, and it forms an entirely general starting point for noise calculations for a large variety of systems. The next task in the general program is to extract the greater ( $\tau > \tau'$ ) part from Eq. C.19. This is straightforward for the first line, but appears complicated for the remaining terms because of the two-particle Green functions. Here, I make a Hartree-Fock level approximation to the two-particle Green functions performing the following approximation

$$\begin{aligned}
G_1^{dd}(\tau, \tau', \tau_1, \tau_2) &\approx G(\tau, \tau_2) G(\tau', \tau_1) - G(\tau, \tau_1) G(\tau', \tau_2) \\
G_2^{dd}(\tau, \tau', \tau_1, \tau_2) &\approx G(\tau, \tau') G(\tau_1, \tau_2) - G(\tau, \tau_2) G(\tau_1, \tau') \\
G_3^{dd}(\tau, \tau', \tau_1, \tau_2) &\approx G(\tau_1, \tau) G(\tau', \tau_2) - G(\tau', \tau) G(\tau_1, \tau_2) \\
G_4^{dd}(\tau, \tau', \tau_1, \tau_2) &\approx G(\tau_2, \tau) G(\tau_1, \tau') - G(\tau_1, \tau) G(\tau_2, \tau').
\end{aligned} \tag{C.20}$$

When substituting these expressions to Eq. C.19, I observe that the two kinds of terms are generated: terms where the  $\tau_1$  and  $\tau_1$ -integrals can be done separately, and terms where the two integrals are intertwined. The terms of the first kind, which I call "disconnected" terms can be shown to be perfectly canceled by the  $-\langle I_L \rangle^2$  in the Eq. C.4. This cancellation was desirable, because otherwise the zero-frequency component  $S(\omega = 0)$  would acquire an anomalous zero-frequency delta-peak. The remaining "connected" terms, which give the noise spectrum within Hartree-Fock approximation (or in any other mean-field approxima-

tion), read

$$\begin{aligned}
S(\tau, \tau') = & \frac{1}{2} \left( \frac{e}{\hbar} \right)^2 \left\{ \sum_k |V_k|^2 \left[ g_k(\tau', \tau) G(\tau, \tau') \right. \right. \\
& + g_k(\tau, \tau') G(\tau', \tau) \left. \right] + \sum_{k, k'} |V_k|^2 |V_{k'}|^2 \int d\tau_1 \int d\tau_2 \times \\
& \times \left[ -g_k(\tau_1, \tau) g_{k'}(\tau_2, \tau') G(\tau, \tau_2) G(\tau', \tau_1) \right. \\
& + g_k(\tau_2, \tau) g_{k'}(\tau', \tau_1) G(\tau, \tau') G(\tau_1, \tau_2) \\
& + g_k(\tau, \tau_1) g_{k'}(\tau_2, \tau') G(\tau', \tau) G(\tau_1, \tau_2) \\
& \left. \left. - g_k(\tau, \tau_1) g_{k'}(\tau', \tau_2) G(\tau_2, \tau) G(\tau_1, \tau') \right] \right\} + h.c. \tag{C.21}
\end{aligned}$$

I consider now the greater component of the various terms in Eq. C.21. For the first two terms the result is obtained readily:

$$\begin{aligned}
& \left[ g_k(\tau', \tau) G(\tau, \tau') + g_k(\tau, \tau') G(\tau', \tau) \right]^> \\
& = g_k^<(t', t) G^>(t, t') + g_k^>(t, t') G^<(t', t). \tag{C.22}
\end{aligned}$$

The terms with the double integrations come in two different types. The first one is, which I rearrange slightly,

$$\begin{aligned}
& \left[ \int d\tau_1 G(\tau', \tau_1) g_k(\tau_1, \tau) \int d\tau_1 G(\tau, \tau_1) g_{k'}(\tau_2, \tau') \right]^> \\
& = \int dt_1 \left[ G^r(t', t_1) g_k^<(t_1, t) + G^<(t', t_1) g_k^a(t_1, t) \right] \times \\
& \times \int dt_2 \left[ G^r(t, t_2) g_k^>(t_2, t') + G^>(t, t_2) g_k^a(t_2, t') \right]. \tag{C.23}
\end{aligned}$$

Analogously, the second type of term is written as

$$\begin{aligned}
& \left[ G(\tau, \tau') \int d\tau_1 g_k(\tau', \tau_1) G(\tau_1, \tau_2) g_{k'}(\tau_2, \tau) \right]^> \\
& = G^>(t, t') \int dt_1 \int dt_2 \left[ g_k^r(t', t_1) G^r(t_1, t_2) g_k^<(t_2, t) + \right. \\
& + g_k^r(t', t_1) G^<(t_1, t_2) g_k^<(t_2, t) + \\
& + \left. g_k^<(t', t_1) G^a(t_1, t_2) g_k^a(t_2, t) \right]. \tag{C.24}
\end{aligned}$$

The remaining terms in Eq. C.21 are treated in the same way. The resulting expression contains thirty terms, and there is no need to present it here, because its structure is obvious from the terms discussed above. I here simply consider the zero-frequency component of the noise under stationary conditions. Then, all the time integrals are convolutions, and the zero-frequency noise is simply the frequency integral:  $S(0) = \int d(t-t') S(t-t') = \int d\varepsilon / (2\pi) S(\varepsilon) \equiv S$ . After lengthly but straightforward calculations, I get the equation written in Eq. 3.49 of the main text. Equation 3.49 is a well-known, and important result. The first term accounts for thermal noise (i.e., it vanishes at zero temperature), while the second term is a nonequilibrium term, which vanishes at zero bias.

## Current-density fluctuation

For the mixed current-density contribution in the second line of Eq. 3.44 of the main text, I have (for the lead  $\alpha$ )

$$\begin{aligned}
M_\alpha(t, t') &= \langle \{ \delta I_\alpha(t), \delta n(t') \} \rangle = \\
&= \langle \{ I_\alpha(t), n(t') \} \rangle - 2 \langle I_\alpha \rangle^2 \langle n \rangle^2 \\
&= \frac{ie}{\hbar} \sum_{k_\alpha} \left[ V_{k_\alpha} \langle c_{k_\alpha}^\dagger(t) d(t) d^\dagger(t') d(t') \rangle \right. \\
&\quad \left. - V_{k_\alpha}^* \langle d^\dagger(t) c_{k_\alpha}(t) d^\dagger(t') d(t') \rangle \right] + h.c. - \langle I_\alpha \rangle^2 \langle n \rangle^2.
\end{aligned} \tag{C.25}$$

As for the the current noise spectrum  $S$  of the previous section, in what follows I shall be particularly concerned with the zero-frequency component of  $M_\alpha(t, t')$ ,  $M_\alpha(\omega = 0) = \int d(t - t') M_\alpha(t - t')$  that is the relevant quantity in the adiabatic expansion. In order to evaluate the (nonequilibrium) expectation values occurring in Eq. C.25 in a systematic way, I first define the following contour-ordered two-particle Green functions

$$\begin{aligned}
G_{1,\alpha}^{Mcd}(\tau, \tau') &= i^2 \langle T_C c_{k_\alpha}^\dagger(\tau) d(\tau) d^\dagger(\tau') d(\tau') \rangle, \\
G_{2,\alpha}^{Mcd}(\tau, \tau') &= i^2 \langle T_C d^\dagger(\tau) c_{k_\alpha}(\tau) d^\dagger(\tau') d(\tau') \rangle.
\end{aligned} \tag{C.26}$$

In terms of the previous Greens function in Eq. C.26, The nonequilibrium current-density noise correlator  $M$  is then given by

$$\begin{aligned}
M_\alpha(t, t') &= \frac{ie}{\hbar} \sum_{k_\alpha} \left[ V_{k_\alpha} G_{1,\alpha}^{Mcd,>}(t, t') + \right. \\
&\quad \left. - V_{k_\alpha}^* G_{2,\alpha}^{Mcd,>}(t, t') \right] + h.c. - \langle I_\alpha \rangle^2 \langle n \rangle^2,
\end{aligned} \tag{C.27}$$

where  $G_{i,\alpha}^{Mcd,>}(t, t')$  are the greater than components of the contour-ordered counterparts  $G_{i,\alpha}^{Mcd}(\tau, \tau')$  defined in Eq. C.26. Following the same reasoning as previous section, i.e. performing an S-matrix expansion of the above Green functions and making Hartree-Fock approximation, one can show that

$$\begin{aligned}
M_\alpha(t, t') &\simeq \frac{e}{\hbar} \left\{ G^>(t, t') \left[ \int_C d\tau_1 G(t, \tau_1) \Sigma_\alpha(\tau_1, t') \right]^< \right. \\
&\quad - G^<(t', t) \left[ \int_C d\tau_1 \Sigma_\alpha(t, \tau_1) G(\tau_1, t') \right]^> +, \\
&\quad + G^<(t, t') \left[ \int_C d\tau_1 G(t, \tau_1) \Sigma_\alpha(\tau_1, t') \right]^> \\
&\quad \left. - G^>(t', t) \left[ \int_C d\tau_1 \Sigma_\alpha(t, \tau_1) G(\tau_1, t') \right]^< \right\}.
\end{aligned} \tag{C.28}$$

where  $\Sigma_\alpha$  is the self-energy contribution due to the coupling to lead  $\alpha$  and the integration is extended along the Keldysh contour. The function,

$$f(t, t') = \left[ \int_C d\tau_1 G(t, \tau_1) \Sigma_\alpha(\tau_1, t') \right]^< \quad (\text{C.29})$$

can be calculated using Langreth's rules [80], giving

$$\begin{aligned} f(t, t') &= \int dt_1 G^r(t, t_1) \Sigma_\alpha^<(t_1, t') \\ &+ G^<(t, t_1) \Sigma_\alpha^a(t_1, t'), \end{aligned} \quad (\text{C.30})$$

where  $\Sigma_\alpha^a$  is the advanced component of the  $\alpha$ -lead self-energy. In the adiabatic approximation, I consider the zero-order terms of all functions  $G$  and  $\Sigma$ . After lengthly but straightforward calculations, starting from Eq. C.28 and taking into account that  $D^{H\lambda} = [M_L(0) - M_R(0)]/2$ , I get the first line expression in Eq. 3.48 of the main text.

# Appendix D

## The Density Matrix Renormalization Group

The simulation of a quantum mechanical system is generally a very hard task: one of the reasons is related to the number of parameters required to represent a quantum state, which usually grows exponentially with the number of constituents of the system. However, if one is interested in the ground state properties of a one-dimensional system, the number of parameters is limited for non critical systems, or grows polynomially for a critical one [175]. This means that it is possible to simulate them by considering only a relevant smaller portion of the entire Hilbert space. This is the key idea on which all the numerical renormalization algorithms rely. Starting from some microscopic Hamiltonian in a Hilbert space of dimension  $d$ , degrees of freedom are iteratively integrated out and accounted for by modifying the original Hamiltonian. The new Hamiltonian will thus exhibit modified, as well as new couplings; renormalization group approximations typically consist in physically motivated truncations of the set of couplings newly generated by the elimination of degrees of freedom. In this way one obtains a simplified effective Hamiltonian that should catch the essential physics of the system under study. The key for the success of these techniques rests on scale separation: in continuous phase transitions, for example, the diverging correlation length sets a natural low-energy scale which dominates the physical properties; fluctuations on shorter length scales may be integrated out and summed up into quantitative modifications of the long-wavelength behavior [82].

The Density Matrix Renormalization Group (DMRG) in its first formulation given by White [83, 84] is a numerical technique for finding accurate approximations to the ground state and the low-lying excited states of strongly interacting one-dimensional quantum lattice systems, such as the Heisenberg model or Bose-Hubbard models. In this Appendix, I will describe the basics of the DMRG numerical method (for a more detailed exposition, I refer the reader to Ref. [176]). In Sec. D.1, DMRG truncation idea as well as infinite and finite DMRG algorithms will be explained. In section D.2, I will discuss a method to calculate dynamical correlation functions with DMRG.

### D.1 The DMRG algorithm

As already pointed out in the introduction, the tensorial structure of the Hilbert space of a composite system leads to an exponential growth of the resources needed for the simulation with the number of the system constituents. However, if one is interested in the ground state properties of a one-dimensional system, the number of parameters is limited for non critical systems or grows polynomially for a critical one [175]. This implies that it is possible

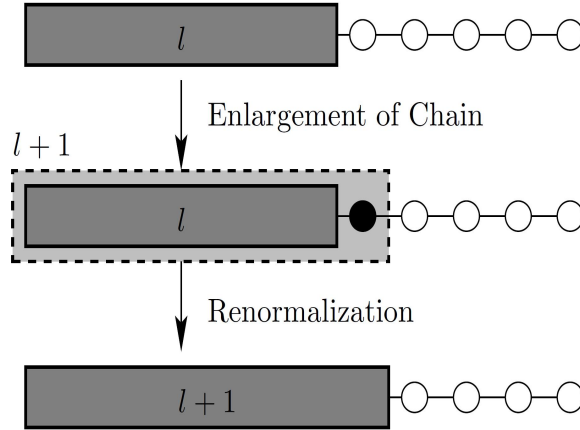


Figure D.1: Schematic plot of the real-space renormalization.

to rewrite the state of the system in a more efficient way, i.e., it can be described by using a number of coefficients which is much smaller than the dimension of the Hilbert space. Equivalently, a strategy to simulate ground state properties of a system is to consider only a relevant subset of states of the full Hilbert space. This idea is at the heart of the so called *real-space blocking renormalization group*, which I briefly describe below discussing the DMRG algorithm, and is reminiscent of the renormalization group (RG) introduced by Wilson [82].

The DMRG-algorithm starts with a quantum chain (also called *block*) of length  $l$ , that is sufficiently small to be represented numerically on a computer (Fig. D.1). Then, the chain is enlarged sequentially by one site to increase the system size. In order to reduce the exponentially growing dimension of the Hilbert space, after each enlargement step the system is projected onto a fixed number  $m$  of relevant Hilbert space states as sketched in Fig.D.1. All remaining states are cut off and neglected for the next iteration step. Obviously the crucial question arises which states are in that sense "relevant".

White and Noack[85] found that keeping only the lowest lying energy eigenstates, generally does not give a good decimation procedure. This can be understood considering the toy model of a single non-interacting particle hopping on a discrete one-dimensional lattice. If one starts with a small system, say block A in Fig.D.2, the lowest lying eigenstates (dashed curves in Fig.D.2) for the single particle in the box have nodes at the lattice end of block A. If the system is enlarged by doubling the system to obtain the compound block AA, the new lowest lying eigenstates have a maximum amplitude at the compound block center. Therefore it cannot be approximated well by a restricted number of block states, i.e. eigenstates of the two blocks which have nodes at the center of the compound block. To avoid imposing the wrong boundary conditions by considering separate blocks A, White[83] had the idea to embed the block A in some environment to mimic a larger system from the beginning.

The DMRG algorithm follows this idea using the so called density-matrix projection described in the next section as a procedure to select the relevant states [83, 84].

### D.1.1 DMRG-projection

The idea of the density-matrix projection is to embed a small system into a larger one to mimic a large system. Using the information given by the reduced density-matrix of the small system (S), the information of the 'environment' (E) is implicitly included to decide which are the relevant states to be chosen when enlarging the small system up to the desired length  $L$ . Let us describe this procedure in more detail. Assume that one has reached



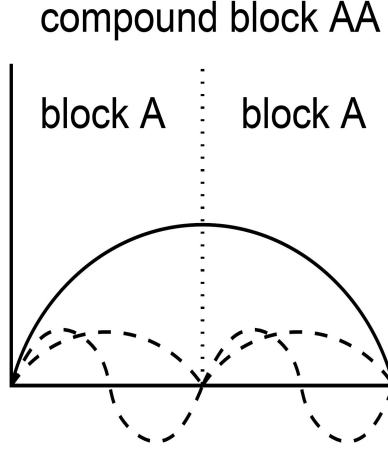


Figure D.2: Two blocks A are connected to form the compound block AA. The dashed lines are the lowest energy eigenstates of the separate blocks A, the solid line sketches the lowest energy eigenstate of the compound block AA.

a chain of length  $l$  with an  $m$ -dimensional Hilbert space with states  $\{|w_{m_l}^S\rangle\}$ . To grow the system one new site is added, i.e. the basis of the new Hilbert space  $\mathcal{H}_S$  is given by  $\{|w_{m_l}^S \sigma^S\rangle\} = \{|w_{m_l}^S\rangle |\sigma^S\rangle\}$ , where  $\{|\sigma^S\rangle\}$  are the  $N_{site}$  local states of the new site. In order to avoid strong boundary effects the system (S) is embedded into an ‘environment’ (E) which was constructed in the same way. I denote its basis states by  $\{|w_{m_l}^E \sigma^E\rangle\}$ . I call the two parts the system and the environment block, and both together the ‘superblock’. The aim of the density-matrix projection is to determine a small set of  $m^S < k := \dim \mathcal{H}_S$  states  $\{|w_{m_{l+1}}^S\rangle\} \in \mathcal{H}_S$  ( $m_{l+1} = 1 \dots m^S$ ) which are important to represent a certain state  $|\psi\rangle$ , e.g. the ground state, (also called *target state*) of the superblock

$$\begin{aligned} |\psi\rangle &= \sum_{m_l=1}^{m^S} \sum_{\sigma^S=1}^{N_{site}} \sum_{m'_l=1}^{m^E} \sum_{\sigma^E=1}^{N_{site}} \psi_{m_l \sigma^S m'_l \sigma^E} |w_{m_l}^S \sigma^S\rangle |w_{m'_l}^E \sigma^E\rangle \\ &\equiv \sum_{i,j} \psi_{ij} |i\rangle_S \otimes |j\rangle_E. \end{aligned} \quad (D.1)$$

Here, I expanded  $|\psi\rangle$  into the orthonormal bases  $|i\rangle_S$  ( $i = 1 \dots k$ ) and  $|j\rangle_E$  ( $j = 1 \dots k$ ) of the system  $\mathcal{H}_S$  and environment  $\mathcal{H}_E$ , respectively. The relevant states  $|w_{m_{l+1}}^S\rangle$  are the states which span the  $m^S$ -dimensional subspace  $\Upsilon \subset \mathcal{H}_S$  such that the vector

$$|\tilde{\psi}\rangle = \sum_{m_{l+1}j} \tilde{\psi}_{m_{l+1}j} |w_{m_{l+1}}^S\rangle \otimes |j\rangle_E, \quad (D.2)$$

minimizes the functional of the quadratic deviation

$$S(|\tilde{\psi}\rangle) := \||\tilde{\psi}\rangle - |\psi\rangle\|^2. \quad (D.3)$$

In the following it is shown that the ‘relevant’ states  $|w_{m_{l+1}}^S\rangle$  are given by the eigenvectors corresponding to the larger eigenvalues of the reduced density-matrix

$$\rho_S := Tr_E |\psi\rangle \langle \psi|, \quad (D.4)$$

where  $Tr_E := id_S \otimes Tr_E$  labels the partial trace over the environment block. I interpret the coefficients  $\psi_{ij} = \psi$  and  $\tilde{\psi}_{ij} = \tilde{\psi}$  as  $k \times k$  matrices. Then, the density-matrix  $\rho_S$  can be written as  $\rho_S = \psi \psi^\dagger$  and the functional  $S(|\psi\rangle)$  can be expressed as

$$S(\tilde{\psi}) = tr(\tilde{\psi} - \psi)^\dagger (\tilde{\psi} - \psi). \quad (D.5)$$

The functional  $S$  can be related to the eigenvalues of the reduced density-matrix by using the *singular value decomposition* theorem. According to this theorem there exist two orthogonal matrices  $U$  and  $V$  of dimension  $k \times k$  such that

$$\psi = UDV^\dagger, \quad \text{where } D = \text{diag}(\lambda_1 \dots \lambda_k). \quad (\text{D.6})$$

The so-called singular values  $\lambda_i$  are the square roots of the eigenvalues of  $\rho_S$ , since I can write

$$\rho_S = UDD^\dagger U^\dagger = UD^2U^\dagger. \quad (\text{D.7})$$

Inserting Eq. D.6 into Eq. D.5 and using the cyclic invariance of the trace, I obtain

$$S(\tilde{\psi}) = \text{Tr}(\tilde{D} - D)^\dagger(\tilde{D} - D), \quad (\text{D.8})$$

with  $\tilde{D} = U\tilde{\psi}V^\dagger$ . In this form it can be seen that  $S$  is minimized, if  $\tilde{D}$  is a diagonal matrix of rank  $m^S$ , whose diagonal elements are given by the leading singular values, i.e.

$$\tilde{D} = \text{diag}(\lambda_1, \dots, \lambda_{m^S}, 0, \dots, 0). \quad (\text{D.9})$$

Without loss of generality the  $\lambda_i$  were assumed to be sorted:  $\lambda_1 \geq \lambda_2 \geq \dots \geq \lambda_k$ . I can now explicitly construct  $|\tilde{\psi}\rangle$  which minimizes  $S$  using eigenvectors  $|w_{m_{l+1}}^S\rangle$  to leading  $m$  eigenvalues of  $\rho_S$ :

$$\begin{aligned} |\tilde{\psi}\rangle &= \sum_{ij} (U\tilde{D}V^\dagger) |i\rangle_S \otimes |j\rangle_E \\ &= \sum_{m_{l+1}} \tilde{D}_{m_{l+1}, m_{l+1}} \underbrace{\left( \sum_i U_{im_{l+1}} |i\rangle_S \right)}_{|w_{m_{l+1}}^S\rangle} \otimes \underbrace{\left( \sum_j V_{jm_{l+1}}^* |j\rangle_E \right)}_{|w_{m_{l+1}}^E\rangle} \\ &= \sum_{m_{l+1}=1}^m \lambda_{m_{l+1}} |w_{m_{l+1}}^S\rangle \otimes |w_{m_{l+1}}^E\rangle. \end{aligned} \quad (\text{D.10})$$

Note, that the same number of states has to be kept for the system and the environment block, i.e.  $m := m^S = m^E$ . If the same projection is performed interchanging the system and environment block, one finds that both reduced density-matrices have the same non-zero eigenvalues even if system and environment were different. This is also reflected in the guaranteed existence of the so-called Schmidt decomposition of the wave function [177],

$$|\psi\rangle = \sum_{\alpha} \lambda_{\alpha} |w_{\alpha}^S\rangle |w_{\alpha}^E\rangle, \quad \lambda_{\alpha} = 0. \quad (\text{D.11})$$

The number of positive  $\lambda_{\alpha}$  is bounded by the dimension of the smaller of the bases of system and environment. To summarize, I have proven that the relevant states of the system block to represent the target state, e.g. the ground state, of a larger quantum chain including the environment are optimally given by the leading  $m$  eigenvectors of the reduced density-matrix  $\rho_S$ . The performance of the method depends critically on the decay of the eigenvalues of the reduced density-matrix. Some insight into the quality of the truncation approximation made by the projection can be gained by the so-called truncated weight

$$P := 1 - \sum_{i=1}^m \lambda_i^2, \quad (\text{D.12})$$

which measures how much of the norm of  $|\psi\rangle$  is lost. However, due to the additional sources of 'environmental' (errors errors by the only approximate similarity of the environment block to the 'real' environment) the total error in the observables calculated are often much larger than the truncated weight. A good control over the total error can in most cases be obtained by a careful convergence analysis in the number  $m$  of states kept.

More information about the limits of the DMRG was obtained by [178, 179, 180, 181, 182, 183] by studying the ability of the DMRG decimation procedure to preserve the entanglement of  $\psi$  between system and environment in the context of quantum information science [177, 184]. By this a better understanding of the reasons of the breakdown of the DMRG in two-dimensional systems has been obtained in terms of the growth of bipartite entanglement in such systems [181, 183].

In the next two subsections the two DMRG algorithms, the so-called infinite-system and the finite-system algorithm[84] are introduced. Often, a combination of both algorithms is applied to obtain an increased accuracy of the numerical results.

### D.1.2 Infinite-system DMRG

The infinite-system algorithm is designed for computing the ground state (or low-energy spectrum) of a quantum chain in the thermodynamic limit ( $L \rightarrow \infty$ , where  $L$  is the desired length of the system). The main idea consists in growing the left and right blocks by adding one site at a time. As I add sites, the basis of the blocks will grow, until I reach the desired maximum number of states  $m$ . At this point I need to start applying the density matrix truncation on both blocks. This process is repeated until I reach a desired system-size, or the energy is below a pre-defined tolerance. The algorithm illustrated in Fig.D.3 could be outlined as below:

1. Construct a system of size  $l$  with the Hilbert space  $\mathcal{H}^S = \{|w_{m_l}^S\rangle\}$  with dimension  $m^S$  which is small enough to be treated exactly. The operators used, including the Hamiltonian, are known in this basis. In the same way construct the environment block.
2. Enlarge the system block by one site, i.e. the Hilbert space becomes of dimension  $N^S = m^S N_{site}$  and is formed by the states  $|w_{m_l}^S \sigma^S\rangle$ . The environment block is enlarged, similarly. The added sites are often called 'free' or 'active' sites.
3. Join the two blocks to form the superblock of length  $2l + 2$  (Fig. D.3). The dimension of the Hilbert space of the superblock is given by  $N^S N^E$ .
4. Determine the target state. If the target state is the ground state this is done by determining the ground state of the Hamiltonian of the superblock for example by the Lanczos algorithm .
5. Perform the density-matrix projection for the system, i.e. determine from the reduced density-matrix  $\rho_S$  as in Eq. D.4, the eigenvalues, ordered by their values, and the corresponding eigenstates. Form a new reduced basis by taking only the  $m^S$  eigenstates  $|w_{m_{l+1}}^S\rangle$  corresponding to the largest eigenvalues. Repeat this step to construct the reduced basis and the projection matrix for the environment.
6. Project the operators of interest acting on the system and the environment block, including the Hamiltonian, onto the new basis of the system and the environment block, respectively. The projection matrix  $T^{S/E}$  of dimension  $N^{S/E} \times m^{S/E}$  is given

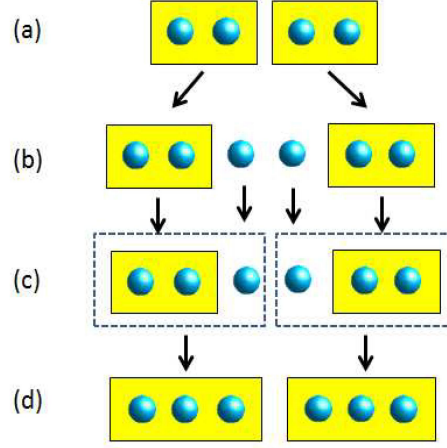


Figure D.3: Step-by-step illustration of the block-growing scheme in the infinite-size DMRG algorithm: After obtaining the new blocks from the previous step (a), I add a new site to each block (b), I build the superblock and obtain the ground-state (c), and I calculate the reduced density-matrix, and rotate to the basis of the eigenvectors with  $m$  largest eigenvalues to build the new blocks for the next step (d).

by taking the eigenvectors as columns. Repeat step (2) to (6) until the desired final length  $L$  of the system is reached.

7. Calculate the physical quantities of interest, like expectation values for the ground state energy, from the effective state obtained.

Obviously, the chain length  $l$  grows successively by each iteration step until it reaches the desired length, whereas the dimensions  $m$  of the system and the environment block stay constant. By this infinite-system analysis, highly precise estimates of various properties of the infinitely large quantum chain are possible.

The scheme given above is only a rough sketch of the DMRG algorithm. An implementation of a DMRG program generally facilitates various numerical know-how to increase the performance and to save computer memory. E.g. if some quantum numbers are conserved, the fact can be utilized to reduce operators to a block structure, such that vanishing matrix elements do not have to be stored. The most time consuming part of the algorithm is found in the computation of the ground state, step (4). Here, the Lanczos [192] or Davidson [193] algorithm are typically used due to their high performance.

### D.1.3 Finite-system DMRG

The infinite-system algorithm does not give satisfactory results in all cases of interest. Problems arise if the environment in the early growing of the chain does not resemble the system of final length closely enough, for example, if the system is inhomogeneous. Then the states retained in the early stage do not have to be important for the desired final state. Here the finite-system algorithm helps out. The idea is to optimize the chosen basis for a system of fixed length  $L$  by shifting the 'free' sites through the system. To do this the system is built up to a desired length  $L$  with the infinite-system algorithm, but in subsequent steps one of the blocks grows to the cost of the other block shrinking (see Fig. D.1.3). In each step the reduced basis transformation is only performed for the growing block. Assume the system block grows and the environment block shrinks. Then as before in the infinite-system algorithm one site is added to the system block, but at the same time one site is removed

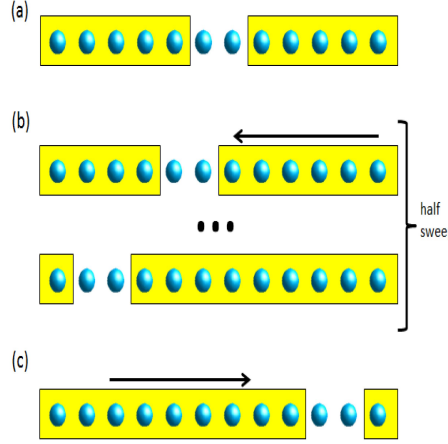


Figure D.4: Schematic illustration of the finite-size DMRG algorithm: The infinite-size iteration stops when I reach the desired system size. Then, I start sweeping from left to right, and right to left. During the sweeping iterations, one block grows, and the other one "shrinks". The shrinking block is retrieved from the blocks obtained in the previous sweep in the opposite direction, which are stored in memory or disk.

from the environment block, i.e. one has to use the previously stored basis of the smaller block. When the environment block approaches the end of the chain it becomes at some step exactly describable and the role of the shrinking and growing blocks are interchanged. A complete shrinkage and growth sequence for both blocks is called a 'sweep'. The advantage of this algorithm is that the system has reached its final length  $L$  and the chosen basis states can be optimized taking its full length into account. Usually the finite-system algorithm finds the best approximation to the ground state, and only very rarely it is trapped into some metastable state.

## D.2 Dynamical correlation functions using DMRG

Since its development, the DMRG has been successfully used to calculate static properties of ground states and low-lying excited states in various low dimensional strongly interacting systems. Energies can be determined with highest precision, and the calculation of time-independent correlation functions is easy and high accuracy can be achieved. The calculation of dynamical properties is more difficult.

Typically, the zero-temperature dynamic response of a quantum system is given by a dynamical correlation function (with  $\hbar = 1$ )

$$G_X(\omega + i\eta) = -\frac{1}{\pi} \left\langle \psi_0 \left| X^\dagger \frac{1}{E_0 + \omega + i\eta - H} X \right| \psi_0 \right\rangle, \quad (\text{D.13})$$

where  $H$  is the time-independent Hamiltonian of the system,  $E_0$  and  $|\psi_0\rangle$  are its ground-state energy and wavefunction,  $X$  is the quantum operator corresponding to the physical quantity which is analyzed, and  $X^\dagger$  is the Hermitian conjugate of  $X$ . A small real number  $\eta > 0$  is used to shift the poles of the correlation function into the complex plane. The spectral function  $G_X(\omega + i\eta)$  is also the Laplace transform (up to a constant prefactor) of the zero-temperature time-dependent correlation function

$$G_X(t \geq 0) = \langle \psi_0 | X^\dagger(t) X(0) | \psi_0 \rangle, \quad (\text{D.14})$$

where  $X(t)$  is the Heisenberg representation of the operator  $X$ . In general, one is interested in the imaginary part of the correlation function for  $\eta \rightarrow 0$

$$I(\omega + i\eta) = \Im G_X(\omega + i\eta) = \frac{1}{\pi} \left\langle \psi_0 \left| X^\dagger \frac{\eta}{(E_0 + \omega - H)^2 + \eta^2} X \right| \psi_0 \right\rangle. \quad (\text{D.15})$$

Let  $\{|n\rangle, n = 0, 1, 2, \dots\}$  be the complete set of eigenstates of  $H$  with eigenenergies  $E_n$  ( $|0\rangle$  corresponds to the ground state  $|\psi_0\rangle$ ). The spectrum D.15 can be written

$$I(\omega + i\eta) = \frac{1}{\pi} \sum_n |\langle n|X|0\rangle|^2 \frac{\eta}{(E_0 + \omega - E_n)^2 + \eta^2}. \quad (\text{D.16})$$

$E_n - E_0$  is the excitation energy and  $|\langle n|X|0\rangle|^2$  the spectral weight of the  $n$ -th excited state. Obviously, only states with a finite spectral weight contribute to the dynamical correlation function. Typically, the number of contributing excited states scales as a power of the system size  $N$  (while the Hilbert space dimension increases exponentially with  $N$ ). In principle, one can calculate the contributing excited states only and reconstruct the spectrum from the sum over these states D.16.

The simplest method for computing excited states within DMRG is to target the lowest  $M$  eigenstates  $|\psi_s\rangle$  instead of the sole ground state using the standard algorithm. In that case, the density matrix is formed as the sum

$$\rho = \sum_{s=1}^M c_s \rho_s \quad (\text{D.17})$$

of the density matrices  $\rho_s = |\psi_s\rangle\langle\psi_s|$  for each target state [188]. As a result, the DMRG algorithm produces an effective Hamiltonian describing these  $M$  states accurately. Here the coefficients  $c_s > 0$  are normalized weighting factors ( $\sum_s c_s = 1$ ), which allows to vary the influence of each target state in the formation of the density matrix. This approach yields accurate results for some problems such as the Holstein polaron [189]. In most cases, however, this approach is limited to a small number  $M$  of excited states (of the order of ten) because DMRG truncation errors grow rapidly with the number of targeted states (for a fixed number of density-matrix eigenstates kept). This is not sufficient for calculating a complete spectrum for a large system and often does not even allow for the calculation of low-energy excitations.

In the following section, I will discuss a more sophisticated technique for calculating dynamical properties expressed by Eq. D.15 and used in the last Chap. of this thesis: the Correction Vector method.

## D.2.1 Correction Vector

A very accurate approach for generating dynamical spectra is the correction vector method [186]. This method has been successfully applied in the DMRG context [187].

The correction vector method allows a very accurate calculation of a dynamical correlation function targeting a correction vector at a particular frequency. The spectrum can be calculated directly (without targeting a lot of excited states of the Hamiltonian) for a given  $z = \omega + i\eta$  including the following states must be included as target states:

$$|0\rangle \quad \text{the ground state} \quad (\text{D.18})$$

$$|X\rangle = X|0\rangle, \quad \text{the first "Lanczos" vector} \quad (\text{D.19})$$

$$|x(z)\rangle = \frac{1}{\omega - z} |X\rangle. \quad \text{the correction vector} \quad (\text{D.20})$$

Since a finite broadening factor  $\eta$  is used, the correction vector becomes complex. To avoid the use of complex numbers, I split the correction vector into real and imaginary part, both used as target states:

$$|x(z)\rangle = |x_{RE}(z)\rangle + i|x_{IM}(z)\rangle. \quad (\text{D.21})$$

The equation for the correction vector is split into real and imaginary parts  $|x_{RE}(z)\rangle$  and  $|x_{IM}(z)\rangle$ , and the imaginary part is found by solving

$$[(H - \omega)^2 + \eta^2]|x_{IM}(z)\rangle = -\eta|X\rangle \quad (\text{D.22})$$

using the conjugate gradient method[190]. Note that this equation system gets more singular as  $\omega$  gets closer to an eigenenergy of the Hamiltonian, and as the broadening factor  $\eta$  gets smaller. For large  $\eta$  the Hamiltonian is close to a diagonal matrix, and the conjugate gradient method converges much faster than for small  $\eta$ . This means that a large  $\eta$  results in short calculation times, but it also limits the resolution of the spectrum. The convergence is also slowed down because energy gaps in  $H - \omega$  are squared in Eq.D.22, and the convergence rate of the conjugate gradient method depends on the gap between the lowest and the next lowest eigenvector.

The real part of the correction vector is calculated directly:

$$|x_{RE}(z)\rangle = \frac{1}{\eta}(H - \omega)|x_{IM}(z)\rangle. \quad (\text{D.23})$$

Using the correction vector, the Green's function can be calculated directly:

$$G(z) = \langle X|x(z)\rangle. \quad (\text{D.24})$$

Taking these states ( $|0\rangle$ ,  $|X\rangle$ , and  $|x(z)\rangle$ ) as target states and optimizing the DMRG basis to represent them allows for a very precise calculation of the Green's function for a given frequency  $\omega$  and broadening factor  $\eta$ . Unfortunately, the correction vector has to be calculated separately for every  $\omega$ . If the correction vector does not change very rapidly with  $\omega$ , the DMRG basis that is optimized to represent the correction vector at a certain  $\omega$ , should also be able to represent correction vectors for nearby frequencies.

# Appendix E

## Magnetic field correction to the hopping matrix element for a particle in a tight-binding ring

Let us consider the Schrodinger equation for a single particle in a ring given by a tight-binding chain in absence of a magnetic flux threading the ring (I use  $\hbar = e = c = 1$ )

$$\left[ \left( -i \frac{\partial}{\partial x} \right)^2 + \sum_{i=1,L} V(x - R_i) \right] f(x) = E f(x), \quad (\text{E.1})$$

It can be shown that a general solution of this equation can be written as a superposition of Wannier orbitals (Ashcroft and Mermin),

$$f(x) = \sum_{i=1,L} a_i \phi(x - R_i), \quad (\text{E.2})$$

which automatically satisfies the periodic boundary condition imposed by the ring geometry

$$f(x + L) = f(x). \quad (\text{E.3})$$

With second quantization  $a_i$  ( $a_i^*$ ) are promoted to annihilation (creation) operators and the Hamiltonian is given by

$$\hat{H} = \int dx \hat{f}^\dagger(x) H(x) \hat{f}(x), \quad (\text{E.4})$$

explicitly

$$\hat{H} = \sum_{l=1,L} t(R_{l+1} - R_l) (\hat{a}_{l+1}^\dagger \hat{a}_l + \hat{a}_l^\dagger \hat{a}_{l+1}), \quad (\text{E.5})$$

where the tight binding matrix element can be written in terms of 1st quantized Wannier orbitals  $\phi(x - R_i)$  and the periodic potential  $V(x)$

$$t(R_{l+1} - R_l) = \int dx \phi^*(x - R_l) V(x - R_{l+1}) \phi(x - R_{l+1}). \quad (\text{E.6})$$

Let us suppose to consider that  $l = L$  is the first site of the left lead and that  $l + 1 = mol$  is the central molecular site of my Hamiltonian. Changing variables in the integral described above to  $x' = x - R_L$  I obtain

$$t(R_{mol} - R_L) = \int dx' \phi^*(x') V(x' - (R_{mol} - R_L)) \phi(x' - (R_{mol} - R_L)). \quad (\text{E.7})$$



Considering now the possibility that  $R_{mol}$  can change by a quantity  $\delta$  due to molecule oscillation  $R_{mol} \simeq R_{mol}^{(0)} - \delta$ , I get

$$t(R_{mol} - R_L) = \int dx' \phi^*(x') V(x' - d_{(0)} + \delta) \phi(x' - d_{(0)} + \delta), \quad (\text{E.8})$$

where I have defined  $R_{mol}^{(0)} - R_L = d_{(0)}$  as the distance between the first site of the left lead and the molecule when this latter is in its equilibrium position. Changing again the integration variables in Eq. (E.8) to  $x = x' - d_{(0)} + \delta$  I have,

$$t(R_{mol} - R_L) = \int dx \phi^*(x + d_{(0)} - \delta) V(x) \phi(x), \quad (\text{E.9})$$

and finally, if  $\delta/R_{mol}^{(0)} \ll 1$ , expanding to the first order in  $\delta$  I get

$$t(R_{mol} - R_L) = t_{(0)} - \alpha \delta, \quad (\text{E.10})$$

where,

$$t_{(0)} = \int dx \phi^*(x + d_{(0)}) V(x) \phi(x), \quad (\text{E.11})$$

and

$$\alpha = \int dx \partial_x \phi^*(x + d_{(0)}) V(x) \phi(x). \quad (\text{E.12})$$

Let us now introduce a magnetic flux threading the ring. The Eq. (E.1) modifies according to the 'minimal substitution'

$$\partial_x = \partial_x - iA(x), \quad (\text{E.13})$$

obtaining

$$\left[ \left( -i \frac{\partial}{\partial x} - A(x) \right)^2 + \sum_{i=1,L} V(x - R_n) \right] F(x) = EF(x), \quad (\text{E.14})$$

where now the solution can be expressed in terms of the old solution (Eq. (E.2)) obtained in absence of magnetic field

$$F(x) = \sum_{i=1,L} a_i \Psi(x - R_i), \quad (\text{E.15})$$

where

$$\Psi(x - R_i) = e^{-i \int_0^{x-R_i} A(x') dx'} \phi(x - R_i). \quad (\text{E.16})$$

I suppose that the vector potential is independent on  $x$  and such that  $\oint A dl = \phi$ , where  $\phi$  is the magnetic flux threading the ring. This in turn implies that  $A = \phi/L$  where  $L$  is the ring length. If the molecule is motionless and kept in its equilibrium position, from equation Eq. (E.7) I get that the hopping matrix element  $t(R_{mol} - R_L)$  modifies into

$$t_B(R_{mol} - R_L) = t(R_{mol} - R_L) e^{-i \int_{R_L}^{R_{mol}} A dx'} = t(R_{mol} - R_L) e^{-i \phi/N}, \quad (\text{E.17})$$

where  $N$  is the number of sites of the chain ( $L/d_{(0)} = N$ ).

Now I consider the magnetic flux corrections to coefficients  $t_0$  and  $\alpha$  given by Eqs. (E.11, E.12).  $t_{(0)}$  is modified trivially as in Eq. (E.17), because does not involve spatial derivatives of Wannier functions.  $\alpha$  deserves a careful observation: if one consider

$$\alpha = \int dx \partial_x \Psi^*(x + d_{(0)}) V(x) \Psi(x), \quad (\text{E.18})$$

trasforming **only** the wave function one obtain an imaginary correction term (taking into account Eq. (E.16))

$$\alpha = \alpha_{(0)} + i \phi/L, \quad (\text{E.19})$$

and  $\alpha$  gets a non trivial correction term due to magnetic flux.

# Bibliography

- [1] N. J. Tao, Nat. Nanotechnol. (2006), **1**, 173.
- [2] M. P. Blencowe, Contemporary Physics, **46**, 249-264, (2005).
- [3] G. E. Moore, Electronics Magazine, Vol. **38**, Number 8, April 19, (1965).
- [4] T. Ito and S. Okazaki, Nature **406**, 1027-1031 (2000).
- [5] A. Aviram and M.A. Ratner, Chem. Phys. Lett. **29**, 277 (1974).
- [6] M.A. Reed, C. Zhou, C.J. Muller, T.P. Burgin, and J.M. Tour, Science **278**, 252 (1997).
- [7] A. S. Blum, J. G. Kushmerick, *et al.*, Nat. Mater. **4**, 167-172. (2005).
- [8] S. Kubatkin, A. Danilov, M. Hjort, J. Cornil, J.-L. Bredas, N. Stur-Hansen, P. Hedegard, and T. Bjørnholm, Nature **425**, 698–701 (2003).
- [9] D. M. Eigler, C. P. Lutz, and W. E. Rudge, Nature **352**, 600–603 (1991).
- [10] S. J. Tans, A. R. M. Verschueren, and C. Dekker, Nature **393**, 49–52 (1998).
- [11] G. A. Steele, A. K. Huttel, B. Witkamp, M. Poot, H. B. Meerwaldt, L. P. Kouwenhoven, and H. S. J. van der Zant, *Science* **325**, 1103 (2009).
- [12] A. K. Huttel, G. A. Steele, B. Witkamp, M. Poot, L. P. Kouwenhoven, and H. S. J. van der Zant, *Nano Lett.* **9**, 2547 (2009).
- [13] P. K. Hansma, Physics Reports **30**(2), 145-206 (1977).
- [14] R. D. Mattuck, *A Guide to Feynman Diagrams in the Many-Body Problem*, Dover Publications, Inc., Mineola, N. Y., 2nd edition, 1992 (Republication of work from 1976).
- [15] B. C. Stripe, M. A. Rezaei, and W. Ho, Science **280**, 1732–1735 (1998).
- [16] D. Kockmann, B. Poelsema, and H. J. W. Zandvliet, Nano Lett., **9** (3), 1147-1151, 2009.
- [17] J. Morekin and J. W. Ekin, J. Appl. Phys. **58**, 3888-3895 (1985).
- [18] H. Park, A. K. L. Lim, A. P. Alivisatos, J. Park, and P. L. McEuen, Appl. Phys. Lett. **75**, 301-303 (1999).
- [19] H. Park, J. Park, A. K. L. Lim, E. H. Anderson, A. P. Alivisatos, and P. L. McEuen, Nature **407**, 57–60 (2000).
- [20] S. Braig and K. Flensberg, Phys. Rev. B **68**, 205324 (2003).
- [21] T. Novotny, A. Donarini, and A.-P. Jauho, Phys. Rev. Lett. **90**, 256801 (2003).

- [22] R. H. M. Smit, Y. Noat, C. Untiedt, N. D. Lang, M. C. van Hemert, and J. M. van Ruitenbeek, *Nature* **419**, 906–909 (2002).
- [23] J. Chen, M. A. Reed, A. M. Rawlett and J. M. Tour, *Science* **286**, 1550-1552 (1999).
- [24] F. Chen, J. He, C. Nuckolls, T. Roberts, J. E. Klare, and S. Lindsay, *Nano Letters* **5**, 503-506, (2005).
- [25] B. Xu, P. Zhang, X. Li and N. Tao, *Nano Letters* **4**, 1105-1108 (2004).
- [26] M. Galperin, A. Nitzan and M. A. Ratner, *Nano Lett.*, **5**(1), 125 (2005).
- [27] D. Mozyrsky, M. B. Hastings, and I. Martin, *Phys. Rev. B* **73**, 035104 (2006).
- [28] F. Pistolesi, Ya. M. Blanter, and I. Martin, *Phys. Rev. B* **78**, 085127 (2008).
- [29] A. Nocera, C. A. Perroni, V. Marigliano Ramaglia, and V. Cataudella, *Phys. Rev. B* **83**, 115420 (2011).
- [30] Z. K. Keane, J. W. Ciszek, J. M. Tour and D. Natelson, *Nano Letters* **6** 1518-21 (2006).
- [31] R. A. Kiehl, J. D. Le, P. Candra, R. C. Hoyer and T. R. Hoyer, *Applied Physics Letters* **88** 172102 (2006).
- [32] W. Wang, T. Lee, M. A. Reed, *Phys. Rev. B* **68**, 035416 (2003).
- [33] Y. Selzer; M. A. Cabassi, T. S. Mayer, D. L. Allara, *J. Am. Chem. Soc.*, **126**, 4052 (2004).
- [34] D. R. Stewart, D. A. A. Ohlberg, P. A. Beck, C. N. Lau, R. Stanley Williams, *Appl. Phys. A*, **80**, 1379 (2005).
- [35] M. Poot, E. Osorio, K. O'Neill, J. M. Thijssen, D. Vanmaekelbergh, C. A. van Walree, L. W. Jenneskens and H. S. J. van der Zant, *Nano Letters* **6** 1031-5, (2006).
- [36] S. Skourtis and A. Nitzan, *The Journal of Chemical Physics* **119** 6271-6276 (2003).
- [37] X. M. H. Huang, C. A. Zorman, M. Mehregany, and et al., *Nature*, **421**, 496, (2003)
- [38] H. G. Craighead, *Science* **290**, 1532 (2000).
- [39] A. N. Cleland. *Foundations of Nanomechanics*. Springer, Heidelberg, 2002.
- [40] R. H. Blick, A. Erbe, L. Pescini, and et.al., *J. Phys.: Cond. Matter.*, **14** R905-945, (2002).
- [41] R. Knobel and A. N. Cleland, *Nature* **424**, 291 (2003).
- [42] M. D. LaHaye, O. Buu, B. Camarota and K. C. Schwab, *Science* **304**, 74 (2004).
- [43] K. L. Ekinci, M. L. Roukes, *Rev. Sci. Instrum.* **76**, 061101 (2005).
- [44] K. C. Schwab, M. L. Roukes, *Phys. Today* **58**, 36 (2005).
- [45] A. Cho. *Science*, **299** 36-37, (2003).
- [46] M. P. Blencowe, *Science*, **304** 56-57, (2004).

- [47] A. Naik, O. Buu, M. D. LaHaye, and *et.al.*, Nature, **443**, 193-196, 2006.
- [48] H. B. Meerwaldt, G. A. Steele, H. S. J. van der Zant, arXiv:1205.4921v1 [cond-mat.mes-hall], To appear in "Fluctuating Nonlinear Oscillators", Oxford University Press, edited by Mark Dykman.
- [49] A. Nocera, C. A. Perroni, V. Marigliano Ramaglia, and V. Cataudella, Phys. Rev. B **86**, 035420 (2012).
- [50] A. Nocera, C. A. Perroni, V. Marigliano Ramaglia, and V. Cataudella, arXiv:1212.0267 [cond-mat.mes-hall].
- [51] A. C. Hewson, The Kondo Problem to Heavy Fermions (Cambridge University Press, 1993).
- [52] S. Y. Savrasov, G. Kotliar, and E. Abrahams, Nature **410** (2001).
- [53] J. H. Shim, K. Haule, and G. Kotliar, Nature **446**, 513 (2007).
- [54] L. P. Kouwenhoven and L. I. Glazman, Phys. World **14**, 33 (2001).
- [55] D. Goldhaber-Gordon et al., Nature **391**, 156 (1998).
- [56] S. M. Cronenwett, T. H. Oosterkamp, and L. P. Kouwenhoven, Science **281**, 540 (1998).
- [57] W. Liang et al., Nature (London) **417**, 725 (2002)
- [58] L. H. Yu *et al.*, Nano Lett. **4**, 79 (2004).
- [59] A. N. Pasupathy et al., Nano Lett. **5**, 203 (2005).
- [60] A. Zhao, Q. Li, L. Chen, H. Xiang, W. Wang, S. Pan, B. Wang, X. Xiao, J. Yang, J. G. Hou, Q. Zhou, Science **309**, 1542- 1544 (2005).
- [61] L. H. Yu *et al.*, Phys. Rev. Lett. **93**, 266802 (2004).
- [62] H. Park *et al.*, Nature (London) **407**, 57 (2000).
- [63] J. J. Parks, A. R. Champagne, G. R. Hutchison, S. Flores-Torres, H. D. Abruna, and D. C. Ralph *Phys. Rev. Lett.* **99**, 026601 (2007).
- [64] V. Madhavan *et al.*, Science **280**, 567 (1998).
- [65] J. Li, W.-D. Schneider, R. Berndt, B. Delley, Phys. Rev. Lett. **80**, 2893-2896 (1988).
- [66] W. G. van der Wiel, S. De Franceschi, T. Fujisawa, J. M. Elzerman, S. Tarucha, and L. P. Kouwenhoven, Science, **289** 2105-2108, (2000).
- [67] T. Rejec and Y. Meir, Nature **442**, 900-903 (2006).
- [68] B. J. van Wees et al., Phys. Rev. Lett. **60**, 848 (1988).
- [69] Y. Meir, N. S. Wingreen, and P. A. Lee. Phys. Rev. Lett., **70** 2601-2604, (1993).
- [70] L. Y. Gorelik, A. Isacsson, M. V. Voinova, B. Kasemo, R. I. Shekhter, and M. Jonson. Phys. Rev. Lett., **80** 4526-4529, (1998).
- [71] D. Fedorets, Phys. Rev. B, **68** 033106 (2003).

- [72] D. Fedorets, L. Y. Gorelik, R. I. Shekhter, and M. Jonson. Europhysics Letters (EPL), **58** 99-104, (2002).
- [73] D. Fedorets, L. Y. Gorelik, R. I. Shekhter, and M. Jonson, Phys. Rev. Lett., **92** 166801, (2004).
- [74] T. Novotny, A. Donarini, and A.-P. Jauho, Phys. Rev. Lett., **90** 256801, (2003).
- [75] T. Novotny, A. Donarini, C. Flindt, and A.-P. Jauho, Phys. Rev. Lett., **92** 248302, (2004).
- [76] D.V. Scheible *et al.*, Phys. Rev. Lett. **93**, 186801 (2004), D.V.Scheible, R.H.Blick, Appl.Phys.Lett. **84**, 4632 (2004).
- [77] A.Erbe *et al.*, Phys. Rev. Lett. **87**, 096106 (2001).
- [78] S. Datta, *Electronic Transport in Mesoscopic Systems* (Cambridge University Press, Cambridge, 1995).
- [79] R. Kubo, Rep. Prog. Phys. 29, 255-284 (1966).
- [80] H. Haug and A.-P. Jauho, *Quantum Kinetics in Transport and Optics of Semiconductors*, 2nd ed.,Springer, 2008.
- [81] L.V. Keldysh, Zh. Eksp. Teor. Fiz. **47**, 1515 (1964). [Sov. Phys. JETP **20**, 1018 (1965)]
- [82] K. Wilson, Rev. Mod. Phys. **47**, 773 (1975).
- [83] S. R. White, Phys. Rev. Lett. **69**, 2863 (1992).
- [84] S. R. White, Phys. Rev. B **48**, 10345 (1993).
- [85] *Density-Matrix Renormalization*, edited by I. Peschel, X. Wang, M. Kaulke, and K. Hallberg (Springer, Berlin, 1999).
- [86] U. Schollwöck, Annals of Physics 326, 96 (2011).
- [87] S. R. White and A. E. Feiguin, Phys. Rev. Lett. **93**, 076401 (2004).
- [88] Daley A. *et al.*, J. Stat. Mech. (2004) P04005.
- [89] L. G. G. V. Dias da Silva, F. Heidrich-Meisner, A. E. Feiguin, C. A. Busser, G. B. Martins, E. V. Anda, and E. Dagotto, Phys. Rev. B **78**, 195317 (2008).
- [90] S. Kirino, T. Fujii, J. Zhao, K. Ueda, J. Phys. Soc. Japan **77**, 084704 (2008); S. Kirino *et al.*, Physica E, Vol. **42**, 2010, pp 874-877.
- [91] Y. Meir and N.S. Wingreen, Phys. Rev. Lett. **68**, 2512 (1992)
- [92] Gerald D. Mahan, Many Particle Physics, Plenum, 3rd edition, 2000.
- [93] A. L. Fetter, J. D. Walecka: Quantum Theory of Many-Particle Systems (McGraw-Hill, New York, 1991).
- [94] J. Rammer, Quantum Field theory of non equilibrium states, Cambridge University Press, 2007.

- [95] Reed M.A., Zhou C., Muller C.J., Burgin T.P., Tour J.M., *Science* **278**, 252 (1997)
- [96] Reichert, J. et al. *Phys. Rev. Lett.* **88**, 176804 (2002).
- [97] T. Holstein, *Ann. Phys. (N.Y.)* **8**, 325 (1959).
- [98] M. Galperin, M. A. Ratner, and A. Nitzan, *J. Phys.: Condens. Matter* **19**, 103201 (2007).
- [99] Wang W., Lee T., Kretzschmar I. and Reed M. A., *Nano Lett.* **4**, 643 (2004).
- [100] D. A. Ryndyk, R. Gutierrez, B. Song and G. Cuniberti, Preprint 0805.0628v1, (2008).
- [101] J. Koch and F. von Oppen, *Phys. Rev. Lett.* **94**, 206804 (2005).
- [102] J. Koch, F. von Oppen and A. V. Andreev, *Phys. Rev. B* **74**, 205438 (2006).
- [103] F. Cavaliere, E. Mariani, R. Leturcq, C. Stampfer and M. Sassetti, *Phys. Rev. B* **81**, 201303 (2010).
- [104] R. Hussein, A. Metelmann, P. Zedler, and T. Brandes, *Phys. Rev. B* **82**, 165406 (2010).
- [105] J. Splettstoesser, M. Governale, J. König, and R. Fazio, *Phys. Rev. Lett.* **95**, 246803 (2005).
- [106] F. Cavaliere *et al.*, *New J. Phys.* **10**, 115004 (2008).
- [107] W. P. Su, J. R. Schrieffer, and A. J. Heeger, *Phys. Rev. Lett.* **42**, 1698 (1979).
- [108] A. J. Heeger, S. Kivelson, and J. R. Schrieffer, *Rev. Mod. Phys.* **60**, 781 (1988).
- [109] H. Ness, S. A. Shevlin, and A. J. Fisher, *Phys. Rev. B* **63**, 125422 (2001).
- [110] Y. Asai, *Phys. Rev. B* **78**, 045434 (2008).
- [111] G. A. Kaat and K. Flensberg, *Phys. Rev. B* **71**, 155408 (2005).
- [112] R. Messina and R. Passante, *Phys. Rev. A* **76**, 032107 (2007).
- [113] R. L. Honeycutt, *Phys. Rev. A* **45**, 600 (1992).
- [114] R.L. Honeycutt, *Phys. Rev. A* **45**, 604-610 (1992).
- [115] J. D. Bao, R. W. Li, W. Wu, *J. Comput. Phys.* **197**, 241 (2004).
- [116] A. Mitra , I. Aleiner and A. Millis, *Phys. Rev. Lett.* **94**, 076404 (2005).
- [117] B. Witkamp, M. Poot, and H. S. J. van der Zant, *Nano Lett.* **6**, 2904 (2006).
- [118] A. D. O'Connell, M. Hofheinz, M. Ansmann, R. C. Bialczak, M. Lenander, E. Lucero, M. Neeley, D. Sank, H. Wang, M. Weides, J. Wenner, J. M. Martinis, and A. N. Cleland, *Nature* **464**, 697 (2010).
- [119] N. Bode, S. V. Kusminskiy, R. Egger, and F. von Oppen, *Phys. Rev. Lett.* **107**, 036804 (2011).
- [120] N. Bode, S. V. Kusminskiy, R. Egger, and F. von Oppen, *Beilstein J. Nanotechnol.* **3**, 144 (2012).

- [121] G. Weick, and Dominique M.-A. Meyer, *Phys. Rev. B* **84**, 125454 (2011).
- [122] A. Metelmann, and T. Brandes, *Phys. Rev. B* **84**, 155455 (2011)
- [123] R. Hussein, A. Metelmann, P. Zedler, and T. Brandes, *Phys. Rev. B* **82**, 165406 (2010).
- [124] G. Labadze and Ya. M. Blanter, arXiv:1007.5186 [cond-mat.mes-hall] (2010).
- [125] S. D. Bennett, L. Cockins, Y. Miyahara, P. Grutter, and A. A. Clerk, *Phys. Rev. Lett.* **104**, 017203 (2010).
- [126] Ya. M. Blanter, O. Usmani, and Yu. V. Nazarov, *Phys. Rev. Lett.* **93**, 136802 (2004).
- [127] Ya. M. Blanter, O. Usmani, and Yu. V. Nazarov, *Phys. Rev. Lett.* **94**, 049904(E) (2005).
- [128] A. D. Armour, M. P. Blencowe, and Y. Zhang, *Phys. Rev. B* **69**, 125313 (2004).
- [129] G. Weick, F. von Oppen, and F. Pistolesi, *Phys. Rev. B* **83**, 035420 (2011).
- [130] S. Ramakrishnan, Y. Gulak, and H. Benaroya, *Phys. Rev. B* **78**, 174304 (2008).
- [131] T. Holstein, *Ann. Phys. (N.Y.)* **8**, 325 (1959).
- [132] N. Traverso Ziani, G. Piovano, F. Cavaliere, and M. Sassetti, *Phys. Rev. B* **84**, 155423 (2011).
- [133] A. A. Clerk and S. Bennett, *New J. Phys.* **7**, 238 (2005).
- [134] F. Pistolesi and S. Labarthe, *Phys. Rev. B* **76**, 165317 (2007).
- [135] A. H. Nayfeh and D. T. Mook, *Nonlinear oscillations* (Wiley Classics Library Edition, 1995).
- [136] D. R. Schmid, P. L. Stiller, Ch. Strunk, A. K. Huettel, *New Journal of Physics* **14**, 083024 (2012).
- [137] J. O. Island, V. Tayari, A. C. McRae, and A. R. Champagne, *Nano Lett.* **12**, 4564-4569 (2012).
- [138] B. Witkamp, M. Poot, and H. S. J. van der Zant, *Nano Lett.* **6**, 2904 (2006).
- [139] H. B. Meerwaldt, G. Labadze, B. H. Schneider, A. Taspinar, Y. M. Blanter, H. S. J. van der Zant, G. A. Steele, *Phys. Rev. B* **86**, 115454 (2012).
- [140] D. H. Cobden and J. Nygard, *Phys. Rev. Lett.* **89**, 046803 (2002).
- [141] M. Bockrath, D. H. Cobden, P. L. McEuen, N. G. Chopra, A. Zettl, A. Thess, and R. E. Smalley, *Science* **275**, 1922 (1997).
- [142] S. J. Tans, M. H. Devoret, H. Dai, A. Thess, R. E. Smalley, L. J. Geerligs, and C. Dekker, *Nature (London)* **386**, 474 (1997).
- [143] F. Cavaliere, E. Mariani, R. Leturcq, C. Stampfer, and M. Sassetti *Phys. Rev. B* **81**, 201303 (2010)

- [144] C.A. Perroni, A. Nocera, V. Marigliano Ramaglia, and V. Cataudella, Phys. Rev. B **83**, 245107 (2011).
- [145] C.A. Perroni, V. Marigliano Ramaglia, and V. Cataudella, Phys. Rev. B **84**, 014303 (2011).
- [146] F. Gargiulo, C.A. Perroni, V. Marigliano Ramaglia, and V. Cataudella, Phys. Rev. B **84**, 245204 (2011); V. Cataudella, G. De Filippis and C.A. Perroni, Phys. Rev. B **83**, 165203 (2011).
- [147] C.A. Perroni and V. Cataudella, Phys. Rev. B **85**, 155205 (2012); C.A. Perroni and V. Cataudella, Europhysics Letters **98**, 47004 (2012).
- [148] R. I. Shekhter, L.Y. Gorelik, L. I. Glazman, and M. Jonson, Phys. Rev. Lett. **97**, 156801 (2006).
- [149] D. Radic, A. Nordenfelt, A. M. Kadigrobov, R. I. Shekhter, M. Jonson, and L.Y. Gorelik, Phys. Rev. Lett. **107**, 236802 (2011).
- [150] working in progress
- [151] G. Rastelli, M. Houzet, L. I. Glazman and F. Pistolesi, Comptes Rendus Physique **13**(5) 410-425 (2012).
- [152] G. Rastelli, M. Houzet and F. Pistolesi, Eur. Phys. Lett., **89** 57003 (2010).
- [153] G. A. Skorobogatko, S. I. Kulinich, I. V. Krive, R. I. Shekhter, and M. Jonson, Low Temp. Phys., **37**(12), 1032-1037 (2011).
- [154] L. I. Glazman and M. E. Raikh, Pis'ma Zh. Eksp. Teor. Fiz. **47**, 378 (1988) [JETP Lett. **47**, 452 (1988)]; T. K. Ng and P. A. Lee, Phys. Rev. Lett. **61**, 1768 (1988); J. Paaske *et al.*, Phys. Rev. B **70**, 155301 (2004).
- [155] A. Mitra *et al.*, Phys. Rev. B **69**, 245302 (2004), and references therein; E. Vernek *et al.*, Phys. Rev. B **72**, 121405(R) (2005).
- [156] K. A. Al-Hassanieh, C. A. Busser, G. B. Martins, and E. Dagotto, Phys. Rev. Lett. **95**, 256807 (2005).
- [157] J. Mravlje and A. Ramsak, Phys. Rev. B **78**, 235416 (2008).
- [158] C. A. Balseiro, P. S. Cornaglia, and D. R. Grempel, Phys. Rev. B **74**, 235409 (2006)
- [159] L. G. D. Silva, E. Dagotto, Phys. Rev. B **79** 155302 (2009)
- [160] T. Rejec and A. Ramsak, Phys. Rev. B **68**, 035342 (2003)
- [161] V. Meden, U. Schollwöck, Phys. Rev. B **67**, 035106 (2003); Phys. Rev. B **67**, 193303 (2003). See also R. A. Molina *et al.*, Eur. Phys. J. B **39**, 107 (2004).
- [162] A. E. Feiguin, C. A. Busser, Phys. Rev. B, **84**, 115403 (2011).
- [163] V. Ferrari *et al.*, Phys. Rev. Lett. **82**, 5088 (1999)
- [164] T. D. Kühner and S. R. White, Phys. Rev. B **60**, 335-343 (1999).
- [165] S. R. White and A. E. Feiguin, Phys. Rev. Lett. **93**, 076401 (2004).



- [166] C. Zhang, E. Jeckelmann and S. R. White, Phys. Rev. B **60**, 14092-14104 (1999).
- [167] E. Gull, *et al.*, Rev. Mod. Phys. **83**, 349 (2011).
- [168] R. Bulla, T. A. Costi, and T. Pruschke, Rev. Mod. Phys. **80**, 395 (2008).
- [169] C. L. Kane and Matthew P. A. Fisher, Phys. Rev. Lett. **5** 68, 1220 (1992)
- [170] P. Simon, and I. Affleck, Phys. Rev. B **64**, 085308 (2001).
- [171] F. Verstraete, M. M. Wolf, D. Perez-Garcia, and J. I. Cirac, Phys. Rev. Lett. **96**, 220601 (2006); N. Schuch, M. M. Wolf, F. Verstraete, and J. I. Cirac, Phys. Rev. Lett. **100**, 030504 (2008).
- [172] O. P. Sushkov, Phys. Rev. B, **64**, 155319 (2001).
- [173] C. Zhang, E. Jeckelmann, and S. R. White, Phys. Rev. Lett. **80**, 2661-2664 (1998).
- [174] S. R. White, Phys. Rev. B **72**, 180403(R) (2005).
- [175] G. Vidal, Phys. Rev. Lett. **91**, 147902 (2003).
- [176] U. Schollwock, Rev. Mod. Phys. **77**, 259 (2005).
- [177] M. A. Nielsen and I. L. Chuang. Quantum computation and quantum communication. Cambridge University Press, 2000.
- [178] T. J. Osborne and M. A. Nielsen, Quant. Inf. Proc., **1** 45, (2002).
- [179] C. M. Dawson and M. A. Nielsen, Phys. Rev. A, **69** 052316 (2004).
- [180] H. L. Haselgrove, M. A. Nielsen, and Osborne, Phys. Rev. A, **69** 032303 (2004).
- [181] G. Vidal, J. I. Latorre, E. Rico, and A. Kitaev, Phys. Rev. Lett., **90** 227902 (2003).
- [182] J. Gaite, quant-ph/0301120, 2003.
- [183] J. I. Latorre, E. Rico, and G. Vidal, Quant. Inf. and Comp., **4** 048 (2003).
- [184] C. H. Bennett and D. P. DiVincenzo, Nature **404** 247 (2000).
- [185] K. A. Hallberg, Phys. Rev. B **52**, 9827 (1995).
- [186] Z. G. Soos and S. Ramasesha, J. Chem. Phys. **90**, 1067 (1989).
- [187] S. Ramasesha, S. K. Pati, H. R. Krishnamurthy, Z. Shuai, and J. L. Bredas, Synth. Met. **85**, 1019 (1997).
- [188] S.R.White, D.A. Huse, Phys. Rev. B **48**(6), 3844 (1993)
- [189] E. Jeckelmann, H. Fehske, in Proceedings of the International School of Physics "Enrico Fermi" - Course CLXI Polarons in Bulk Materials and Systems with Reduced Dimensionality (IOS Press, Amsterdam, 2006), pp. 247-284.
- [190] W. H. Press, B. P. Flannery, S. A. Teukolsky, and W. T. Vetterling, Numerical Recipes in FORTRAN: The Art of Scientific Computing, 2nd ed. Cambridge, England: Cambridge University Press, pp. 413-417, 1992.

- [191] S. R. White and A. E. Feiguin, Phys. Rev. Lett. **93**, 076401 (2004).
- [192] C. Lanczos, J. Res. Nat. Bur. Stand. **45**, 255 (1950). D. G. Pettifor e D. L. Weaire, The Recursion Method and Its Applications, Springer Series in Solid-State Sciences, Vol. 58 (Springer, Berlin/Heidelberg, 1985).
- [193] E. Davidson, Computers in Physics **7**, 519 (1993); J. Comput. Phys. **17**, 87 (1975).

# Acknowledgments

Desidero ringraziare innanzitutto il Dott. Carmine Antonio Perroni e il Prof. Vittorio Cataudella per gli insegnamenti e il sostegno che mi hanno dato durante tutto il triennio di Dottorato. La loro presenza è stata costante e fondamentale per il mio percorso di formazione. Un ringraziamento speciale è rivolto al Prof. Marigliano per i suoi consigli sia nell'ambito dell'attività di ricerca che nella vita privata.

Volevo ringraziare il Prof. Adrian Feiguin per avermi concesso la possibilità di studiare nel suo gruppo di ricerca nella graziosa Laramie (Wyoming, USA). Lo ringrazio per i suoi insegnamenti, i suoi consigli e soprattutto per la sua pazienza, ospitalità e disponibilità. Un saluto particolare a Carlos Busser e a Mohammad Soltanieh-ha per avermi accompagnato come un amico nella mia prima esperienza di vita all'estero.

Un doveroso ringraziamento al coordinatore del Dottorato, Prof. Settimio Mobilio, a Francesca Federici e Susanna Venezia per la loro pazienza e per aver gestito egregiamente la parte burocratica del mio Dottorato.

Ringrazio il Dott. Fabio Cavaliere e la Prof. Maura Sassetti per i consigli e le utilissime discussioni fatte durante le diverse visite a Genova e Napoli.

Un ringraziamento ad Andreas Huttel per lo scambio di idee ed avermi invitato a Regensburg per il mio primo seminario all'estero.

Ringrazio tutti "i ragazzi" dell'aula dottorandi che hanno accompagnato le mie giornate di studio all'università.

Un pensiero d'affetto ai miei amici di sempre, Dario e Mimmo che hanno condiviso con me la maggior parte dei momenti di svago e divertimento in questo triennio. Un saluto particolare al mio amico "Lussemburghese" Giuseppe con cui ho condiviso una piacevole vacanza in Calabria.

Ringrazio i miei genitori e miei fratelli che mi hanno sostenuto sia nei momenti di gioia che in quelli di difficoltà, senza di loro non avrei mai raggiunto questo traguardo.

Infine, un tenero bacio è rivolto alla "mia" Sara, che mi ha sostenuto con il suo amore e la sua pazienza, condividendo tutte le mie scelte durante l'arco del Dottorato.